FLOW IN AXIAL TURBOMACHINERY CASCADES

by

Ashok Kumar Singhal

Thesis submitted for the degree of
Doctor of Philosophy
in the Faculty of Engineering
University of London
and
for the Diploma of Membership
of Imperial College

Mechanical Engineering Department
Imperial College of Science and Technology
London SW7, England

May 1977

TO MY WIFE, SANGEETA

ABSTRACT

A numerical procedure is described for predicting steady, two-dimensional flow in axial turbomachinery cascades. The procedure is of the finite-difference type and its main distinguishing features are:

(a) steady-flow equations are solved in a physical plane;

(b) a non-orthogonal coordinate system is employed in which streamlines form one set of grid lines; and

(c) the solution is obtained by an iterative, forward-marching, integration scheme which requires one-dimensional storage for all variables except pressure.

As a result of the above-mentioned features, the procedure is simple, accurate and economical. It is widely applicable too. For instance, it can be used for incompressible, subsonic, supersonic or transonic flows. Viscous effects, including those of turbulence, can be accounted for, and if desired the heat transfer can also be calculated simultaneously. The cascade can be stationary or rotating, and the axial variations of blade-tip radii are permissible.

An experimental investigation of flow through an impulse cascade is also reported. Small flaps are attached at the trailing edges of the blades; and the flap inclination is regarded as the main parameter of the study.

Measurements of pressures and velocities are taken by using pitot probes. It is observed that the flow is affected very significantly even by the small flaps (e.g. flap length/blade chord = $\frac{1}{8}$).

Finally, the prediction procedure is validated by solving a number of problems which cover a wide range of geometry and flow conditions. The selected examples have been divided into three groups. In the first one, flow is assumed to be inviscid. Eight problems, for which analytical or experimental data are available, have been selected. In each case, computed results are compared with the available data and good agreement is observed. In the second group only one cascade is considered. The flow is treated as turbulent and the calculations are made with and without heat transfer. The computed results are quite plausible; there are no experimental data for comparing the heat-transfer predictions. In the last group, the present experimental flow situations are simulated. It is observed that the effects of training-edge flaps are predicted very satisfactorily.

These examples verify the capabilities and usefulness of the developed procedure.

PREFACE

This thesis presents the main result of my research activities at Imperial College during the period July 1974 to May 1977. The major efforts and time have been spent in the development of prediction procedures for fluid-flow and heat-transfer problems which have direct application in the industry. This was motivated by my supervisor, Professor D. Brian Spalding, and by my previous work experience with the Tata Consulting Engineers, Bombay, India.

For the first one year I used the GENMIX program, Patankar and Spalding (1970), for the following two purposes:

(i) To predict flow and heat transfer in a number of parabolic flow situations.

(ii) To test and demonstrate the applicability of the k-ε model of turbulence for the external boundary layers under a large variety of stream-wise pressure gradients.

The problems of the first group comprised of: diffusion flames, ejectors (confined jet flows), flow in diffusers, flow with transpiration cooling, flow over rough surfaces, unsteady heat conduction, and unsteady lake flow. In the second group, the test cases of the following two conferences were solved:

(i) The Stanford conference on turbulent boundary layers, held at the Stanford University, USA in 1968.

(ii) The Euromech (60) colloquium on three-dimensional turbulent boundary-layer calculations, held at the Technical University (NTH), Trondheim, Norway in 1975.

The computations of the Stanford cases have been described in the report - Singhal and Spalding (1975); while the results of Trondheim cases were presented at the Euromech colloquium, reported by East (1975).

In the last two years, most of my research activities centred around the development and validation of the "partially-parabolic" procedure for axial-flow turbomachinery cascades; this procedure shares many novel features of GENMIX; and is described, in detail, in the present thesis.

I must now express my gratitude to all those who provided help and cooperation in various ways at the different stages of research. First of all I am grateful to Professor Spalding for his continuous guidance, encouragement and interest; most of the work presented in this thesis is based on his suggestions. Apart from the numerical procedures, I have learnt a lot from his own adherence to the exacting standards in technical writing and various other activities. It has been a privilege to have worked with him.

My coming to Imperial College was largely due to the advice of my Master's degree supervisor, Dr. S.V. Patankar, whose affection and encouragement have always been valuable to me. During the main course of developmental work, cooperation and technical discussions with Drs. D.G. Tatchell and A. Thyagaraja have been very valuable. I am also thankful to Dr. A.S.C. Ma and Mr. F. Bell for their suggestions and help in the experimental work. Drs. V.S. Pratap and A.K. Majumdar have been far more than helpful in various technical and non-technical matters. I have also enjoyed the friendship with Tim Maxwell and George Carroll, whose cheerful and carefree attitudes maintained a light atmosphere in Room 484. Informal discussions with other research workers - Andrew Pollard, Amra Serag-el-din, Essam Khalil and K. Srinivasan, have been too important to escape mention. I had also benefited from the association with many visiting post-doctoral fellows, of which I am glad to mention Drs. V. Ganesan, K. Suzuki, G.D. Mallinson and S. Kanbour. Dr. Mallinson introduced me to the computer graphics and provided a computer program for the contour plots. Coleen King, Sue Farmiloe and Marguerite Farrell assisted in various administrative matters; and Miss E.M. Archer and Mrs. S. Boot cheerfully provided the excellent library services. Thanks are also due to Rosemary Willox for preparing the typescript of this thesis.

Finally, I wish to acknowledge gratefully the generous financial aid provided by Combustion Heat and Mass Transfer Ltd., England.

London
May, 1977

A.K. Singhal

CONTENTS

		Page No.
ABSTRACT		1
PREFACE		3
CONTENTS		6
1.	INTRODUCTION	
1.1	The problem considered	11
1.2	Practical relevance	15
1.3	Objective and scope of present work	15
2.	REVIEW OF PAST WORK	
2.1	Introduction	18
2.2	Existing prediction procedures	
2.2.1	Analytical methods	18
2.2.2	Hodograph methods	19
2.2.3	Matrix methods	20
2.2.4	Streamline curvature methods	20
2.2.5	Time-marching methods	21
2.3	Available experimental data	22
2.4	Concluding remarks	23
3.	THE PREDICTION PROCEDURE	
3.1	Introduction	24
3.2	Main features of the procedure	
3.2.1	Characterization	24
3.2.2	Coordinate system	25

Page No.

3.2.3 Dependent variables 29

3.2.4 Numerical solution scheme 29

3.3 Governing equations 31

3.4 Solution-procedure details

3.4.1 Staggered-grid practice 32

3.4.2 Upwind-differencing practice 36

3.4.3 Calculation of auxiliary quantities 36

3.4.4 Treatment of transonic flow 39

3.4.5 Treatment of viscous flow 43

3.4.6 Local correction of pressure 46

3.4.7 Block correction of pressure 48

3.5 Boundary conditions 50

3.6 Sequence of calculation steps 53

4. FURTHER EXTENSION OF THE PREDICTION PROCEDURE

4.1 Introduction 56

4.2 Calculation of a turbulent flow 56

4.3 Simultaneous calculation of heat transfer 61

4.4 Calculation of a quasi three-dimensional flow 64

4.5 Calculation of flow in a rotating cascade 67

5. EXPERIMENTAL INVESTIGATION

5.1 Flow geometry and main parameters of study 69

5.2 Description of the experimental apparatus

5.2.1 General layout 71

5.2.2 The test section 74

Page No.

5.2.3 Measuring instruments 78

5.2.4 The traversing mechanism 81

5.3 Experimental procedure 81

5.4 Presentation and analysis of measured data 87

5.5 Concluding remarks 95

6. PREDICTIONS OF INVISCID, ADIABATIC FLOWS

6.1 Introduction 96

6.2 Example 1: Incompressible flow past a cylinder placed in a channel 97

6.3 Example 2: Subsonic flow in a NASA turbine stator cascade 99

6.4 Example 3: Transonic flow in Hobson's first impulse cascade 102

6.5 Example 4: Transonic flow in Hobson's second impulse cascade 106

6.6 Example 5: Transonic flow in a VKI gas turbine cascade 106

6.7 Example 6: Transonic flow in a VKI steam turbine cascade 109

6.8 Example 7: Transonic flow in a NGTE nozzle-guide-vane (NGV) cascade 114

6.9 Example 8: Transonic flow in the MIT-VKI-IV nozzle-guide-vane cascade 119

6.10 Computational details 129

6.11 Concluding remarks 130

7. PREDICTIONS OF VISCOUS FLOWS WITH AND WITHOUT HEAT TRANSFER

7.1 Introduction 131

7.2 Physical inputs 132

		Page No.
7.3	Turbulent adiabatic flow	133
7.4	Turbulent flow with heat transfer	136
7.5	Concluding remarks	142
8.	PREDICTIONS OF PRESENT EXPERIMENTAL FLOWS	
8.1	Introduction	143
8.2	Computational details	144
8.3	Presentation of results	147
8.4	Discussion	147
8.5	Concluding remarks	163
9.	CONCLUSIONS	
9.1	Achievements of the present study	164
9.2	Suggestions for future work	165
REFERENCES		168
NOMENCLATURE		180
APPENDIX A:	Equations of the motion in the non-orthogonal coordinate system	184
APPENDIX B:	The momentum-conservation equations for viscous flow	187
APPENDIX C:	The pressure-correction equation	191
APPENDIX D:	Formula for block correction of pressure	200
APPENDIX E:	Conservation equation for the stagnation enthalpy	202

		Page No.
APPENDIX F:	The circumferential-direction momentum-conservation equation for a variable stream annulus	206
APPENDIX G:	Convergence-improvement devices	209
APPENDIX H:	Report on "Prediction of two-dimensional boundary layers with the aid of k∿ε model of turbulence"	211

CHAPTER 1

INTRODUCTION

1.1 The problem considered

Flow through an axial turbine or compressor is a complex three-dimensional phenomenon. Its analysis is greatly simplified by division into two stages:

(i) a two-dimensional "through-flow" analysis which neglects circumferential variations; and

(ii) a two-dimensional "blade-to-blade flow" analysis in which radial equilibrium is assumed and the flow is analysed on a surface of revolution.

Both the analyses are useful in design. The former analysis establishes the overall geometrical dimensions, e.g. radii of hub and casing; while the latter one is required for developing the satisfactory blade profiles. Further details of their applications are given by Wu (1951) and Horlock (1973 a & b).

This thesis is concerned with the analysis of blade-to-blade flows. Both theoretical and experimental investigations are included. The main outcome is a numerical procedure for solving the "direct" problem, i.e. predicting flow past a given cascade geometry.

A general view of the flow geometry is illustrated in Fig. 1.1. The solution domain is represented by a stream sheet, shown by the chain-dotted lines. Its top and bottom surfaces, ABCDEFGH and abcdefgh, are stream surfaces, i.e. fluid does not cross these surfaces. Similarly the side faces, ABba, CDdc, EefF, and GghH, are also stream surfaces. The inlet and exit planes, AahH and DdeE, are parallel to the plane passing through the leading edges of the blades. The thickness, t, and mean radius, r, of the stream sheet can vary only in the axial direction and can be specified according to the local radii of hub and casing. For the cascades of twisted blades, several stream sheets, e.g. located at the root, mean and tip sections of the blades, are analysed independently. In a stream sheet, if t and r are uniform, then the flow can be regarded as a plane flow; Fig. 1.2 represents details of such a flow situation.

The important features of the problem considered are:

(i) strong curvature in the flow passage,

(ii) circumferential periodicity,

(iii) compressibility effects (subsonic, supersonic or transonic),

(iv) viscous effects,

(v) turbulence,

(vi) heat transfer,

(vii) rotation of blades, and

(viii) flow convergence resulting from the variations of blade height and hub radius.

It should also be mentioned here that the first three features are, often, more important than the remaining ones.

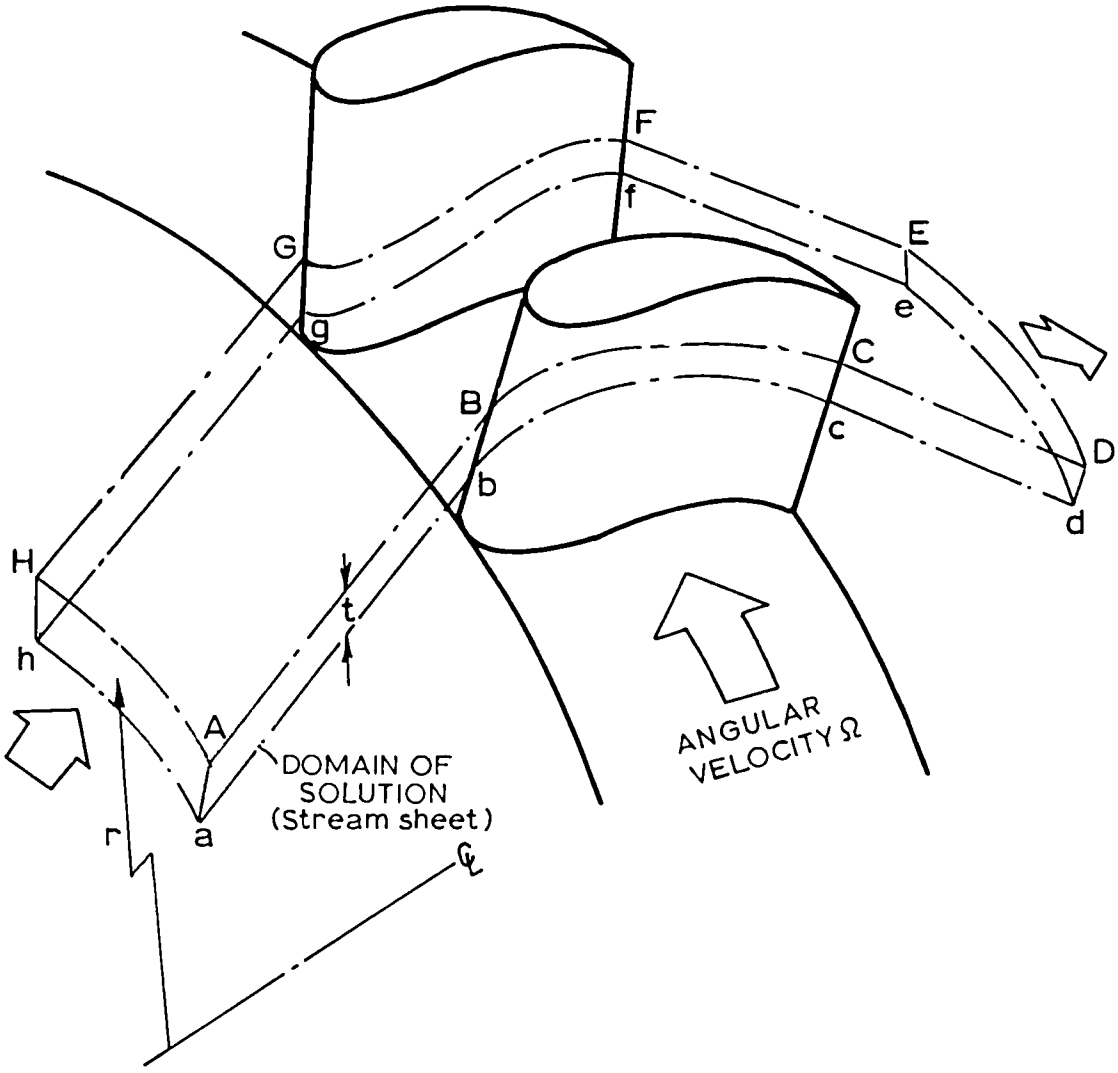


Fig. 1·1 The flow situation considered

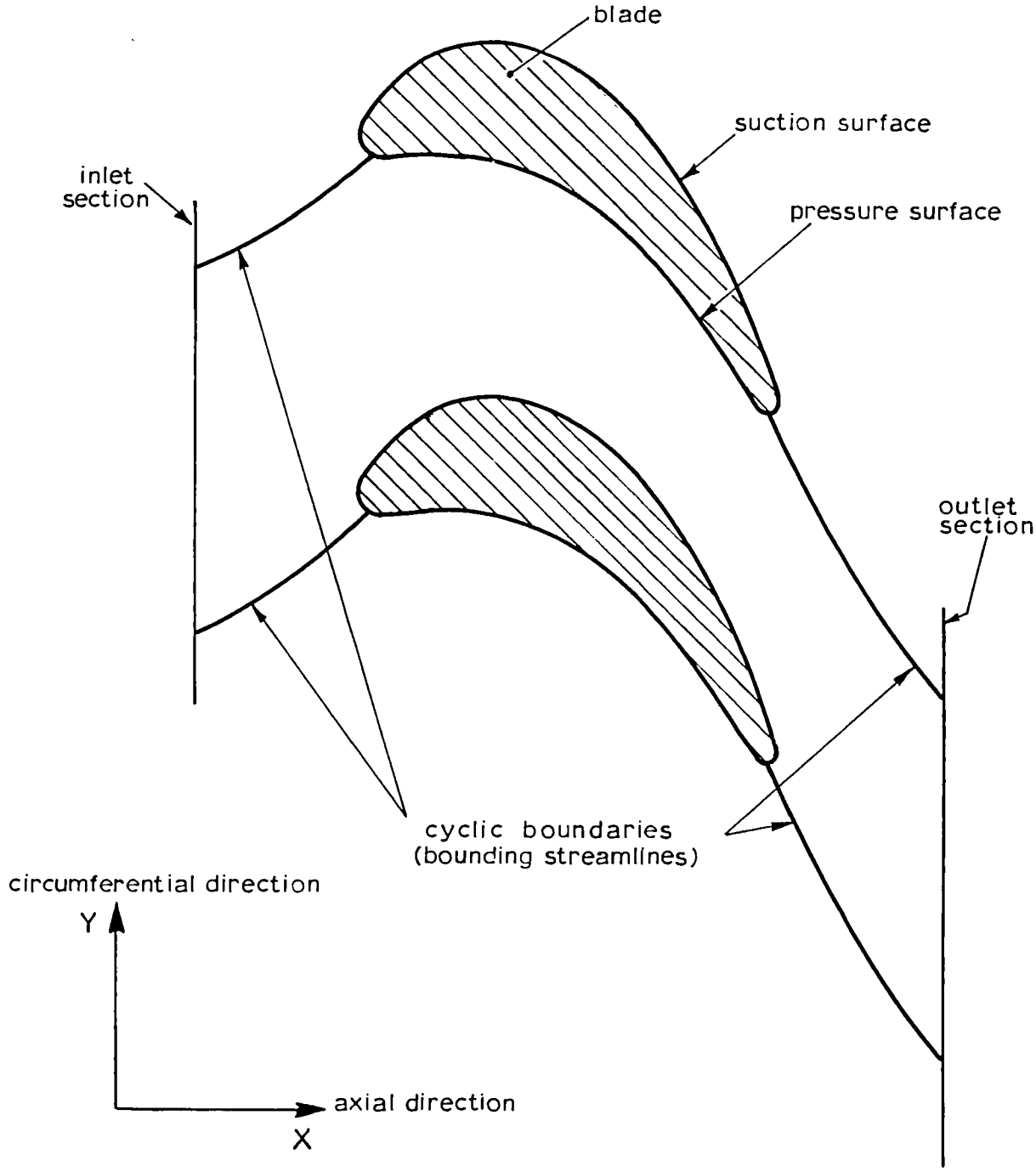


Fig. 1.2 The plane flow geometry

1.2 Practical relevance

Although the blade-to-blade flow analysis yields a complete definition of the flow field, the following two quantities are of paramount importance:

(i) blade surface pressure distributions,

(ii) flow outlet direction.

A precise knowledge of surface pressure distributions is important both from the aerodynamic and mechanical design considerations. This is particularly true for the high Mach number, highly loaded blade rows because: (a) the flow is very sensitive to the blade profile; and (b) the design of blade-cooling system also depends on the pressure distribution.

The knowledge of flow outlet direction is required for the satisfactory design of the next row of blades.

1.3 Objective and scope of present work

Objective

The primary objective of the present work has been to develop and test a numerical prediction procedure which can be used in the design and performance analysis of axial turbomachinery cascades. It is aimed that the procedure satisfies all the necessary requirements of a good design tool; i.e. it must be simple, accurate, widely applicable and economical.

Scope of work

The work presented in this thesis can be divided mainly into the following three categories.

(i) Development of the prediction procedure:

The prediction procedure has been developed to account for all the eight flow-features, listed in Section 1.1. In accordance to their relative importance, the primary emphasis has been given to the first three features, viz. curvature, circumferential periodicity and compressibility. It may be remarked here that the prediction procedure is not limited to cascade flows; it can be easily applied to general parabolic- and partially-parabolic-flow problems.

(ii) Experimental investigation

An experimental investigation has been carried out to examine the influence of trailing-edge flaps in a subsonic cascade flow. The flap inclination has been regarded as the main parameter. Pressures and velocities have been measured with the aid of pitot probes. The measured data also supplement the information used for validation of the prediction procedure.

(iii) Validation of the prediction procedure

In order to test the capabilities of the prediction procedure, a number of problems have been selected as test cases. These problems include cascades with high camber, large turning angle and sharp curvature changes;

e.g. impulse cascades, gas turbine cascades and nozzle guide vanes, etc. The selected problems can also be classified as incompressible, subsonic and transonic flow problems. In most of the cases, the flow has been assumed to be inviscid and adiabatic. In two test cases, flow through cascade is treated as turbulent; and in one of these cases heat transfer calculations have also been performed.

For the outline of the thesis, the reader is referred to the list of contents.

CHAPTER 2

REVIEW OF PAST WORK

2.1 Introduction

This chapter briefly reviews the existing prediction procedures and experimental studies for cascade flows. Methods for both direct and indirect problems are discussed. On the experimental side, status of the available information is summarised.

2.2 Existing prediction procedures

2.2.1 Analytical methods

In the past the velocity and pressure distributions around the blades in a cascade have been calculated by two-dimensional plane flow methods which involve distributed sources, sinks and vortices; e.g. Schlichting (1955), Martensen (1959) and Wilkinson (1967). Some other methods, viz. Howell (1948), Hall and Thwaites (1963) etc., employ the potential-flow picture-plane transformation techniques. All these methods are limited to incompressible, inviscid flow calculations. These methods have been extremely useful in the early development of turbomachines; however, for the present day needs, they are rather too restricted.

2.2.2. Hodograph methods

The basic technique of hodograph transformation is described in several books, e.g. Guderley (1972). Its main feature is that the components of flow velocity are used as independent variables and the stream function as the main dependent variable. The choice of independent variables makes this technique suitable for solving an "indirect" problem, i.e. designing a blade profile which will sustain the required surface-velocity distribution.

Various hodograph methods have been developed in the past; some of the recent ones are those of: Uenishi (1971), Garbedian and Korn (1971), and Hobson (1974). These methods have been found satisfactory for the design of several plane cascades, for both incompressible and compressible flows. However, their applicability is limited due to the following:

(a) calculations are made in a hodograph plane and often there are difficulties in transformation of the solution to the physical plane;

(b) viscous effects can not be included;

(c) only plane cascades can be designed; and

(d) transonic flow calculations pose difficulties in matching the solutions of subsonic and supersonic flow regions which are often calculated differently, in the hodograph methods.

2.2.3 Matrix methods

In the matrix technique, equations of motion are formulated in terms of a stream function. The region of interest is covered by a fixed grid and an algebraic equation is obtained, by using finite-difference approximations, for every interior grid point in terms of the stream function at that and neighbouring points. This sytem of nonlinear equations is expressed in the form of a matrix which is then solved by an iterative process.

Methods based on this approach have been reported by Smith and Frost (1970), and Silvester and Fitch (1970). These methods have been successful in solving the incompressible and subsonic flow problems; but not so for general transonic flow problems.

2.2.4 Streamline curvature methods

The streamline curvature methods, also called the stream filament methods, employ a floating grid formed by the guessed streamlines and the so called "quasi-orthogonals", e.g. pitchwise lines. Equations of motion are solved along the coordinate lines. At each cross-stream station, first the calculated velocity distribution is corrected to satisfy the overall continuity condition; and, then, the geometrical properties of the streamlines are recalculated, to be used in the next iteration. An iterative, forward-marching integration procedure is employed.

The first method of this kind, for blade-to-blade flow application, was reported, with full FORTRAN listing, by Katsanis (1968). The method was very successful for subsonic flow calculations. Subsequent publications are: Katsanis (1969), Wilkinson (1970), and Bindon and Carmichael (1971). It has been shown that these methods are satisfactory in situations where the Mach numbers are equal to or slightly greater than one. No further developments, reporting their applications to high Mach number supersonic or transonic flows, are known.

2.2.5 Time-marching methods

In the time-marching approach, unsteady inviscid flow equations are solved, usually, by an explicit finite-difference technique. A steady-state solution is obtained as the asymptotic limit of transient flow calculations.

McDonald (1971), and Gopalkrishnan and Bozzola (1971) reported two methods for transonic flows in cascades. McDonald used an integral representation of conservation equations, over each control volume, and called it a "finite area" method. Gopalkrishnan and Bozzola employed the McCormack's finite-difference technique (1969). Some more recent and improved methods are: Denton (1975), Kurzrock and Novick (1975), and Delaney and Kavanagh (1976).

All these methods have been more successful, particularly for transonic flows, than those mentioned in the previous sections (viz. 2.2.1 - 2.2.4). However, the time-marching methods have two inherent disadvantages:

(i) usually a great many time steps are required before a steady-state solution is reached; therefore, computations are expensive;

(ii) computer-storage requirements are also large because all the variables must be stored for the whole flow domain.

2.3 Available experimental data

The numerical/analytical procedures must be validated by comparing their predictions with the experimental observations. For this purpose one needs reliable experimental data in several geometrical and flow conditions which are representative of large number of practical situations. Several such experimental investigations have been reported in the literature; some of these, commonly used for validation purposes, are: Forster (1964), Hiett and Johnston (1964), Whitney et al. (1967), Johnston and Smart (1967), Monsarrat et al. (1969), Griepentrog (1970), Sulam et al. (1970), Huffman et al. (1971), Gostelow and Smith (1973), VKI Lecture Series Nos. 59, 84 (1973, 1976).

The reported data cover a wide range of flow conditions, i.e. incompressible, subsonic and transonic flows in both turbine and compressor cascades. Most of them are for plane cascades. In a few cases of VKI Lecture Series 84 (1976), axial variations of stream-sheet thickness are allowed. Experimental data for the rotating-cascade flows are not yet available.

2.4 Concluding remark

From Section 2.2, it is obvious that though there are several prediction procedures, most of them are either limited in application or very expensive in computations. Gostelow (1973) also expressed a similar view in his review article of compressible flow theories for airfoil cascades.

On the experimental side, the situation is more satisfactory. Except for the flows in rotating cascades, there is enough data available which can be used for validation purposes.

CHAPTER 3

THE PREDICTION PROCEDURE

3.1 Introduction

This chapter describes the prediction procedure developed for steady, two-dimensional, blade-to-blade flow in axial turbomachines. Though all the eight flow-features, listed in Section 1.1, can be accounted for; only the curvature, compressibility and circumferential periodicity are considered in the first few sections of this chapter so as to highlight the fundamental details of the procedure. Later, the viscous effects are also included. Discussion of the remaining four flow-features is postponed for the next chapter because their introduction does not require any basic change in the procedure.

3.2 Main features of the procedure

3.2.1 Characterization

The present method solves steady-flow equations by a finite-difference, iterative, forward-marching integration scheme, described in Section 3.2.3; and it can be characterized as an "iterative space-marching" method. The term "space-marching" has been adopted to distinguish it from the "time-marching" methods, essential feature of which were mentioned in Section 2.2.5.

The present method can also be regarded as a combination of the Patankar-Spalding (1967) procedure for predicting two-dimensional "parabolic" flows, with the so-called "semi-elliptic" (Spalding, 1971) or "partially-parabolic" method (Pratap and Spalding, 1975, 1976) of handling "elliptic" flow without flow reversal.

The novelties of the present method reside in the choices of:

(a) the coordinate system,

(b) the dependent variables, and

(c) the numerical solution scheme.

These will now be described.

3.2.2 Coordinate system

A non-orthogonal coordinate system is employed in which the coordinate lines are:

(a) streamlines,

(b) a family of straight lines, parallel to lines through the leading edges of the blades.

A typical grid is shown in Fig. 3.1. The two independent variables are axial distance x, and stream function ψ. Grid spacings can be non-uniform in both x and ψ distributions. It should be pointed out here that the positions of streamlines in the x,y plane are not known

in advance, instead they are the outcome of computations. The main advantages of this coordinate system are as follows:

(i) Arbitrary-shaped boundaries, e.g. blade surfaces, can be handled very conveniently and accurately.

(ii) The governing flow equations are considerably simplified because the mass fluxes across the control-volume faces are known. For instance, in Fig. 3.2 the mass fluxes through faces 1 and 2 are equal to $\Delta\psi$; and mass fluxes through faces 3 and 4 are equal to zero.

(iii) The "false viscosity" which afflicts numerical solution procedures in which streamlines cross grid lines obliquely is therefore absent.

(iv) Constant-x lines (pitchwise lines) are particularly suitable for the imposition of the "cyclic" boundary conditions outside the blade passage, according to which flow properties at either limit of the lines, although unknown, must be identical. They are also convenient for interpretation of the computed results.

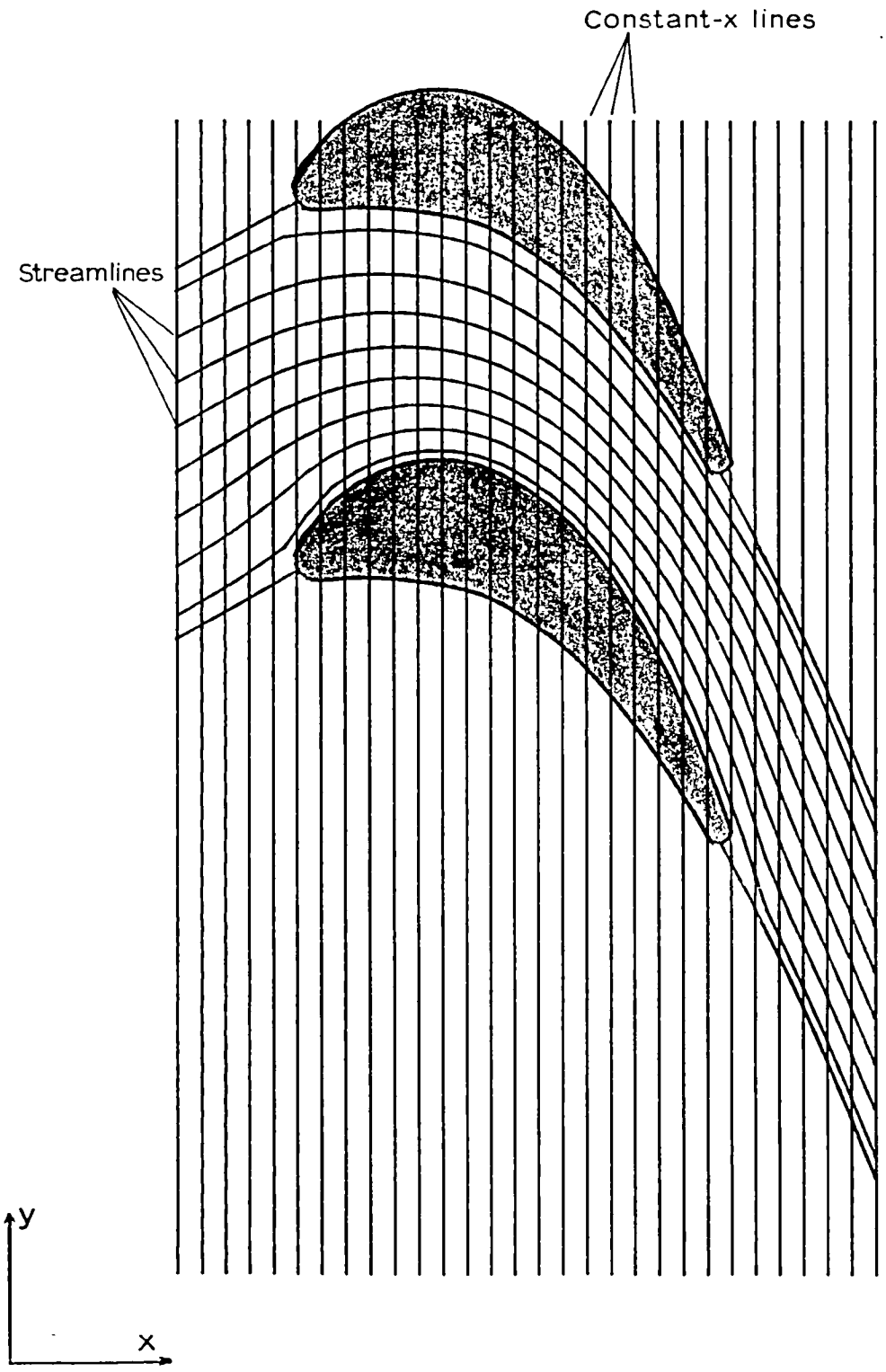


Fig. 3-1 The non-orthogonal grid

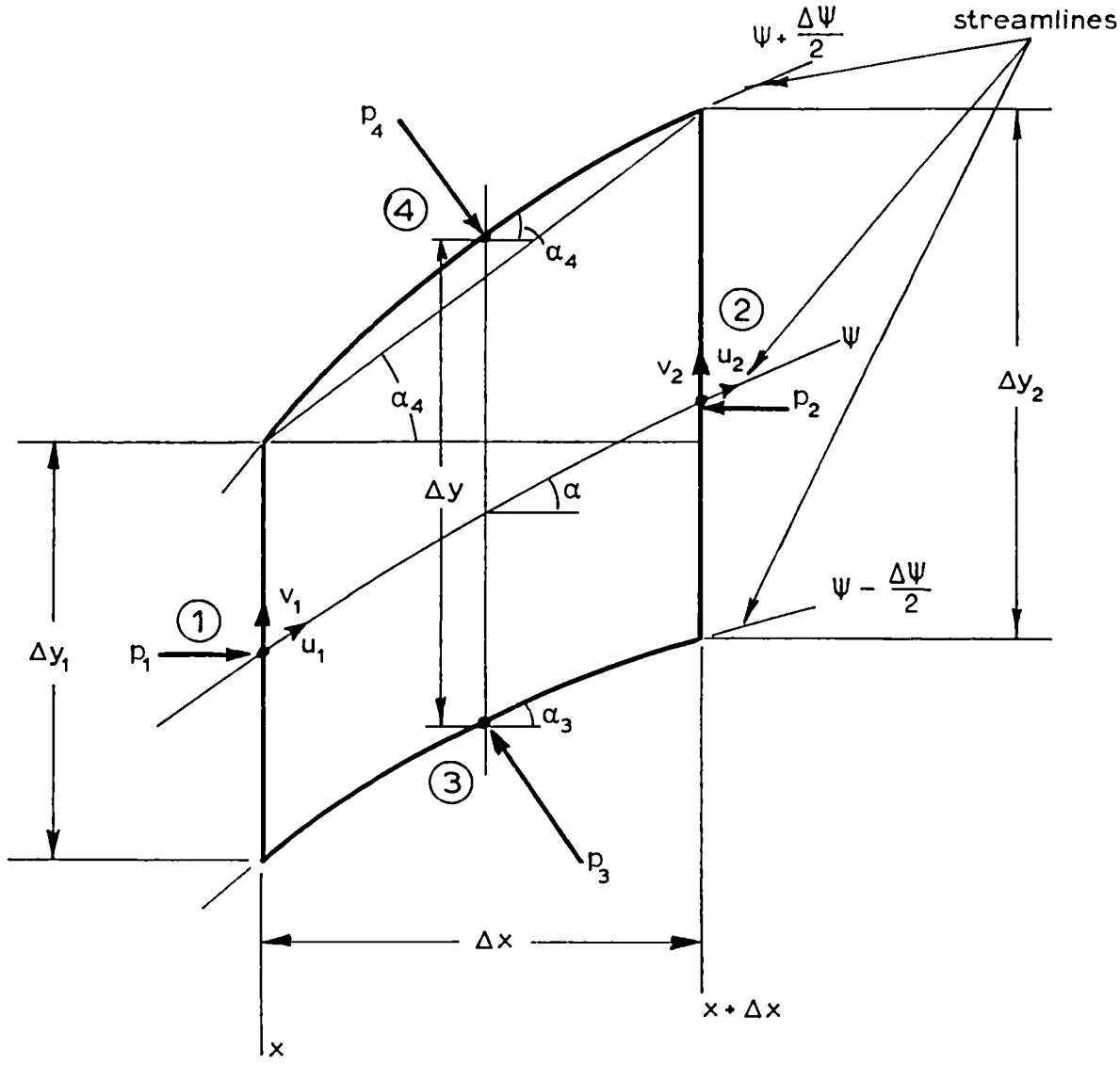


Fig. 3·2 A typical control volume

3.2.3 Dependent variables

The following variables are treated as dependent variables, the values of which are to be found at all grid points:

(i) streamwise velocity, u;

(ii) y-direction component of velocity, v;

(iii) fluid pressure, p; and

(iv) fluid density, ρ.

It must be noted that the selected velocities are aligned with the coordinate lines, and thus are not orthogonal to each other. The advantage of this practice is that the momentum-conservation equation for each velocity contains only one pressure-gradient term, i.e. u depends on $\frac{\partial p}{\partial s}$ and v on $\frac{\partial p}{\partial y}$.

The choice of velocity components has been the most critical factor in the success of the scheme.

3.2.4 Numerical solution scheme

The method employs an iterative, forward-marching integration scheme which assumes the flow situation to be "partially parabolic", Pratap and Spalding (1976). This means that downstream events are presumed to influence upstream ones only by way of pressure; for viscous effects in the upstream direction are negligible, at high Reynolds numbers; and recirculation (closed streamlines) is absent.

The distinctive features of the adopted procedure are:

(i) A guess-and-correct procedure is employed for the calculation of the correct pressure field. A two-dimensional storage is provided for the pressure.

(ii) The flow variables (u,v,p,ρ and all auxiliary quantities) are calculated at the grid nodes of one cross-stream section at a time. Thus, all variables except the pressure are provided only one-dimensional storage.

(iii) The solving operation moves from line to line in a downstream direction. Several sweeps of the flow domain are made from upstream to downstream. In each sweep a better estimate of the pressure field is obtained.

Further details of the calculation steps are given in Section 3.6.

It can be noted from the above description that the computer-storage requirements are minimal. The saving, as compared with time-marching methods, becomes even more significant when additional dependent variables such as turbulence kinetic energy, stagnation enthalpy, etc. are also to be solved.

3.3 Governing equations

In order to calculate the four dependent variables (u,v,p and ρ), we need four equations: the two equations of motion (conservation of momentum), the equation for kinematic compatibility of flow and the thermodynamic equation of state. For the selected coordinate system, the equations of motion are not readily available; however, these can easily be derived by applying the momentum-conservation law to a control volume as shown in Fig. 3.2. Derivations of these equations are presented in Appendix A. Here, a full set of governing equations for a plane, two-dimensional, inviscid, compressible flow is written as follows:

Streamwise momentum-conservation equation:

$$u_2^2 - u_1^2 = \frac{2\gamma}{\gamma-1}\left(\frac{p_1}{\rho_1} - \frac{p_2}{\rho_2}\right) \quad ; \quad (3.1)$$

y-direction momentum-conservation equation:

$$\Delta\psi(v_2 - v_1) = (p_3 - p_4).\Delta x \quad ; \quad (3.2)$$

Equation for kinematic compatibility of flow:

$$\Delta Y_2 - \Delta Y_1 = \Delta x.(\tan \alpha_4 - \tan \alpha_3) \quad ; \quad (3.3)$$

Equation of state:

$$\rho = \rho_o \left(\frac{p}{p_o}\right)^{1/\gamma} \quad . \quad (3.4)$$

The meanings of the symbols are explained in the nomenclature.

Equations (3.1) and (3.2) have been derived in Appendix A. Equation (3.3) is simply a geometrical relation between the heights of vertical faces and the inclinations of stream surfaces of control volume of Fig. 3.2. Both Δy and α are auxiliary quantities and are calculated from the primary variables ρ, u and v, as will be explained in Section 3.4.3. The kinematic-compatibility equation is used as the basis of the pressure-correction equation, Section 3.4.6; and it can be regarded as the counterpart of the continuity equation in a fixed-grid coordinate system. Equation (3.4) is valid for isentropic flow; more general relations can be incorporated if desired.

It may be noted that in equations (3.1) to (3.4), no restrictions are placed on curvature and compressibility effects.

3.4 Solution-procedure details

3.4.1 Staggered-grid practice

Fig. 3.3 shows the manner in which the flow variables are located on the finite-difference grid. The pressure and other scalar flow-properties are stored at the grid nodes while the velocity components are placed at the mid-node locations. The boomerang-shaped envelopes enclose the points which are identified by a common grid-number index.

This arrangement of "staggered" locations facilitates accurate calculations of the pressure gradients that affect the velocity components. This practice is similar to those of Harlow and Welch (1965), and Patankar and Spalding (1972).

The staggered-grid system, explained above, also necessitates the use of different control volumes for the velocity components and pressure; these are shown in Fig. 3.4. It may be noted that the control volumes for velocity components are such that in the directions along the velocities, the edges of the control volumes pass through the grid nodes which lie on either side of the velocity. Similarly, the boundaries of the pressure control volume pass through the locations of velocity components.

A slightly different practice is adopted for locating the velocities near the boundaries of the solution domain. Fig. 3.5 illustrates this practice; it may be noted that one component of velocity is located at the same location as that of the boundary pressure. Fig. 3.5 also shows the pressure control volumes for the near-boundary grid nodes. No control volumes are required for the boundary grid points because the flow variables u,v,p and ρ are calculated only at the internal grid points; their boundary values are either known or they can be deduced, if required, from the calculated internal distributions.

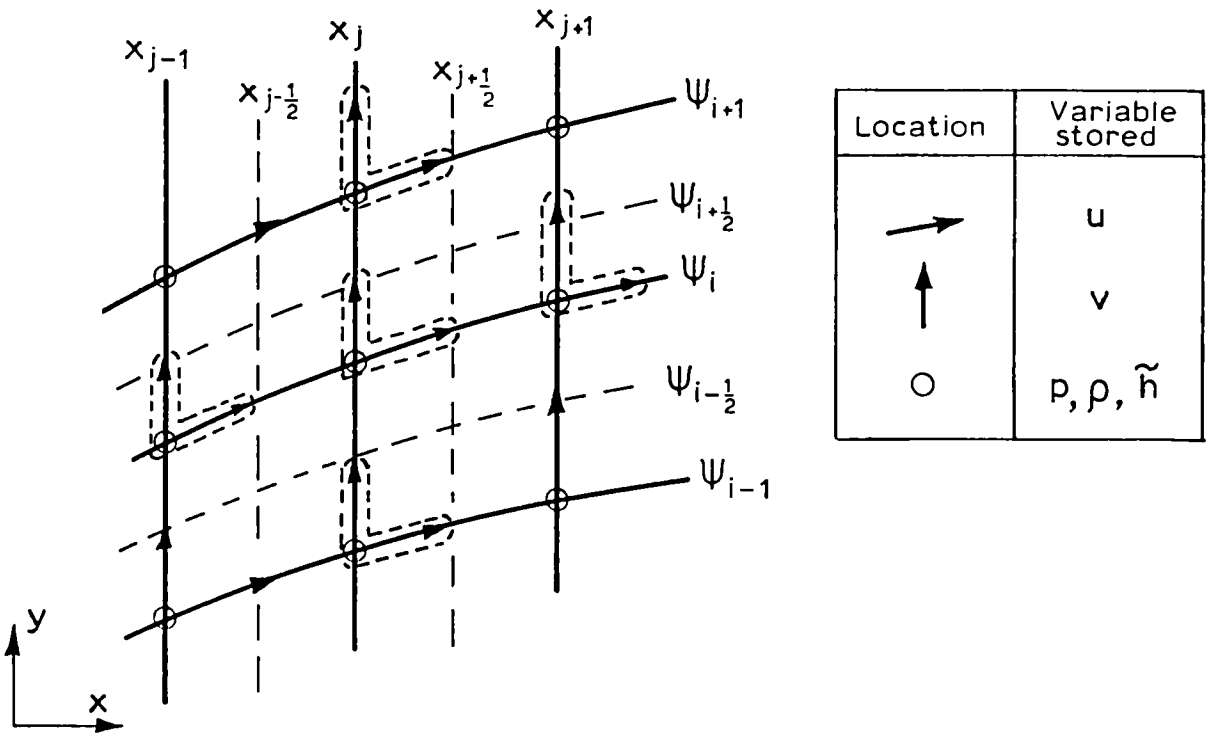


Fig. 3·3 Location of variables on the finite-difference grid

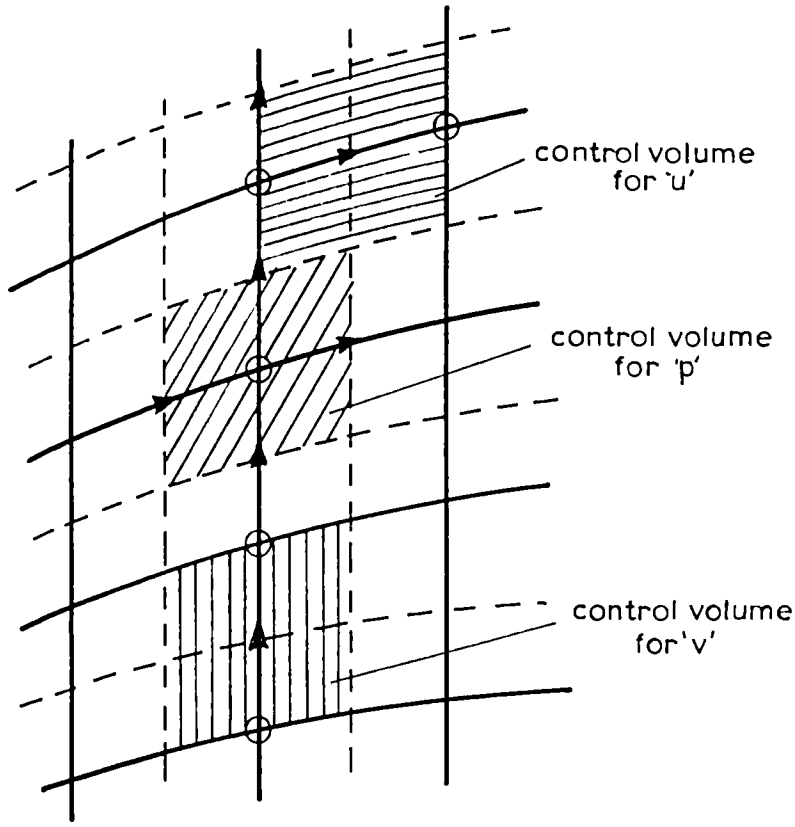


Fig. 3·4 Control volumes for velocity components and pressure

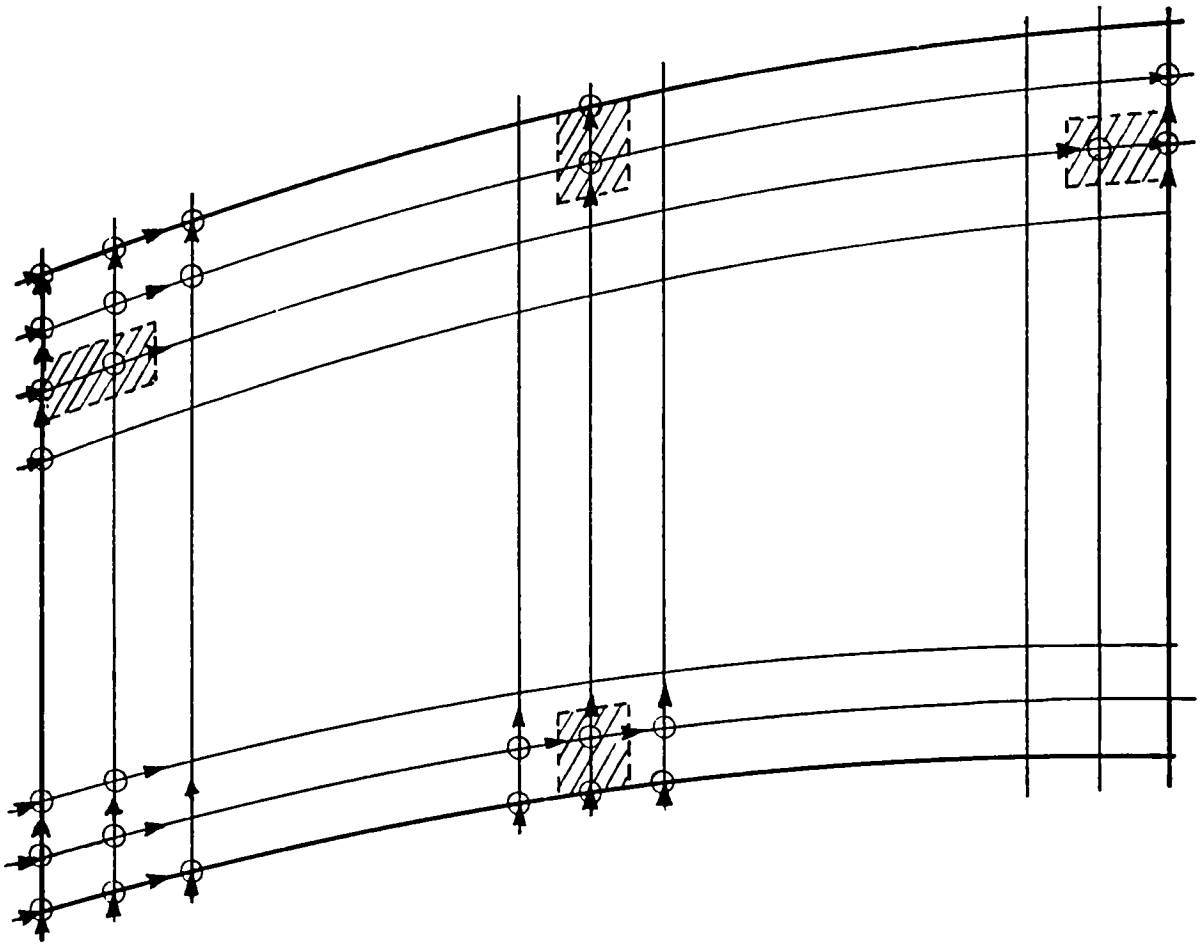


Fig. 3·5 Velocity storage locations and pressure control volumes near the boundaries

3.4.2 Upwind-differencing practice

In order to adapt the momentum-conservation equations to the staggered-grid system, the "upwind" differences of momentum fluxes are used; the final forms of these equations, as employed in the solution procedure, are

$$u_e^2 - u_w^2 = \frac{2\gamma}{\gamma-1}\left(\frac{p_P}{\rho_P} - \frac{p_E}{\rho_E}\right) \quad ; \quad (3.5)$$

$$(\Delta\psi)_n \ (v_n - v_{nw}) = (p_P - p_N)\ \Delta x \quad ; \quad (3.6)$$

where suffixes refer to Fig. 3.6.

The upwind-difference practice, though implemented in different ways in different numerical methods, is well known to be numerically stable for fluid dynamics problems.

3.4.3 Calculation of auxiliary quantities

As mentioned in Section 3.3, α and Δy are calculated from the primary variables; the relationships used are:

Kinematics of flow: $\alpha = \sin^{-1}\left(\frac{v}{u}\right)$; (3.7)

Continuity : $\Delta y = \frac{\Delta\psi}{\rho u \cos\alpha}$; (3.8)

In Equation (3.7), v and u are velocities interpolated for the point at which α is to be calculated. In Equation (3.8), the term $\rho u \cos\alpha$ should be evaluated at the centre of the control-volume face for which Δy is to be calculated. Both α and Δy are used for the kinematic-

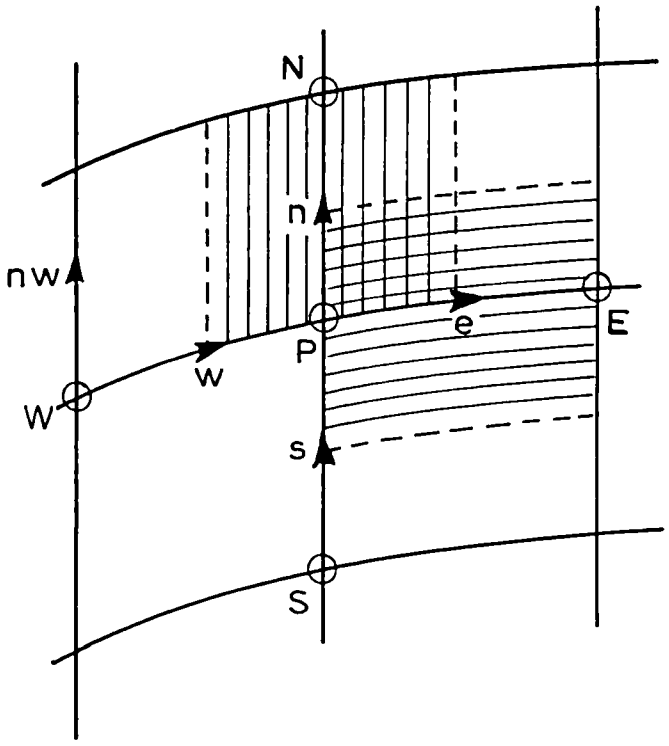


Fig. 3·6 Control volumes and grid notations used in the description of finite-difference equations for velocity components.

(N, S, E, W signify North, South, East and West directions relative to the centre node P)

compatibility condition, Equation 3.3, which will be further discussed in Section 3.4.6.

Equation (3.8) is also used in the calculation of y-distances, between gridlines (streamlines) at a constant-x section, as follows:

$$y_{i+1} - y_i = \frac{\psi_{i+1} - \psi_{i+\frac{1}{2}}}{(\rho u \cos\alpha)_{i+1}} + \frac{\psi_{i+\frac{1}{2}} - \psi_i}{(\rho u \cos\alpha)_i} \quad . \quad (3.9)$$

Equation (3.9) implies a stepwise variation of $(\rho u \cos\alpha)$ as shown in Fig. 3.7. This is consistent with the assumptions made for the variations of each property, ρ, u and α, in deriving basic equations from the control-volume analysis.

A slightly different practice is adopted near to the lateral boundaries, streamlines 1 and n, so as to provide means of representing steep variations of $(\rho u \cos\alpha)$ which can, often, be present due to steep variations of u near the boundaries. For explanation purpose, let us consider the boundary represented by streamline no. 1. The y-distance between streamlines 1 and 2 is calculated as:

$$y_2 - y_1 = \frac{\psi_2 - \psi_1}{\Psi (\rho u \cos\alpha)_2} \quad ; \quad (3.10)$$

$$\Psi = \frac{\int_{y_1}^{y_2} (\rho u \cos\alpha) dy}{(\rho u \cos\alpha)_2 \, (y_2 - y_1)} \quad . \quad (3.11)$$

Here Ψ is a shape factor which accounts, in a gross manner, for the variation of $\rho u \cos\alpha$. For instance, Ψ can take values

like 1.0, 0.9 and 0.5 respectively for profiles a, b and c in Fig. 3.8. Profile 'a' represents a symmetry plane or a wall in an inviscid flow. Profile 'b' is typical of turbulent wall-boundary-layer flow. And profile 'c' can exist if the boundary lies in the wake region of flow. Means of estimating Ψ can be devised based on the observations of the physical behaviour of flow. This practice of y-distance calculations is similar to the one used in the boundary-layer procedure of Spalding (1975).

3.4.4 Treatment of transonic flow

In a transonic flow both subsonic- and supersonic-flow regions are present and their interface boundaries are not known apriori. In the present procedure, the governing flow equations are solved in an identical manner at each grid node irrespective of the local flow condition (subsonic or supersonic). However, the elliptic and hyperbolic behaviours of the subsonic and supersonic regions are expressed through the differing ways of computing the mass velocity (ρu). The quantity ρu is used in Equation (3.8) for calculating the cell-face height Δy.

For this purpose a "convective-velocity" practice (Spalding, 1976) has been adopted. According to this practice, ρu at a typical location, point e in Fig. 3.9, is calculated as follows:

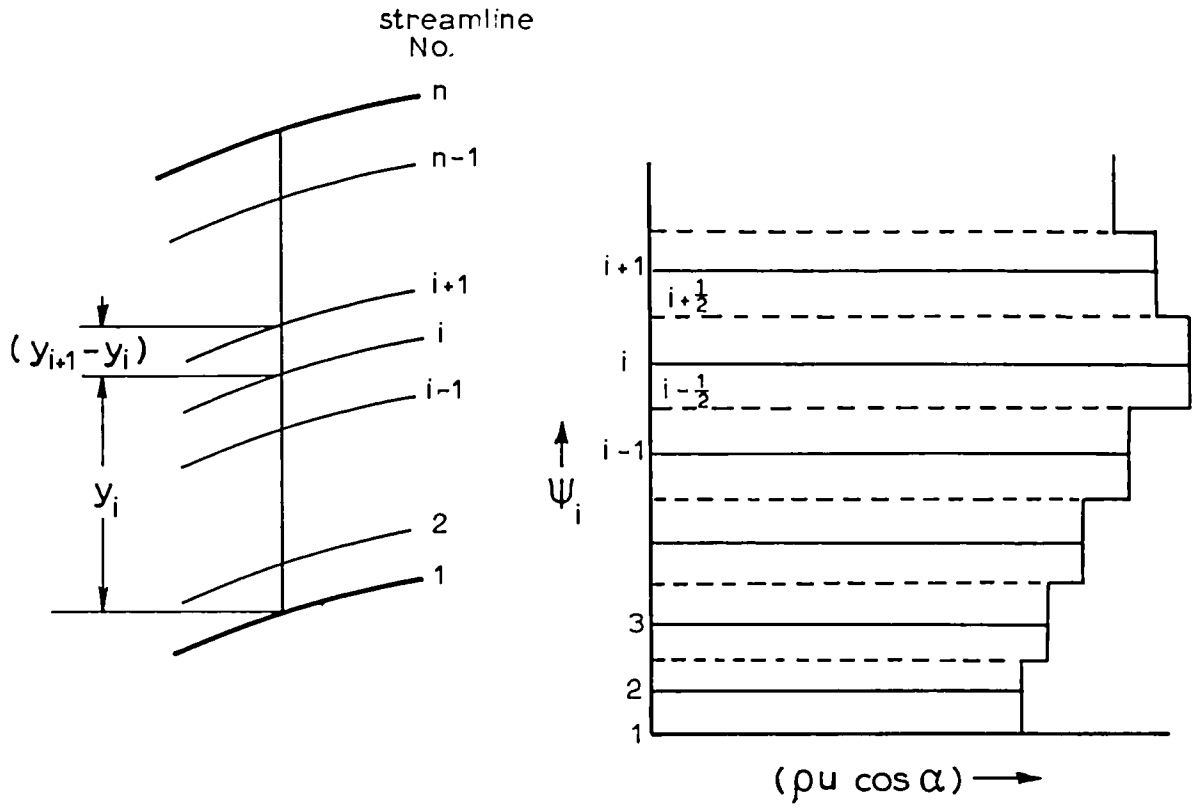
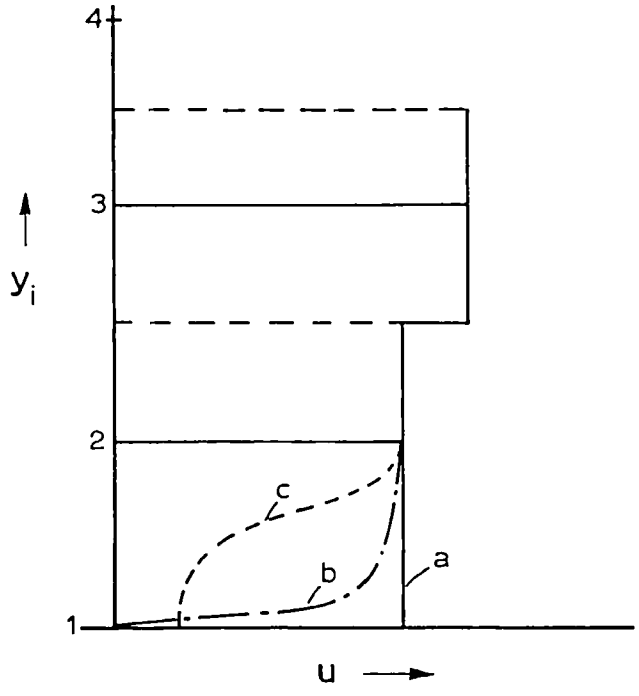


Fig.3·7 Diagrams illustrating the y-distances and the stepwise profile of $(\rho u \cos\alpha)$



Velocity profile	Type of flow or boundary
a	Inviscid flow or symmetry boundary
b	Turbulent flow
c	Wake type flow

Fig.3·8 Typical velocity profiles in the near-boundary region

$$(\rho u)_e = \rho_P \cdot u_{convective} \quad , \quad (3.12)$$

where $u_{convective} \equiv u_e \cdot \left(\frac{p_E}{p_P}\right)^{1/\gamma}$, for $M_e < 1$; and

$u_{convective} \equiv u_w$, for $M_e \geq 1$.

Here M_e stands for the Mach number at point e, calculated from the known approximate values of u, p and ρ.

For an isentropic flow, the above prescription can also be interpreted as follows:

$(\rho u)_e = \rho_E u_e$, for $M_e < 1$; and

$(\rho u)_e = \rho_P u_w$, for $M_e \geq 1$.

The main implications of this practice are:

(i) In a supersonic region, $(\rho u)_e$ is independent of the downstream pressure p_E. This enforces the principle that influences cannot travel upstream in supersonic flow.

(ii) In the flow regions where Mach numbers are close to or greater than unity, the large density changes provoke no numerical instability; for, in the product $\rho_P u_w$ or $\rho_E u_e$, velocity is considered at an upstream point relative to the location of density; and therefore, for a pressure change at the location of density, the considered ρ and u always vary in the opposite directions.

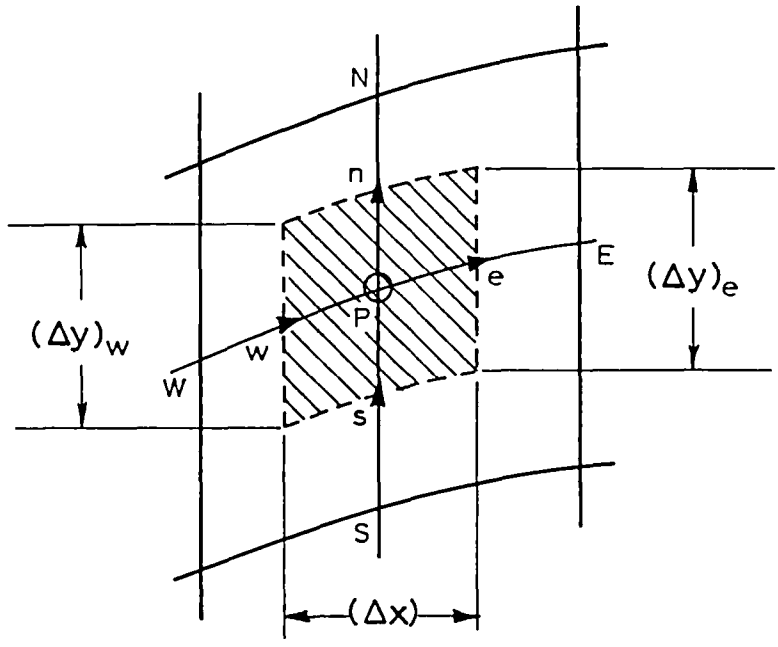


Fig.3·9 Control volume used in the kinematic-compatibility condition and pressure-correction equation for grid node P

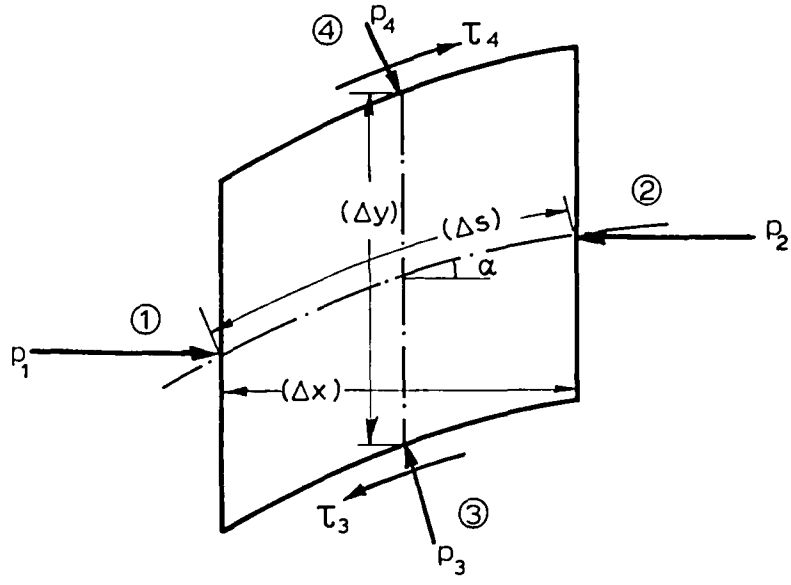


Fig.3·10 Pressure and shear forces on a typical control volume

It should be remarked that this deliberate contrivance of features in the finite-difference equations which conform to known features of real flows is both necessary and proper. Finite-differencing "loses" information which the differential equations possess; and sometimes this "loss" must be artificially made good.

3.4.5 Treatment of viscous flow

In a viscous (laminar or turbulent) flow, momentum transfer takes place by way of both convection and diffusion. It is also known that at high Reynolds numbers, the diffusion of momentum is negligible in streamwise direction and is predominant in a direction normal to the streamlines. Therefore in the parabolic and partially-parabolic flows, e.g. boundary-layer and cascade flows, it is generally sufficient to account for the momentum diffusion across the streamlines.

Fig. 3.10 illustrates a control volume in which τ's represent the shear stresses at stream surfaces. According to the Newton's law of viscosity, the shear stress τ can be regarded as the momentum-diffusion flux in the direction normal to streamline and it can be related to the local velocity gradient as:

$$\tau = \mu \frac{\partial u}{\partial n} \quad , \quad (3.13)$$

where μ is viscosity of fluid. If the flow is turbulent, μ is replaced by the so-called "effective viscosity", μ_{eff}; means of ascribing μ_{eff} are discussed in the next chapter in Section 4.2.

In accordance with the above-mentioned arguments, the momentum-conservation equations for viscous flow are derived in Appendix B. The final form of finite-difference equation for u-velocity is written, with reference to Fig. 3.11, as follows:

$$(A_i + B_i + u_i^*)\, u_i = A_i u_{i+1} + B_i u_{i-1} + u_i^{*2} \quad , \quad (3.14)$$

where u_i^* represents the u-velocity obtained from inviscid-flow equation (3.5); and the coefficients A and B contain local viscosity and grid dimensions. It may be noted that, in Equation (3.14), u_i is connected to u_{i+1} and u_{i-1}. Thus at a constant-x section, all u_i's, $i = 2,3,\cdots,(n-1)$, must be solved simultaneously subject to the appropriate boundary conditions. The shear stress at a solid surface can be calculated by using a suitable wall function such as the one explained in Section 4.2.

The y-direction momentum-conservation equation remains same as Equation (3.6).

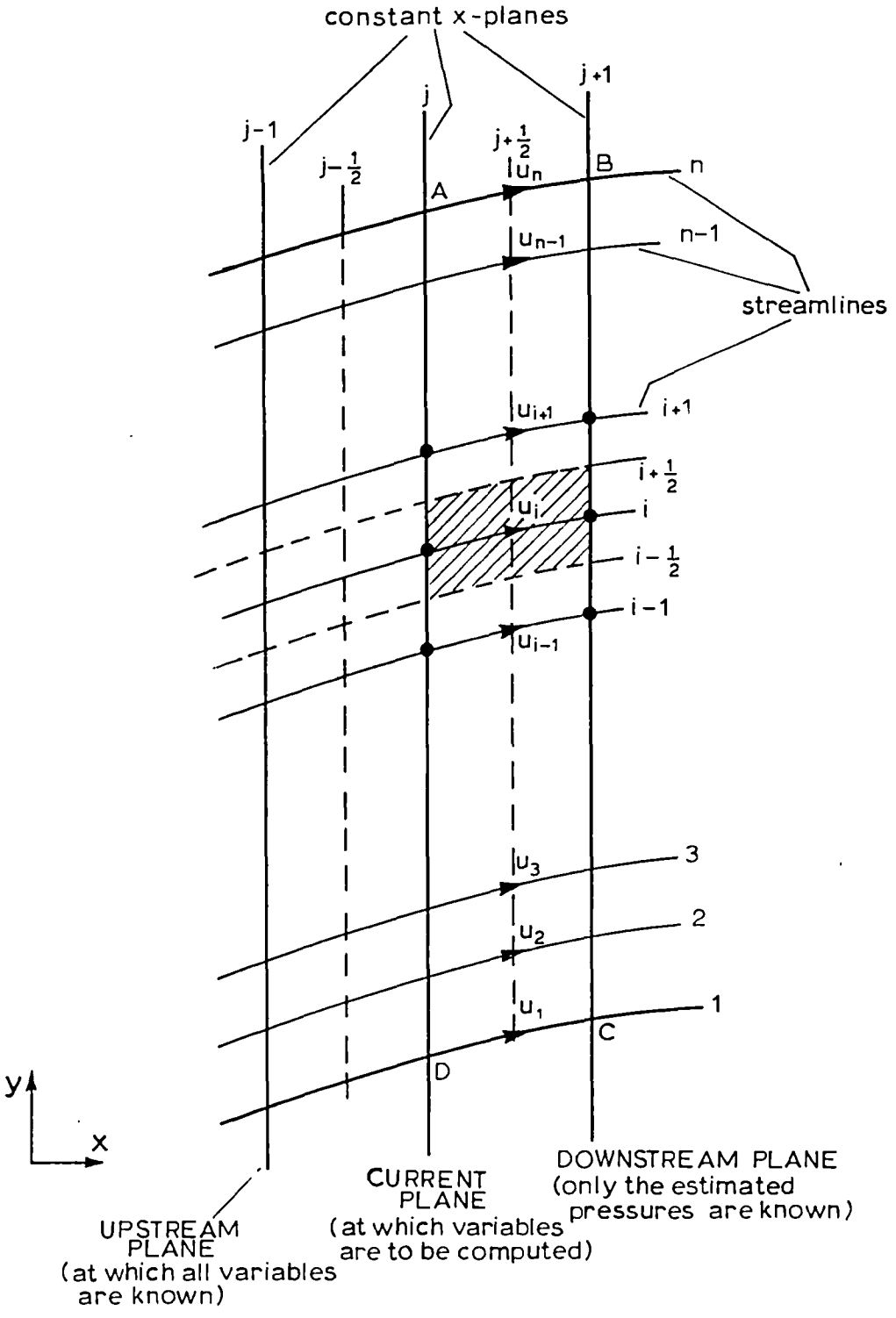


Fig. 3·11 Diagram illustrating the notations used in equation 3·14 and section 3·4·7

3.4.6 Local correction of pressure

As already mentioned in Section 3.2.4, a guess-and-correct procedure is employed for obtaining the correct pressure field. The approach is based on the SIMPLE (Semi-Implicit Method for Pressure-Linked Equations) algorithm of Patankar and Spalding (1972). The central idea is: first, to solve the momentum-conservation equations, using approximate values of pressures; and, then, to correct the pressures and velocities so that the continuity, or in the present case, kinematic-compatibility, requirement is satisfied at each grid node. These corrections are calculated by solving pressure-correction equations for grid nodes of one cross-stream section at a time.

The SIMPLE algorithm was originally developed for the calculations of incompressible flows in fixed-grid coordinate systems. For its successful application to the present method, the pressure-correction equation must take full account of the following features:

(a) floating, non-orthogonal grid;

(b) non-orthogonality of the velocity components; and

(c) compressibility of fluid.

Full derivation of the pressure-correction equation is described in Appendix C; here, its final form is presented with reference to Fig. 3.9. It is:

$$(A_N + A_S + A_E + A_W)\ p'_P = A_N p'_N + A_S p'_S + \varepsilon_P \quad . \quad (3.15)$$

The A coefficients contain mass fluxes, areas and inclinations of control-volume faces. The ε_P term expresses the kinematic-compatibility error, for grid node P, as calculated below:

$$\varepsilon_P \equiv (\Delta y^*_e - \Delta y^*_w) - \Delta x.(\tan \alpha^*_n - \tan \alpha^*_s) \quad ; \quad (3.16)$$

where superscript *, given to Δy and α, denotes that these quantities are based on an approximate pressure field.

Equation (3.15) is the pressure-correction equation for grid node P. Similar equations are obtained for the other grid nodes at the constant-x section under consideration. Simultaneous solution of these equations yields the required values of pressure corrections. The corresponding corrections in u, v and ρ are then calculated as explained below.

Let us confine our attention to the values associated with the control volume shown in Fig. 3.9. The velocity corrections v'_n, v'_s and u'_w are calculated by using Equations (C.24), (C.25) and (C.28) respectively. No correction is applied to the velocity u_e because the convective effect of u'_w nullifies the independent correction u'_e, given by Equation (C.27). The convection effect can be understood by examining the u-momentum equation, Equation (A.5) or Equation (A.1). Finally, the density ρ_P is recalculated by using the corrected pressure p_P.

3.4.7 Block correction of pressures at constant-x lines

In addition to the above-mentioned local pressure-corrections, block (or uniform) pressure-corrections are also applied. Suppose, section j in Fig. 3.11 represents the cross-stream section under consideration (note that the corresponding u-velocities lie at section $j+\frac{1}{2}$); then, the local corrections are applied to the pressures of section j and the block corrections are applied to the pressures of sections j and j+1. The objective of these block corrections is to ensure that the calculated overall width of flow, at section $j+\frac{1}{2}$, is exactly equal to the actual dimension. This condition can also be regarded as the kinematic-compatibility condition for the control volume ABCD, assuming that the calculated width of the upstream section, $j-\frac{1}{2}$, is exact.

The block corrections are calculated in two steps: first, a total block correction ($\bar{p}'$) is calculated by Equation (D.2), derived in Appendix D; and, then $\bar{p}'$ is divided into two components, $\bar{p}'_C$ and $\bar{p}'_D$, respectively for current (j) and downstream (j+1) planes, as follows:

$$\bar{p}'_C = M^2 \bar{p}' \quad ; \quad (3.16)$$

$$\bar{p}'_D = -(1 - M^2) \bar{p}' \quad ; \quad (3.17)$$

where M stands for the maximum of local Mach numbers, calculated at the u-velocity locations. If at any point,

Mach number is greater than 1.0; then, M is assigned a value of 1.0.

The implications of the above practice, Equations (3.16) and (3.17), are:

(i) If the flow is incompressible, $\bar{p}'_C = 0$; i.e. pressure correction is applied only at the downstream plane.

(ii) When flow is supersonic, at the whole or part of cross section, $\bar{p}'_D = 0$; i.e. pressure correction is applied only to the current plane. This ensures that the calculated flow areas as section $(j+\frac{1}{2})$ are not affected by the pressure changes at the downstream section (j+1).

(iii) In a subsonic flow, the correction $\bar{p}'_D$ is of the opposite sign than that of $\bar{p}'_C$. This implies that both the corrections either increase or decrease the u-velocities at section $(j+\frac{1}{2})$ and thus are complementary to each other.

After calculating the block corrections, $\bar{p}'_C$ and $\bar{p}'_D$, the u-velocities are corrected, at each grid line at section $(j+\frac{1}{2})$, as follows:

$$u'_i = \frac{1}{(\rho u)_i} (\bar{p}'_C - \bar{p}'_D) \qquad . \quad (3.18)$$

No corrections are required for v-velocities. The densities are recalculated from the corrected pressures.

Finally, it may be remarked that the block corrections improve the pressure levels while the local corrections modify the pressure distributions at cross-stream planes. Their roles are further elucidated in Section 3.6 which presents the sequence of calculation steps of the whole procedure.

3.5 Boundary conditions

For a typical cascade-flow problem, the solution domain and its boundaries have been shown in Fig. 1.2; here, we describe a manner in which the flow conditions are specified at these boundaries.

Inlet plane: Stagnation pressure and density, and flow direction, are specified.

Outlet plane: Static pressure is specified.

In some cases, where the exit flow condition is subsonic, static pressure can also be prescribed at the inlet plane instead of at the exit plane. In these circumstances, the exit static pressure is an outcome of the solution, and the boundary condition for the outlet plane can be changed to one of the following two types:

(i) cross-stream variation of pressure is specified, or

(ii) streamwise derivative of pressure is specified.

Solid boundaries: Local surface inclinations, with reference to the x-direction, are specified.

Dividing streamline boundaries, upstream and downstream of the cascade

These are treated in the same way as solid boundaries, except that their local inclinations are calculated, as explained below, from the periodicity ("cyclic boundary") conditions.

Fig. 3.12 shows a typical arrangement of streamlines in the cyclic-boundary region. The bounding streamlines are numbered as 1 and n. The line 2' is a pseudo streamline which is parallel to streamline 2 and displaced from it by a distance equal to pitch. Periodicity of flow implies that the flow properties are identical at corresponding points such as A and A', B and B', D and D', etc.

In order to determine the inclination α_B, the velocity v_B is calculated by applying Equation (3.6) to the control volume, shown by the shaded area in Fig. 3.12, and the value of streamwise velocity u_B is interpolated from the u-velocities of the adjoining points, viz. C, D, E and F. Then α_B is simply calculated from Equation (3.7).

Near-round-edge regions: In the regions close to the round edges of the blades, large changes of flow properties occur over short distances which are of the same order as the grid size. At present, these regions are treated in

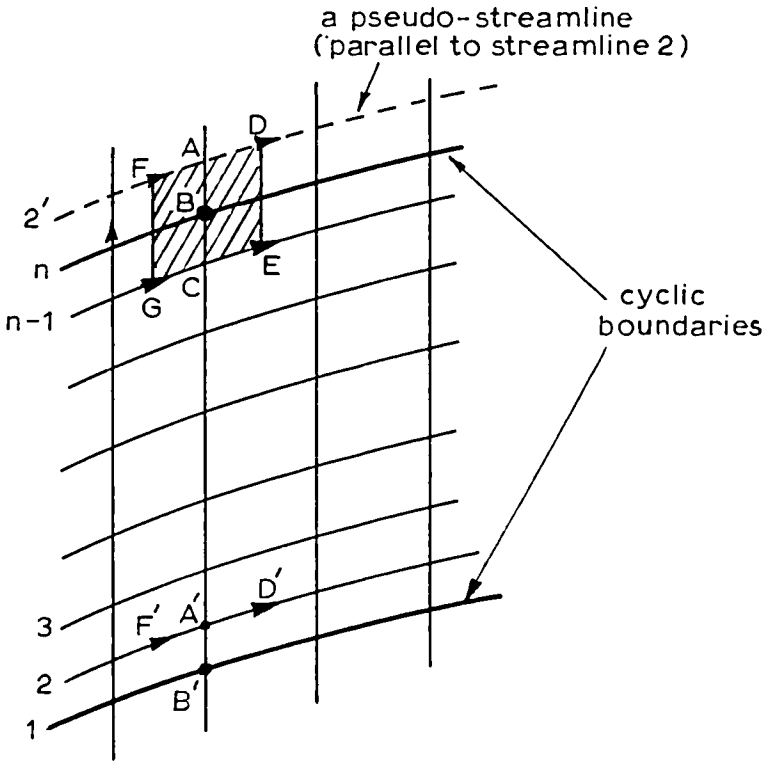


Fig. 3.12 Streamlines in the cyclic-boundary region

an approximate manner, i.e. by placing small "cusps" at the round edges. At the leading edge, a cusp is made symmetrical to the inlet flow direction, while a trailing-edge cusp satisfies the Kutta-Joukowski condition of zero load. More sophisticated practices can be easily incorporated in the procedure.

3.6 Sequence of calculation steps

The main features of the numerical-solution scheme have been outlined in Section 3.2.4; and in the subsequent sections all other necessary details have been explained. Now in this section, the overall solution scheme is presented by describing the sequence of calculation steps. These steps are:

(1) The pressure field is first assigned guessed values. For example, the pressure may be assumed to be uniform in the y-direction and to vary linearly in the axial direction.

(2) Inlet distributions of u and ρ are obtained from the static pressure and the stagnation flow conditons (p_o, ρ_o), by using isentropic-flow relations, as:

$$\rho = \rho_o \cdot \left(\frac{p}{p_o}\right)^{1/\gamma} \quad ; \quad \text{and}$$

$$u = \left[2 \cdot \frac{\gamma}{\gamma-1} \cdot \frac{p_o}{\rho_o} \cdot \left\{ 1 - \left(\frac{p}{p_o}\right)^{\frac{\gamma-1}{\gamma}} \right\} \right]^{\frac{1}{2}} .$$

Velocity component v is deduced from u and the given α.

(3) At the next downstream section, ρ, u and v are calculated by solving Equations (3.4), (3.5) and (3.6) respectively. If the flow is viscous, u-velocity equations, Equation (3.14), are solved simultaneously by applying the tri-diagonal matrix algorithm (TDMA) along the line of constant x.

(4) From the just computed velocities and densities, the streamline inclinations, α's, and the y-distances, Δy's, are computed as explained in Section 3.4.3.

(5) Now, the block corrections are applied, as explained in Section 3.4.7, to the pressures of the current and the next downstream section. The corresponding corrections to u and ρ are applied and α's and Δy's are recalculated.

(6) Next, the local pressure-corrections are calculated by solving the pressure-correction equations, Equation (3.15), by TDMA. All the pressures, densities and velocities, associated with the current section, are corrected and α's and Δy's are recalculated.

Calculations of this step can be, if required, repeated before proceeding to the next step. Details of this practice, together with those of some other convergence-improvement devices, are given in Appendix G.

(7) The block corrections are applied, again, as in step (5).

(8) The next downstream section is chosen; and steps 3 to 7 are repeated. This step-wise march is continued until the end of the flow domain is reached. This completes one marching sweep; and a new, improved, two-dimensional distribution of pressure has been obtained.

(9) Steps 2 to 8 are repeated until the pressure corrections or the kinematic-compatibility errors have become smaller than a pre-assigned value. On the last sweep, the converged distributions of velocities, pressure and other quantities of interest are printed out.

CHAPTER 4

FURTHER EXTENSION OF THE PREDICTION PROCEDURE

4.1 Introduction

In this chapter, the prediction procedure is extended to include the following features of the cascade flows:

(i) turbulence;

(ii) heat transfer;

(iii) rotation; and

(iv) flow convergence resulting from variation of hub radius and blade height.

Each of the above features is described in two parts: in the first one, the relevant physical details are presented and in the second, the required alterations in the procedure are explained.

4.2 Calculation of a turbulent flow

More often than not, the cascade flows are turbulent. Full analysis of a turbulent flow, by solving the time-dependent equations for the instantaneous values of velocities, is a formidable task. A practical way is: to solve the equations for time-mean velocities with the aid of a suitable 'turbulence model'. The basic function of a turbulence model is to relate, in a hypothetical way, the local state of

turbulence to the mean-flow properties. A large number of such propositions are available in the literature and several of these have been discussed by Launder and Spalding (1972), and Harlow (1973). From these references, it can be inferred that most of the commonly used models are based on the "eddy viscosity" concept. Any model from this category can be easily employed in the present prediction procedure. Now we briefly describe the eddy-viscosity approach and a simple turbulence model which has been presently adopted for demonstration.

Eddy-viscosity approach

According to the eddy-viscosity approach, the shear stress in a turbulent flow is related to the local velocity gradient in the same manner as in a laminar flow. For example, if we consider a parallel flow in x-direction such that the mean velocity $\bar{u} = \bar{u}(y)$; then, the shear stress τ can be expressed as:

$$\tau = \mu_{eff} \cdot \frac{\partial \bar{u}}{\partial y} \quad ; \quad (4.1)$$

$$\mu_{eff} = \mu_t + \mu \quad ; \quad (4.2)$$

where μ_t is "turbulent" or "eddy" viscosity and μ_{eff} is "effective" viscosity.

The effective viscosity is allowed to vary from point to point; but, at any point in the flow domain, it is assumed to be isotropic. Thus, μ_{eff} can be regarded as a scalar

property of flow and its values should be ascribed by independent means such as a turbulence model.

Prandtl's mixing-length model

At present, the Prandtl's mixing-length model is employed; and, accordingly, the turbulent contribution to effective viscosity is calculated as:

$$\mu_t = \rho l^2 \left|\frac{\partial u}{\partial y}\right| \quad ; \quad (4.3)$$

where l is the mixing length and its local values should be prescribed empérically. The adopted l-distribution is shown in Fig. 4.1; it can also be expressed by the following relations:

$$l = Ky \text{ when } y \leq \frac{\lambda}{k} y_A \quad ; \quad (4.4)$$

$$l = \lambda y_A \text{ when } y > \frac{\lambda}{k} y_A \quad ; \quad (4.5)$$

where k and λ are the two empérical constants having values of 0.4 and 0.12 respectively. Fig. 4.1 also shows that the adopted l-distribution is an approximation to the one deduced from the experimental data of plane channel flows, Fediaevsky (1936). Similar approximations (ramp-type distributions) have been also used in many other flow situations by Ng et al. (1967), Patankar and Singhal (1972), and Spalding (1975).

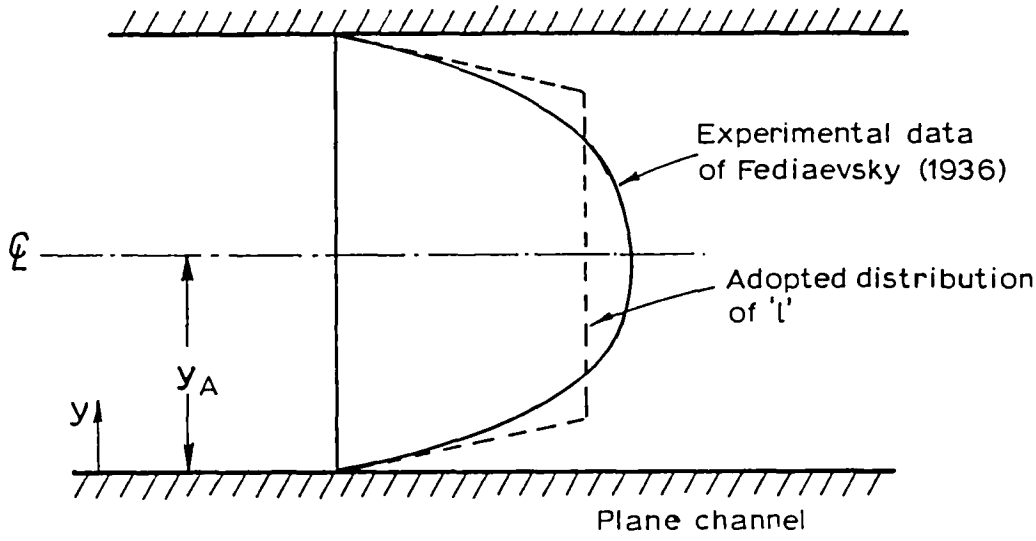


Fig.4·1 The mixing-length distribution

Remarks on adequacy of the turbulence model

The Prandtl's mixing-length model is known to be satisfactory for equilibrium flows, e.g. boundary-layer flows wth zero or mild pressure gradients. Generally in cascade flows, there are regions of steep favourable and adverse pressure gradients; and, therefore, a higher level model will be more adequate. A two-equation model, the $k\sim\varepsilon$ model of turbulence,has been tested and found satisfactory for the boundary layers exhibiting a large variety of pressure gradients; a separate report, Singhal and Spalding (1975), has been prepared on this work and a copy is enclosed as Appendix H of this thesis.

Calculation of wall shear stress

In order to calculate the wall shear stresses from the velocity profiles, semi-empirical formulae or "wall functions" are required. The basis and derivations of wall functions under different flow situations are explained by Patankar and Spalding (1970); here the following one, based on the logarithmic law of wall, has been adopted:

$$s = \left[\frac{K}{\log(ERs^{\frac{1}{2}})}\right]^2 \quad ; \quad (4.6)$$

where shear-stress coefficient $s \equiv \dfrac{\tau_S}{(\rho u^2)_C}$; and

Reynolds number $R \equiv \left[\dfrac{\rho u y}{\mu}\right]_C$.

Here suffixes S and C respectively denote the surface (wall) and a point close to it. The constants K and E are of the order of 0.4 and 9.0 respectively. If desired, Equation (4.6) can be modified to account for the pressure-gradient effects; e.g. as explained in Van Den Berg (1973) and Spalding (1975).

Alterations in the procedure

From the computational point of view, the treatment of viscous flows has been already explained in Section 3.4.5. In order to account for turbulence, only the following two changes are required:

(i) incorporation of means of ascribing μ_{eff} values, e.g. Equations (4.3), (4.4) and (4.5);

(ii) incorporation of a wall function for turbulent flows, e.g. Equation (4.6).

It may be noted that in Equations (4.3) to (4.6), values of ρ, u and y, which are yet to be computed, are required. For this purpose, the presumption of upstream values has been found adequate.

4.3 Simultaneous calculation of heat transfer

Calculation of heat transfer is important, particularly for the cascades of high-temperature gas turbines. The present prediction procedure can easily make such calculations by solving an additional equation, for the conservation of

stagnation enthalpy, simultaneously with the flow equations described in the previous chapter.

The stagnation enthalpy, $\tilde{h}$, is defined as:

$$\tilde{h} = C_p T + \frac{u^2}{2} \quad . \quad (4.7)$$

A conservation equation for $\tilde{h}$ is derived by considering the energy balance for a control volume; details of the derivation and of the associated auxiliary relations are given in Appendix E. The final form is written, with the help of grid-numbering notations of Fig. 3.11, as follows:

$$(\Delta\psi_i + A_i + B_i)\tilde{h}_i = A_i\tilde{h}_{i+1} + B_i\tilde{h}_{i-1} + C_i \quad ; \quad (4.8)$$

where coefficients A_i and B_i contain effective exchange coefficients of heat and C_i contains upstream value of $\tilde{h}_i$ and kinetic-heating term. This equation has the same form as Equation (3.15). Thus at a constant-x line, $\tilde{h}$'s can be calculated with the aid of TDMA and subject to appropriate conditions at the boundary grid nodes. At the blade surfaces, boundary conditions are provided by specifying either temperatures or heat fluxes; while in the outside regions, upstream and downstream of the cascade, these are determined by the condition of circumferential periodicity.

Calculation of heat-transfer coefficient at a solid surface

At a solid surface only one of the two quantities, i.e. temperature or heat flux, is specified; and the other quantity is deduced from the temperature of the near-wall grid node and the heat-transfer coefficient (Stanton number)

prevailing at the fluid-solid interface. The node temperature is calculated from the equation of state; while the heat-transfer coefficient is calculated by employing the following wall function (Patankar and Spalding, 1970):

$$S = \frac{s}{\sigma_t \, (1 + s^{\frac{1}{2}}.P)} \qquad ; \quad (4.9)$$

where Stanton number $S \equiv - \dfrac{J_s}{(\tilde{h}_{s,ad} - \tilde{h}_s)(\rho u)_c}$;

shear-stress coefficient s is same as defined in Equation (4.6); suffix 'ad' denotes the adiabatic value; and P is a function of the laminar Prandtl number σ and its supposed turbulent counterpart, σ_t. The employed P function is:

$$P = 9.0 \left(\frac{\sigma}{\sigma_t} - 1\right) \left(\frac{\sigma_t}{\sigma}\right)^{\frac{1}{4}}$$

Alterations in the procedure

For heat transfer calculations, the procedure is modified by incorporating the provisions of solving Equations (4.8) and (4.9). The overall solution scheme remains same as explained in Section 3.6, except that step 4 is modified to imply that the equations for ρ, u, v and $\tilde{h}$ are solved.

4.4 Calculation of quasi three-dimensional flow, resulting from axial variation of hub radius and blade height

So far only the plane flows have been considered. In this section it is explained how the procedure can account for the flow convergence resulting from the axial variation of hub radius and blade height.

For analysis purpose, a stream sheet, as shown in Fig. 1.1, is considered. Its thickness and mean radius are specified, as a function of axial distance. Since these dimensions do not vary in the circumferential direction, it is also called as an axi-symmetric stream annulus. It may be reminded here that the flow is not axisymmetric. The flow properties are still considered to vary in the axial and circumferential directions and to be constant in the radial direction; the latter is due to the assumption of radial equilibrium. In the literature, such a flow is commonly called "quasi three-dimensional".

Fig. 4.2 illustrates the cross-section of a stream annulus in the meridional plane. The mean surface of stream annulus can be obtained by revolving the generator line, AB, about the axis, z. Let r and θ be the radial and circumferential directions respectively. Also suppose that x is the distance measured along the generator line AB. Then, the surface of revolution can be called as a 'x-θ' surface and the following observations can be made:

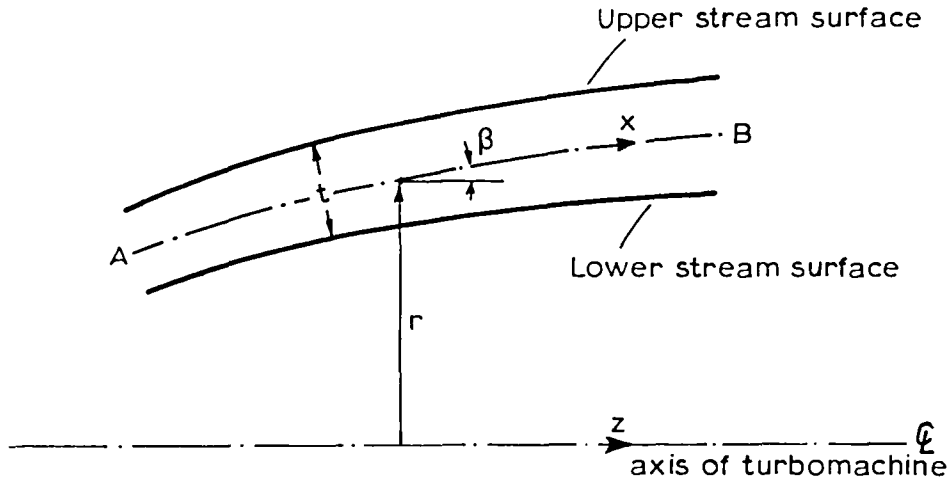


Fig. 4·2 Cross section of a stream annulus in the meridional plane

(a) x and θ directions are normal to each other.

(b) By considering $y \equiv r\theta$, x and y have the same meanings as used in the description of procedure in Chapter 3.

(c) Stream sheet thickness, t, and mean radius, r, can be specified as functions of x.

(d) By considering t = 1 and r = a constant, the problem reduces to that of a plane flow.

Let us now examine the governing equations for an inviscid, adiabatic, compressible flow. Equations (3.1), (3.3) and (3.4) are still valid irrespective of the fact that the solution surface x-y is no longer a plane surface. However, Equation (3.2) should be modified to account for the coriolis force resulting from the curvature of x-y surface. Derivation of this equation is presented in Appendix F; its final form is:

$$(\Delta\psi)\cdot(v_2 - v_1) = (p_3 - p_4).\Delta x.t - v_1\left(\frac{\sin\beta}{r}\right).\Delta x.\Delta\psi \quad , \quad (4.10)$$

where r, t and β are related to the local geometrical dimensions of the stream sheet; and all other symbols have the same meaning as in Equation (3.6).

The continuity relationship, Equation (3.8), also should be modified as:

$$\Delta y = \frac{\Delta\psi}{\rho u \cos\alpha.t} \qquad (4.11)$$

All other details of the procedure remain as explained in Chapter 3.

4.5 Calculation of flow in a rotating cascade

In this section, the prediction procedure is further extended by including the rotation effects.

Suppose the stream annulus, shown in Fig. (4.2), is rotating about the z-axis with a constant angular (anti-clockwise) velocity, Ω. Further, assume that the coordinate system is also rotating about the z-axis with the same angular velocity. Then, the resultant relative flow is steady and it obeys the same physical laws as the absolute flow through the same system at rest.

In such a system the two momentum-conservation equations can be written as follows:

Streamwise momentum-conservation equation:

$$(u_2^2 - u_1^2) = \frac{2\gamma}{\gamma-1}\left(\frac{p_1}{\rho_1} - \frac{p_2}{\rho_2}\right) + \Omega^2 (r_2^2 - r_1^2) \quad ; \quad (4.12)$$

circumferential-direction momentum-conservation equation:

$$\Delta\psi(v_2 - v_1) = (p_3 - p_4).\Delta x.t - \left(\frac{v}{r} - 2\Omega\right).\sin B.\Delta x.\Delta\psi \ . \quad (4.13)$$

Equation (4.12) implies that the "rothalpy" $\left(\frac{u^2}{2} + \frac{\gamma}{\gamma-1}\frac{p}{\rho} - \frac{1}{2}\Omega^2 r^2\right)$ is constant along a streamline; Moore (1964, p. 346). For an incompressible flow, $\gamma = \infty$;

and, therefore, $\frac{u^2}{2} + \frac{p}{\rho} - \frac{1}{2}\Omega^2 r^2$ is constant. The term $(\frac{p}{\rho} - \frac{1}{2}\Omega^2 r^2)$ is often called 'reduced pressure' for the rotating system.

Equation (4.13) is similar to Equation (4.10) except that in the last term, coriolis force due to rotation is also included. This term has been obtained by analysing the θ-direction momentum equation, in the cylindrical coordinates given by Hawthorne (1964, p. 491).

Apart from the above-mentioned changes in momentum-conservation equations, all other details of the prediction procedure remain unaltered.

CHAPTER 5

EXPERIMENTAL INVESTIGATION

5.1 Flow geometry and main parameters of study

An experimental investigation of a two-dimensional, subsonic cascade flow has been carried out to study the influence of small flaps attached at the trailing edges of the blades. The essential features of the flow geometry under consideration are shown in Fig. 5.1. The test cascade consists of seven identical blades and flaps. Static pressures have been measured at the suction and pressure surfaces of the central blade. Flow velocities have also been measured in the downstream region, outside the blades. Full details of the test section and measuring devices are provided in Sections 5.2.2 and 5.2.3.

The main parameters of the present flow situation are:

(a) inlet flow angle, α_{in};

(b) inclination of trailing-edge flaps, α_{flap}.

The latter parameter has been given the prime importance. The flow measurements have been taken for the following values of these parameters:

$\alpha_{in} = 20^{o}$ and 40^{o} ;

$\alpha_{flap} = 0^{o}, -30^{o}, -45^{o}, -60^{o}$ and no flaps.

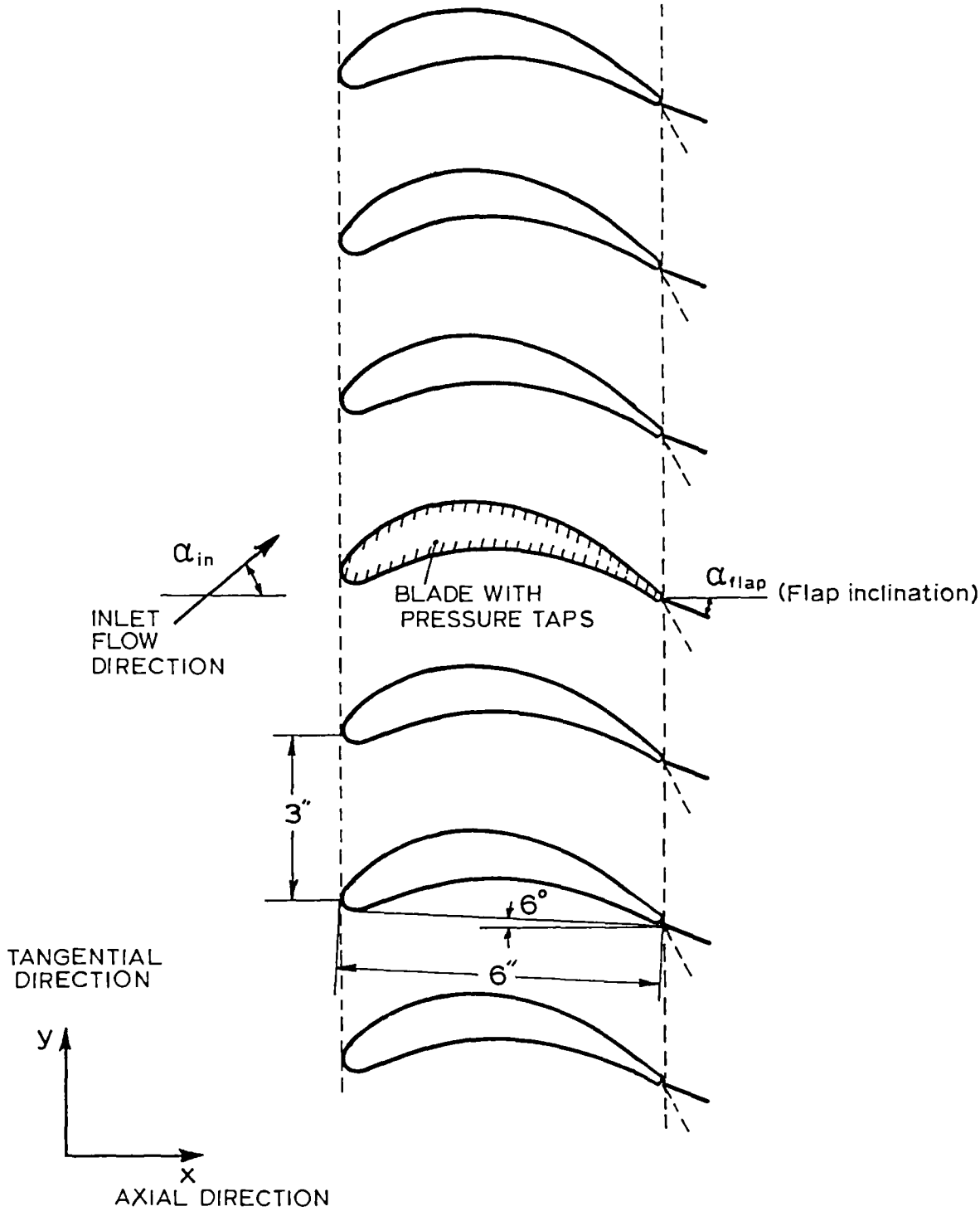


Fig. 5-1 Experimental flow geometry

Thus in all, ten cases have been considered. In the following sections of this chapter, first, the experimental apparatus is described; and, then, the experimental data are presented and analysed.

5.2 Description of the experimental apparatus

5.2.1 General layout

The experiments have been conducted in an open-circuit wind tunnel, in the Gas Dynamics Laboratory of Imperial College. A schematic layout of the experimental apparatus is shown in Fig. 5.2; and a pictorial view is presented in Fig. 5.3. The main apparatus consists of a blower, straight and converging rectangular ducts, an inlet duct and a cascade of impulse blades. The blower is driven by a 15 h.p., D.C. motor which permits continuous variation of speed, up to a maximum of 3000 r.p.m. The straight ducts, located next to the blower, are 14½ ft. long and 22" x 20" in cross section. The converging duct is relatively short. Its length is 1½ ft. and the cross section of its downstream face is 16¾" x 12". Following this duct, there is a so called "inlet duct"; its downstream face is inclined by 40 degrees from the vertical plane. This inclined face serves as the base of the cascade assembly and thus fixes the tangential direction of the cascade. Since the flow direction, guided by the upstream ducts, is horizontal; the inlet flow angle,

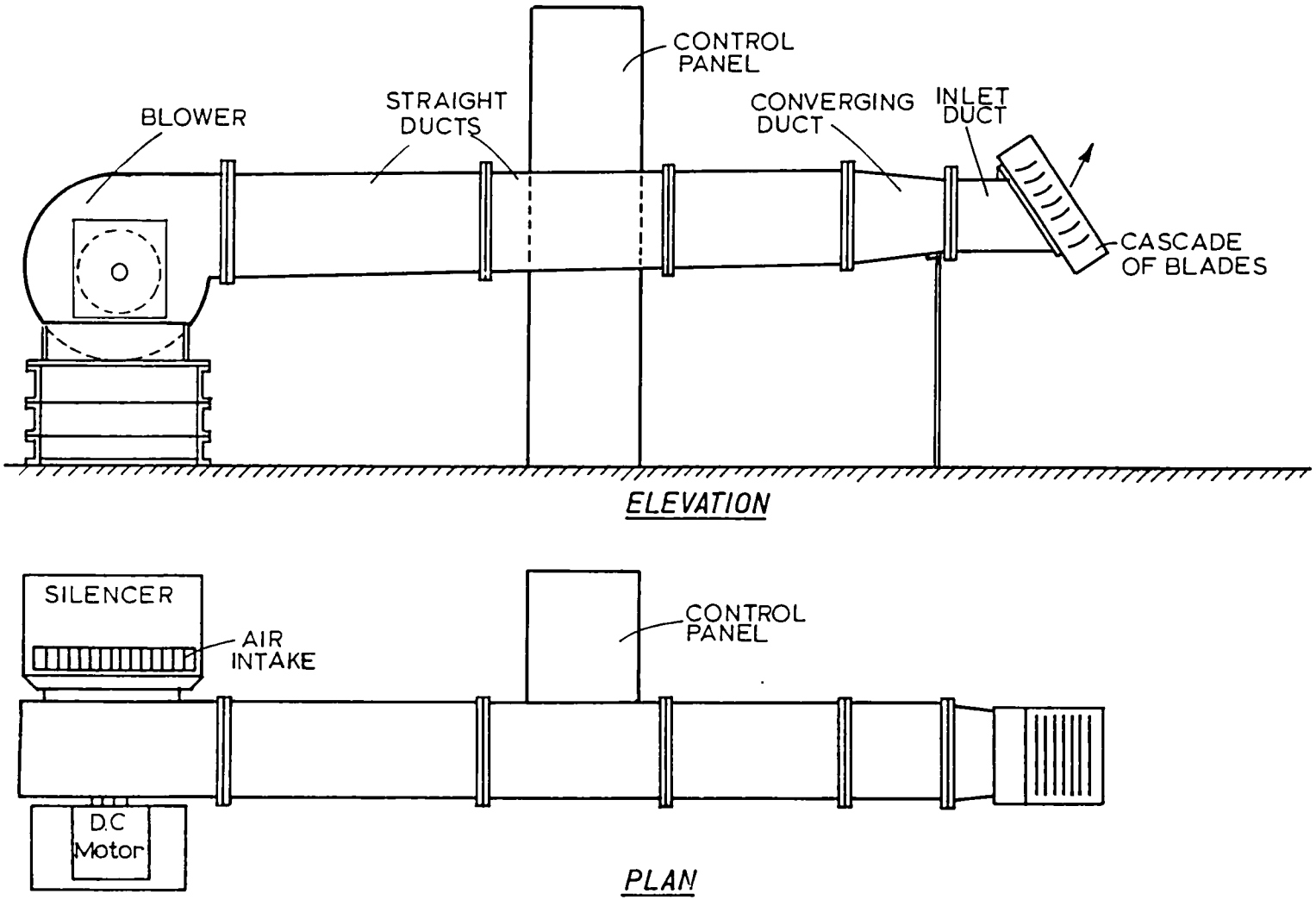


Fig. 5·2 Schematic layout of the experimental apparatus

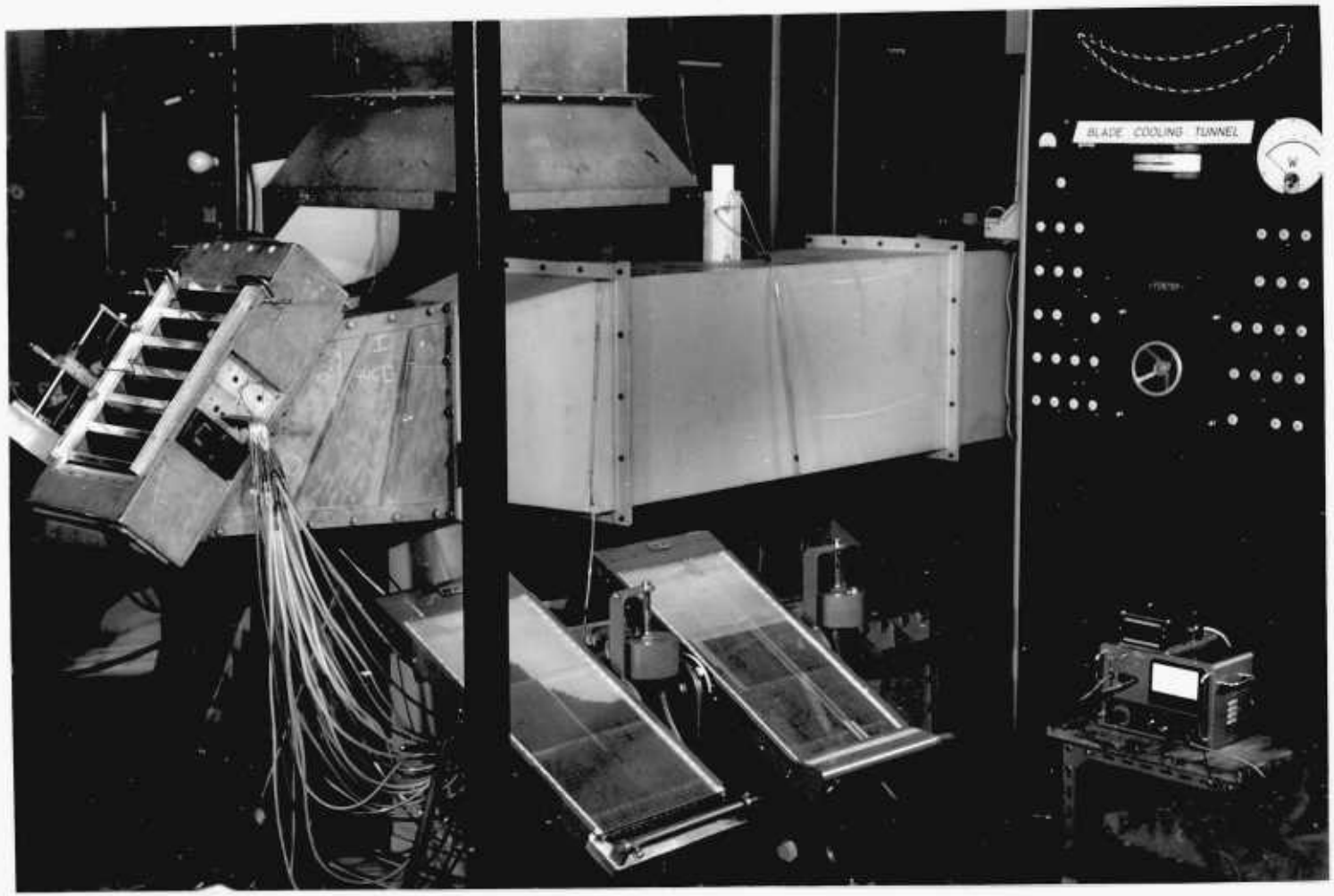


FIG. 5.3 A PICTORIAL VIEW OF THE EXPERIMENTAL APPARATUS

α_{in} as shown in Fig. 5.1, is equal to 40 degrees. There are four such ducts which can make inlet flow angle to be 20^{o}, 30^{o}, 40^{o} and 50^{o} respectively. Only one duct can be used at a time. The cascade assembly is bolted to the inclined face of the inlet duct; and the flow is discharged to the atmosphere. Details of the cascade blades and the attached flaps are given in the next section. The maximum average velocity in the cascade, with the present apparatus, is about 55 ft/sec; the corresponding Mach number is .05 and the Reynolds number, based on the chord length, is 1.5×10^{5}.

5.2.2 The test section

The test section includes a cascade of blades and an assembly of flaps which can be attached to the cascade frame in such a way that one end of each flap joins the trailing edge of a blade. These flaps can be tilted, together, like slats in a venetian blind. The overall arrangement is shown in Fig. 5.4.

The cascade consists of seven impulse type blades which are made of Epoxy resin. Each blade has a cross section as shown in Fig. 5.5; the exact coordinates of the blade profile are given in the fabrication drawings available in the laboratory. All the blades are straight and have a span of 12 inches and a chord of 6 inches. The main geometrical parameters of the cascade are as follows:



FIG. 5.4 VIEW OF THE TEST SECTION

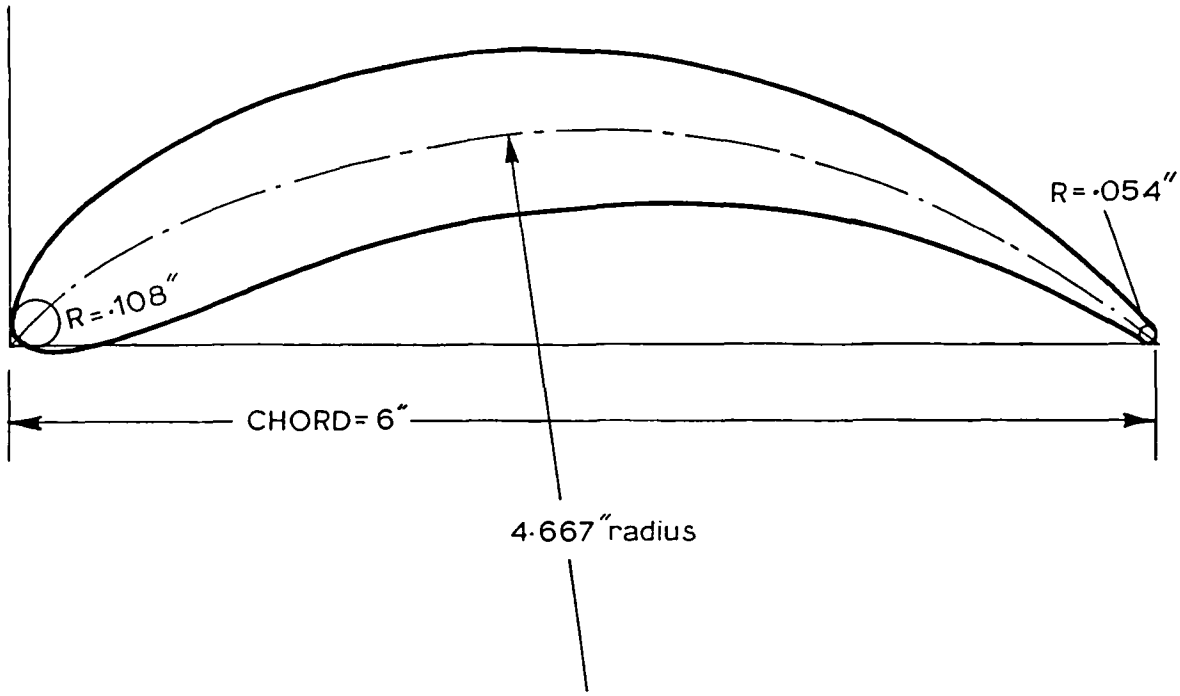


Fig. 5·5 Blade profile

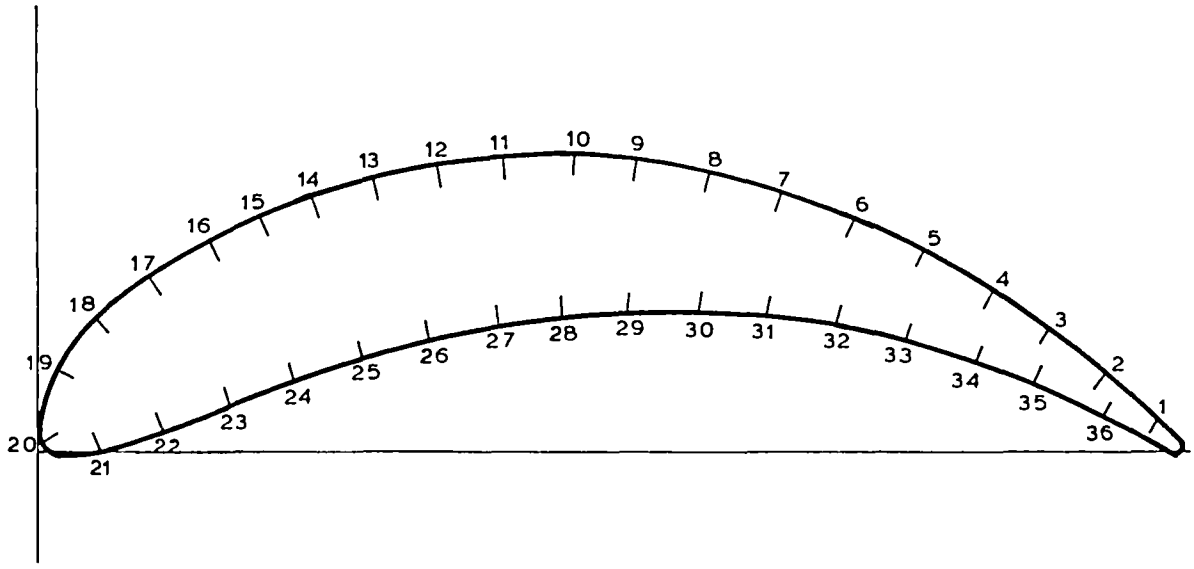


Fig. 5·6 Locations and numbering of the pressure taps

(i) aspect ratio (span/chord) = 2 ;

(ii) pitch-chord ratio (pitch/chord) = 0.5 ;

(iii) stagger (or blade setting) angle, $\delta = -6^{\circ}$ with reference to the axial direction.

One of the blades has a provision for the measurements of static pressures, at both the surfaces. It has 36 pressure-tap holes (made by a BSF 60 drill), located in a manner as shown in Fig. 5.6; the exact locations and other constructional details are given in the corresponding fabrication drawing. This blade is placed in the middle position in the cascade because the periodicity conditions are expected to be better there than near the ends of the cascade.

Flaps

The flaps are made of aluminium and are of the size 11.5" x 0.75" x 0.108". The flap thickness (0.108") has been selected to be equal to the diameter of blade-trailing-edge, so that there is no abrupt change in the metal thickness at the junction of a flap and a blade. One end of each flap has a semi-circular groove; this provides a good seating at the round trailing edge. It may also be noted that the flap width is one eighth of the blade chord and that the flap length is nearly equal to the span of blade.

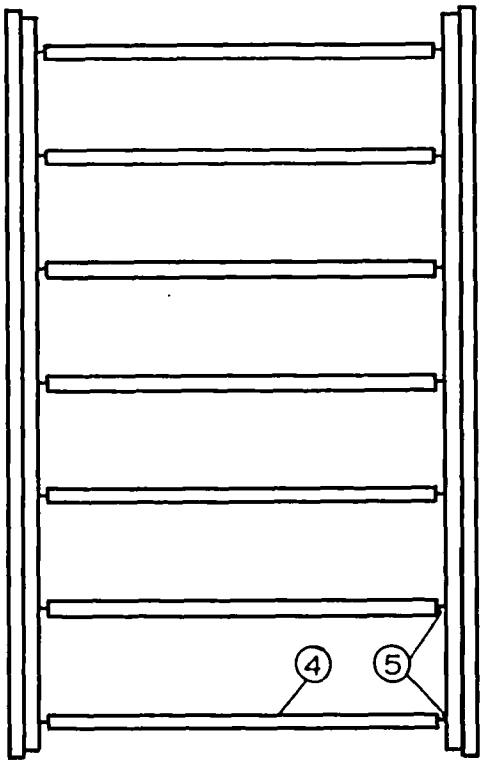
These flaps are fixed into an aluminium frame, at 3 inches interval which is equal to the pitch of blades in

the cascade. The general arrangement is shown in Fig. 5.7. The frame consists, at either end, a base plate, a fixed plate and a movable plate. Both the fixed and movable plates have $\frac{3"}{32}$ ϕ holes at 3" intervals, for adapting the guide pins attached to the flaps. Thus in the assembled condition, all the flaps turn together and are always parallel to each other. The movable plates can be locked in any position by the aid of four lock screws which are fixed to the base plates. Flap inclinations can be measured by a clinometer. This frame of flaps is attached to the cascade frame by using G clamps. Since the flap- and blade-spacings are exactly equal, the alignment of flaps with the trailing edges of blades is quite straightforward.

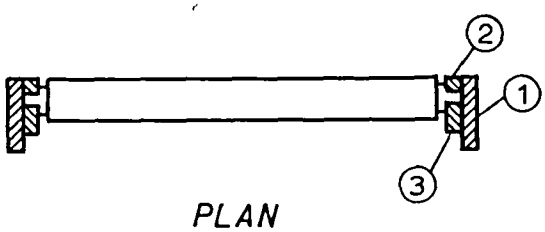
5.2.3 Measuring instruments

In the present investigation, pitot tubes and manometers have been used as the main measuring instruments. Two pitot tubes - one pitot-static tube and the other a 5-hole pitot tube, have been used; their important details are shown in Fig. 5.8. Principles of measuring pressures and velocities by such probes are discussed in Heitt and Powell (1962), and Bryer and Pankhurst (1971).

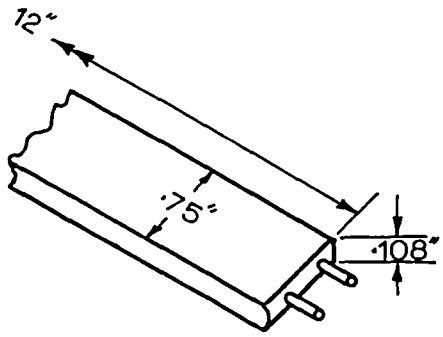
The pitot-static tube has been used to measure the static and total pressure in the upstream duct, while the 5-hole probe has been employed to measure the velocities in the downstream region, outside the cascade. The 5-hole probe had already been calibrated and used for a three-dimensional



ELEVATION



PLAN



FLAP

① Base plate
② Fixed plate
③ Slide plate
④ Flap
⑤ Guide pin

Fig. 5·7 The frame of flaps

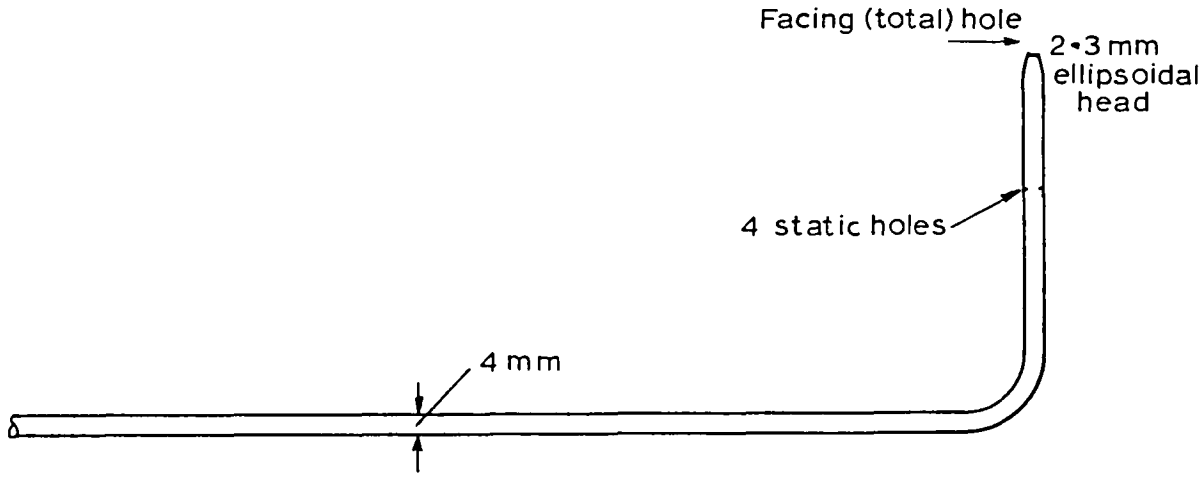


Fig. 5·8(a) The pitot-static tube

(AIRFLOW DEVELOPMENTS Ltd., catalogue No. 7017501)

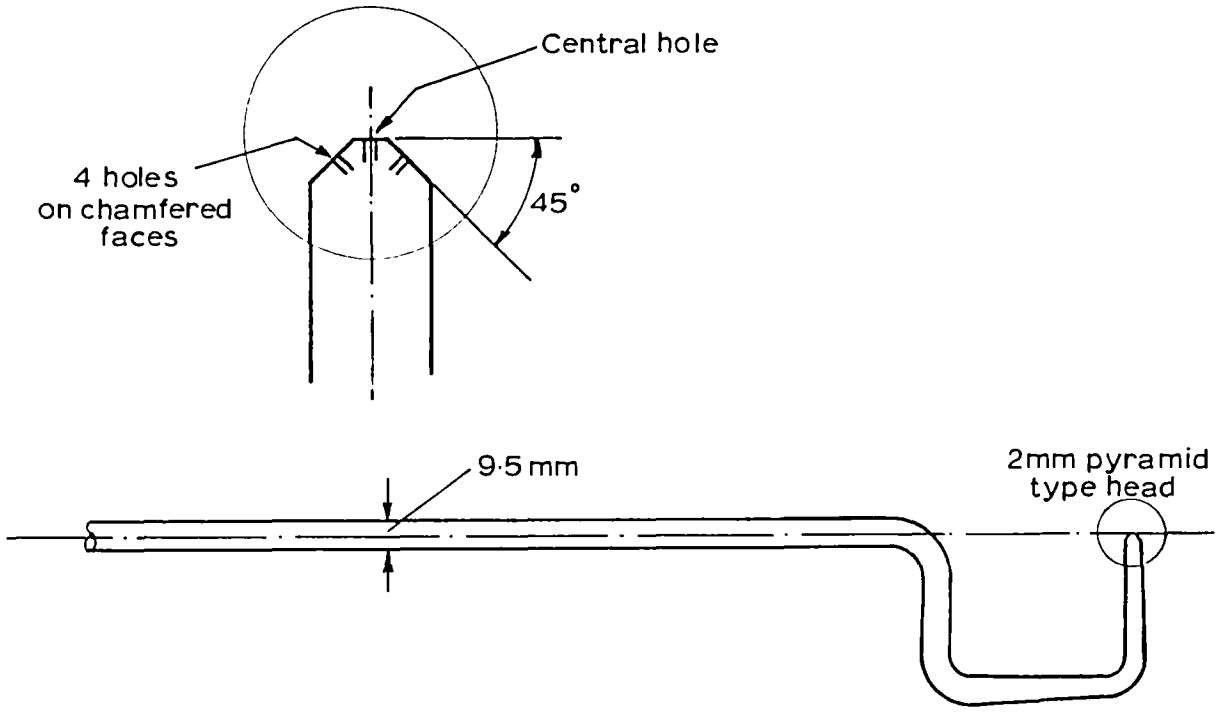


Fig. 5·8(b) The 5-hole pitot probe

(BRYER & PANKHURST, 1971)

flow by Melling (1977). The same calibration curves have been employed here.

Leads of these probes, as well as those of pressure taps, are connected to two multimanometers. Each manometer has a bank of 24 tubes and is filled with paraffin of specific gravity 0.785. Maximum fluid-column height is 24 inches. A micro-manometer has also been used to cross check some of the manometer readings.

5.2.4 The traversing mechanism

The mechanism employed to traverse the 5-hole pitot tube can be seen in Fig. 5.4. It is fixed to a side face of the cascade in such a way that the probe movements are aligned with the tangential and axial directions of the cascade. To make a traverse in the spanwise direction, which is required only to check the two-dimensionality of flow; the probe can be slided, backward and forward, through the support blocks. All these movements are measured on the scales, fixed to the traversing mechanism. The probe can also be rotated about its own axis; and the rotations can be measured on the attached protractor.

5.3 Experimental procedure

As mentioned earlier, the pressure and velocity measurements have been taken with the aid of pitot tubes and manometers. The whole task can be divided into three stages; these are described below:

Stage I: Setting up the instruments

First, the pressure-tap leads were identified, by blowing the compressed air through one hole at a time. The leads were marked corresponding to the numbering system shown in Fig. 5.6. Next, all the leads from pressure taps as well as from pitot tubes, were connected systematically to the manometers, by using appropriate rubber tubes. All the connections and junctions in the tubes were examined to be tight and leak proof. Then, several checks were made, by running the blower and examining the manometer readings, to ensure the correct orders of the connections. Both the manometers were fixed at inclined positions (60 degrees from vertical position), so as to increase the accuracy of the readings.

Stage II: Checks for the periodicity and two-dimensionality of flow

In order to examine the periodicity condition of the flow, the velocities were measured at a tangential section which was located ¾" downstream of the trailing edges, as shown in Fig. 5.9. The resultant velocity profile, shown in Fig. 5.10, displayed that the flow was reasonably periodic. Similarly, to examine the two-dimensionality of the flow, the velocities were measured at several points on a span-wise section, whose location is marked by point A in Fig. 5.9.

The velocity variation is shown in Fig. 5.11. It can be seen that the velocities are fairly uniform.

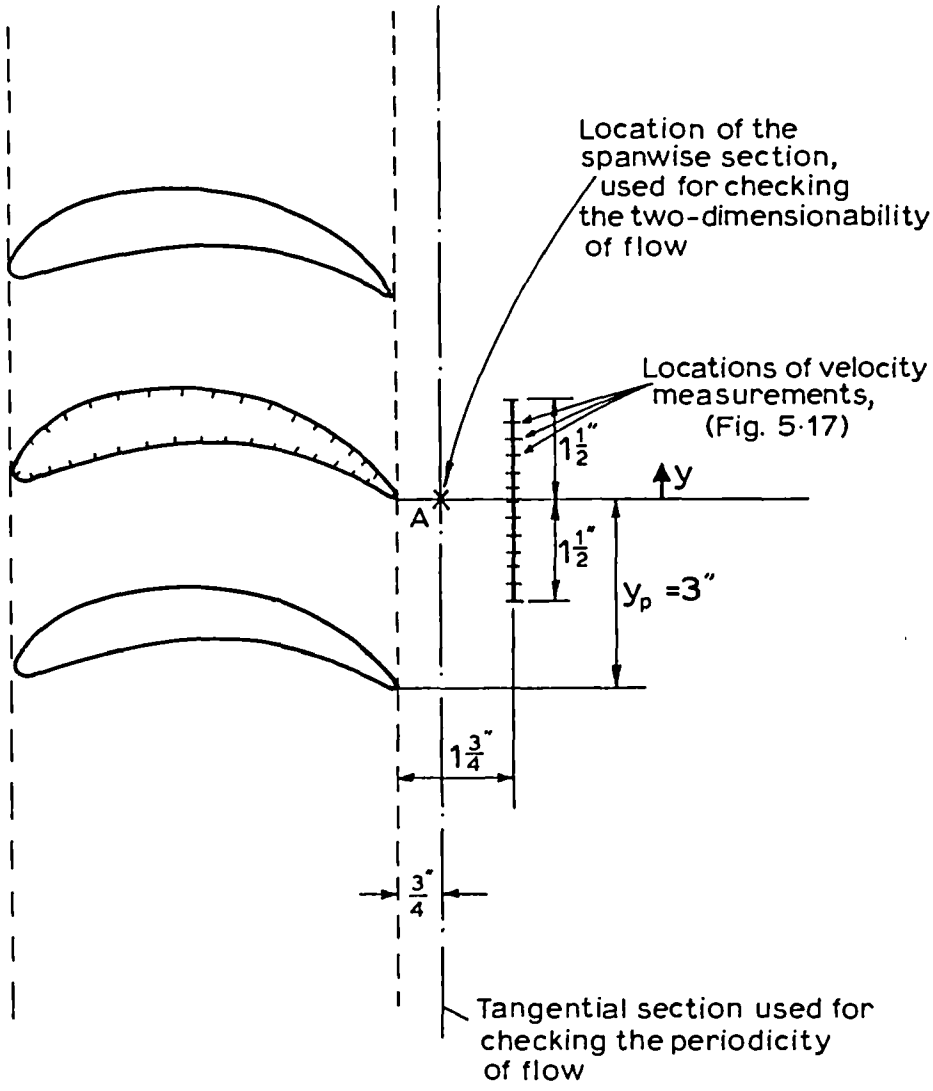


Fig. 5·9 Illustration of locations at which velocities are measured

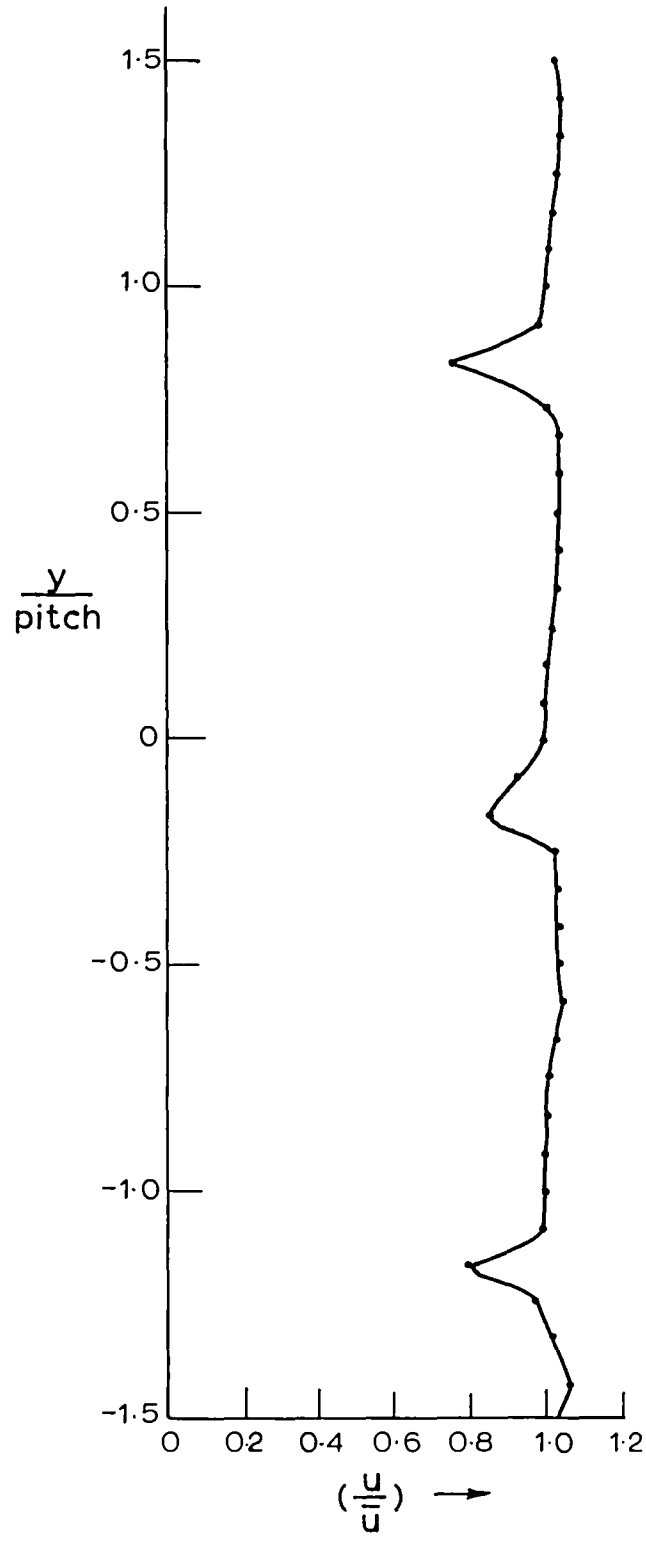


Fig. 5·10 Tangential variation of velocity over three pitch lengths

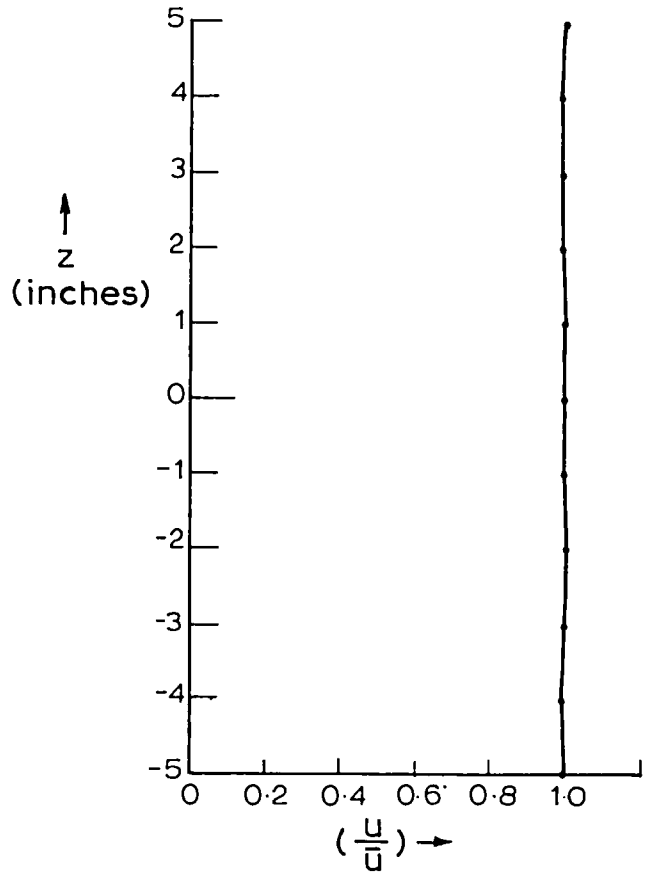


Fig.5·11 Spanwise variation of velocity

Stage III: Final measurements

As mentioned in Section 5.1, two sets of measurements have been taken: one for inlet flow angle, $\alpha_{in} = 40^{o}$; and the other for $\alpha_{in} = 20^{o}$. In each set the following five cases have been considered:

(i) No flaps

(ii) $\alpha_{flap} = 0^{o}$

(iii) $\alpha_{flap} = -30^{o}$

(iv) $\alpha_{flap} = -45^{o}$

(v) $\alpha_{flap} = -60^{o}$.

For each case the following procedure was adopted.

First, the flaps were set, as explained in Section 5.2.2 to the desired value of α_{flap}. Then, in order to avoid the air leakage at the junctions of flaps and blades, sello tapes were pasted on both the sides. Special care was taken for the blade having pressure-tap holes, so as no hole was covered by sello tape and the air leakage was stopped completely. Next, all the manometer levels and connections were checked; and then the blower motor was started and speed was slowly increased to the maximum. After a few minutes stabilizing time, the manometer readings were noted for the following quantities:

(i) static and total pressure at the centre of the upstream duct;

(ii) static pressure at the suction and pressure surfaces of the instrumented blade;

(iii) velocities at a downstream tangential section for one pitch length; the locations of measurement points are shown in Fig. 5.9.

Velocity measurements were taken at the intervals of ¼", i.e. one twelfth of the pitch of cascade. Velocity measurements have been taken only for the cases of Set 1 ($\alpha_{in} = 40^{o}$).

5.4 Presentation and analysis of the measured data

Figs. 5.12 to 5.16 present the measured pressure distributions for the fives case of Set 1 ($\alpha_{in} = 40^{o}$); the respective values of parameters α_{in} and α_{flap} are marked on each diagram. The pressures have been non-dimensionalised by using the average inlet flow properties, as follows:

$$C_p = \frac{p - p_{in}}{\frac{1}{2}\rho u_{in}^2} \quad . \quad (5.1)$$

The velocity profiles, for these cases, at the downstream section mentioned earlier, are shown in Fig. 5.17.

The measured data for Set 2 is not presented in this section; as the complete experimental data are presented in Chapter 8, where these are compared with the predictions of the calculation procedure.

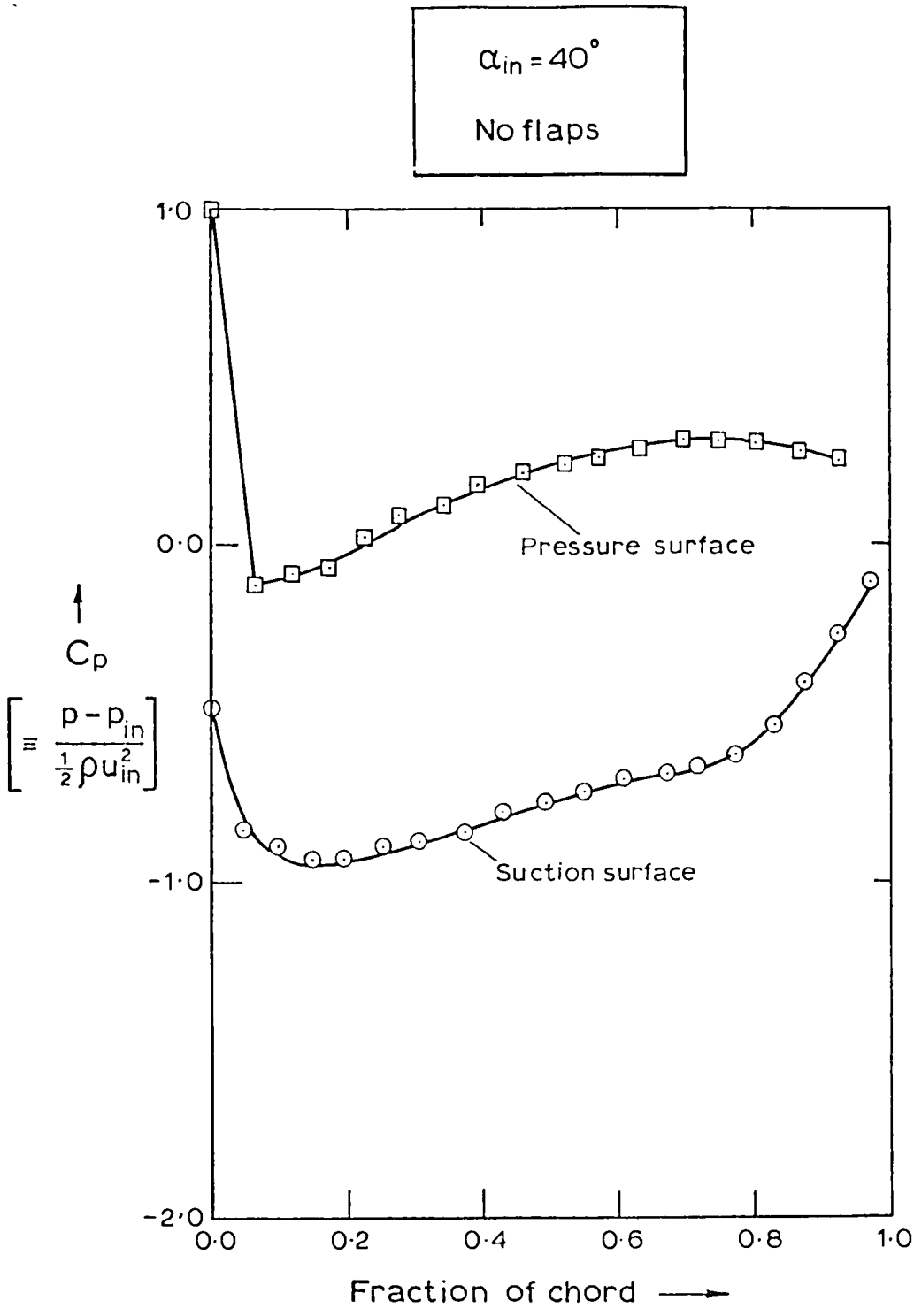


Fig. 5·12 Measured surface pressures

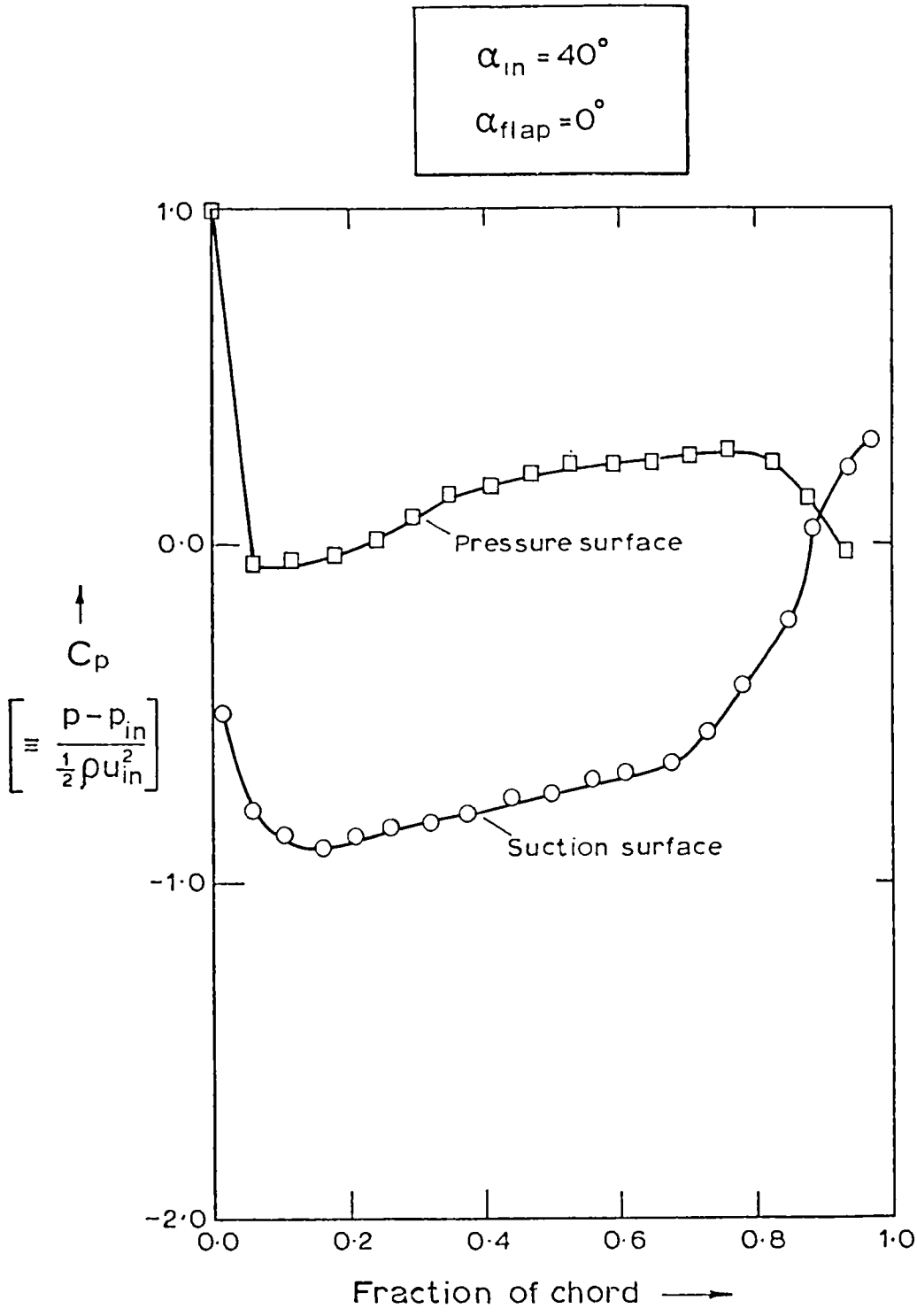


Fig. 5·13 Measured surface pressures

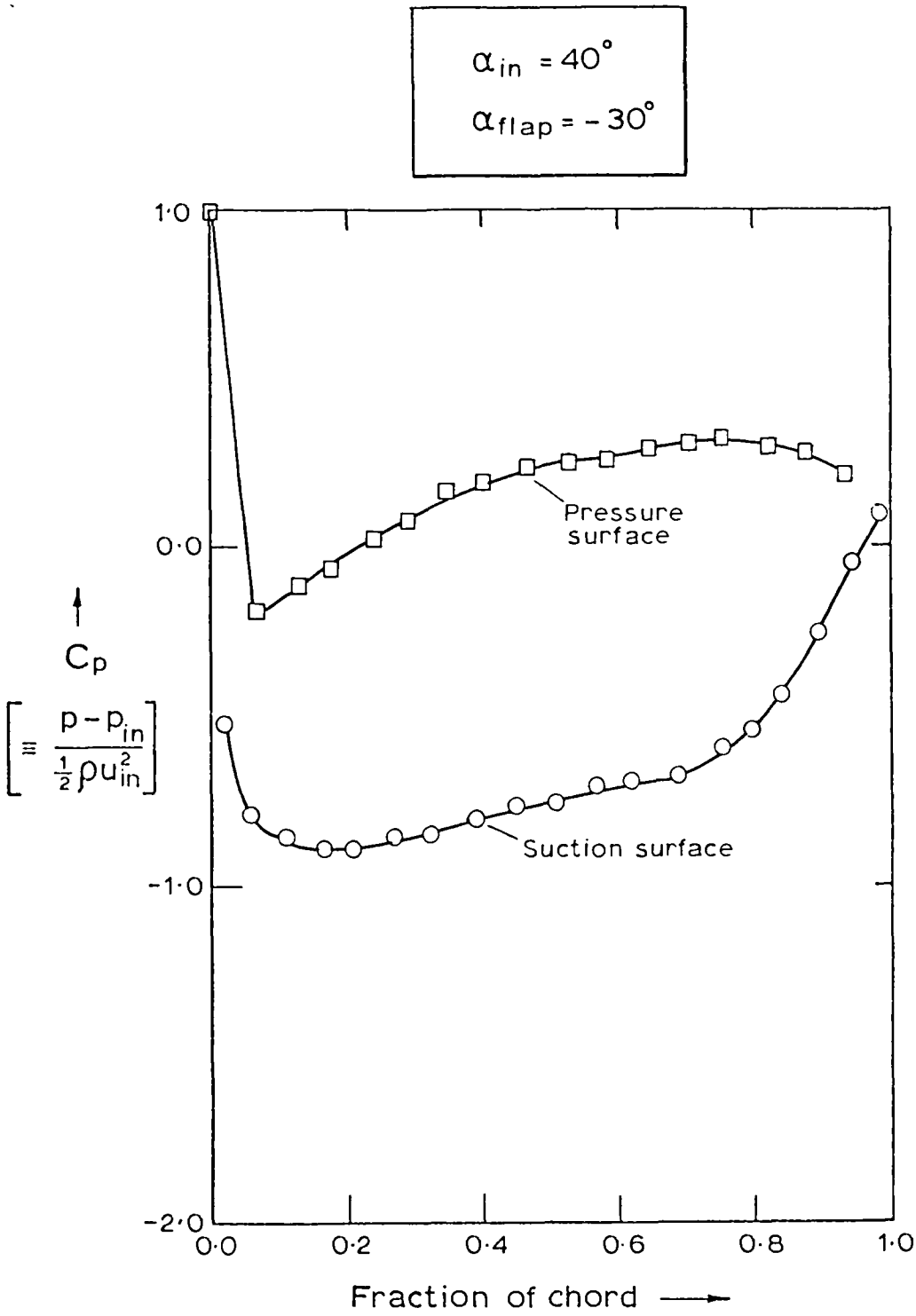


Fig. 5·14 Measured surface pressures

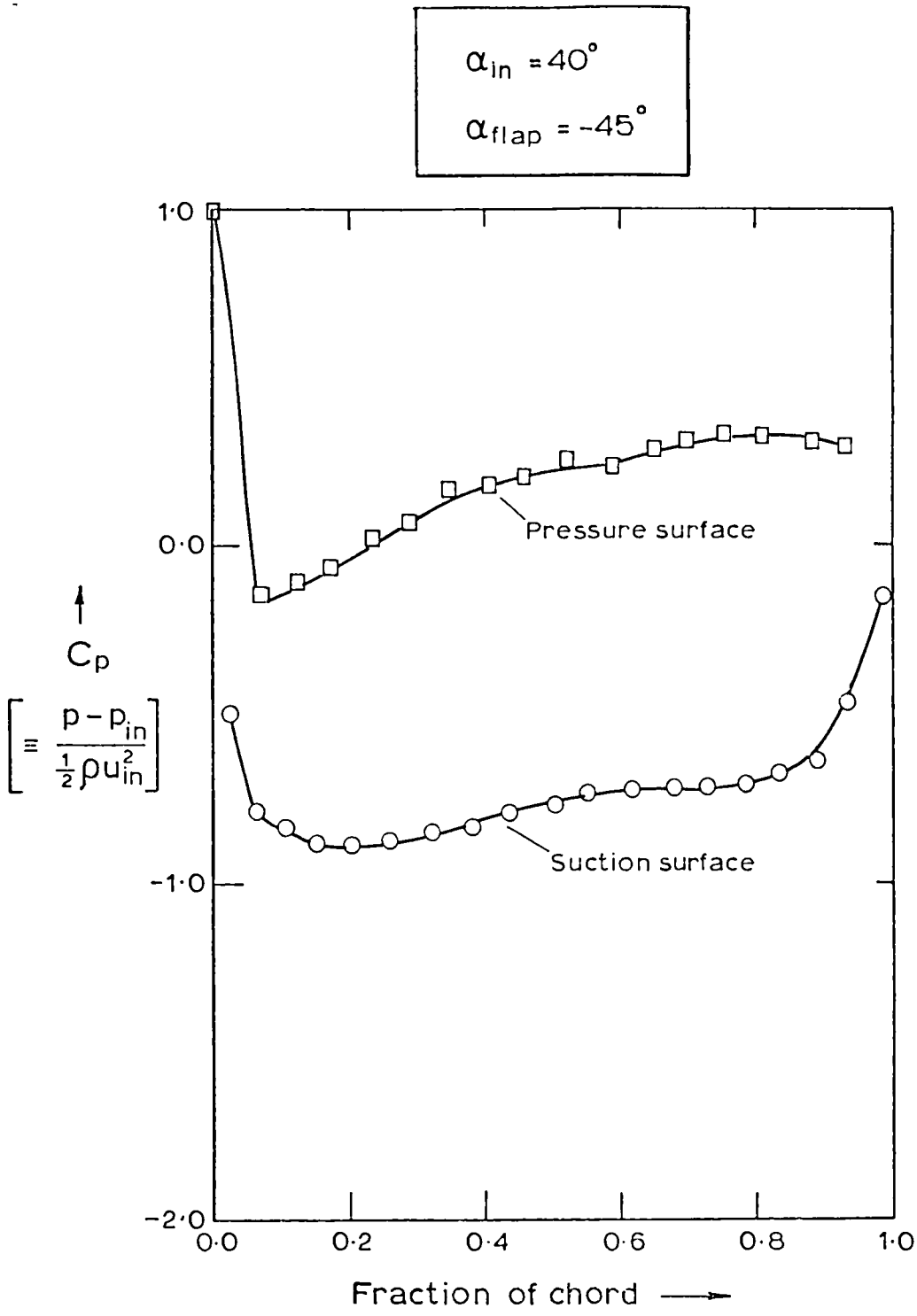


Fig. 5·15 Measured surface pressures

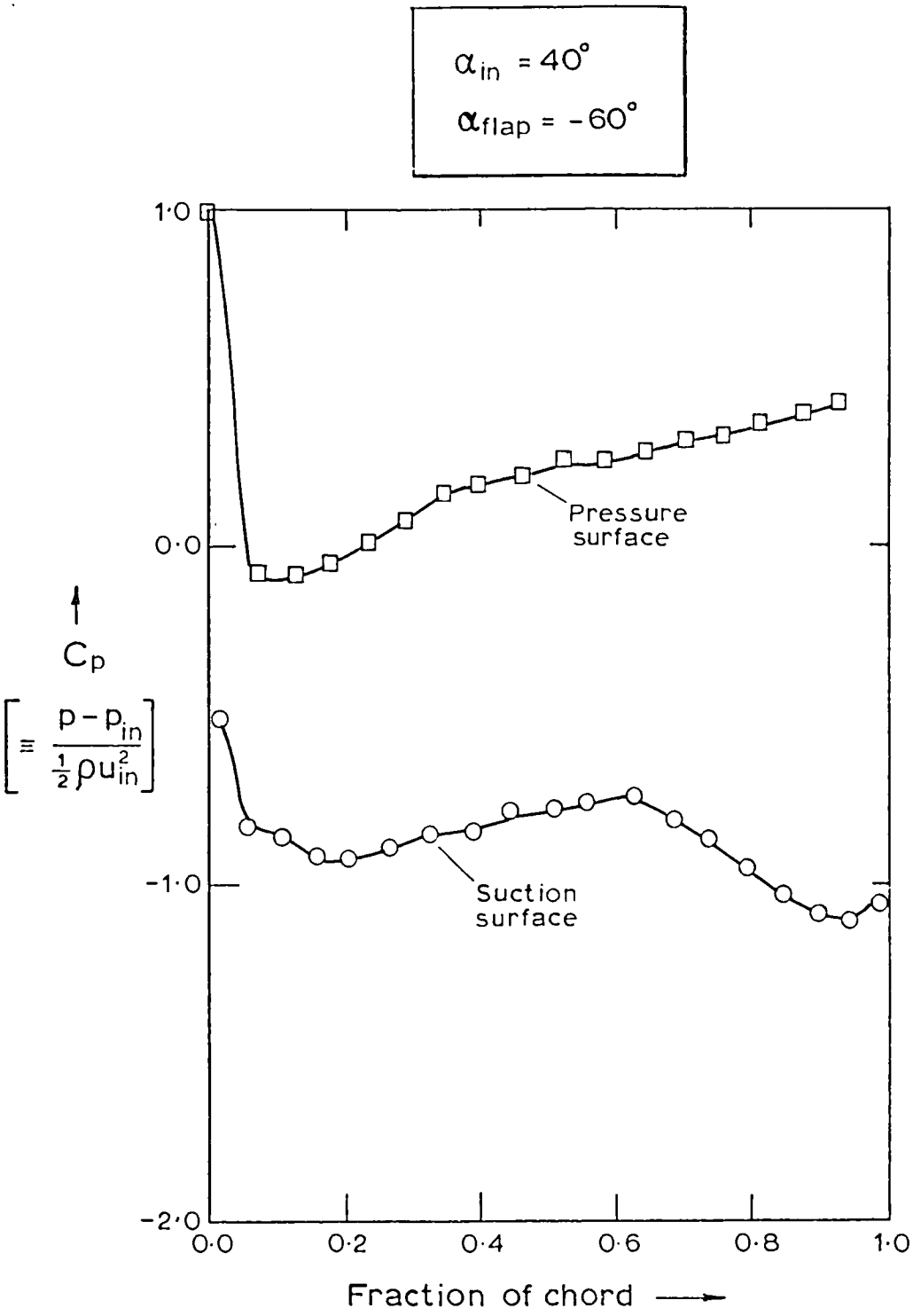


Fig. 5·16 Measured surface pressures

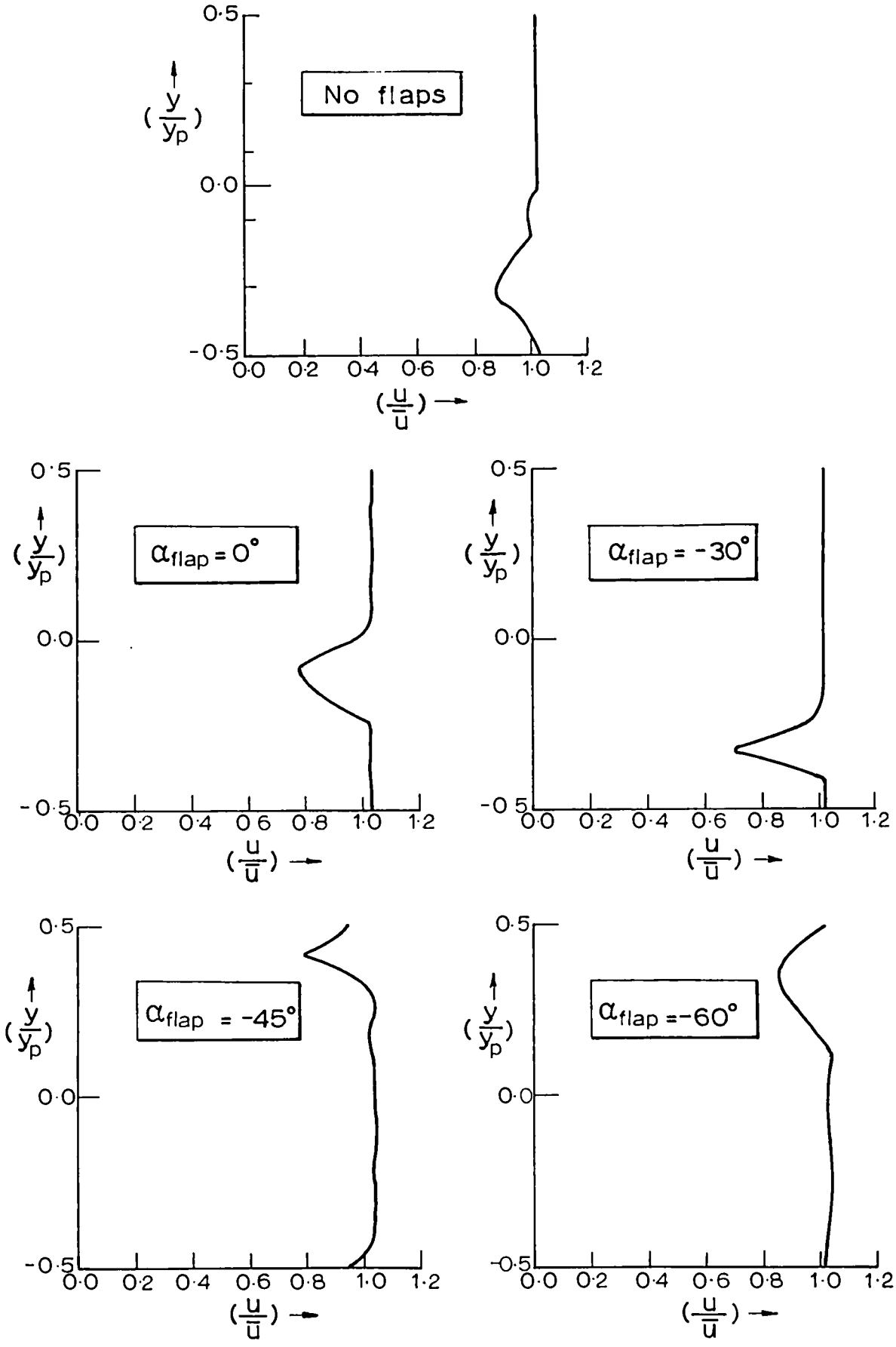


Fig. 5·17 Measured velocity profiles at a tangential section, located $1\frac{3}{4}$" downstream of cascade.

Analysis

From the pressure distributions, displayed in Figs. 5.12 to 5.16, the following points can be observed:

(i) The trailing-edge flaps make significant differences in the surface-pressure variations.

(ii) In the cases of $\alpha_{flap} = 0^{o}$ and -30^{o}, the work output (area between the curves for pressure and suction surfaces) reduces as compared with the case of no flaps.

(iii) Flaps at -45^{o} and -60^{o} positions, tend to increase the work output of the blade.

The work-output changes, mentioned above in (ii) and (iii), are of the correct nature because the trailing-edge flaps are expected to alter the outflow direction; and the work output should also be equal to the change of tangential-direction momentum.

Fig. 5.17 shows that, in each case, the velocity profile is fairly uniform except a small dip which is due to the trailing-edge wake. It is important to note that the the wake-type character of the downstream velocity profile persists even at an axial distance of $1\frac{3}{4}$" which is about 20 times the trailing-edge diameter.

5.5 Concluding remarks

This chapter has described the experimental apparatus, measurement procedure and the collected data. The experimental results have shown that the cascade flow is considerably influenced by the trailing-edge flaps. These data are also used in Chapter 8, for testing the capabilities of the prediction procedure.

CHAPTER 6

PREDICTIONS OF INVISCID, ADIABATIC FLOWS

6.1 Introduction

This chapter is first of the three chapters devoted to the validation of the prediction procedure, described in Chapters 3 and 4.

In this chapter, the capabilities of the prediction procedure are tested particularly with reference to the basic flow-features viz. curvature, circumferential periodicity and compressibility. Eight examples of inviscid, adiabatic flows have been considered; main features of these examples are obvious from their titles. In each case, the computed results are compared with the available analytical or experimental data. It should be remarked here that the comparison of inviscid-flow calculations with experimental data is acceptable in many cascade-flow problems, because the viscous effects are either negligible or limited to small regions.

For each example, the description is divided into two parts, viz. (i) statement of problem, and (ii) presentation of computed results and their comparison with available analytical or experimental results. Computational details of all the examples are summarised in a table at the end of this chapter. Uniform axial grid-spacings have been used unless shown otherwise in the diagrams.

The results presented in this chapter, together with the extract of Chapter 3, have also been reported earlier, in two reports; Singhal and Spalding (1976(a) and 1977).

6.2 Example 1: Incompressible flow past a cylinder placed in a channel

In order to test the basic solution scheme, an inviscid, incompressible flow, without any cyclic boundaries, has been selected as the first example. Fig. 6.1 shows the flow geometry, together with the selected domain of integration and a typical grid arrangement.

An exact analytical solution can be obtained by considering an infinite series of doublets placed at the y-axis, at equal intervals (Milne-Thompson (1962), Ex. 39, p. 229). The resultant stream function is:

$$\psi = U_\infty y - U_\infty . \frac{\pi}{4} . \frac{\sin (\frac{\pi}{2}.y)}{\cosh (\frac{\pi}{2} x) - \cos (\frac{\pi}{2} y)} .$$

The streamline $\psi = 0$ includes the x-axis and the contour of the cylinder.

For numerical computations, the coordinates of the cylinder surface were specified. In addition, the following conditions were supplied as boundary conditions:

(i) uniform inlet velocity;

(ii) zero streamwise gradient of pressure at the exit plane.

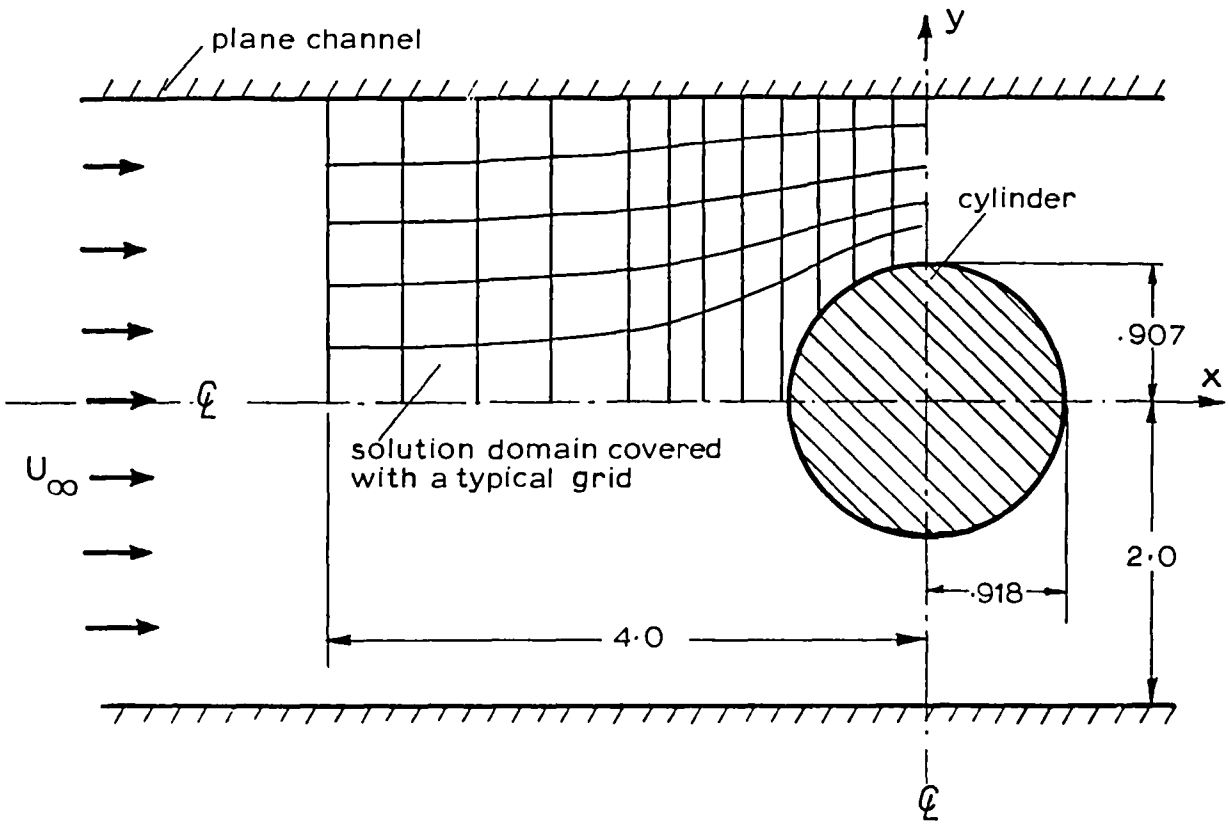


Fig. 6·1 Flow geometry of example 1

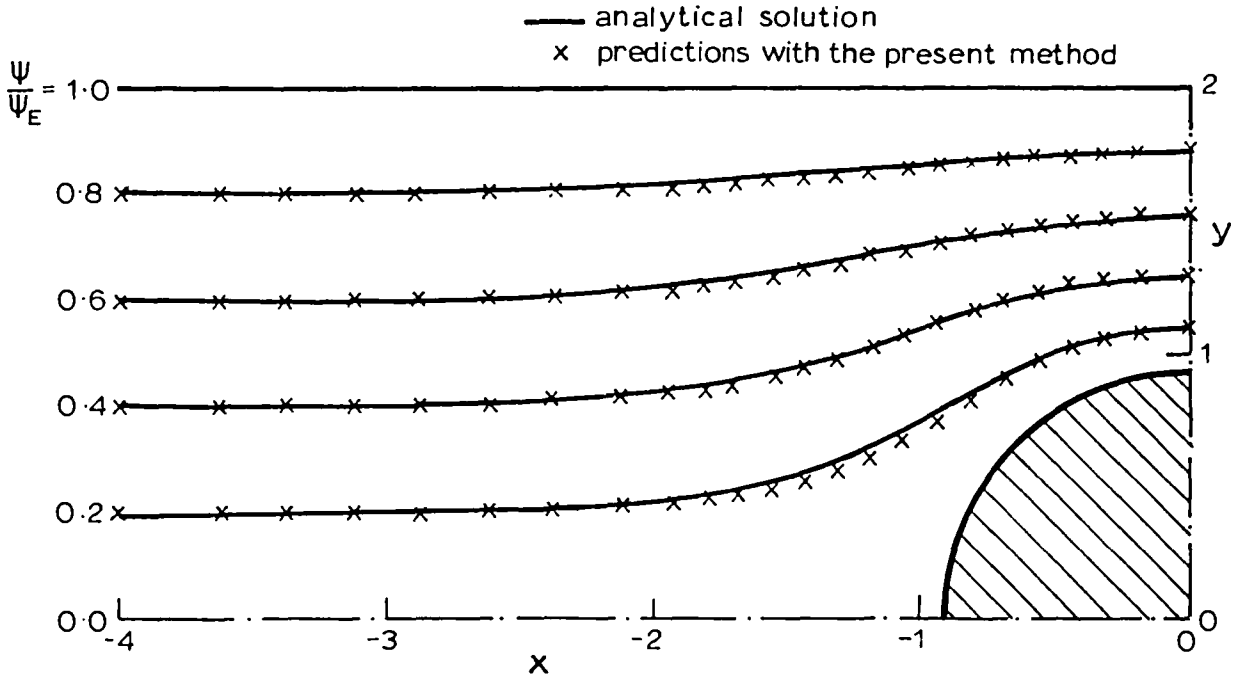


Fig. 6·2 Comparison between prediction and analytical solution of the streamlines

Fig. 6.2 shows the comparison between the predicted and analytically-solved streamlines; the agreement is very satisfactory. In an incompressible flow, other flow-properties viz. pressure and velocities, are uniquely related to the stream-function distribution; therefore, their presentation has been omitted.

6.3 Example 2: Subsonic flow in a NASA turbine stator cascade

In this example, a two-dimensional, compressible flow is considered in a cascade in which flow remains subsonic throughout. The selected problem is flow at the mean-diameter section of a stator of a NASA turbine, operating at the design mass flow rate; relevant experimental data have been reported by Whitney et al. (1967). The cascade geometry is shown in Fig. 6.3. For computations, the fluid is assumed to be a perfect gas of specific heat ratio 1.4. The boundary conditions are applied in the manner explained in Section 3.5.

The predicted surface pressures are converted into Mach numbers in the same manner as the reported experimental static pressures; i.e. by using the isentropic-flow relations, Fig. 6.4 illustrates the predicted and experimental distributions of surface Mach numbers; it can be seen that the predictions agree well with the experimental data.

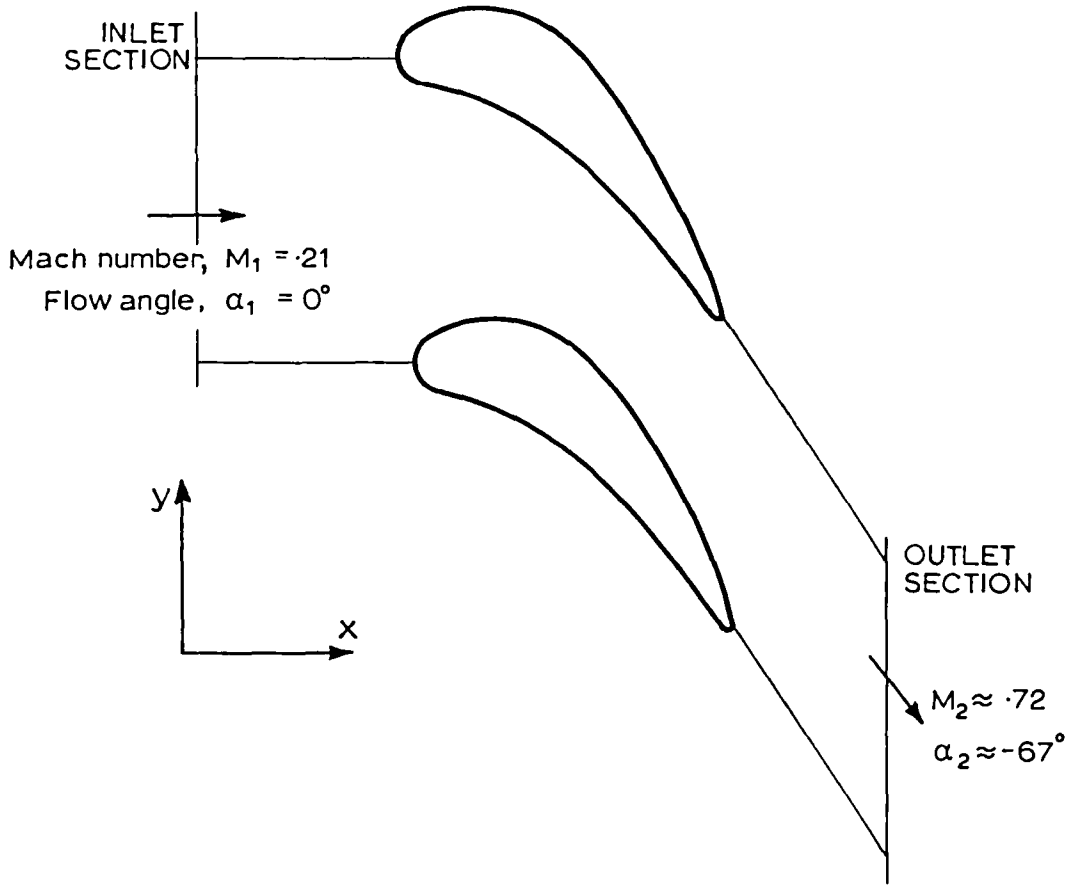


Fig. 6·3 NASA turbine stator cascade

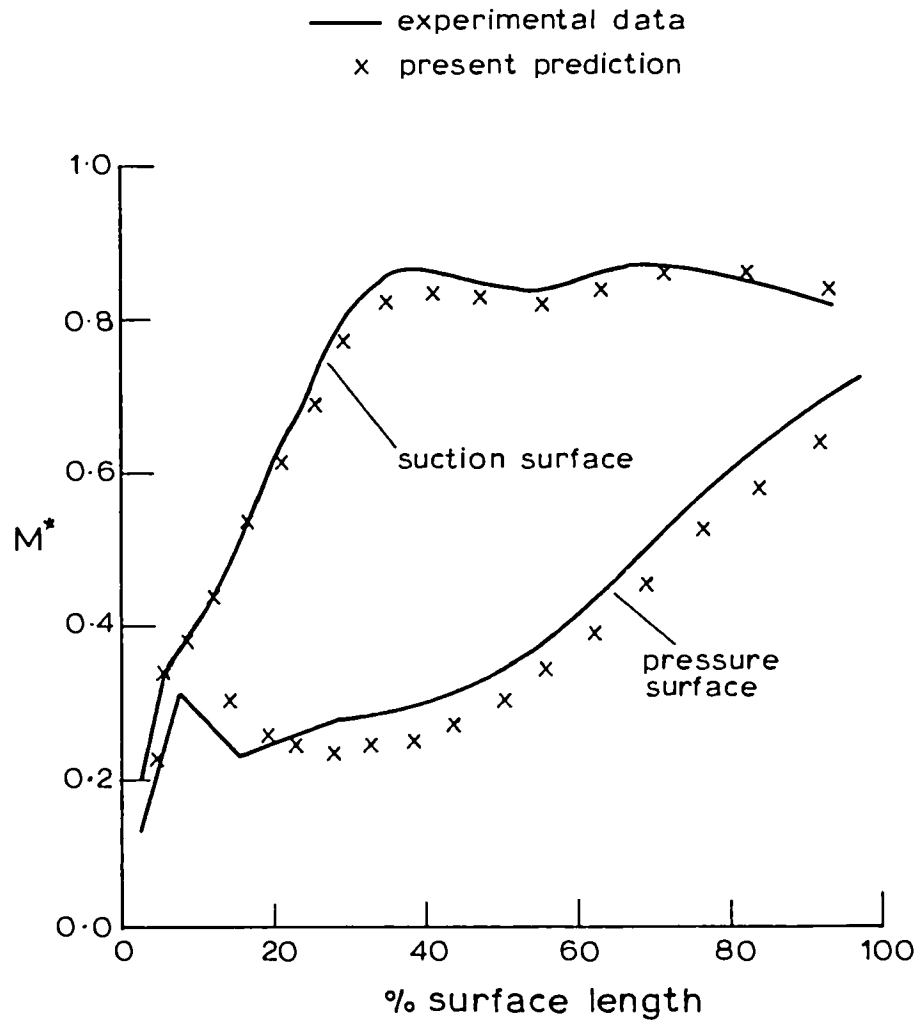


Fig. 6·4 Comparison of predicted surface velocities with experimental data, NASA turbine stator cascade

6.4 Example 3: Transonic flow in Hobson's first impulse cascade

This example considers the first of the two impulse cascades, for which analytical solutions, obtained by the hodograph method, are reported by Hobson (1974).

In this problem, flow is subsonic at both inlet and outlet sections; and there is an embedded supersonic region near the centre of the suction surface. Flow is expected to be free of shocks. The cascade geometry can be seen in Fig. 6.5 or 6.6; note that the blades are symmetrical.

Results

Figs. 6.5 and 6.6 show the computed streamlines and contours of critical Mach number ($M^* = u/u^*$). It may be observed that the computed flow field is fairly symmetrical.

In Fig. 6.7, the computed distributions of surface velocities are compared with the hodograph design data; the agreement is quite good except at the central part of the suction surface, where the predicted velocities are relatively low. No reason is apparent for this discrepancy. However, it may be pointed out here that in a hodograph method an inverse problem is solved, i.e. blade shape is calculated, by a finite-difference technique, for the pre-selected velocity distribution as a function of flow direction; this calculation is no less subject to truncation errors than the present one.

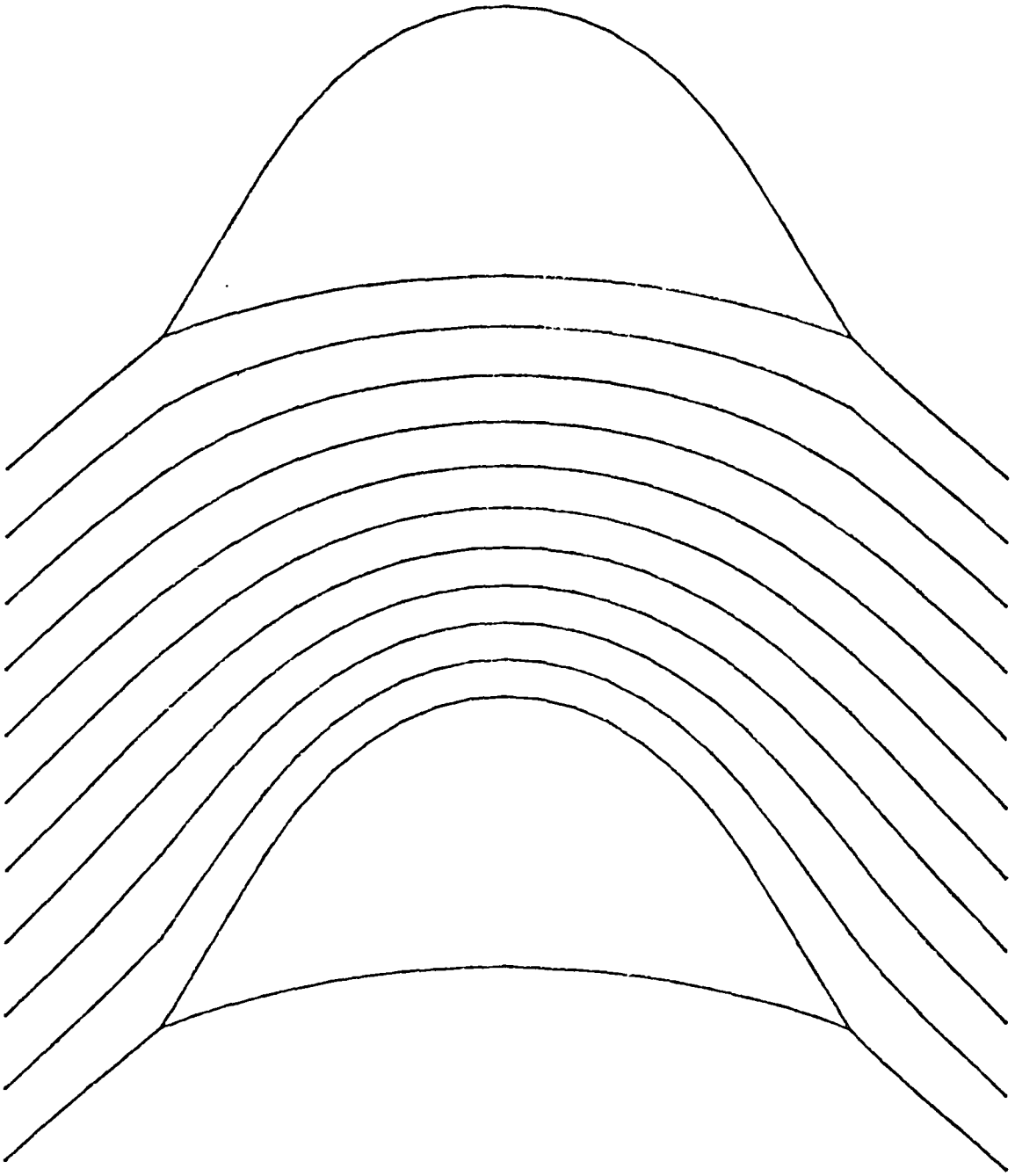


FIG. 6.5. COMPUTED STREAMLINES
HOBSON'S FIRST IMPULSE CASCADE

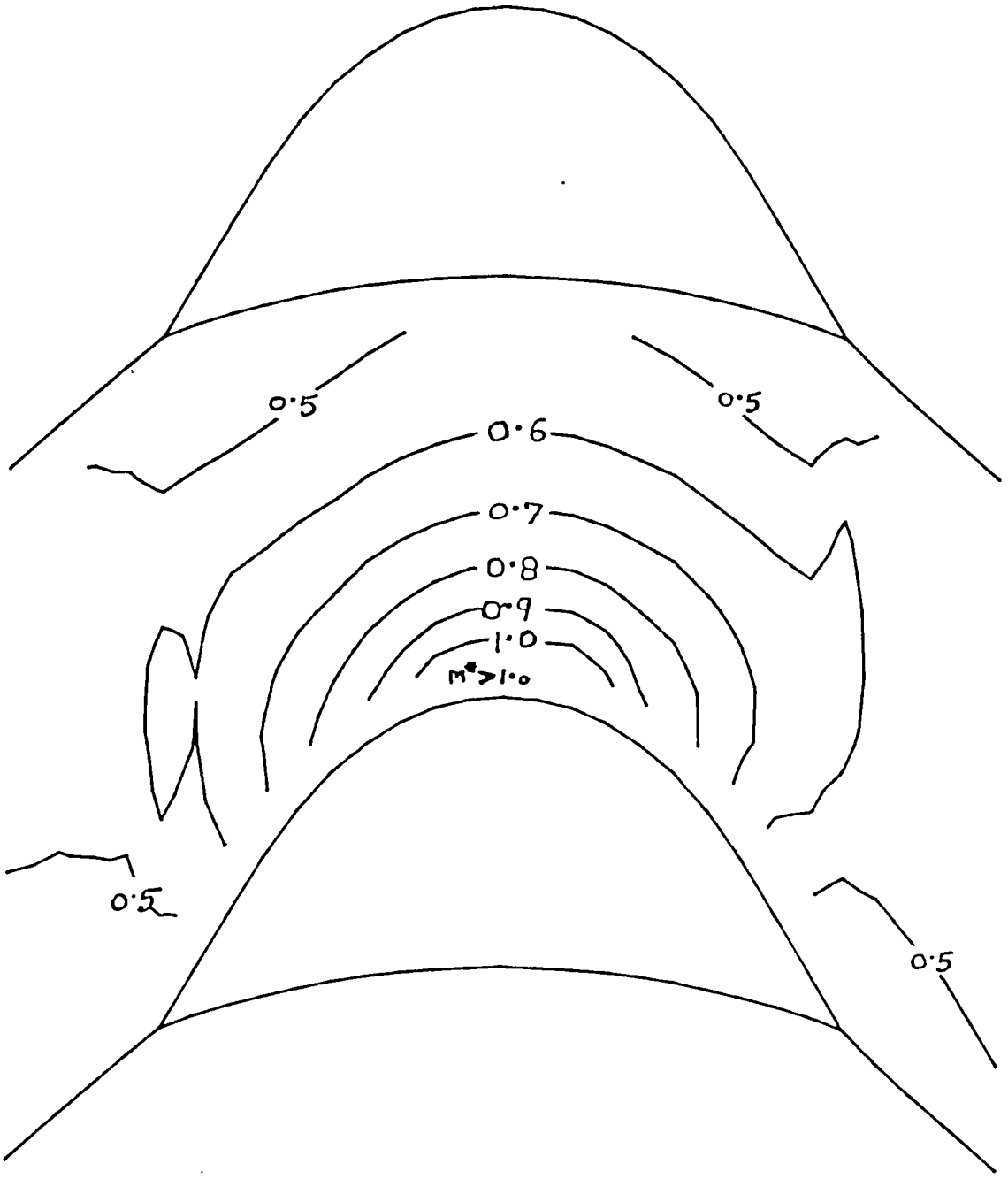


FIG. 6.6 CRITICAL-MACH-NUMBER CONTOURS; HOBSON'S FIRST IMPULSE CASCADE

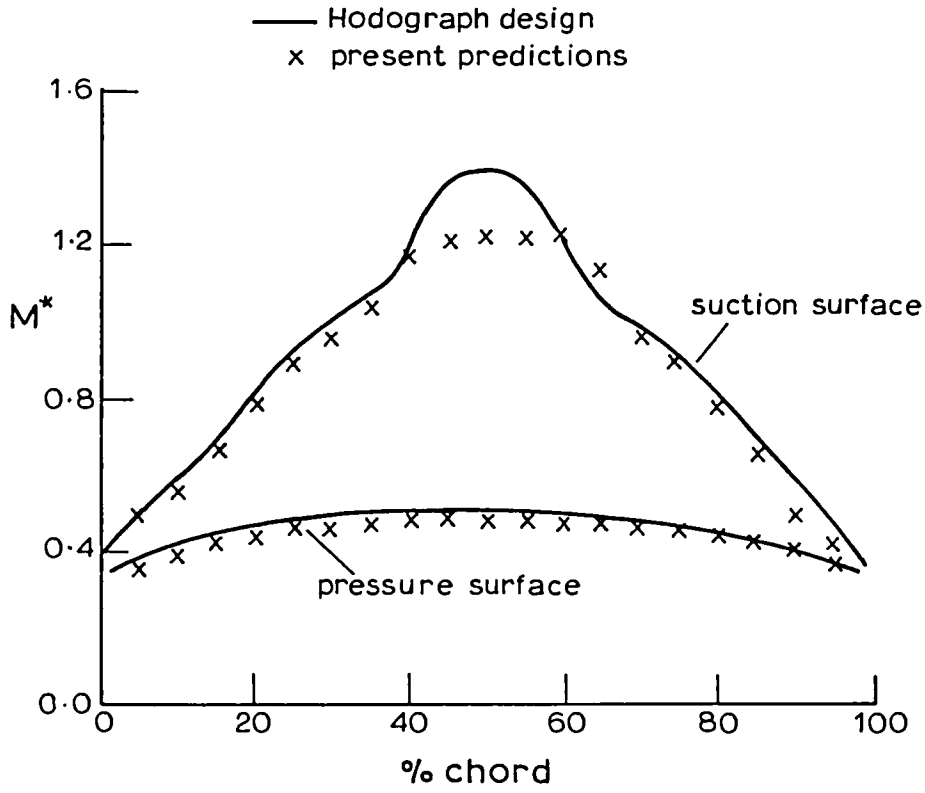


Fig. 6·7 Distribution of surface velocities; Hobson's first impulse cascade

Solutions of other methods, presented at a NATO conference at Cambridge University in 1973, also showed some discrepancies in this region; these solutions are reported by Hobson (1974).

6.5 Example 4: Transonic flow in Hobson's second impulse cascade

This case is very similar to that of example 3, but the impulse blades are relatively of thinner section, and the expected supersonic region is smaller.

Fig. 6.8 illustrates the cascade geometry and the contours of predicted critical-Mach-numbers. It may be noted that in this example also, the calculated flow field is fairly symmetrical. The computed streamlines are not presented as they are of the same pattern as that in Fig. 6.5 and, therefore, do not provide any additional information. Fig. 6.9 demonstrates that the predicted surface velocities agree well with the hodograph design data.

6.6 Example 5: Transonic flow in a VKI gas turbine cascade

This example considers a cascade flow which is subsonic at inlet and supersonic at outlet. Problem specifications, experimental measurements and theoretical predictions by several other methods are reported in Reference 61. The cascade geometry can be seen in Fig. 6.10 or 6.11.

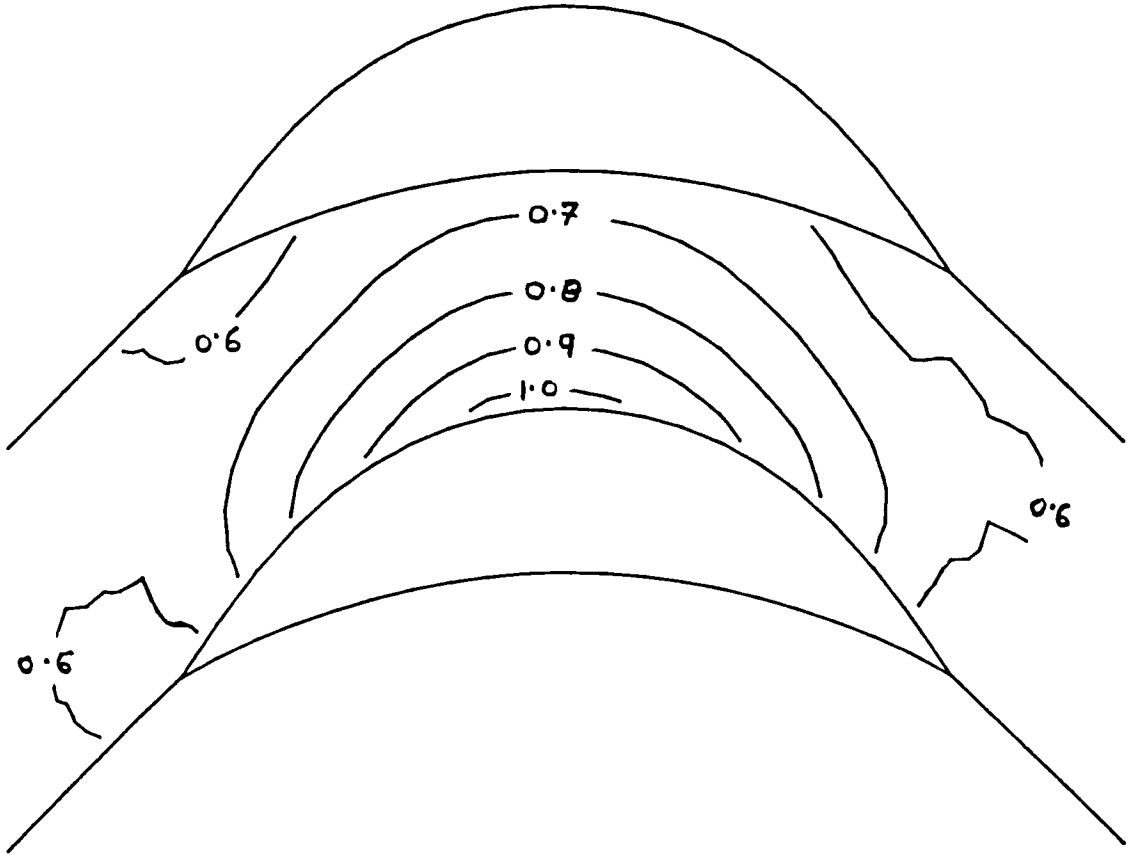


FIG.6.8 CRITICAL-MACH-NUMBER CONTOURS
HOBSON'S SECOND IMPULSE CASCADE

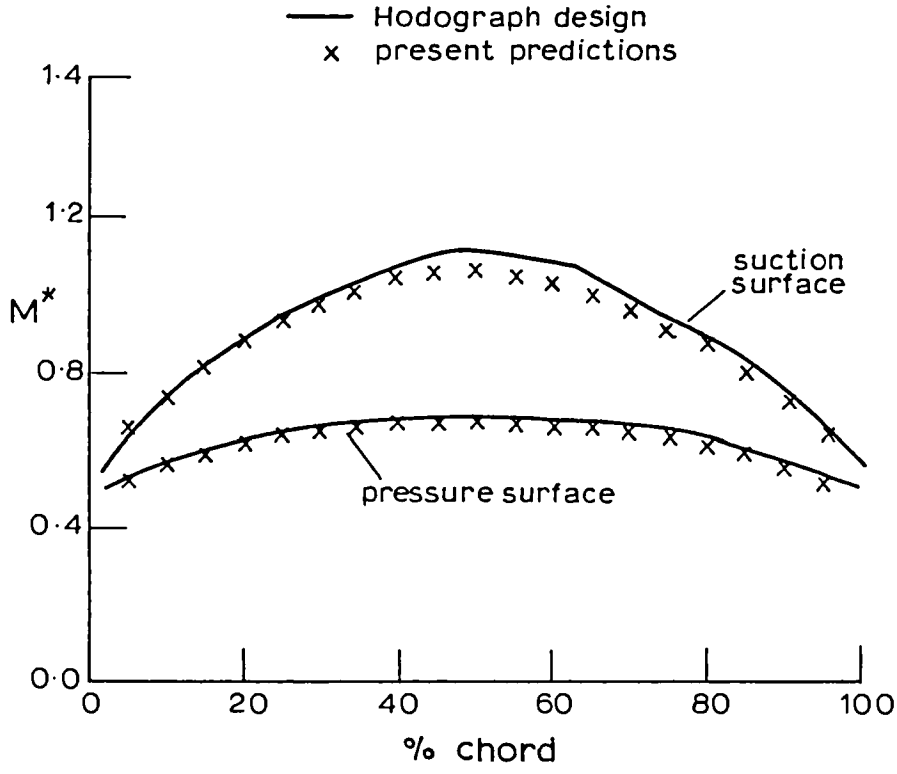


Fig. 6·9 Distribution of surface velocities, Hobson's second impulse cascade

Computations have been made for two different flow conditions, specified by the outlet Mach numbers which are: (i) 1.31 and (ii) 1.11. Figs. 6.10 and 6.11 present the calculated Mach-number contours in the flow field. From these two figures, it can be seen that in the downstream part of the flow domain there are noticeably different shock structures; but, in the upstream region, changes in Mach numbers are insignificant.

Figs. 6.12 and 6.13 compare the predicted and experimental values of surface Mach numbers for the two flow conditions considered. The agreement of the present method with experiments is excellent.

6.7 Example 6: Transonic flow in a VKI stream turbine cascade

This is the second test case from the same reference as that of previous example. It presents a very severe test for any prediction procedure since extremely steep gradients of flow properties occur in both pitchwise and streamwise directions. Fig. 6.14 illustrates the cascade geometry; pitchwise grid lines are also shown to give an idea of the axial grid spacings used in the present computations. The outlet Mach number is specified to be 1.80.

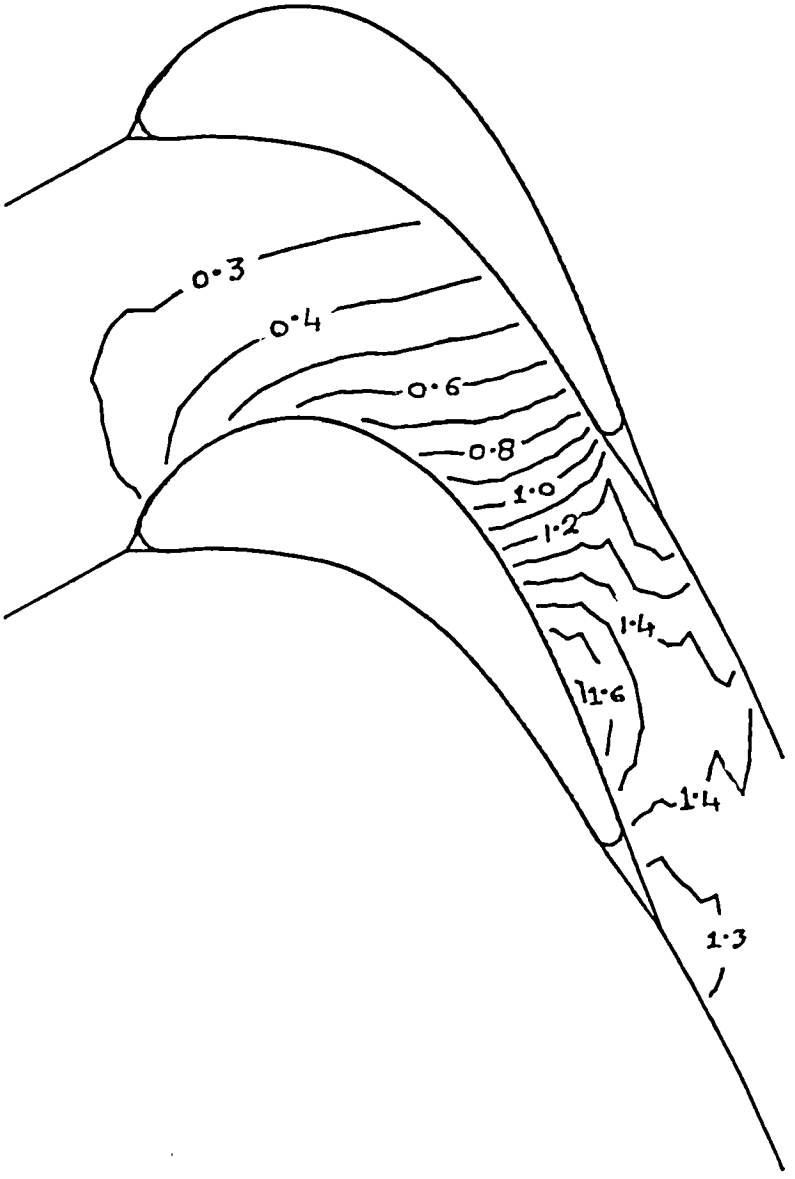


FIG. 6.10 MACH-NUMBER CONTOURS

VKI GAS TURBINE CASCADE (OUTLET MACH NO.=1.31)

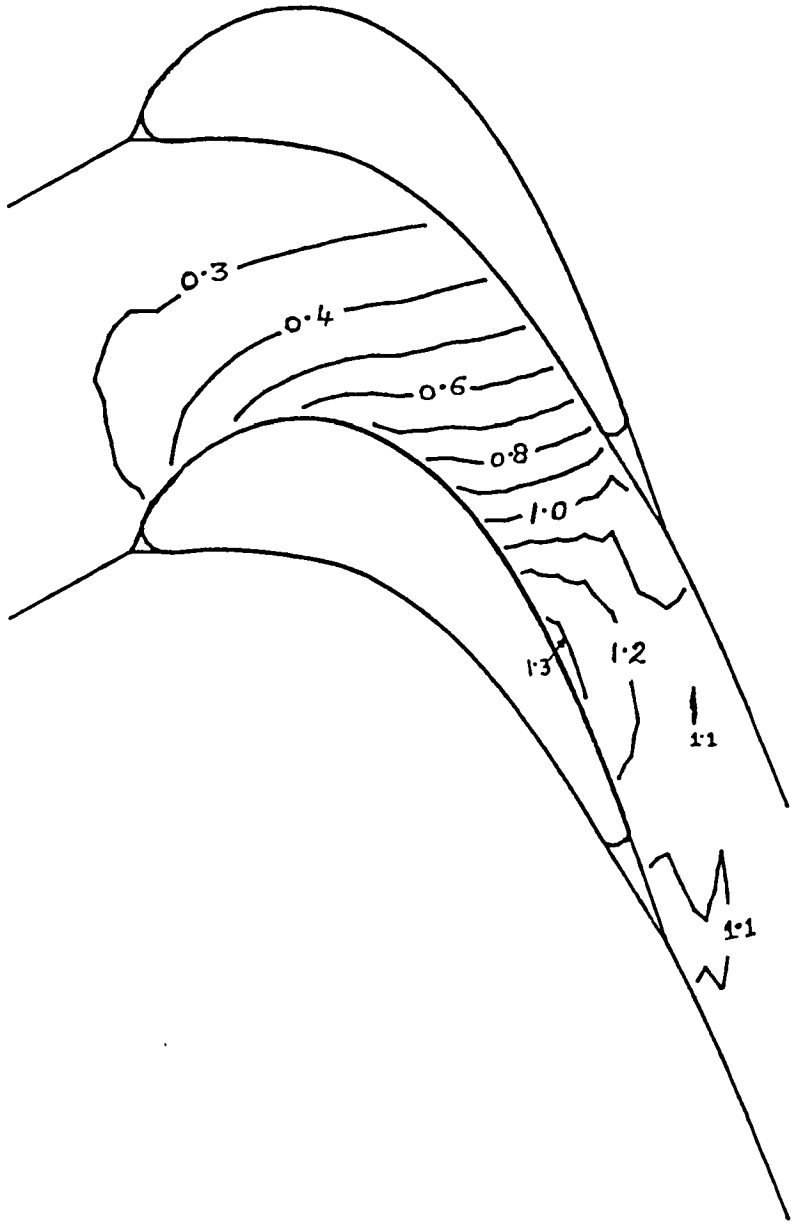


FIG. 6.11 MACH-NUMBER CONTOURS;

VKI GAS TURBINE CASCADE (OUTLET MACH NO.=1.11)

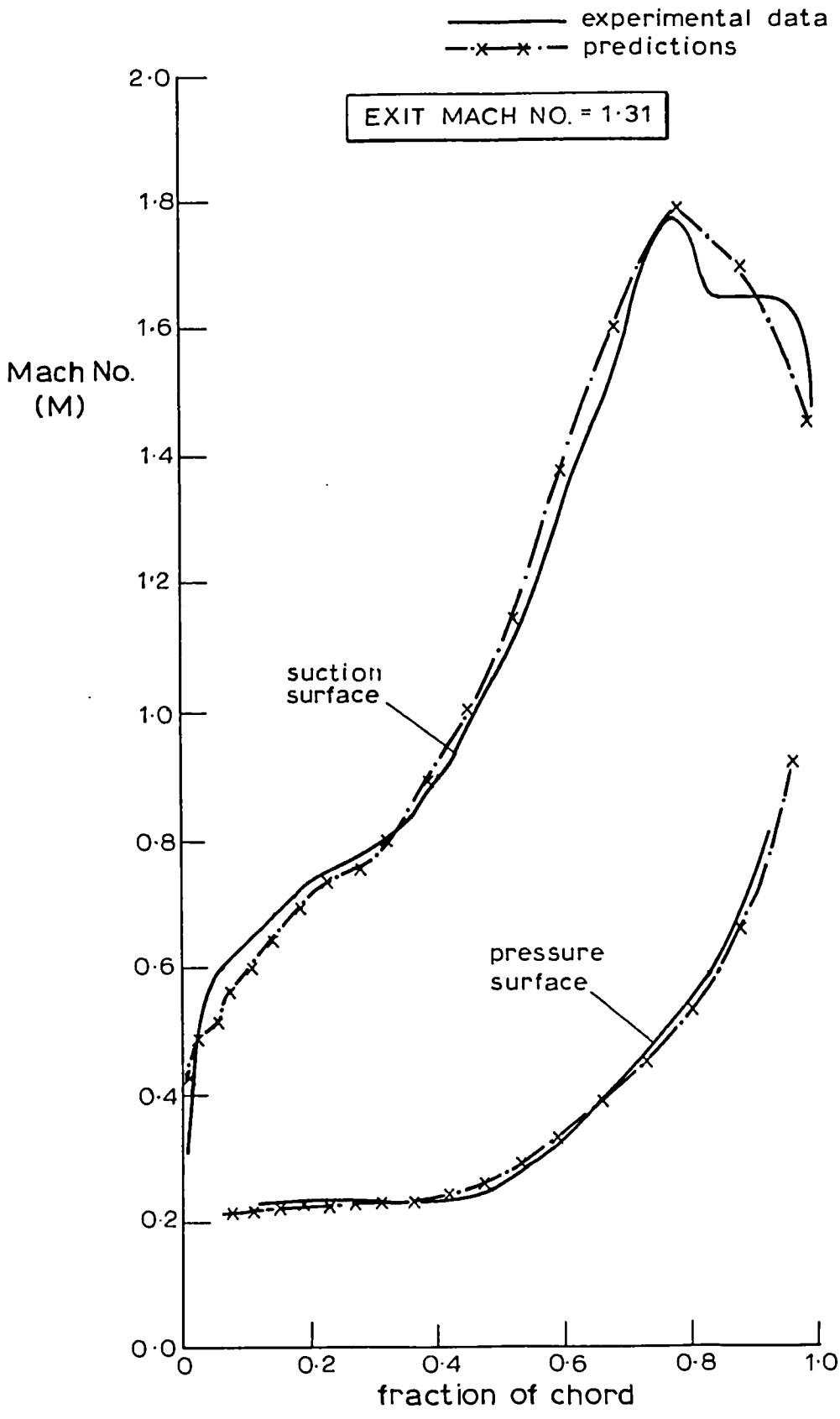


Fig. 6·12 Distribution of surface Mach numbers, VKI gas turbine cascade

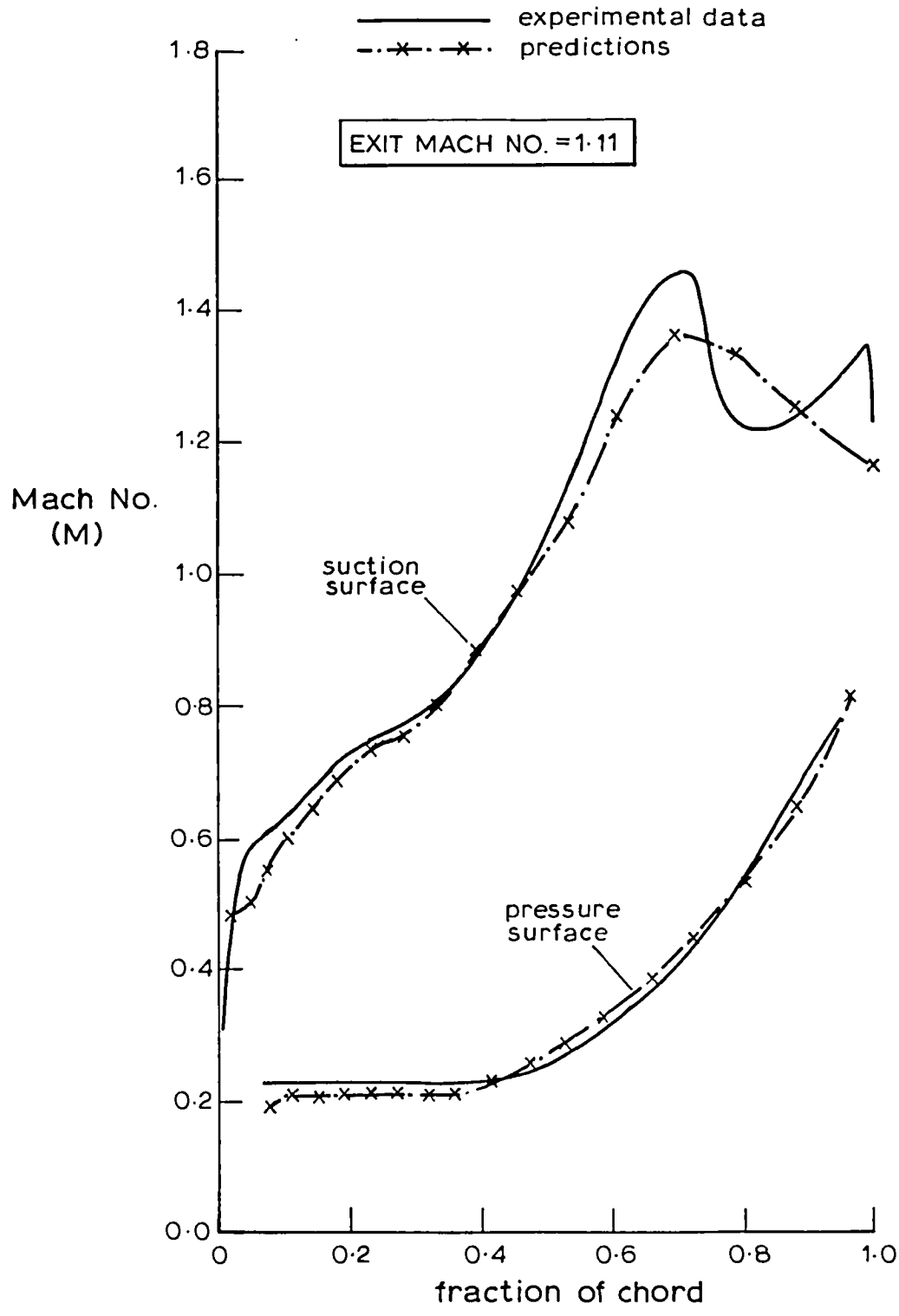


Fig. 6·13 Distribution of surface Mach numbers, VKI gas turbine cascade

The computed streamlines and Mach-number contours, Figs. 6.15 and 6.16, provide a general idea of the flow field. Fig. 6.17 shows the comparison of predicted and experimental surface-Mach-numbers; the general agreement is good over most of the blade surface.

6.8 Example 7: Transonic flow in a NGTE nozzle-guide-vane cascade

This example and the next one are concerned with the transonic flows in cascades of nozzle guide vanes (NGV), which are often used in single-stage, high work-output gas turbines. An important feature of NGV cascades is that the blades are highly "flared" so as to provide the required expansion and turning of the fluid.

The present example has been specified by the National Gas Turbine Establishment (NGTE). No experimental data are available. A set of computed results by Litchfield (1976), obtained with the time-marching method of Denton (1975), has been supplied for comparison. The flow geometry and the computational grid, as used in the present calculations, are shown in Fig. 6.18. The outlet Mach number is specified to be 1.40.

Results

A contour plot of the predicted Mach numbers over the whole flow field is presented in Fig. 6.19. The variations of surface velocities along the axial chord of

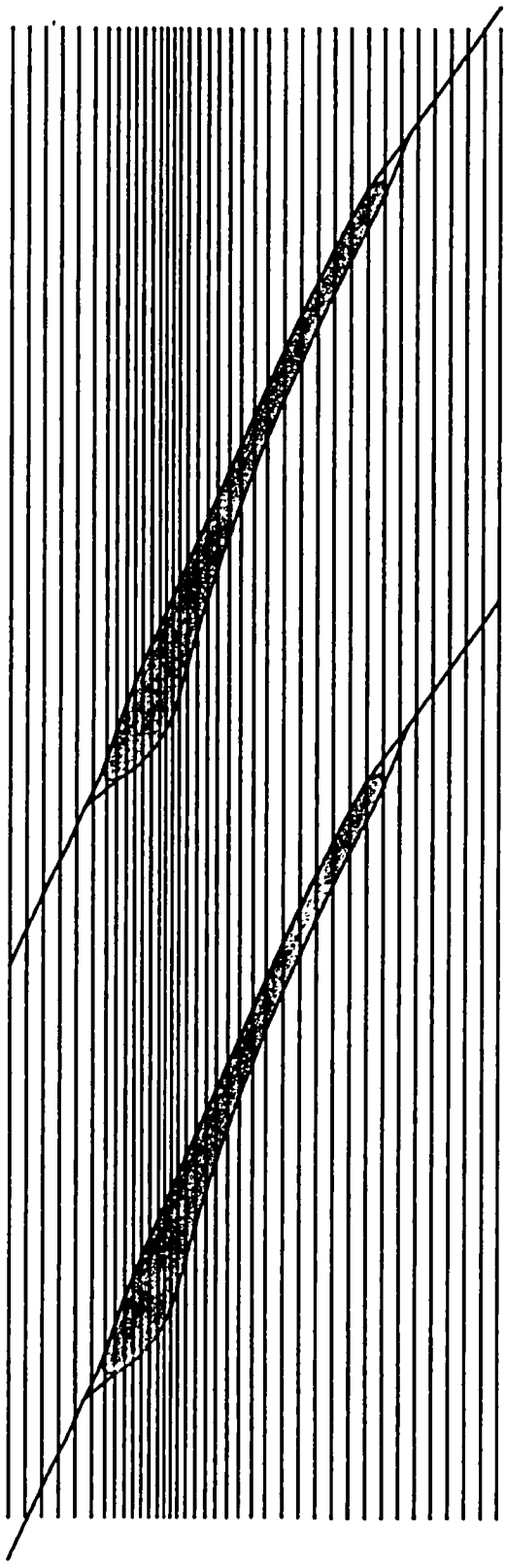


Fig. 6.14 PITCHWISE GRID LINES

VKI STEAM TURBINE CASCADE (OUTLET MACH NO.=1.80

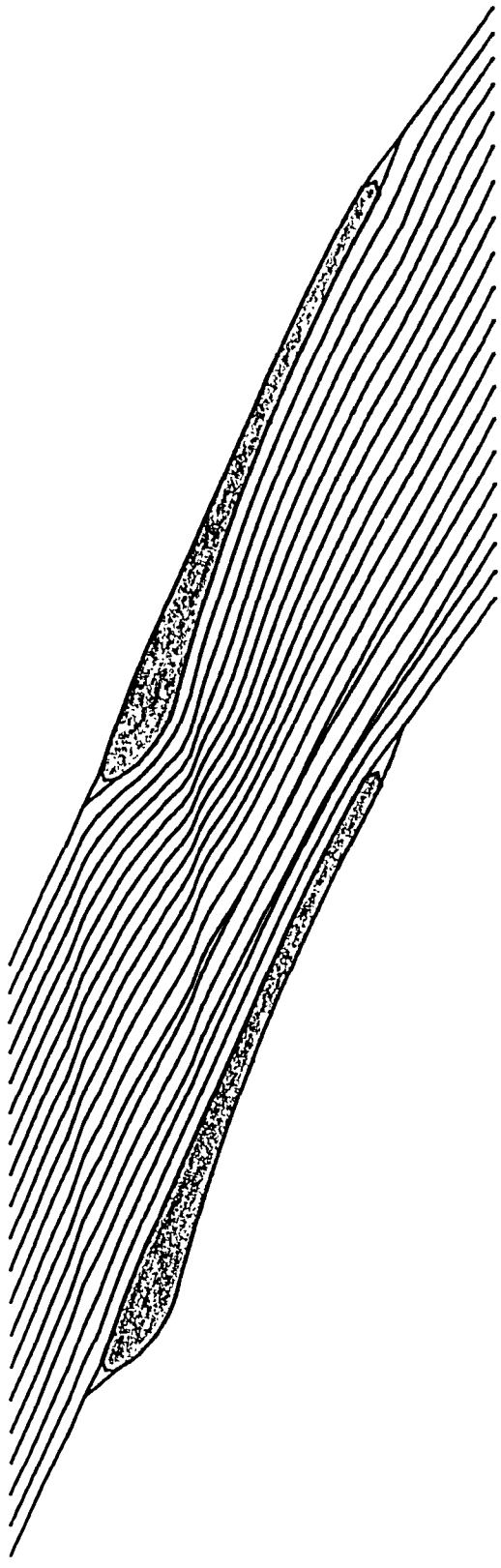


Fig. 6.15 COMPUTED STREAMLINES

VKI STEAM TURBINE CASCADE (OUTLET MACH NO.=1.80

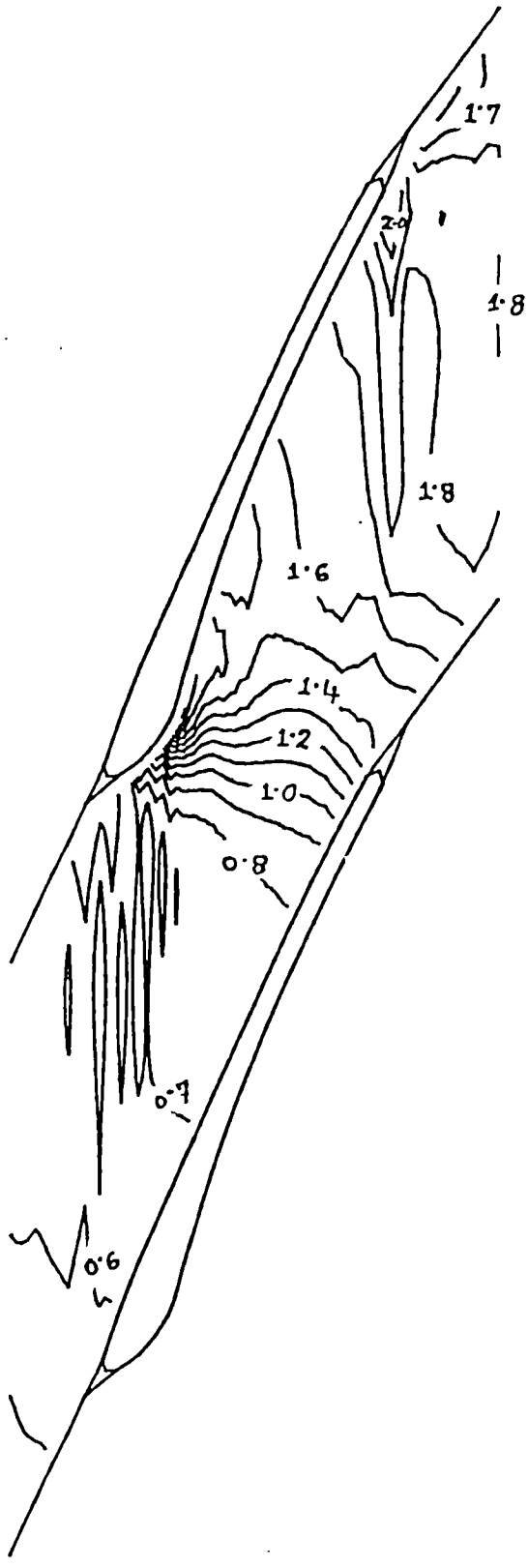


FIG.6.16. MACH-NUMBER CONTOURS

VKI STEAM TURBINE CASCADE (OUTLET MACH NO.=1.80

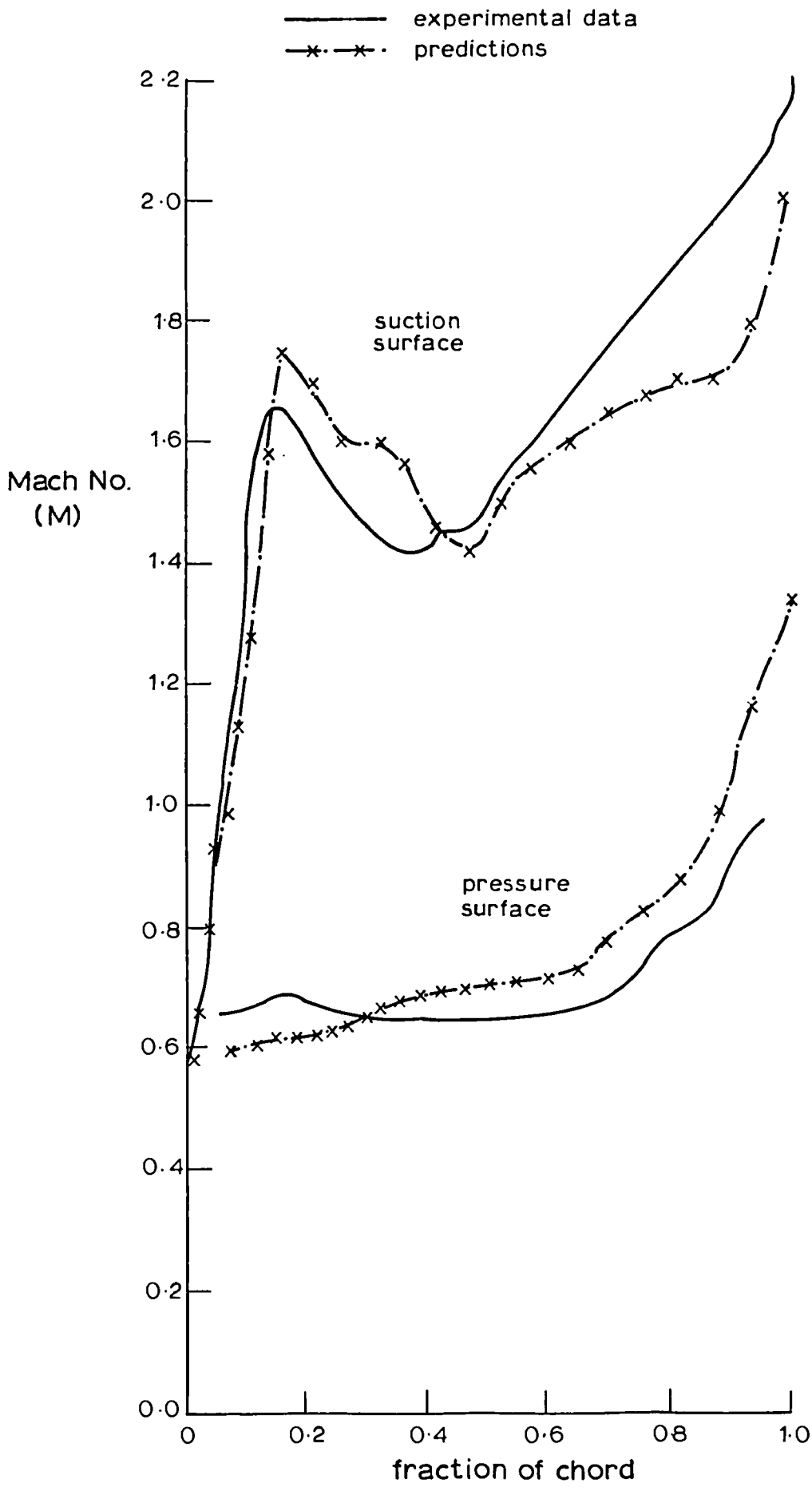


Fig. 6·17 Distribution of surface Mach numbers, VKI steam turbine cascade

blades are shown in Fig. 6.20. For comparison, the available results of NGTE calculations are also plotted in Fig. 6.20.

From Figs. 6.19 and 6.20 it can be seen that, on the pressure surface, the flow accelerates quite smoothly; on the suction surface, acceleration is much more rapid but not so smooth. A significant deceleration (or recompression) is predicted at about 55%-axial-chord position. Fig. 6.19 shows that this recompression takes place in the region of large curvature. It may also be noted that the NGTE calculations, Fig. 6.20, do not predict such a distinct recompression.

No experimental data are available; therefore, no definite conclusion can be drawn about the physical realism of the predicted recompression. However, it is likely that the results of the present procedure are the more accurate, because the use of stream-line coordinates eliminates false diffusion. A further argument is provided in the next section.

6.9 Example 8: Transonic flow in the MIT-VKI-IV nozzle-guide-vane cascade

The MIT-VKI-IV cascade is one of several cascades for which geometrical data and experimental flow characteristics are described in Reference 62. This particular problem has been selected because:

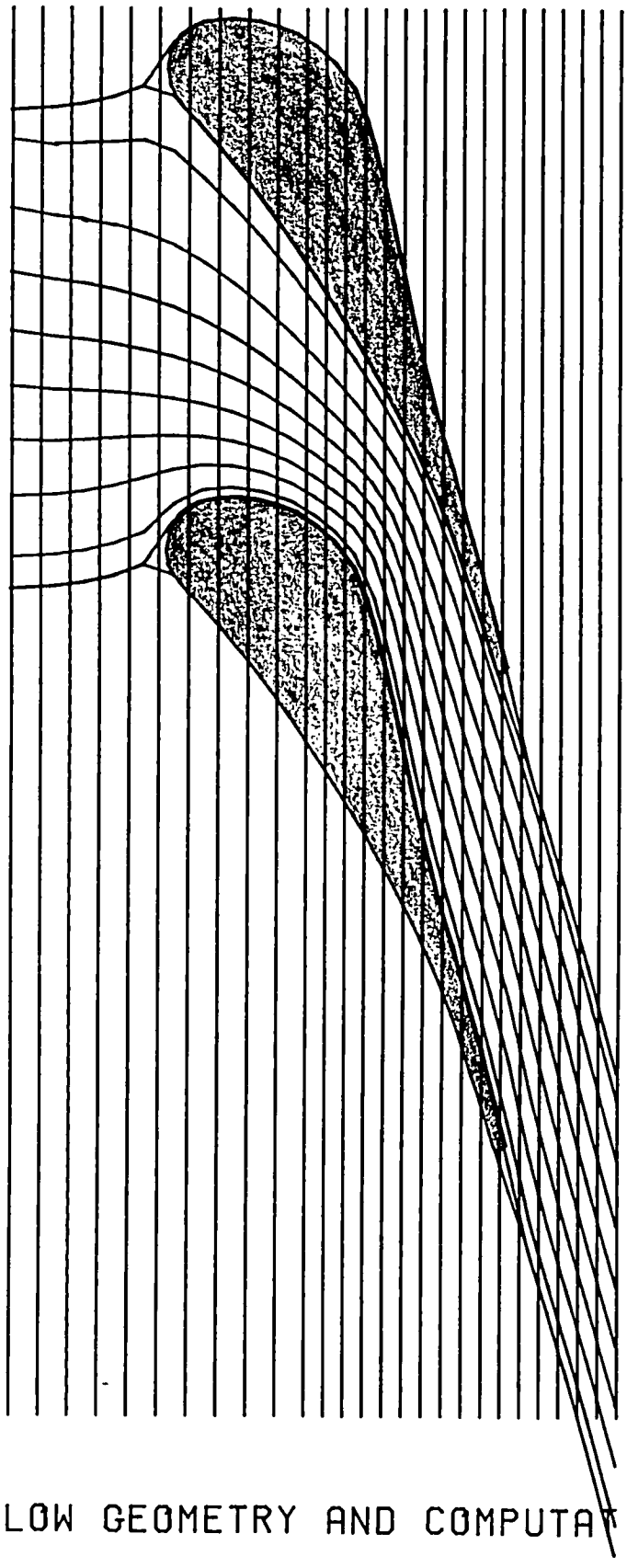


FIG.6.18 FLOW GEOMETRY AND COMPUTATIONAL GRID;
NGTE TURBINE NOZZLE BLADE

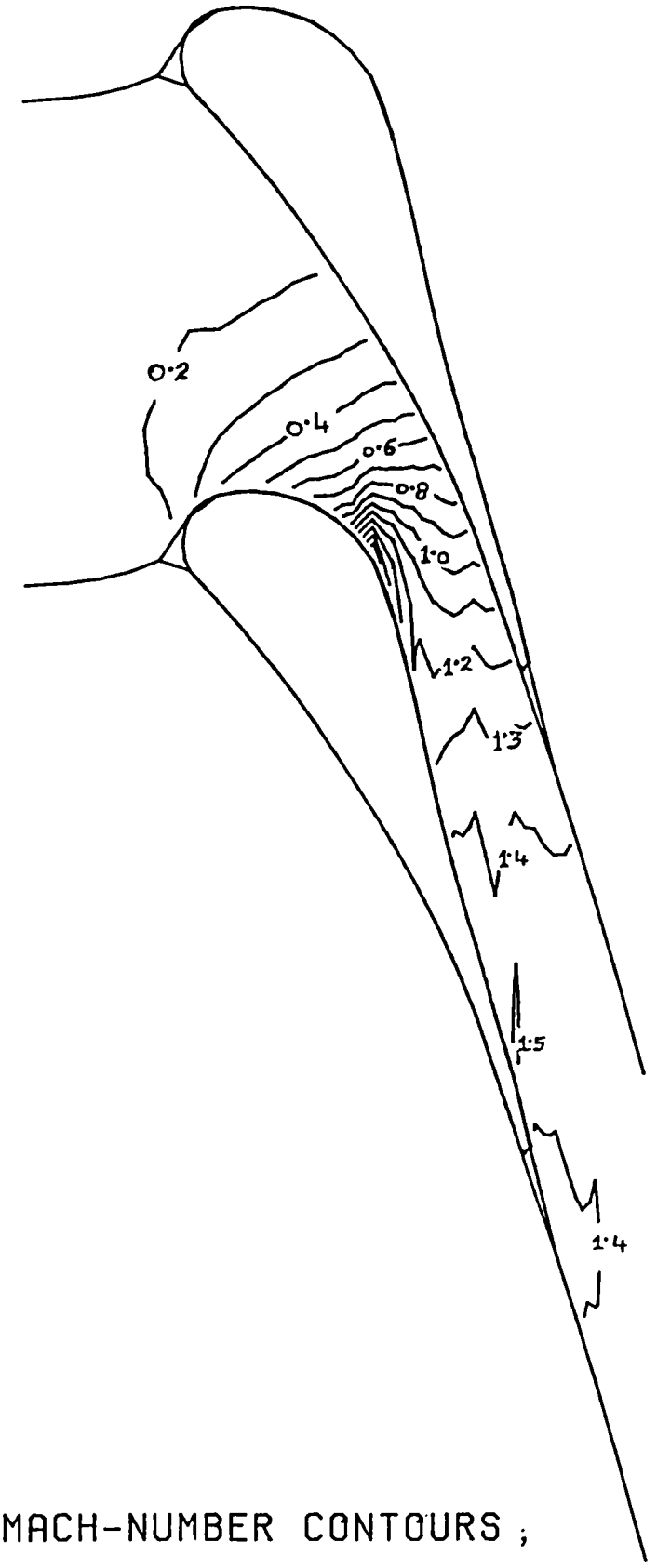


FIG.6.19 MACH-NUMBER CONTOURS ;
NGTE TURBINE NOZZLE BLADE

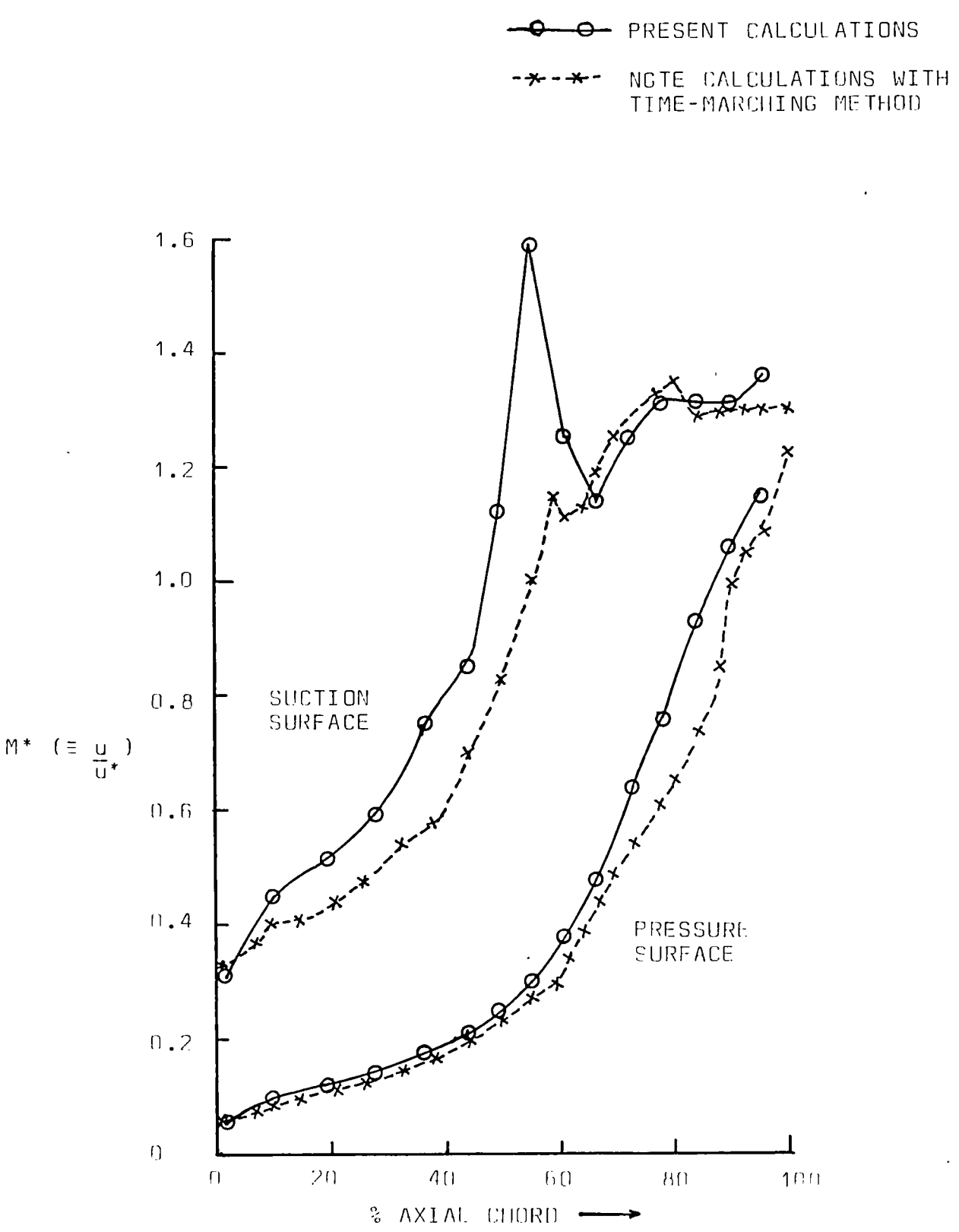


FIG.6.20 SURFACE VELOCITY DISTRIBUTION FOR NGTE TURBINE NOZZLE BLADE

(a) its geometry is similar to that of the NGTE cascade; and

(b) it has also been computed by Bryce and Litchfield (1976), using Denton's (1975) "time-marching" method.

In Reference 62, this cascade has been described under the heating of convergent-divergent cascades; it has been designated MIT-VKI-IV.

The flow geometry and the computational grid, as used in the present calculations, are illustrated in Fig. 6.21. The outlet Mach number is specified to be 1.33. It may be seen, from Fig. 6.21 or 6.22, that at the trailing edge of each blade a "wake strip" has been used instead of a cusp. Its local inclinations are calculated in the standard way, by applying the periodicity conditions. A wake strip represents a better simulation, particularly when the suction and pressure surfaces are parallel, near the trailing edge.

Results

Fig. 6.22 presents the computed Mach numbers in the flow field. To facilitate qualitative comparison with experiments, schlieren photographs are shown in Fig. 6.23. All three pictures are for choked-flow conditions; the exact values of the outlet Mach numbers are not recorded in Reference 62.

Fig. 6.24 shows three sets of surface Mach numbers obtained from:

(i) the present predictions;

(ii) Bryce and Litchfield's predictions; and

(iii) experiments.

Discussion

The schlieren pictures, Fig. 6.23, exhibit regions of shock-recompressions. In Fig. 6.22, the closed contours of predicted Mach numbers 1.3 and 1.4 also indicate such regions of recompression.

In Fig. 6.24, on the pressure surface, both the calculations differ only slightly from each other and from the experimental data; therefore both the methods can be regarded as satisfactory. For the front half of the suction surface, both methods are seen to predict the experimental data fairly well. However, only the present method predicts the rapid rise of Mach number at mid-chord, followed by a recompression. The latter is not in perfect agreement with the experimental data; but the predicted curve does agree the experimental one again on the rear half of the blade.

Bryce and Litchfield have argued that the sharp peaks in the experimental data of Fig. 6.24 are due to shock-boundary-layer interaction and, therefore, cannot be predicted by inviscid solutions. However, the present calculations suggest that the first peak is primarily due to blade-surface curvature and is a feature of inviscid flow. The Bryce-Litchfield argument may, however, well be correct for the second peak, where the boundary layer is thicker.

It may be observed that the NGTE cascade, Fig. 6.18, has much sharper curvature than MIT-VKI-IV, Fig. 6.21. Therefore, the present method, which predicts a sharp Mach-number peak for that cascade (Fig. 6.20) may well be more correct than the time-marching method, which predicts none at all.

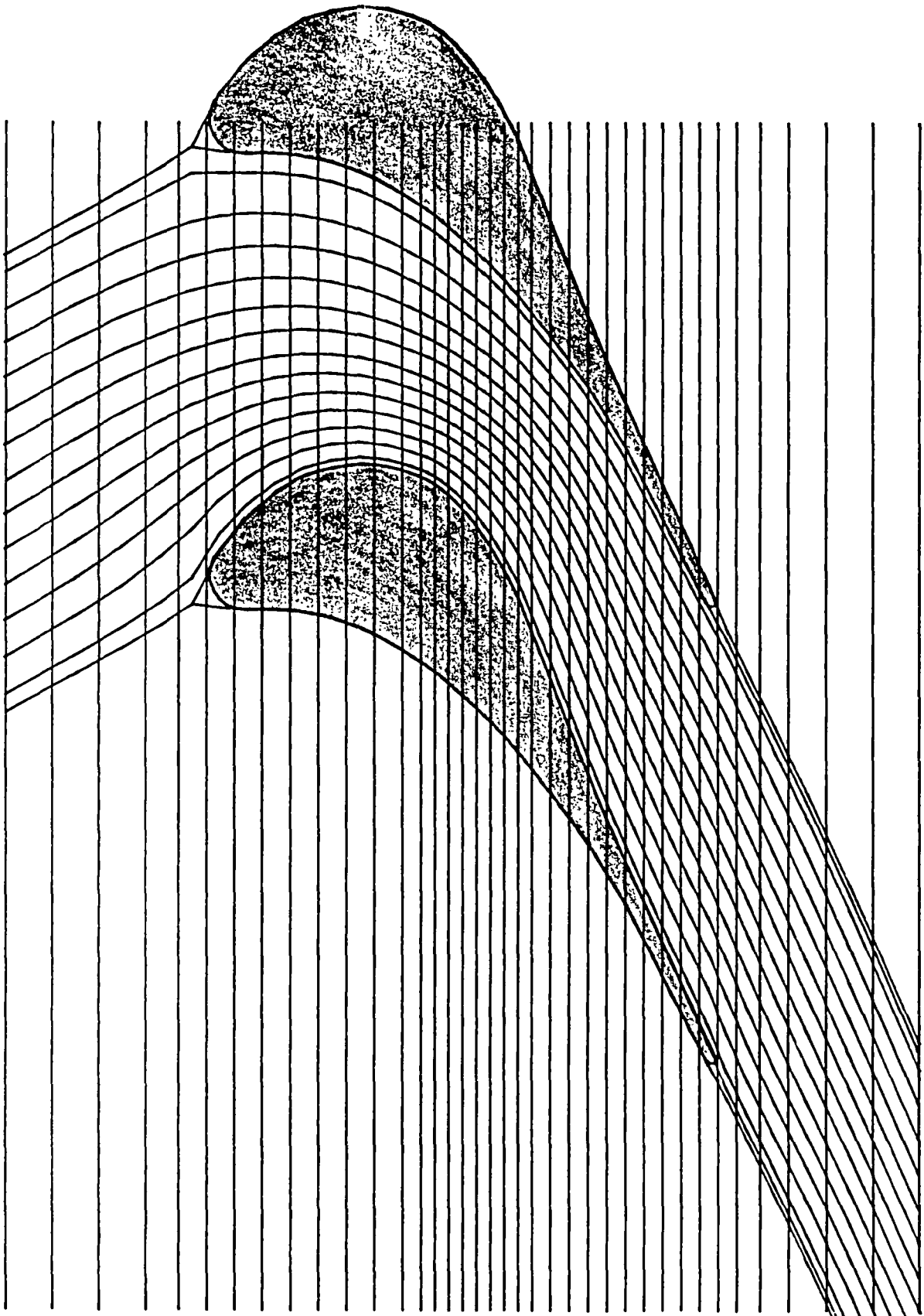


FIG. 6.21 FLOW GEOMETRY AND COMPUTATIONAL GRID; CONVERGENT-DIVERGENT NGV CASCADE (MIT-VKI-4)

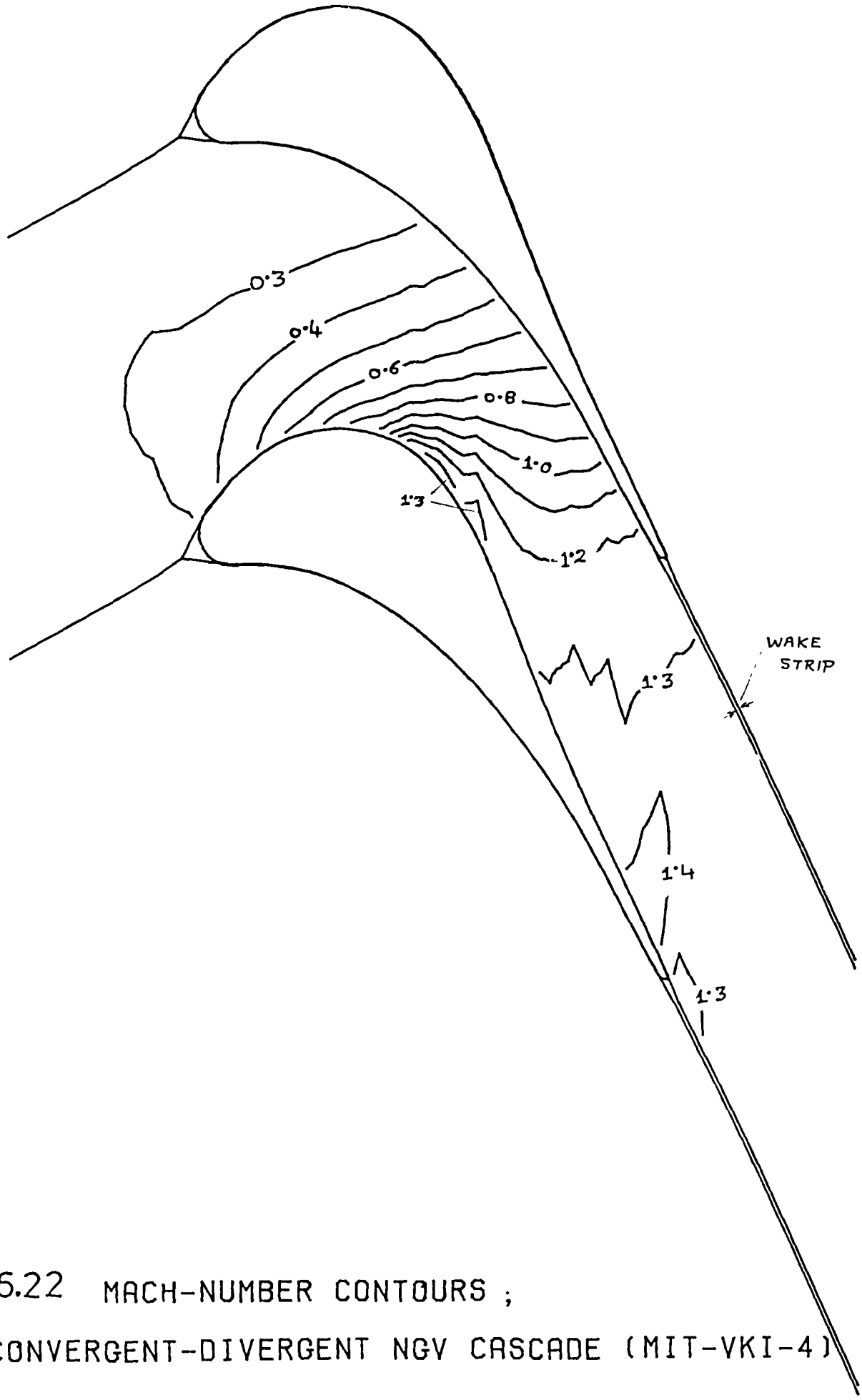


FIG. 6.22 MACH-NUMBER CONTOURS ;
CONVERGENT-DIVERGENT NGV CASCADE (MIT-VKI-4)

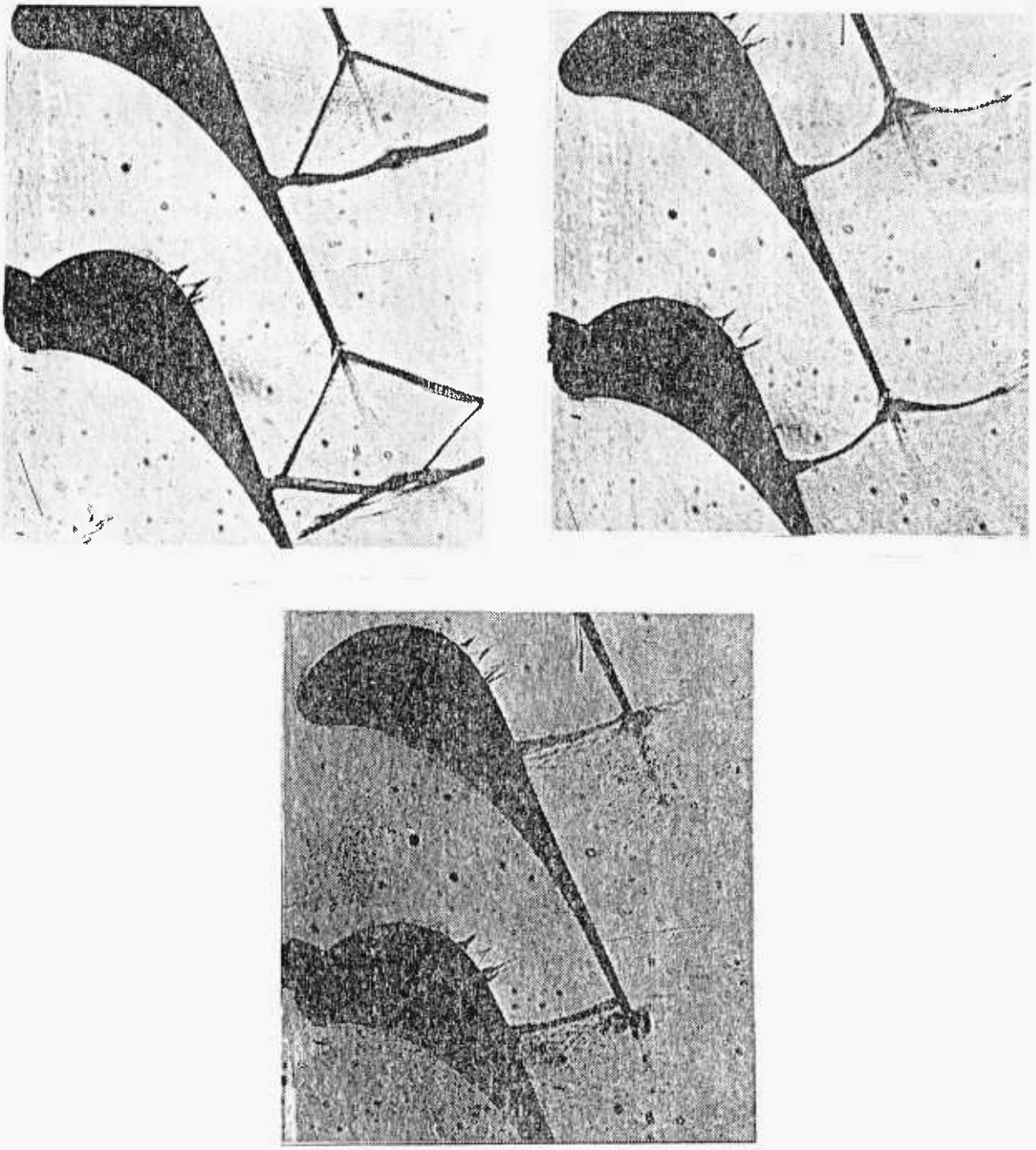


FIG. 6.23 CASCADE MIT-VKI IV

SCHLIEREN PICTURES OF CASCADES AT TRANSONIC OUTLET MACH NUMBERS

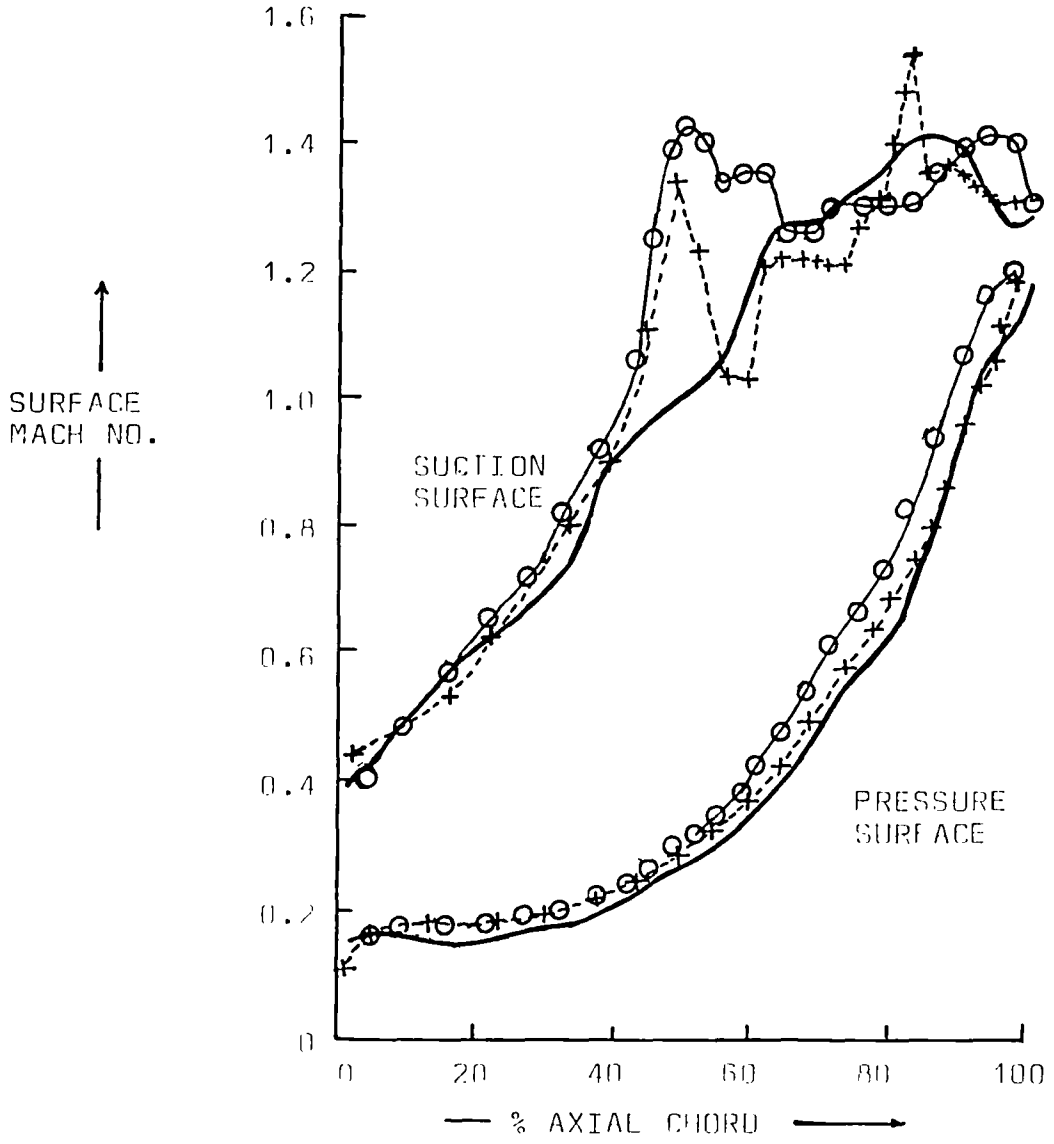


FIG.6.24 DISTRIBUTION OF SURFACE MACH NUMBERS, CONVERGENT-DIVERGENT NGV (MIT-VKI-4).

6.10 Computational details

Computations have been carried out on the CDC 6600 computer of London University. Computational details viz. grid size, number of iterations and execution time required, for each example, are presented in the following table:

Example No. and Identification	Grid size (N_y X N_x)	No. of iterations	Execution time (seconds)
1) The cylinder problem	11 x 25	40	7
2) NASA stator cascade	8 x 27	50	9
3) Hobson's first cascade	11 x 30	50	15
4) Hobson's second cascade	8 x 30	50	10
5) VKI gas turbine cascade	10 x 30	50	20
6) VKI steam turbine cascade	20 x 38	50	52
7) NGTE NGV cascade	10 x 27	75	26
8) MIT-VKI-IV NGV cascade	15 x 38	50	40

It was established, by variations of the grid fineness and by increasing the number of iterations that the physically significant results of the computations were substantially independent of these factors.

6.11 Concluding remarks

The computations reported in this chapter have shown that the present procedure is capable of accurate and economical predictions of incompressible, subsonic and transonic flows. The presented examples, by covering a wide variety of geometries, have also demonstrated the general applicability of the procedure.

CHAPTER 7

PREDICTIONS OF VISCOUS FLOWS WITH AND WITHOUT HEAT TRANSFER

7.1 Introduction

The purpose of this chapter is to demonstrate that the present procedure is capable of calculating viscous flows, both with and without heat transfer. For illustration, the VKI steam turbine cascade, Example 6 of the previous chapter, has been considered. The flow geometry, specified inlet and outlet conditions, and computational grid are retained to be the same as were used in Chapter 6. In order to examine the nature and magnitude of friction and heat transfer effects, the following cases are analysed:

(i) inviscid, adiabatic flow

(ii) viscous, adiabatic flow

(iii) viscous flow with heat rejection at blade surfaces

(iv) viscous flow with heat addition at blade surfaces

Case (i) is the same as reported in the previous chapter; its results are used here for the sake of comparison. In cases (ii) to (iv), the flow is treated as turbulent; the necessary physical inputs and the computed results are described in the following sections.

The results presented in this section have also been reported earlier; Singhal and Spalding (1976(b)).

7.2 Physical inputs

As already explained in Section 4.2, the computations of turbulent flow require a turbulence model; and at present, the Prandtl's mixing length model has been used. The mixing length, l, is calculated by using Equations (4.4) and (4.5), which employ two emperical constants - K and λ. By changing the values of these constants, it is possible to change the magnitude of effective viscosity, μ_{eff}. In the present calculations two sets of constants have been used. These are:

Set 1: $K = 0.4$, $\lambda = 0.12$;

Set 2: $K = 0.8$, $\lambda = 0.24$.

Set 1 represents the normal values of these constants, while in Set 2 their values have been doubled. The use of Set 2 implies a four fold increase in the viscosity. It has been used simply to examine the flow with exaggerated viscous effects. The constant K also appears in the wall function for shear stress, Equation (4.6); the same value of K is used in calculation of both μ_{eff} and wall shear stress.

For heat transfer calculations, the effective Prandtl number, σ_{eff}, has to be prescribed, in addition to μ_{eff}, at every point in the flow field. In the present calculations, σ_{eff} has been assumed to be a constant and equal to unity.

7.3 Turbulent, adiabatic flow

Computations of turbulent, adiabatic flow are performed by using two sets of emperical constants, as explained in the previous section. The resultant surface pressure distributions and velocity profiles at two sections, A-A and B-B in Fig. 7.1, are compared with the corresponding results of inviscid-flow calculations. These results are presented and discussed below.

Surface pressures

Fig. 7.2 illustrates three sets of surface-pressure distributions, calculated respectively with zero, normal and exaggerated viscosity (μ_{eff}). The following observations can be made from the diagram:

(a) Effect of viscosity is noticeable mainly at suction surface between .15 and .45 fraction of chord. This is a region of low pressures and adverse pressure gradient.

(b) In this region, viscosity has smoothed the pressure variation.

(c) Peaks in the pressure profile are shifted towards left.

(d) The above two effects (b and c) are in conformity with the experimental evidence; this can be seen by comparing Figures (7.2) and (6.17). It should be remembered that low pressures correspond to high Mach numbers.

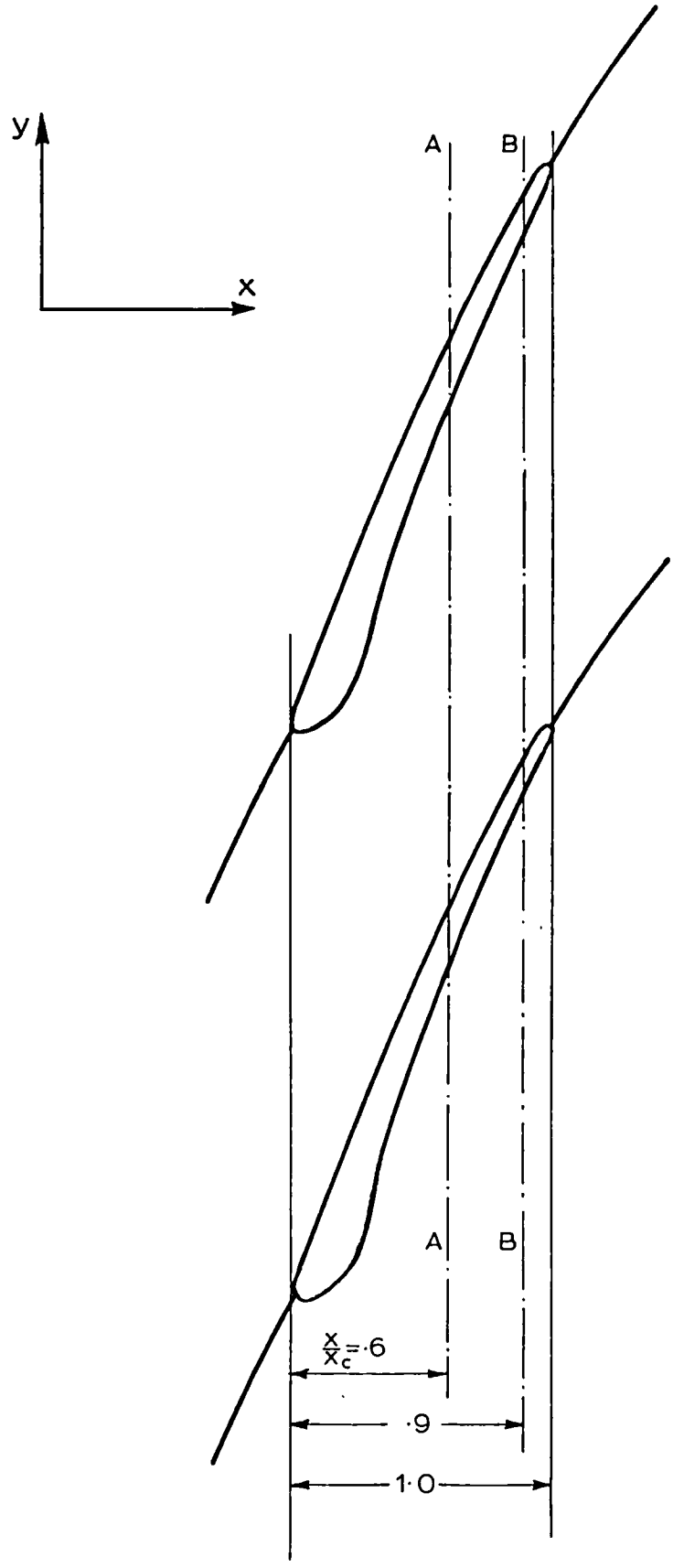


Fig. 7·1 Diagram illustrating the cascade geometry and locations of two sections (A-A and B-B)

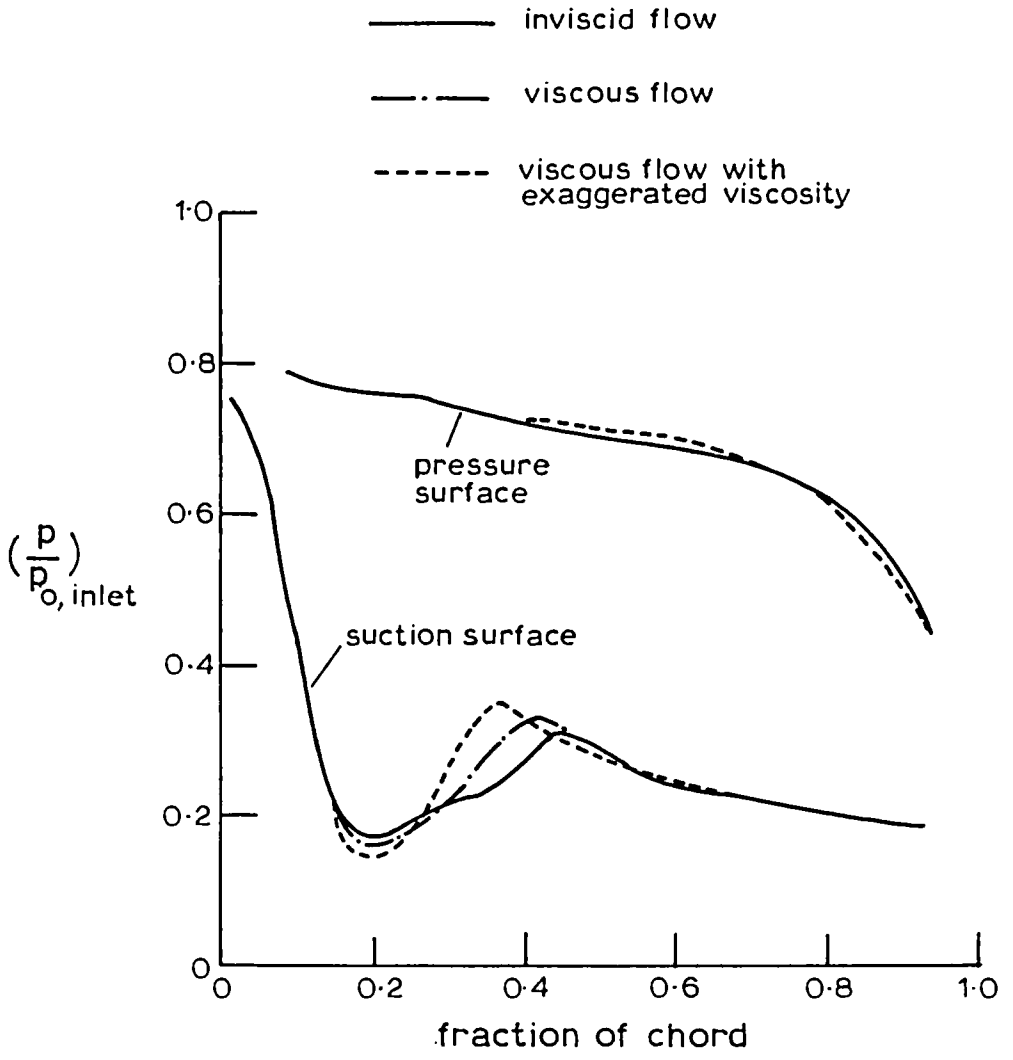


Fig. 7·2 Distribution of surface pressures

Velocity profiles

Fig. 7.3 presents velocity profiles at two sections, located at 60% and 90% axial-chord positions; two sets of velocity profiles - one for inviscid flow and the other for viscous flow (with the exaggerated viscosity), are included. These profiles exhibit the expected trends, which are explained below:

(a) Due to the presence of viscosity, the fluid is accelerated in the low-velocity region and vice versa. In other words, viscosity tends to make velocity profiles more uniform.

(b) In the near-wall regions, velocity profiles are affected significantly because of the no slip condition at wall.

Similar effects are observed at other sections too. Velocity profiles with normal viscosity (i.e. by using Set 1 of constants) showed much smaller effects. Effects of viscosity on the overall flow parameters are discussed in Section 7.4, together with the heat-transfer effects.

7.4 Turbulent flow with heat transfer

As explained in Section 4.3, heat transfer can be calculated by solving an additional equation for stagnation enthalpy, $\tilde{h}$. In this section, computations are presented for two cases, designated as case (iii) and (iv), in which

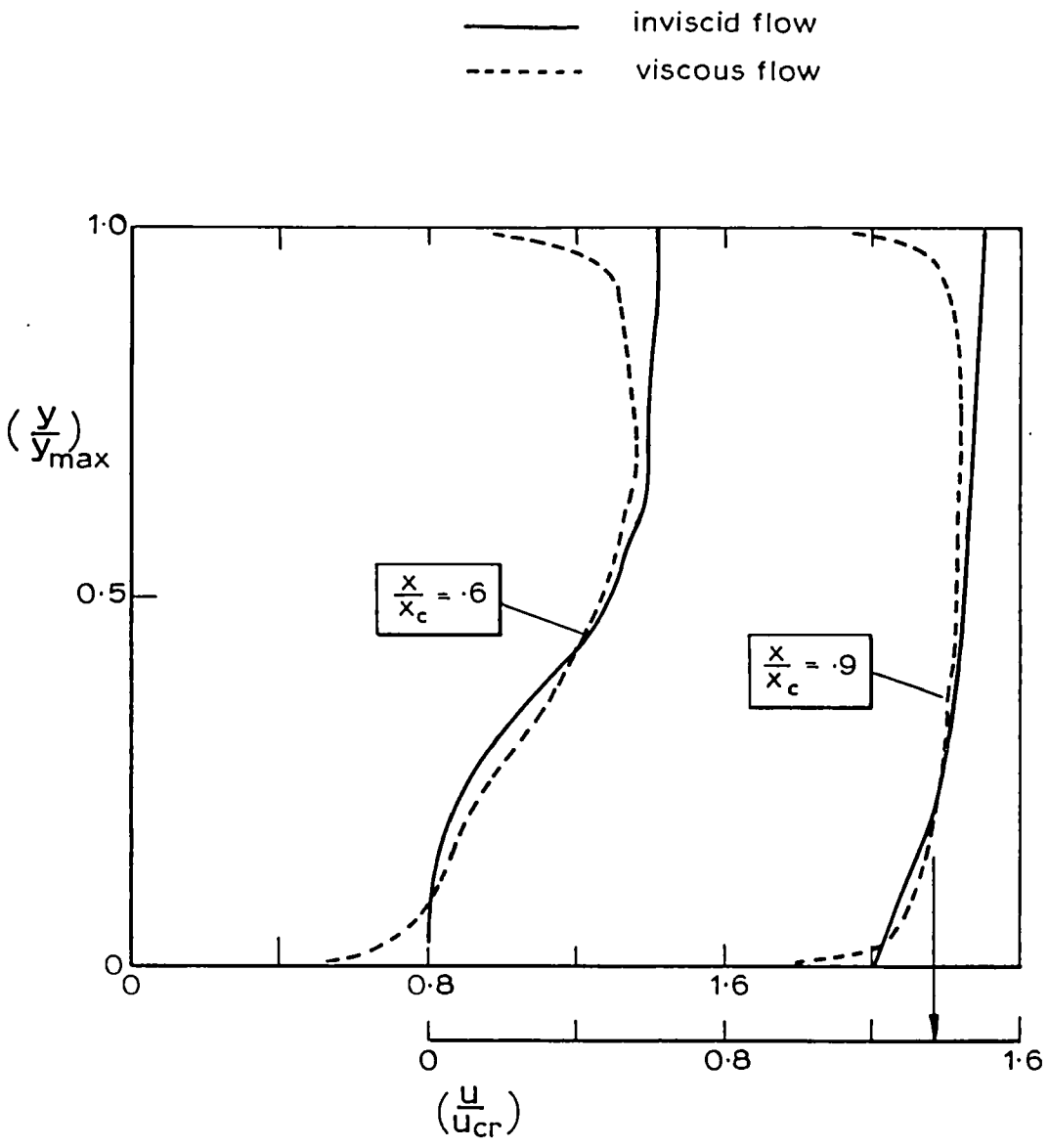


Fig. 7·3 Velocity profiles at two sections shown in Fig. 7·1

blade-surface temperatures are held constant at 150°K and 450°K respectively. The selected temperatures are such that in the first case blades cool the fluid while in the later case, they heat it; Fig. 7.4 illustrates these temperature levels together with the wall temperature variations of case (i) which considers an inviscid, adiabatic flow. The inviscid-flow temperatures have been calculated by using the gas equation $(\frac{T}{T_o} = (\frac{p}{p_o})^{\frac{\gamma}{\gamma-1}})$.

Fig. 7.5 presents temperature profiles at the same two sections at which velocity profiles were presented. At each section, three temperature profiles are displayed: two for the above-mentioned cases and one for the case of inviscid, adiabatic flow. By comparing these profiles, the following observations have been made:

(i) The influence of fixed wall temperatures is confined to the near-wall regions (i.e. approximately $0 < {}^{y}/_{y_{max}} < .15$ and $.85 < {}^{y}/_{y_{max}} < 1.0$).

(ii) In the central part of the sections, the temperature differences between inviscid and turbulent flows are due to the relative acceleration and deceleration of fluid, resulting from the viscous effects. It can also be checked by examining the velocity profiles shown in Fig. 7.3.

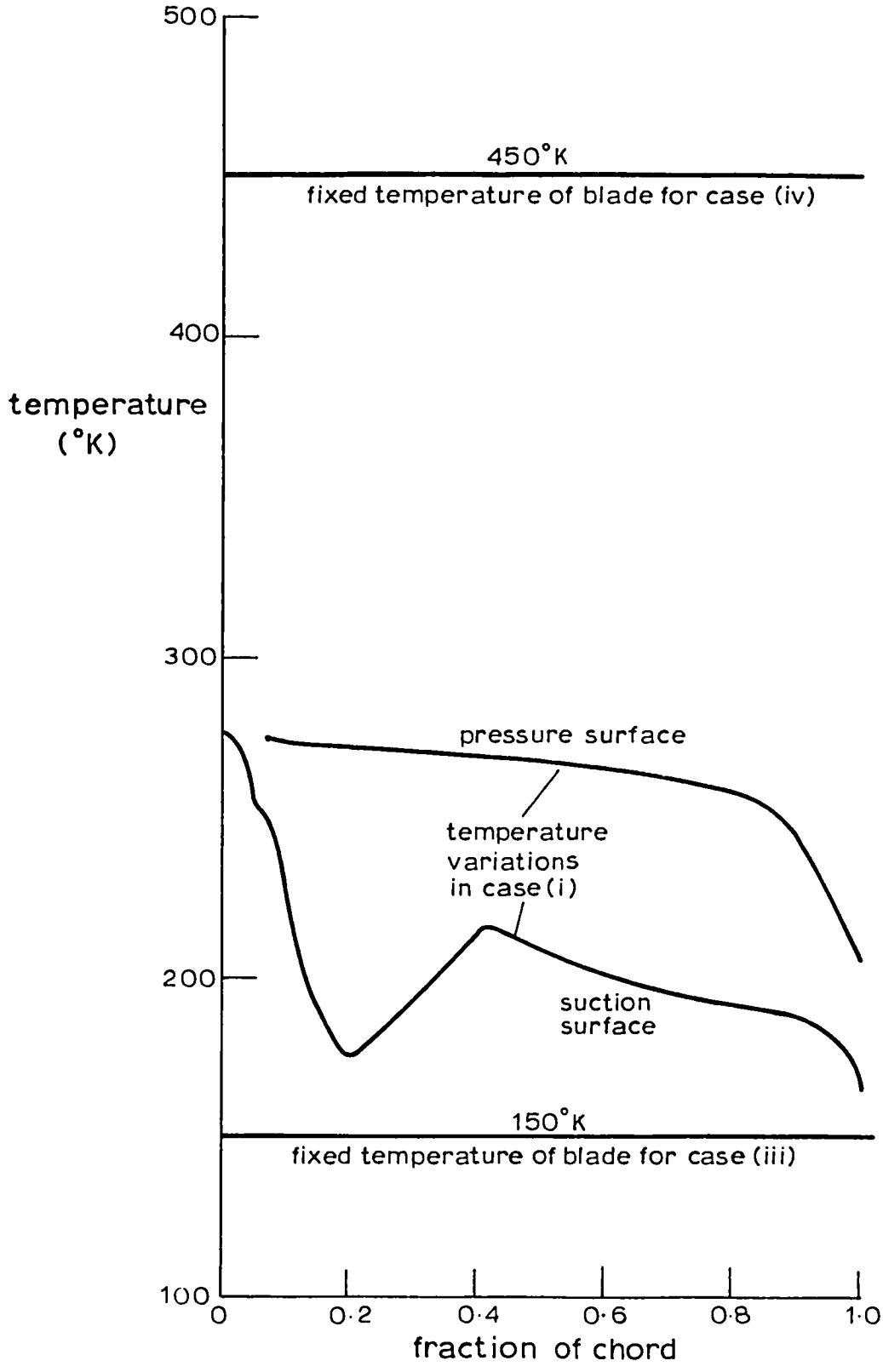


Fig. 7·4 Blade surface temperature variations for cases (i), (iii) and (iv)

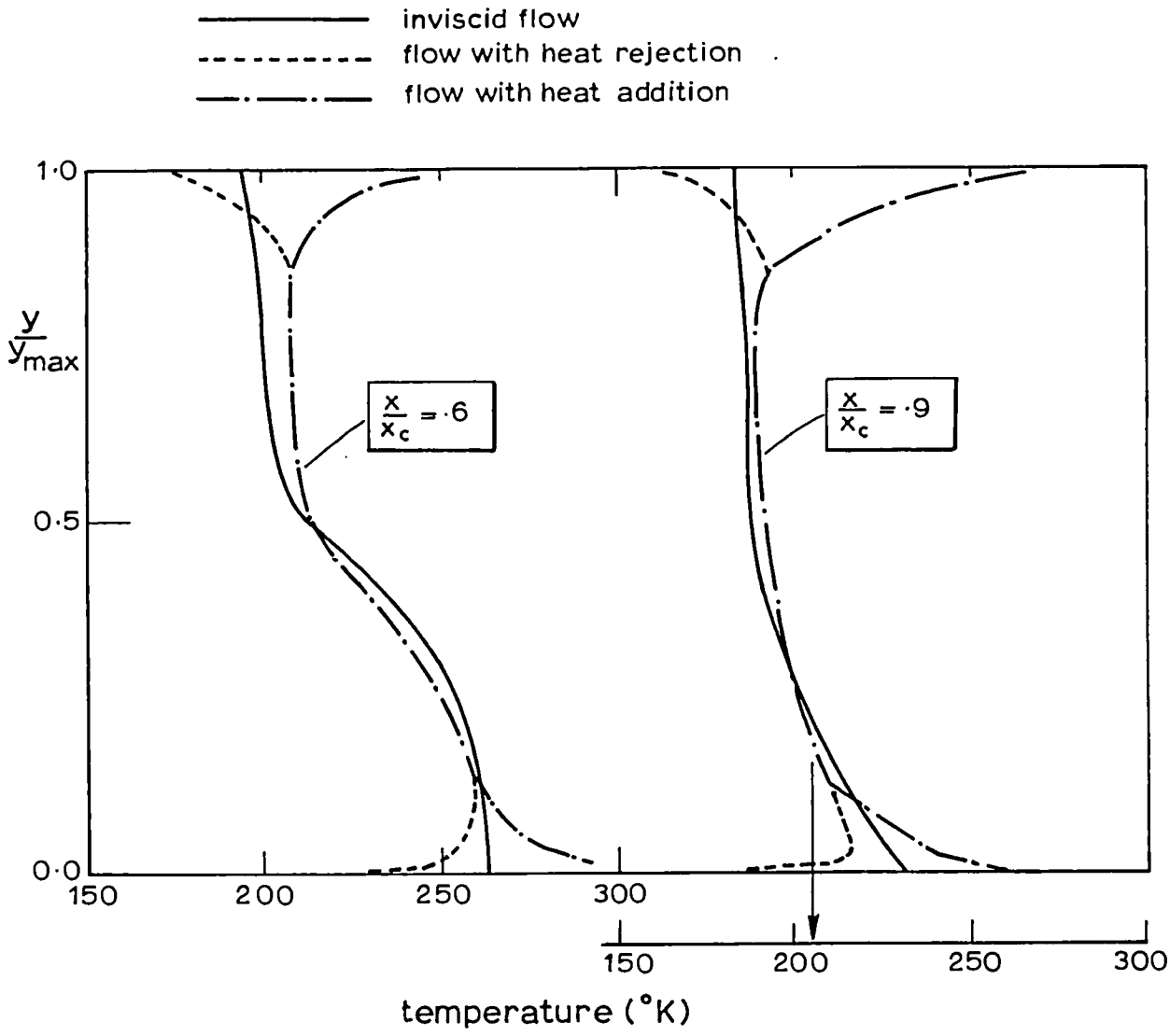


Fig. 7·5 Temperature profiles

Temperature profiles of Fig. 7.5 have been obtained by using the exaggerated viscosities (Set 2 of emperical constants). Use of normal viscosities had similar effects of much smaller magnitudes.

In order further to examine the adequacy of the results, the calculated overall flow parameters, for different cases, are listed in the following table. (For convenience, the execution-time requirements are also indicated in this table):

Case No.	Identification	Calculated values		Execution time required on CDC 6600 computer
		Inlet Mach Number	Exit flow angle (α)	
1	Inviscid flow	.630	58.5^{o}	52 seconds
2	Viscous, adiabatic flow	.630	58.5^{o}	52 seconds
3	Viscous, adiabatic flow*	.615	58.2^{o}	52 seconds
4	Flow with heat rejection*	.615	58.4^{o}	54 seconds
5	Flow with heat addition*	.615	58.1^{o}	54 seconds

* flow with exaggerated viscous effects

From this table, the following points are observed:

(i) Introduction of normal viscosities makes no significant difference in the overall flow parameters.

(ii) The use of exaggerated viscosities reduces the inlet Mach number; which implies a reduction in the mass flow rate.

(iii) Changes in the exit flow angle are such that the heat addition seems to supplement the viscous effects while the heat rejection tends to oppose it. This is in conformity with the basic thermodynamic analysis presented in text books, e.g. Reynolds (1971).

(iv) Increase in computation time, for heat transfer calculations, is very marginal (less than 5 per cent).

7.5 Concluding remarks

The computed results presented in this chapter have shown that the procedure can make realistic predictions of viscous and heat transfer effects in the cascade flows. It is also shown that the inclusion of these effects makes little difference to the computer time requirements.

CHAPTER 8

PREDICTION OF PRESENT EXPERIMENTAL FLOWS

8.1 Introduction

This chapter presents the numerical predictions of all the ten flow situations, considered in the present experimental investigation, explained in Chapter 5. The purpose of this exercise is to further demonstrate the capabilities of the prediction procedure, described in Chapter 3. In the following sections, first, the relevant computational details are explained; and, then, the predicted results are compared with the corresponding experimental ones.

8.2 Computational details

In order to simulate the experimental flow situations, the following information is supplied as input to the procedure:

(i) Cascade geometry.

(ii) Flap width, thickness and its inclination with reference to the axial direction, α_{flap}.

(iii) Inlet flow direction α_{in}.

(iv) Inlet stagnation pressure and density.

(v) Inlet Mach number.

(vi) Condition of uniform pressure distribution at the outlet plane.

Only the values of α_{in} and α_{flap} change from case to case; all other conditions remain identical. Fluid is assumed to be a perfect gas of specific heat ratio 1.4. Inlet stagnation pressure and density are assigned the values of a standard atmosphere; and the inlet Mach number is specified to be 0.1. These values of inlet flow properties are not important because all the results are non-dimensionalised.

Fig. 8.1 illustrates the flow geometry and computational grid for a typical case ($\alpha_{in} = 40^{o}$ and $\alpha_{flap} = -45^{o}$). In the cross-stream direction, 10 grid lines (streamlines) are used, such that the mass flow rate through any two consecutive lines is equal. In the axial direction, the region inside the blades is divided into 20 intervals and the flap region is divided into two intervals. The later interval size depends on the projected flap width on the x-axis. Thus, this interval size is different for each α_{flap} case. For convenience, the same grid-interval size is employed in the further downstream region.

In the following section, predictions of all the ten cases, based on inviscid-flow calculations, are presented. In one case, turbulent-flow calculations were also made; and, as expected, no significant difference was observed.

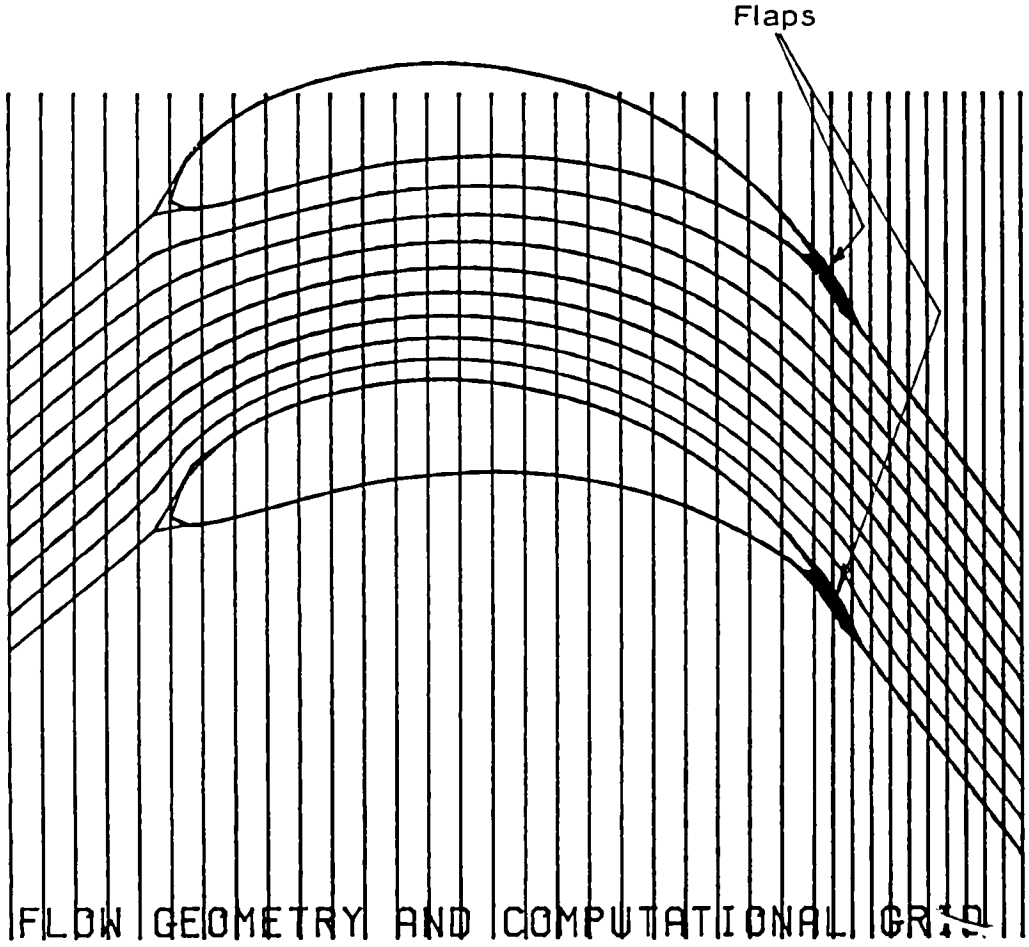


Fig. 8-1
IMPULSE CASCADE (EXPERIMENTS) $\alpha_{in}=40^\circ$
$\alpha_{flap}=-60^\circ$

8.3 Presentation of results

First, results of the five cases of first set ($\alpha_{in} = 40^{o}$) are presented. Figs. 8.2 to 8.6 illustrate the predicted and experimental values of pressure coefficients. The pressure coefficient C_p is defined as in Equation (5.1). For these cases, the pressure contours have also been plotted; these are shown in Figs. 8.7 to 8.11 .

For Set 2 ($\alpha_{in} = 20^{o}$), the pressure distributions (both theoretical and experimental) are displayed in Figs. 8.12 to 8.16 . For this set, the pressure-contour plots are not presented because they are similar to those of previous set.

8.4 Discussion

Figs. 8.2 to 8.6 indicate that the predicted surface-pressure distributions follow the trends of experimental data, very closely for all the flap settings. The agreement is very good in the central and downstream parts of the blade surfaces. In the front 20% of the chord, predictions are not very accurate. These can be improved by using a finer grid; however, for the present investigation, it is not important because the primary objective is to analyse the effectiveness of the trailing-edge flaps.

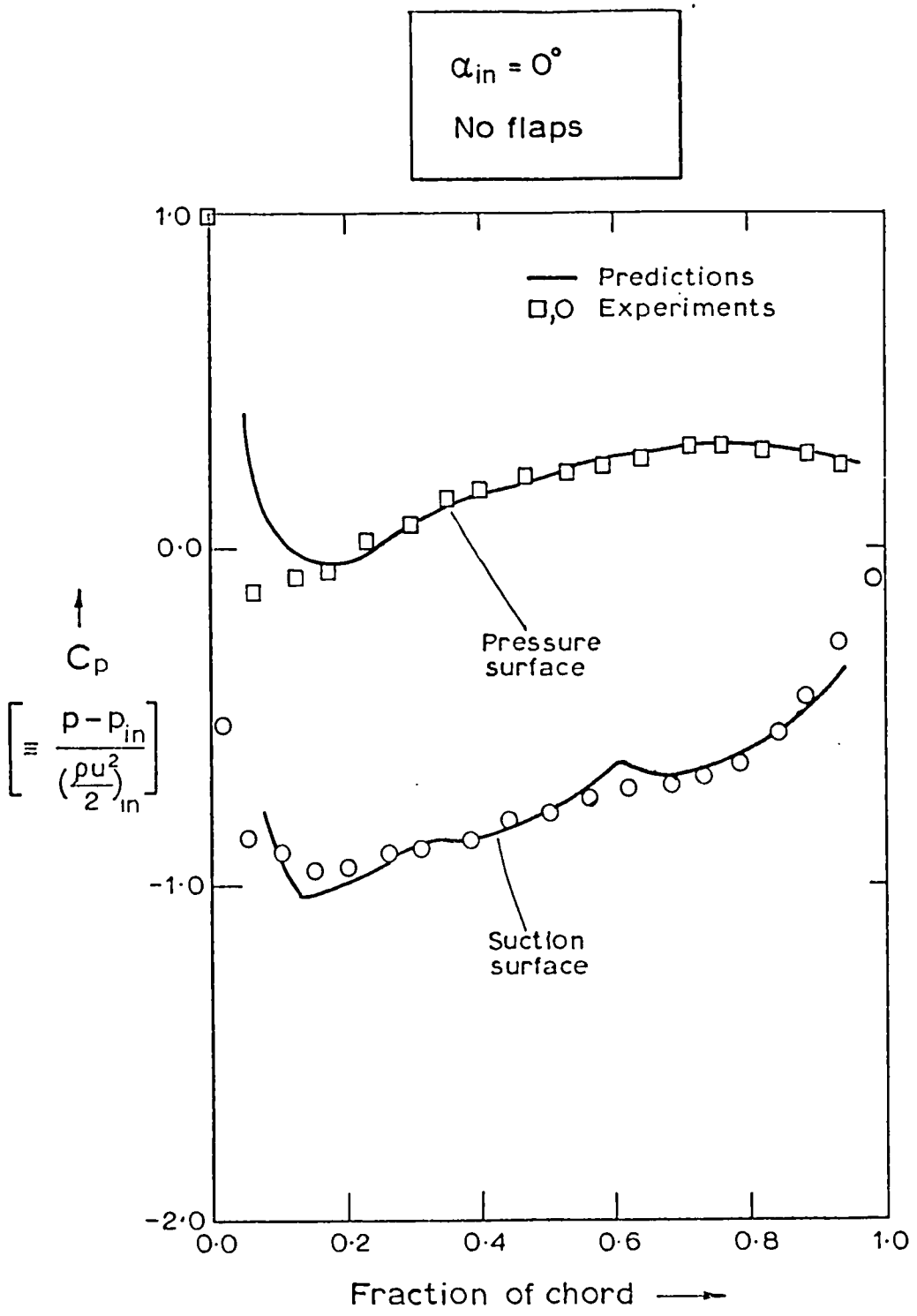


Fig. 8·2 Comparison of experimental and predicted distributions of surface pressures

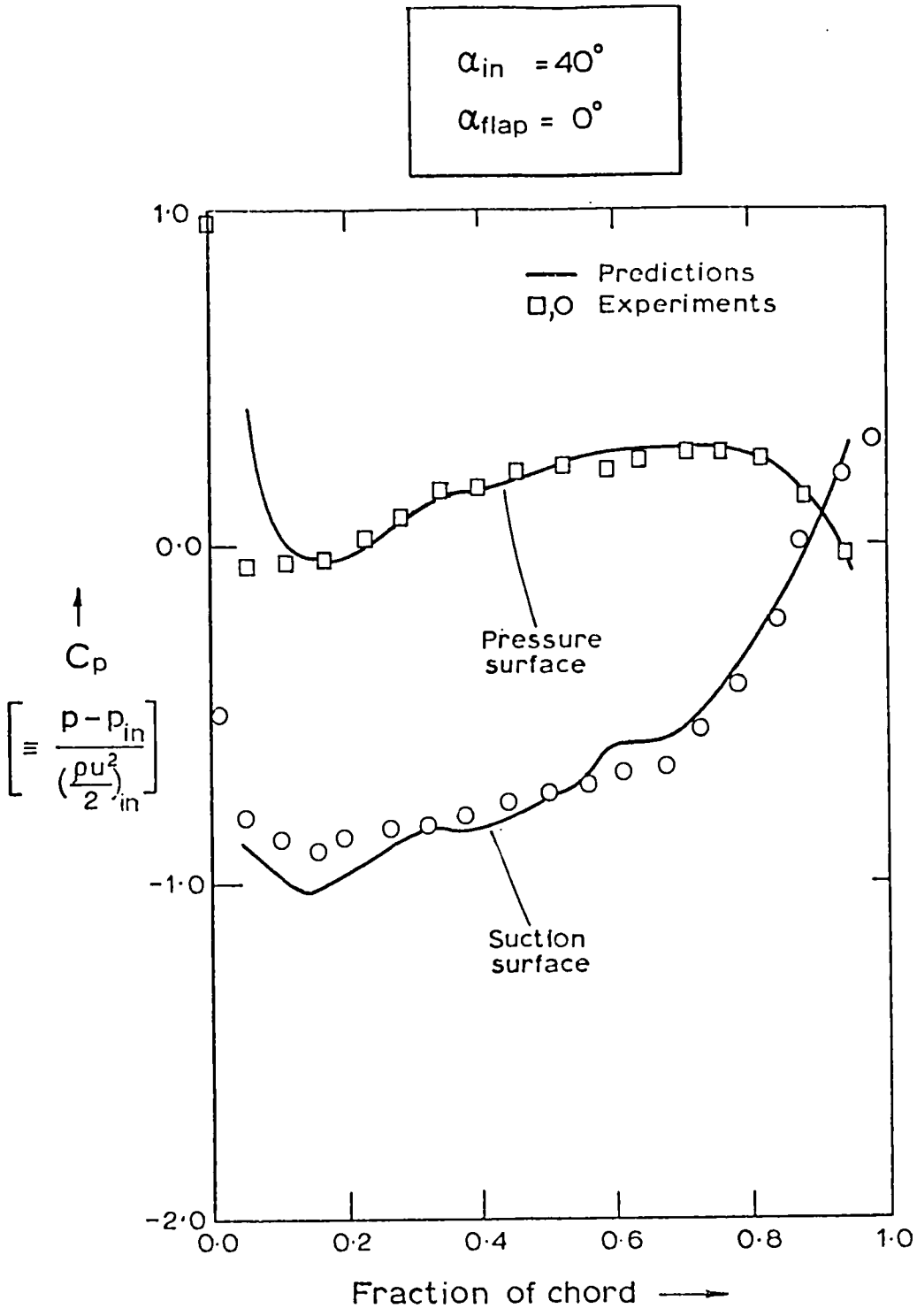


Fig. 8·3 Comparison of experimental and predicted distributions of surface pressures

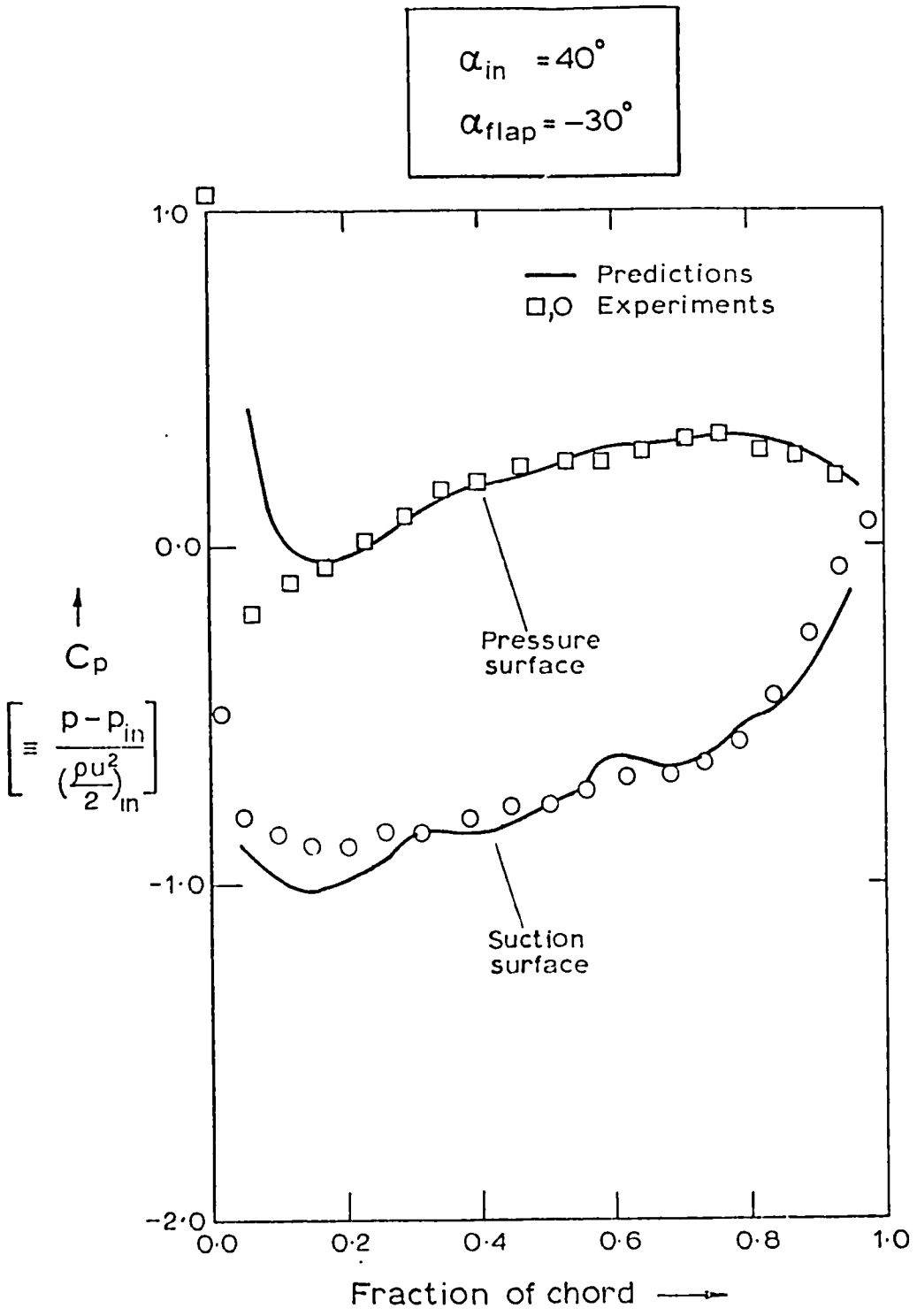


Fig. 8·4 Comparison of experimental and predicted distributions of surface pressures

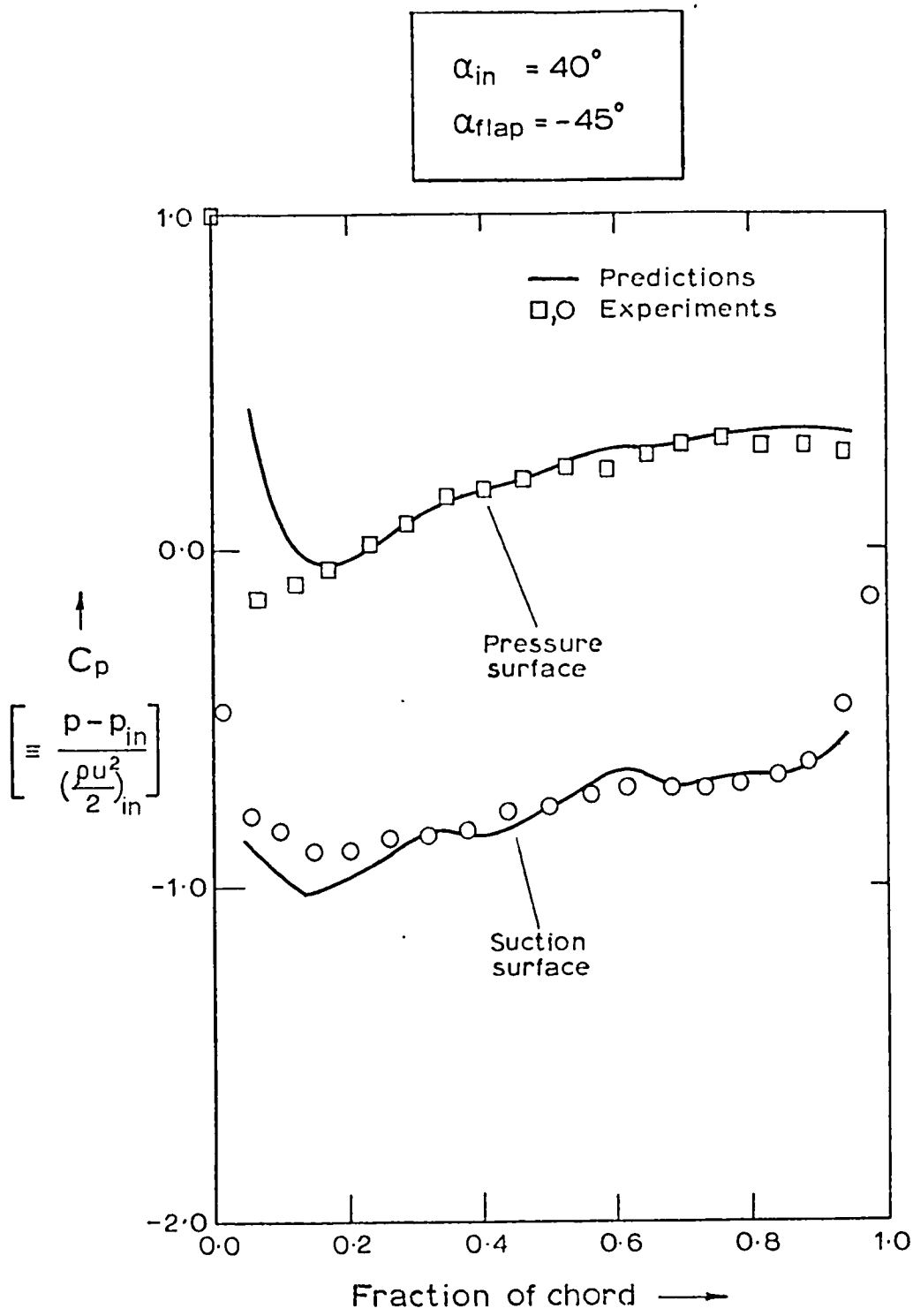


Fig. 8·5 Comparison of experimental and predicted distributions of surface pressures

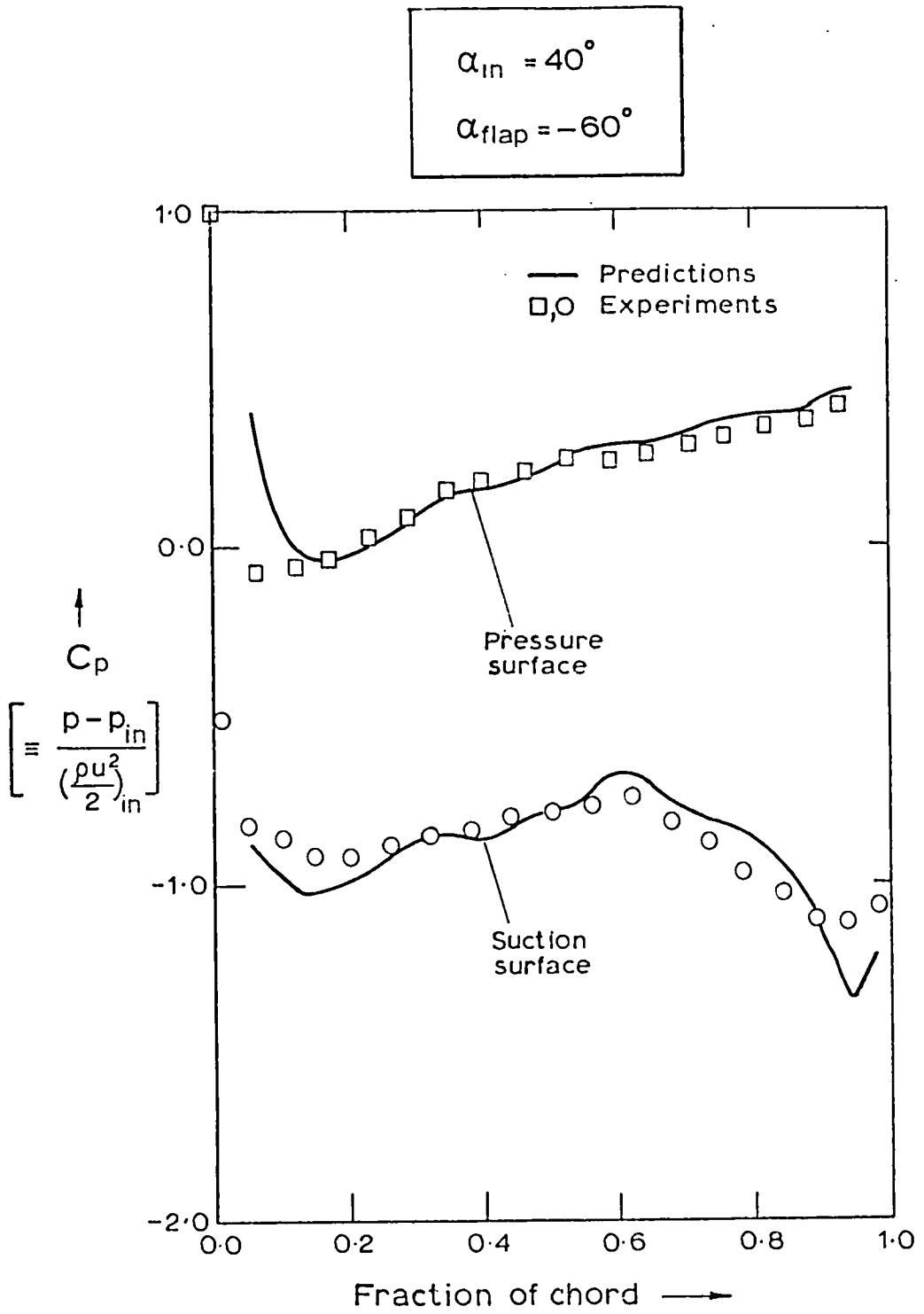


Fig. 8·6 Comparison of experimental and predicted distributions of surface pressures

$\alpha_{in} = 40°$
No flaps

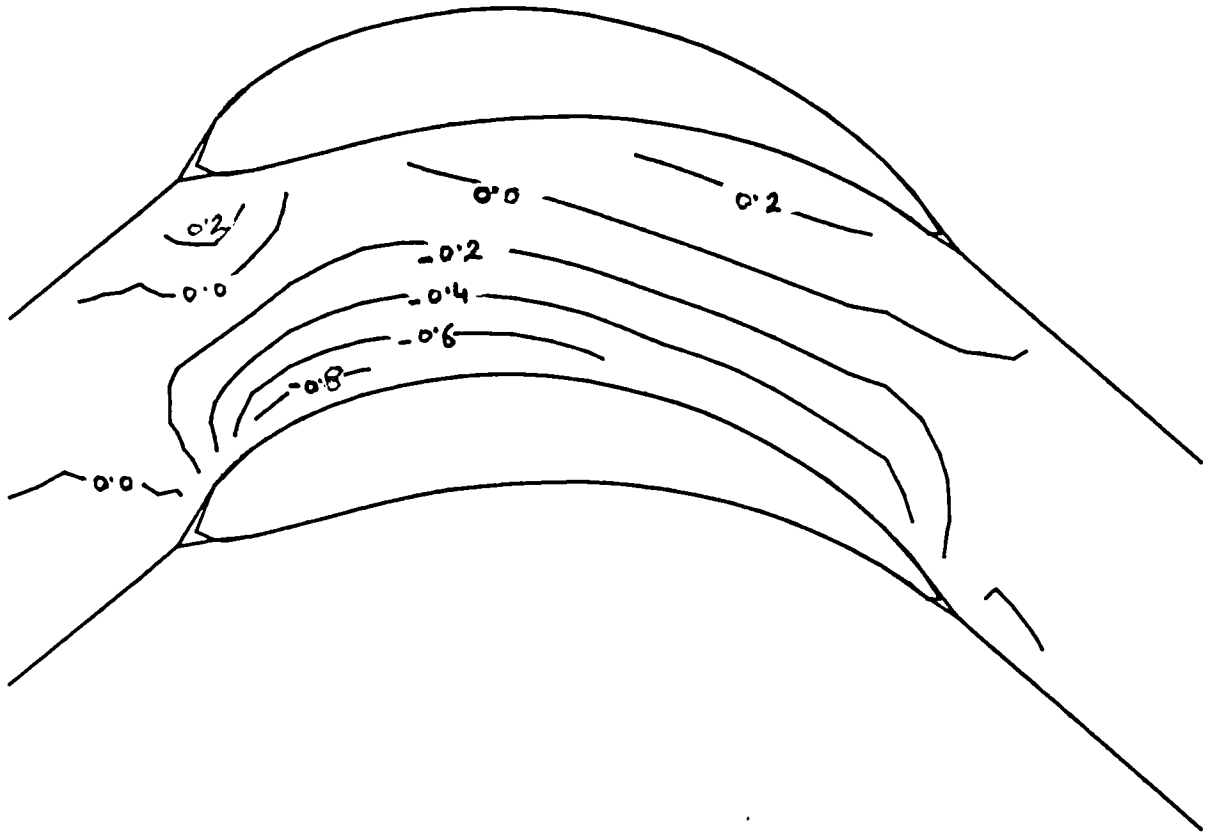


Fig. 8·7 PRESSURE CONTOURS

IMPULSE CASCADE

$\alpha_{in} = 40^\circ$
$\alpha_{flap} = 0^\circ$

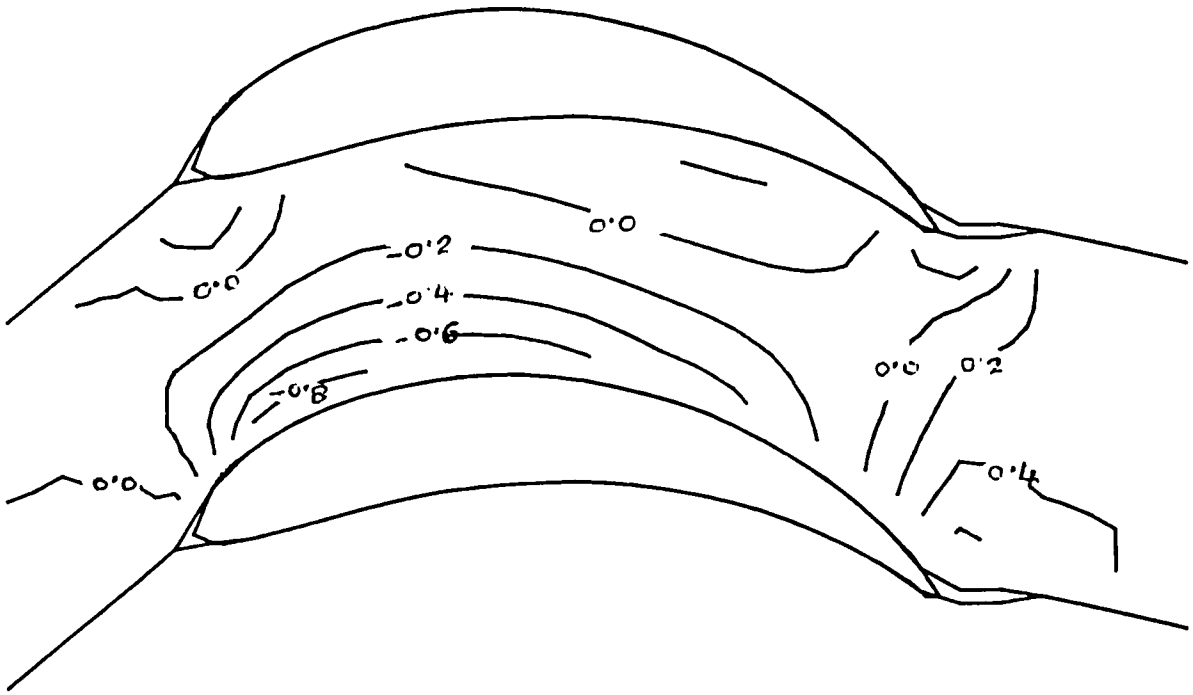


Fig. 8·8 PRESSURE CONTOURS

IMPULSE CASCADE

α_{in} =40°
α_{flap}= -30°

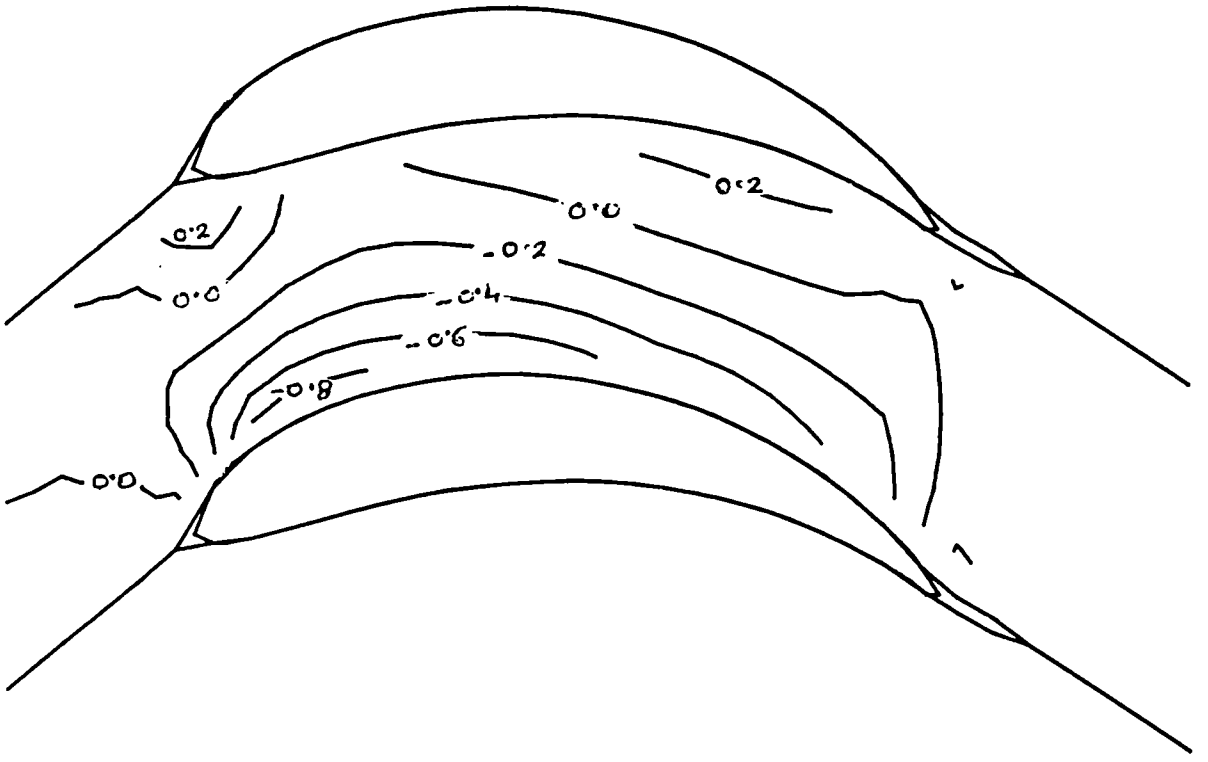


Fig. 8·9 PRESSURE CONTOURS

IMPULSE CASCADE

$\alpha_{in} = 40^{\circ}$
$\alpha_{flap} = -45^{\circ}$

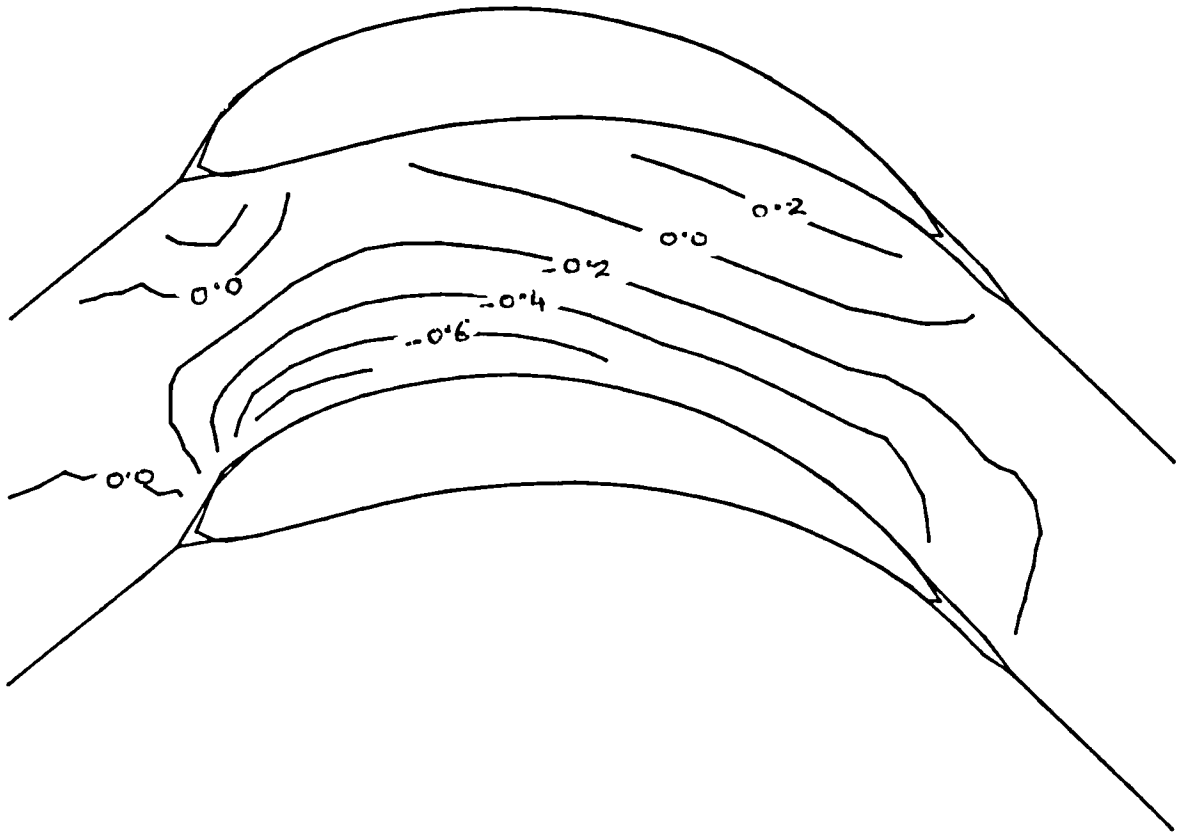


Fig. 8·10 PRESSURE CONTOURS

IMPULSE CASCADE

$\alpha_{in} = 40°$
$\alpha_{flap} = -60°$

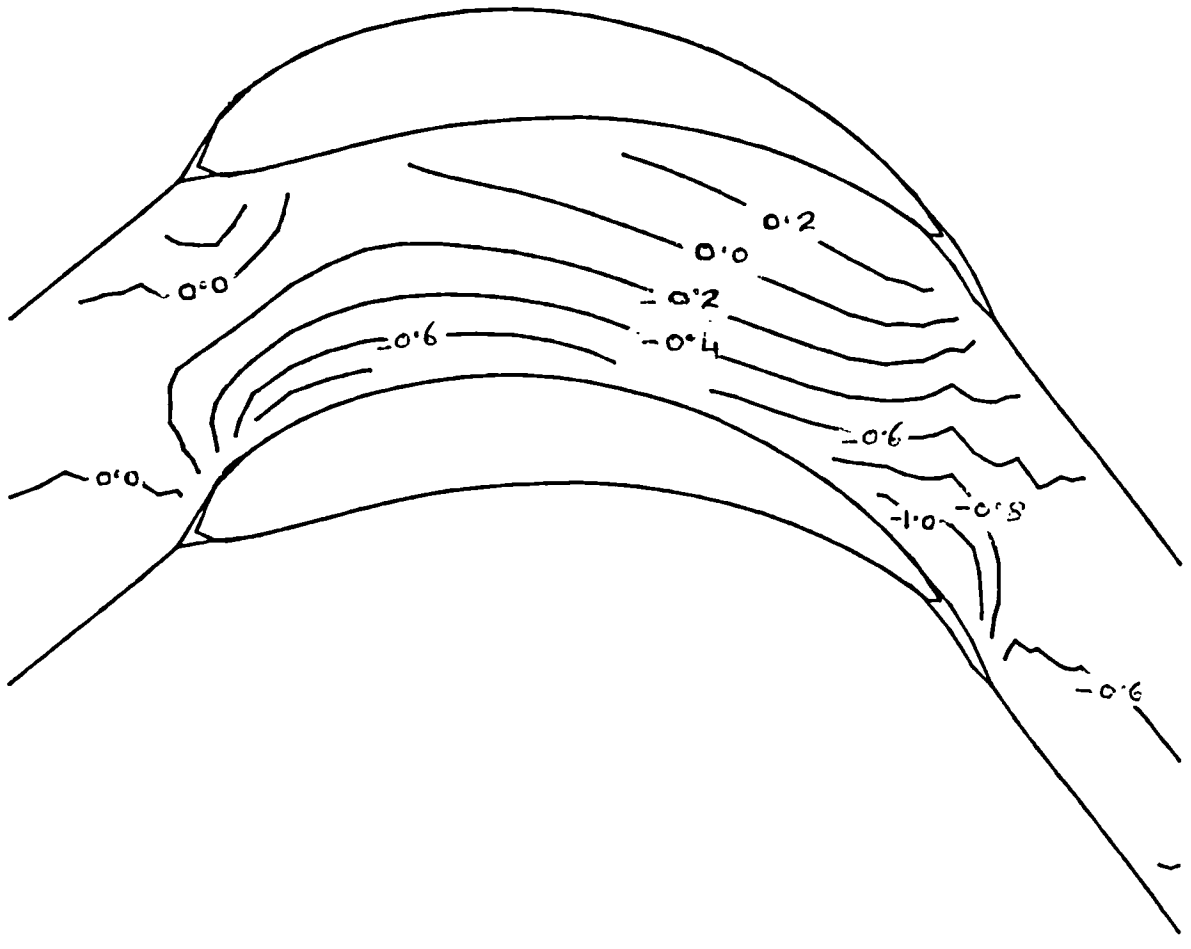


Fig 8.11 PRESSURE CONTOURS

IMPULSE CASCADE

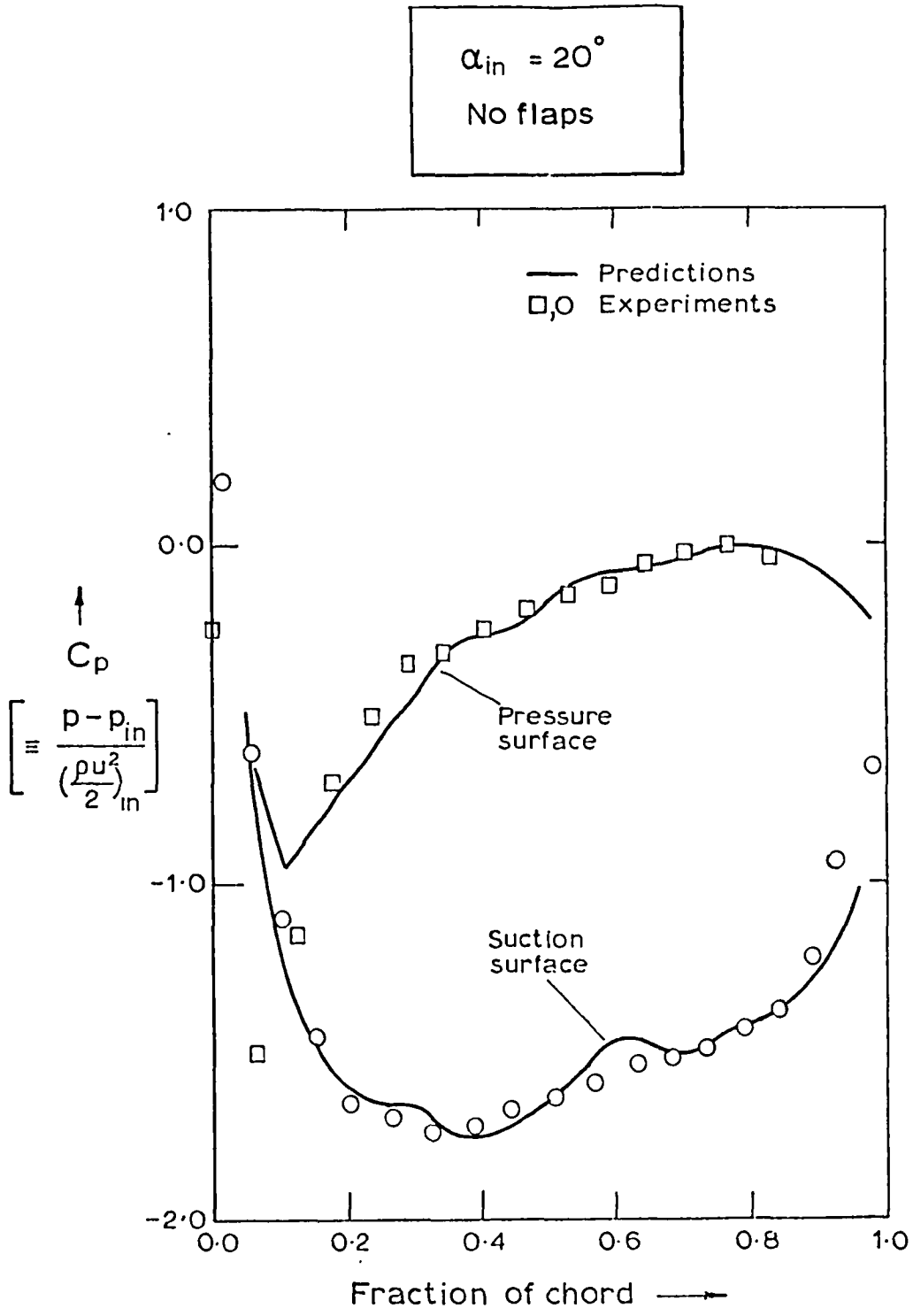


Fig. 8·12 Comparison of experimental and predicted distributions of surface pressures

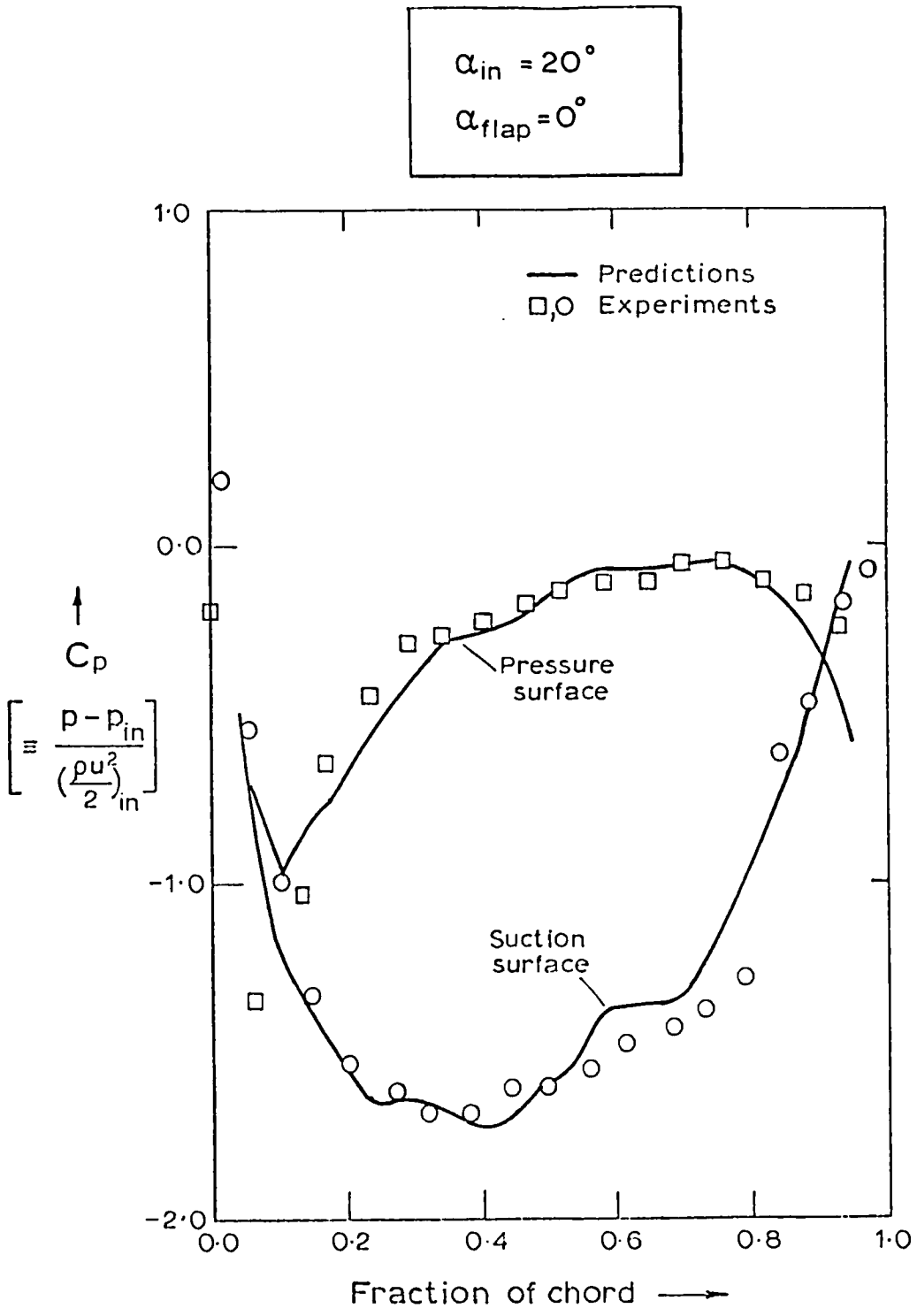


Fig. 8·13 Comparison of experimental and predicted distributions of surface pressures

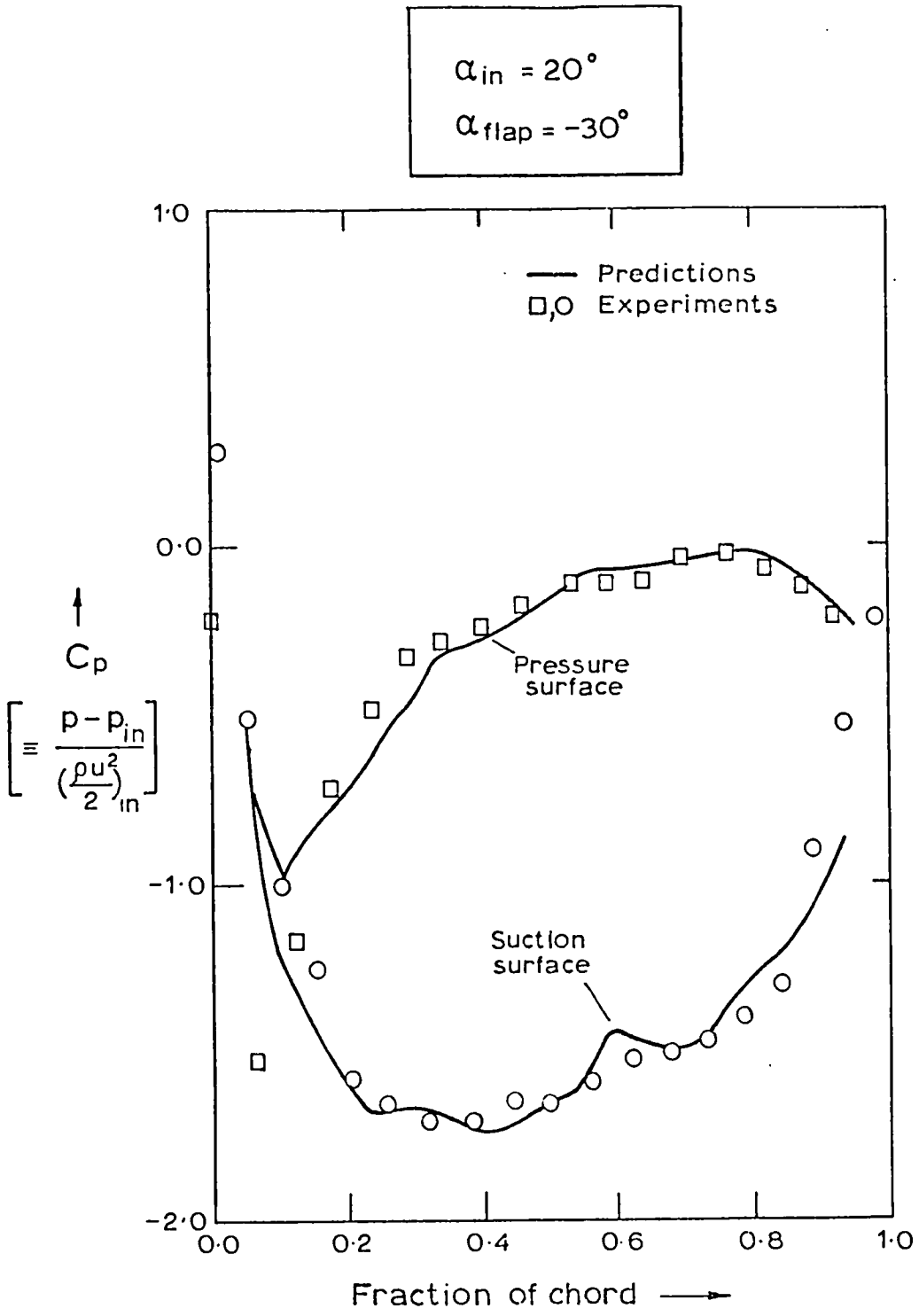


Fig. 8·14 Comparison of experimental and predicted distributions of surface pressures

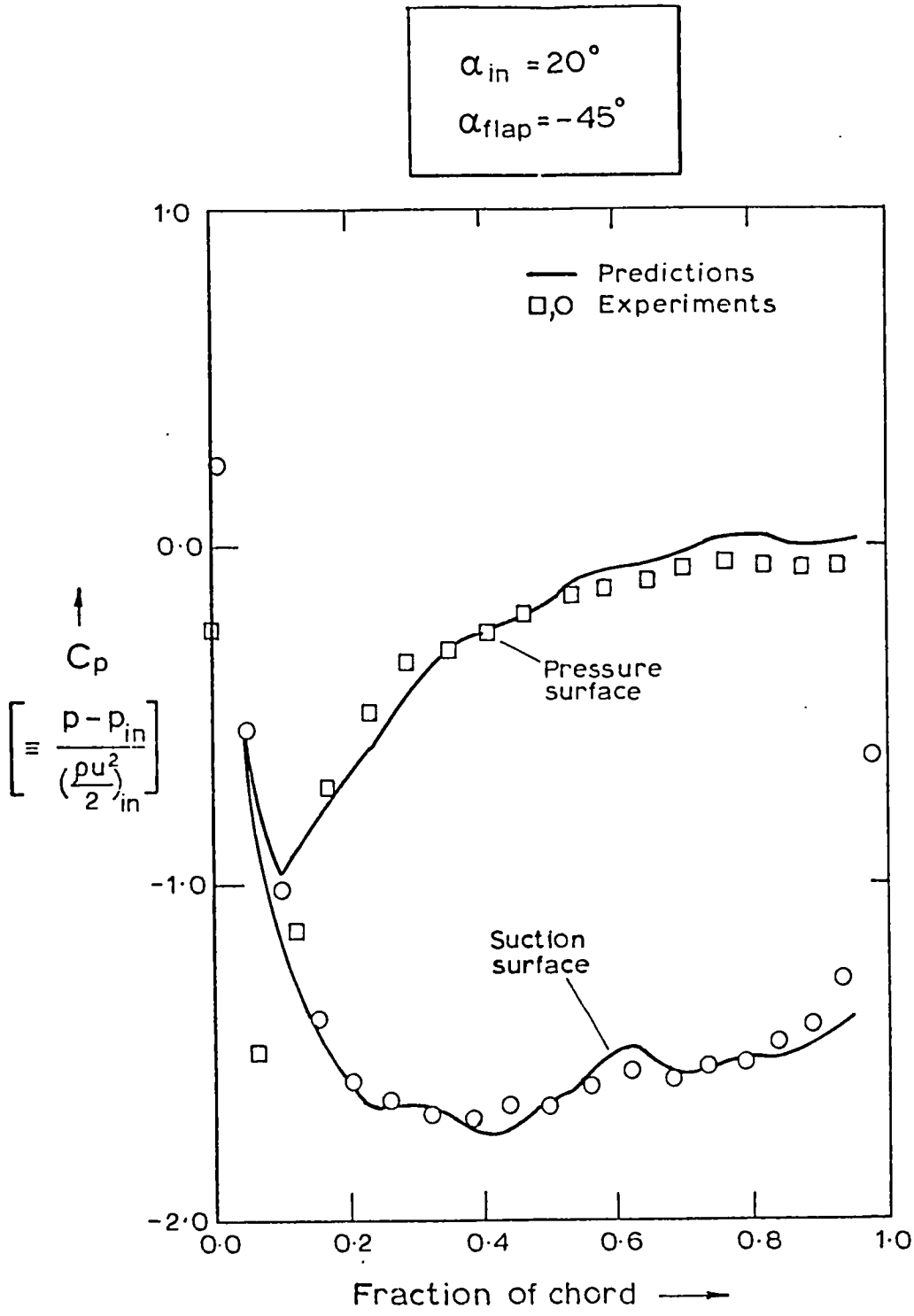


Fig. 8·15 Comparison of experimental and predicted distributions of surface pressures

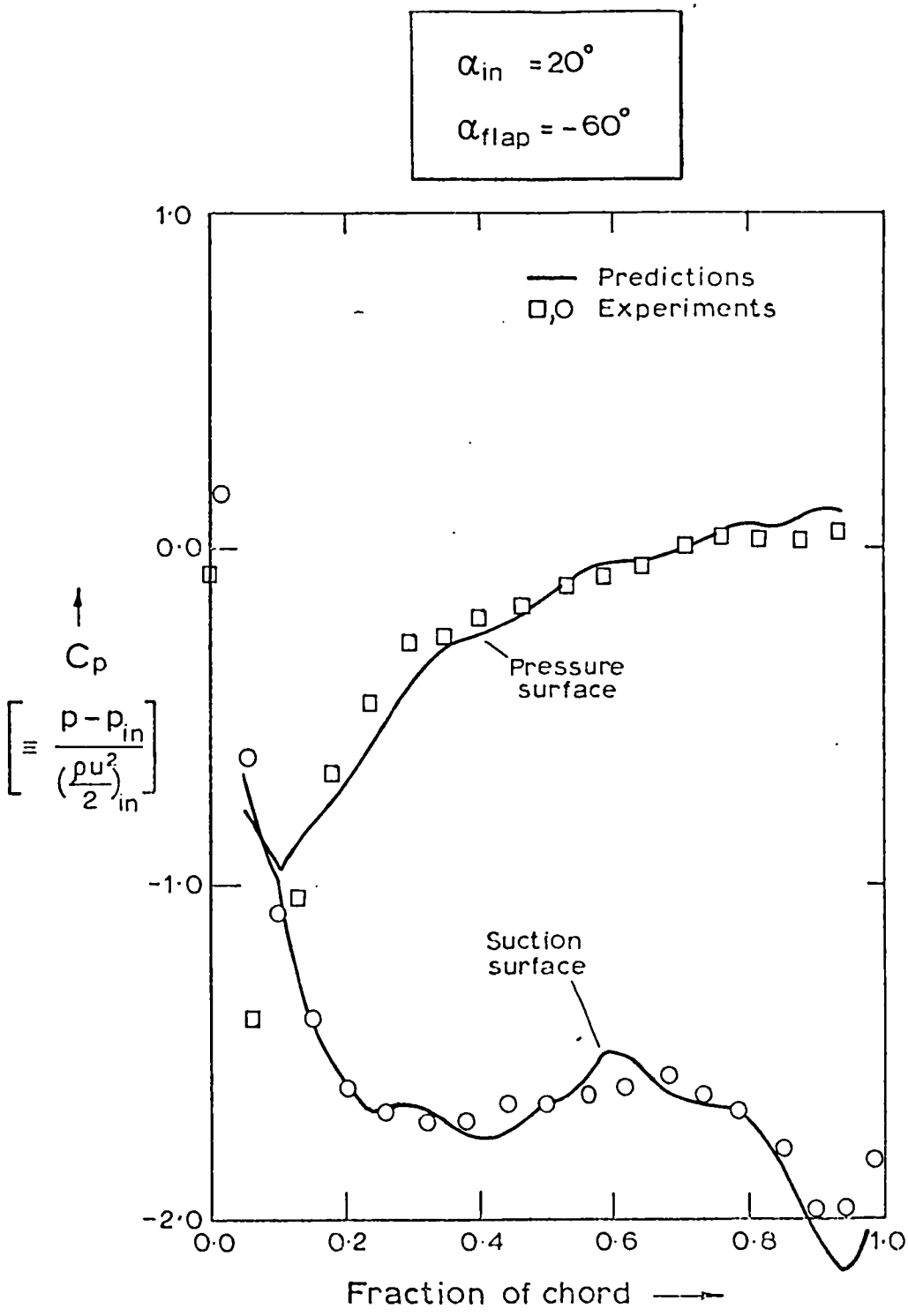


Fig. 8·16 Comparison of experimental and predicted distributions of surface pressures

Figs. 8.7 to 8.11 give a general idea of the changes in the whole pressure field, due to the trailing-edge flaps.

Similar comments hold good for the results of the second set.

8.5 Concluding remarks

The close agreement between the predictions and experimental results, indicates that the prediction procedure could as well have been used to analyse the effectiveness of trailing-edge flaps. This example suggests that the procedure can be a useful analytical tool.

CHAPTER 9

CONCLUSIONS

9.1 Achievements of the present study

The main achievements of the present study can be summarized as follows:

(1) A novel prediction procedure has been developed for two-dimensional partially-parabolic flows, with particular reference to turbine cascades. The main merits of the procedure derive from its use of: (a) the non-orthogonal, streamline coordinate system; (b) the velocity components which are aligned with the local coordinate directions; and (c) the "iterative space-marching" solution scheme which requires only one-dimensional storage for all variables except pressure.

(2) Provisions for all the important features of cascade flows have been built into the procedure; these features are: (a) strong curvature; (b) circumferential periodicity; (c) compressibility; (d) turbulence; (e) heat transfer; (f) rotation of blades; and (g) flow convergence resulting from axial variations of blade height and hub radius.

In accordance with their relative importance, the first three features have been considered in greater details. In dealing with compressibility, special attention has been given to the transonic flows.

(3) An experimental investigation of a subsonic flow through an impulse cascade has been carried out. It has demonstrated the effectiveness of small flaps, attached to the trailing-edges of the blades. The collected experimental data, e.g. blade-surface pressures, for various flap settings, have also been used in the validation of the prediction procedure.

(4) Finally, the prediction procedure has been successfully applied to a number of problems which covered a good variety of geometry and flow conditions. The predicted surface-pressure distributions have generally shown close agreement with the available experimental or analytical data. Other predictions, e.g. streamlines, Mach-number contours, etc., have also exhibited plausible trends. The computer time requirements were very modest too. Thus, it can be concluded that the prediction procedure is widely applicable, accurate and economical.

9.2 Suggestions for future work

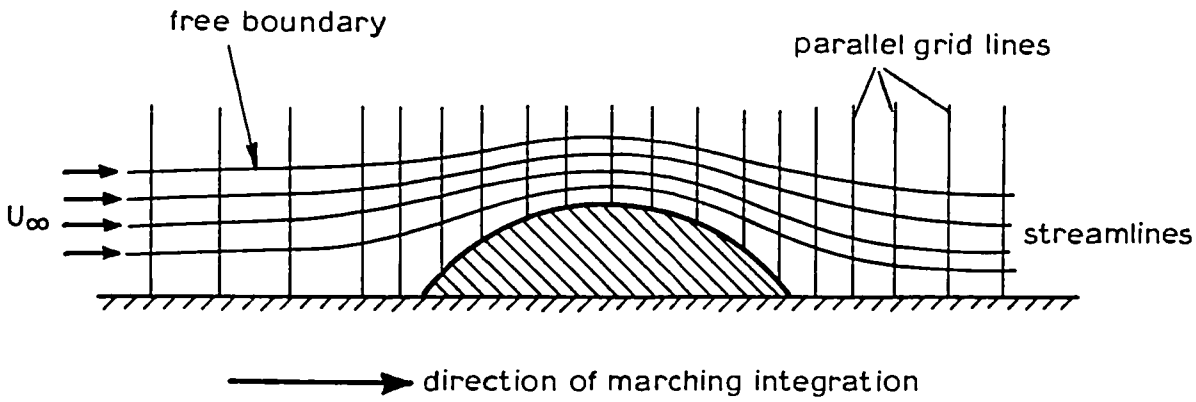
The basic solution scheme of the present procedure has a lot more potential than what has been stated or demonstrated so far. In this section, a few suggestions are made for future work which will further improve the capabilities and applications of the procedure.

(1) Treatment of viscous effects can be greatly improved by carrying out, at the end of each integration sweep, the boundary-layer type calculations for the near-boundary stream tubes, by subdividing them into several thinner strips.

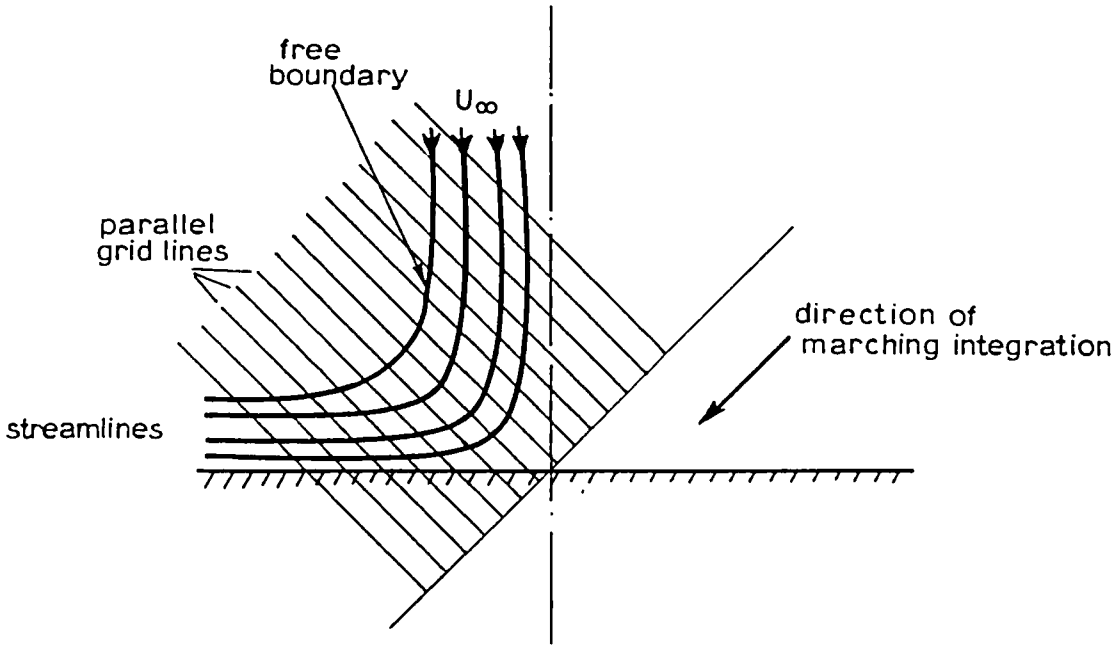
(2) Appropriate semi-empirical formulae should be developed for calculating the momentum deficits in the regions close to the trailing edges of the blades; the motives and approach can be the same as in the development of wall functions.

(3) By incorporating a suitable treatment for a free boundary, the procedure can make very economical predictions of free-surface flows such as: (i) flow over a hump, (ii) plane stagnation flow, etc.; basic details are shown in Fig. 9.1.

(4) A similar procedure can be developed for the through-flow analysis of axial turbomachines.



(a) Flow over a hump



(b) Plane stagnation flow

Fig. 9·1 Examples of free surface flows (with suggested grid arrangements)

REFERENCES

1) BINDON, J.P. & CARMICHAEL, A.D. (1971)
"Streamline curvature analysis of compressible and high Mach number cascade flows." J. Mech. Eng. Sci. Vol. 13, No. 5, pp. 344-357

2) BRYCE, J.D. & LITCHFIELD (1976)
"Experience of the Denton blade-to-blade time marching computer program." ARC 26909, Aero Th. 36

3) BRYER, D.W. & PANKHURST, R.C. (1971)
"Pressure-probe methods for determining wind speed and flow direction." H.M.S.O., London

4) DENTON, J.D. (1975)
"A time marching method for two- and three-dimensional blade to blade flows." ARC R. & M. 3775

5) DELANEY, R.A. & KAVANAGH, P. (1976)
"Transonic flow analysis in axial-flow turbomachinery cascades by a time-dependent method of characteristics." J. Eng. Power, Trans. ASME July 1976, pp. 356-364

6) EAST, L.F. (1975)
"Computation of three-dimensional turbulent boundary layers." EUROMECH 60, Trondheim, 14-16 April 1975, Report FFA TN AE-1211

6a) FEDIAEVSKY (1936)

Rep. Cent. Aerohyd. Inst. Moscow 282, Translated as "Turbulent boundary layer on an aerofoil." NACA TM 822

7) FOSTER, V.T. (1964)

"Turbine-blading development using a transonic variable-density cascade wind tunnel." Proceedings of the Institution of Mechanical Engineers, 1964-65 Vol. 179, Part 1 No. 6

8) GARABEDIAN, P.R. & KORN, D.G. (1971)

"Numerical design of transonic airfoils." Numerical Solution of Partial Differential Equations, Vol. II, pp. 253-269, Academic Press, New York

9) GOPALAKRISHNAN, S. & BOZZOLA, R. (1971)

"A numerical technique for the calculation of transonic flows in turbomachinery." ASME paper 71-GT-42

10) GOSTELOW, J.P. (1973)

"Review of compressible flow theories for airfoil cascade." ASME, J. Eng. Power, Oct. 1973

11) GOSTELOW, J.P. & SMITH, D.J.L. (1973)

"Test cases for turbomachinery flow field computations." CUED/A TURBO/TR 48, June 1973, University Engg. Dept., Cambridge

12) GRIEPENTROG, H. (1970)
"Transonic compressor cascades." AGARD Lect. Ser. No. 39, Advanced Compressors

13) GUDERLEY, K.G. (1972)
"The theory of transonic flow." International monographs in aeronautics and astronautics , Pergamon Press

14) HALL, W.S. & THWAITES, B. (1963)
"On the calculation of cascade flows." ARC CP 806

15) HARLOW, F.H. (1973)
"Turbulence transport modelling." AIAA Selected Reprint Series, Vol. XIV, AIAA New York

16) HARLOW, F.H. & WELCH, J.E. (1965)
"Numerical calculation of time-dependent viscous incompressible flow of fluid with free surface." Physics Fluids, Vol. 8, pp. 2182

17) HAWTHORNE, W.R. (1964)
"Aerodynamics of turbines and compressors." High Speed Aerodynamics and Jet Propulsion, Vol. X
Book: Oxford University Press, London

18) HIETT, G.F. & JOHNSTON, I.H. (1964)
"Experiments concerning the aerodynamic performance of inward flow radial turbines." Proc. Instn. Mech. Engrs. 1963-64, Vol. 178 C Pt. 3I(ii), 28

19) HIETT, G.F. & POWELL, G.E. (1962)
"Three dimensional probe for investigation of flow patterns." The Engineer. Technical Contribution Section, Jan. 26, 1962

20) HOWELL, A.R. (1948)
"A theory of arbitrary aerofoils in cascade", Phil. Mag. 7

21) HOBSON, D. (1974)
"Shock-free transonic flow in turbomachinery cascades." Ph.D. Thesis, Cambridge University, UK

22) HORLOCK, J.H. (1973a)
"Axial flow compressors; Fluid Mechanics and Thermodynamics."
Book: Robert Krieger Publishing Co., Huntington, New York

23) HORLOCK, J.H. (1973b)

"Axial flow turbines; Fluid Mechanics and Thermodynamics." Book: Robert E. Krieger Publishing Co., Huntington, New York

24) HUFFMAN, G.D.; McCLURE, R.B.; HOLTMAN, R.L. & SINNET, G.T. (1971)

"Results of a two-dimensional turbine cascade (AACEII) test." Detroit Diesel Allison Division, General Motors Corp., Indianapolis, Ind. Res. Note 71-47, July 1971

25) JOHNSTON, I.H. & SMART, D.E. (1967)

"An experiment in turbine blade profile design." British Aeronautical Research Council, C.P. 941

26) KATSANIS, T. (1968)

"A computer program for calculating velocities and streamlines on a blade-to-blade stream surface of a turbomachine." N.A.S.A. TN D-4525

27) KATSANIS, T. (1969)

"Fortran program for calculating transonic velocities on a blade-to-blade stream surface of a turbomachine." N.A.S.A. TN D-5427

28) KURZROCK, J.W. & NOVICK, A.S. (1975)
"Transonic flow around rotor blade elements." Journal of Fluid Engineering, Trans. ASME, Series I, Vol. 97, p. 598

29) LAUNDER, B.E. & SPALDING, D.B. (1972)
"Mathematical models of turbulence."
Book: Academic Press

30) LITCHFIELD, M.R. (1976)
Private communications

31) LIEPMANN, H.W. & ROSHKO, A. (1966)
"Elements of gas dynamics."
Book: John Willey Inc.

32) MACCORMACK, R.W. (1969)
"The effect of viscosity in Hyper Velocity Impact Catering." AIAA Paper 69-354, Cincinnati, Ohio

33) MARTENSEN, E. (1959)
"Calculation of pressure distributions over profiles in cascade in two-dimensional potential flow by means of Fredholm integral equation." Archs. ration. Mech. Analysis, 3, (No. 3)

34) McDONALD, P.W. (1971)
"The computation of transonic flow through two-dimensional gas-turbine cascades." ASME Paper 71-GT-89

35) MELLING, D.V. (1977)
"Three-dimensional turbulent flow past rectangular bluff bodies." Ph.D. Thesis, London University

36) MILNE-THOMPSON, L.M. (1962)
"Theoretical Hydrodynamics."
Book: 4th Edition, McMillan & Co.

37) MOORE, F.K. (1964)
"Theory of laminar flows." High Speed Aerodynamics and Jet Propulsion Vol. IV, Princeton University Press

38) MONSARRAT, N.T.; KENNAN, M.J. & TRAMM, P.C. (1969)
"Design report, single-stage evaluation of highly-loaded high-Mach-number compressor stages." N.A.S.A. CR-72562 (Pratt and Whitney Aircraft Division, PWA-3546)

39) NG, K.E.; PATANKAR, S.V. & SPALDING, D.B. (1969)
"The hydrodynamic turbulent boundary layer on a smooth wall, calculated by a finite-difference method." Computation of Turbulent Boundary Layers 1968, AFOSR-IFP-Standford Conference, 1969, p. 356

40) PATANKAR, S.V. & SINGHAL, A.K. (1972)
"Prediction of flow and heat transfer in turbulent cylindrical wall jets." Int. J. Heat & Mass Transfer, Vol. 15, February 1972

41) PATANKAR, S.V. & SPALDING, D.B. (1967)
"A finite-difference procedure for solving the equations of the two-dimensional boundary layer." Int. J. Heat & Mass Transfer, Vol. 10, pp. 1389, 1421

42) PATANKAR, S.V. & SPALDING, D.B. (1970)
"Heat and mass transfer in boundary layers." Book, 2nd edition, Intertext Books, London

43) PATANKAR, S.V. & SPALDING, D.B. (1972)
"A calculation procedure for heat, mass and momentum transfer in three-dimensional parabolic flows." Int. J. Heat & Mass Transfer, Vol. 15, pp. 1787-1806

44) PRATAP, V.S. (1975)
"Flow and heat transfer in curved ducts." Ph.D. Thesis, London University

45) PRATAP, V.S. & SPALDING, D.B. (1975)
"Numerical computations of flow in curved ducts." Aeronautical Quarterly, August 1975

46) PRATAP, V.S. & SPALDING, D.B. (1976)
"Fluid flow and heat transfer in three-dimensional duct flows." Int. J. Heat & Mass Transfer, Vol. 19, Oct. 1976

47) REYNOLDS, A.J. (1971)
"Thermofluid Dynamics."
Book: Willey-Interscience Publication

48) SCHLICHTING, H. (1955)
"Calculation of the frictionless incompressible flow for a given two-dimensional cascade." VDI Forsch. No. 447

49) SILVESTER, M.E. & FITCH, C.M. (1970)
"Matrix methods for the design of cascades to prescribed surface velocity distributions and for fully compressible flow." Fluid Mechanics, Acoustics and Design of Turbomachinery, Part I. Edited by B. Lakshminarayana et al. N.A.S.A., 1974

50) SINGHAL, A.K. & SPALDING, D.B. (1975)
"Predictions of two-dimensional boundary layers with the aid of k-ε model of turbulence." Imperial College Mech. Engg. Dept. Report No. HTS/75/15

51) SINGHAL, A.K. & SPALDING, D.B. (1976a)
"A two-dimensional partially-parabolic procedure for axial flow turbomachinery cascades." ARC 37016 Ae.Th 48

52) SINGHAL, A.K. & SPALDING, D.B. (1976b)
"Computation of simultaneous fluid flow and heat transfer in turbine cascades." ARC 37018 Ae.Th 50

53) SINGHAL, A.K. & SPALDING, D.B. (1977)
"Computations of transonic flows in Nozzle-Guide-Vane (NGV) cascades." Imperial College, Mech. Engg. Dept. Report No. HTS/77/6

54) SMITH, D.J.L. & FROST, D.H. (1970)
"Calculation of the flow past turbomachine blade." Proceedings of the Inst. of Mech. Engrs. Vol. 184, Part 3G(II), 1969-70

55) SPALDING, D.B. (1971)
Unpublished notes at Imperial College, London, Mechanical Engineering Department

56) SPALDING, D.B. (1975)
"GENMIX: A general computer program for two-dimensional parabolic phenomena." Imperial College, Mech. Engg. Dept. Report No. HTS/75/17

57) SPALDING, D.B. (1976)
Unpublished notes at Imperial College, London, Mechanical Engineering Department

58) SPALDING, D.B. (1977)
Private communications

59) SULAM, D.H.; KENNAN, M.J. & FLYNN, J.T. (1970)
"Single stage evaluation of highly-loaded high-Mach-number compressor stages." Vol. 11: Date and Performance, Multiple Circular-Arc Rotor. N.A.S.A. CR-72694 (Pratt and Whitney Aircraft Division, PWA-3772)

60) VAN DEN BERG, B. (1973)
"The law of the wall in two- and three-dimensional turbulent boundary layers." National Aerospace Laboratory, NLR the Netherlands NLR TR 72111U

61) VKI LECTURE SERIES 59 (1973)
"Transonic flows in axial turbomachinery." Von Karman Institute for Fluid Dynamics, Belgium

62) VKI LECTURE SERIES 84 (1976)
"Transonic flows in axial turbomachinery." Vol. I and Vol. II, Von Karman Institute for Fluid Dynamics, Belgium

63) WHITNEY, W.T.; SZANCA, E.M.; MOFFIT, T.P. & MONROE, D.E. (1967)

"Cold air investigation of a turbine for high temperature engine application: turbine design and overall stator performance." N.A.S.A. TN D-3751

64) WILKINSON, D.H. (1967)

"A numerical solution of the analysis and design problems for flow past one or more aerofoils or cascades. Part I - Analysis problem; Part II - Design problem." ARC R & M 3545

65) WILKINSON, D.H. (1970)

"Calculation of blade-to-blade flow in a turbomachine by streamline curvature." ARC R & M 3704

66) WU, C.H. (1951)

"General theory of fluid flow with subsonic or supersonic velocity in turbomachines of arbitrary hub and casing shapes." N.A.C.A. TN 2302

67) WU, C.H. (1953)

"Discussion of 'A practical solution of a three-dimensional flow problem of axial-flow turbomachinery'." Trans. ASME, Vol. 75, July 1953, pp. 802-803

NOMENCLATURE

Symbol	Meaning	Equations of first mention
A,B	coefficients in finite-difference equation	3.14
C_p	specific heat	4.7
C	coefficient in finite-difference equation	4.8
E	constant in logarithmic law of wall	4.6
$\tilde{h}$	stagnation enthalpy	4.7
i	index denoting streamline number	
j	index denoting constant-x section	
J	diffusion flux of heat	E.1
k	turbulence kinetic energy	
K	constant in mixing length distribution and also in logarithmic law of wall	4.4
l	mixing length	4.3
M	mach number	
M*	critical Mach number($^u/u^*$)	
n	distance normal to streamline	3.13
p	pressure	3.1
r	radial distance	4.10
s	distance along streamline	B.1

Symbol	Meaning	Equations of first mention
S	Stanton number	4.9
t	thickness of stream sheet	4.10
u	streamwise velocity or total velocity	3.1
u*	critical (or sonic) velocity	
v	y-direction component of velocity	3.2
w_r, w_θ, w_z	the three velocity components in cylindrical polar coordinates	F.1
x	direction normal to y, e.g. direction of axis of turbomachine or direction of mean stream surface in the meridional plane	3.2,4.10
y	circumferential direction	
z	coordinate in the cylindrical polar coordinate system	F.2

Greek symbols

α	local streamline inclination with reference to the x-direction	3.3
β	angle between x- and z-directions	4.10
β	reduction factor	G.1
γ	ratio of specific heats	3.4
δ	a constant taking the value of 0 or 1 according to local Mach number	C.35
ε	kinematic-compatibility error	3.16
ε	dissipation rate of turbulence	
λ	mixing-length constant	4.4

Symbol	Meaning	Equations of first mention
μ	viscosity	3.13
ρ	density	3.4
σ	Prandtl number	4.9
τ	shear stress	3.13
θ	coordinate in cylindrical polar coordinate system	F.2
ψ	stream function	3.2
Ψ	shape factor	3.10
Ω	angular velocity	4.13

Subscripts

ad	adiabatic	4.9
avg.	average	F.12
C	a point close to the solid surface	4.6
E,W,N,S	refer to grid nodes located in East, West, North and South directions respectively	3.5
e,w,n,s	refer to mid-node locations in the east, west, north and south directions respectively	3.5
eff	effective	4.1
i	i'th streamline location in grid	3.14
j	j'th axial-section in grid	
P	a typical grid node	3.5

Symbol	Meaning	Equations of first mention
S	solid surface	4.6
t	turbulent	4.2
U	upstream	
z,γ,θ	coordinates	
1,2,3,4	refer to control volume of 3.2	3.1
O	refers to the stagnation condition	3.4

Superscripts

'	denotes correction component	3.15
*	denotes approximate value	3.16
*	denotes critical (or sonic) condition	6.4

APPENDIX A

EQUATIONS OF MOTION IN THE NONORTHOGONAL COORDINATE SYSTEM

In this appendix, two momentum-conservation equations - one for streamwise direction and the other for y-direction, are derived by considering the balances of momentum fluxes and forces, acting on the control volume of Fig. 3.2.

Before writing the algebraic expressions, the following points should be noted:

(i) In the control volume, shown in Fig. 3.2, the top and bottom faces (4 and 3) are stream surfaces and the vertical faces (1 and 2) are constant-x planes. Each face is assumed to have a unit thickness, i.e. a plane flow is considered.

(ii) Convection fluxes of mass and momentum across faces 3 and 4 are zero, by definition of a stream surface.

(iii) In a steady state, mass influx through face 1 equals to the mass efflux through face 2. In terms of the notations shown in the diagram, the mass flux is equal to $\Delta\psi$.

(iv) Velocity u_1 is the streamwise (total) velocity at the centre of face 1. It is assumed that this value also represents the average u-velocity over the whole face 1. Similar assumptions are implied for all other flow-variables marked on the control volume.

(v) In an inviscid flow there are no viscous forces (or diffusion of momentum).

(vi) If the body forces are also assumed to be absent, then, only the pressure forces are to be considered.

Thus, for a plane inviscid flow, the two momentum-conservation equations can be written as:

streamwise momentum-conservation equation:

$$\Delta\psi(u_2 - u_1) = (p_1 - p_2).\Delta y.\text{Cos}\ \alpha \quad ; \quad (A.1)$$

y-direction momentum-conservation equation:

$$\Delta\psi(v_2 - v_1) = (p_3 - p_4).\Delta x \quad . \quad (A.2)$$

These equations are valid for both incompressible and compressible flows. Equation (A.2) has no restriction on curvature of flow. Also, it is a linear equation for v because all other variables are independent of v. On the other hand, Equation (A.1) is valid only for the small curvature and it is nonlinear too; Δy and α are auxiliary quantities which are calculated from velocities as explained in Section 3.4.3. This nonlinearity is of the same kind as that in the standard differential equation (for the momentum-conservation along a streamline):

$$\rho u \frac{\partial u}{\partial s} = - \frac{\partial p}{\partial s} \quad , \quad (A.3)$$

where s is distance along the streamline. However, Equation (A.3) is free from the restriction of small curvature. Equation (A.3) can be integrated along s, to relate flow properties at points 1 and 2 in Fig. 3.2, as follows:

for an incompressible flow (constant ρ):

$$u_2^2 - u_1^2 = 2.\frac{(p_1 - p_2)}{\rho} \quad ; \quad (A.4)$$

for a compressible isentropic flow ($\rho \alpha p^{1/\gamma}$)

$$u_2^2 - u_1^2 = \frac{2\gamma}{\gamma-1} \cdot \left(\frac{p_1}{\rho_1} - \frac{p_2}{2}\right) \quad . \quad (A.5)$$

Equation (A.4) can also be obtained from Equation (A.1) by using the continuity relationship (at the mid-section of control volume):

$$\Delta\psi = \rho u \Delta y \mathrm{Cos}\alpha \quad , \quad (A.6)$$

and by assuming that $u = \frac{u_1 + u_2}{2}$.

In Equation (A.5), density variation along the streamline has been accounted for in a general manner so that it is valid at low as well as high Mach numbers; it may be pointed out that at high Mach numbers density variations become very important and the approximations like use of average density become unsatisfactory. Equation (A.4) can be considered as a particular case ($\gamma=\infty$) of Equation (A.5). These equations (A.4 and A.5) can also be regarded as the "total energy" equations (Liepmann and Roshko, 1966); however their main function is to relate the streamwise velocity, u, to the pressure.

APPENDIX B

THE MOMENTUM-CONSERVATION EQUATIONS FOR VISCOUS FLOW

For an inviscid flow, two momentum-conservation equations have been derived in Appendix A. In this appendix, these equations are modified for a viscous flow as explained in Section 3.4.2.

By applying the second law of motion to the control volume of Fig. 3.10, the two equations can be written as:

streamwise momentum-conservation equation:

$$\Delta\psi(u_2 - u_1) = (p_1 - p_2).\Delta y \ \mathrm{Cos}\ \alpha + (\tau_4 - \tau_3).\Delta s \quad ; \quad (B.1)$$

y-direction momentum-conservation equation:

$$\Delta\psi(v_2 - v_1) = (p_3 - p_4).\Delta x + (\tau_4 - \tau_3).\Delta s.\sin^2\alpha \quad . \quad (B.2)$$

The shear stresses, τ's, can be expressed, by using Equation (3.13), as follows:

$$\tau_4 \equiv \left(\mu \frac{\partial u}{\partial n}\right)_4 \quad ;$$

$$\tau_3 \equiv \left(\mu \frac{\partial u}{\partial n}\right)_3 \quad ,$$

where n is the distance normal to the streamline.

Since in the adopted coordinate system, the cross-stream direction (y) is not normal to streamlines, $\frac{\partial u}{\partial n}$ can be calculated only by an elaborate interpolation practice.

However, this practice is not very desirable because it is approximate, expensive in computation and it requires full storage of variables u, y and α. For these reasons, an approximation is made according to which the x-direction component of the momentum diffusion is neglected and only the y-component is accounted for. This is also consistent with the neglect of shear forces on the vertical faces of the control volume. Thus, Equations (B.1) and (B.2) reduce to the following forms:

$$\Delta\psi(u_2 - u_1) = (p_1 - p_2).\Delta y.\text{Cos}\ \alpha + \left\{\left(\mu \frac{\partial u}{\partial y}\right)_4 - \left(\mu \frac{\partial u}{\partial y}\right)_3\right\}.\Delta x \quad ; \quad \text{(B.3)}$$

$$\Delta\psi(v_2 - v_1) = (p_3 - p_4).\Delta x \quad . \quad \text{(B.4)}$$

Equation (B.4) is same as Equation (A.2). In the pressure term of Equation (B.3), the presence of Δy Cos α is undesirable for the reasons already explained in Appendix A, in connection of Equations (A.1) and (A.5). To overcome this difficulty a new form of u-momentum equation is obtained by assuming:

$$u = u^* + u' \quad , \quad \text{(B.5)}$$

where u^* represents the approximate value of u-velocity, obtained by solving the inviscid-flow equation (A.5); and u' denotes the correction component due to the presence of viscous forces. This approach has been suggested by

Spalding (1977); the required algebraic transformations are explained below.

First, Equation (B.3) is rewritten, by using Equations (A.1), (A.5) and (B.5), as follows:

$$u_2^2 = u_2^{*2} + \frac{2.\Delta x}{\rho.\Delta y.\text{Cos }\alpha}\left\{\left(\mu\frac{\partial u}{\partial y}\right)_4 - \left(\mu\frac{\partial u}{\partial y}\right)_3\right\} \quad , \quad \text{(B.6)}$$

where $u_2^{*2} \equiv u_1^2 + \frac{2\gamma}{\gamma-1}\cdot\frac{p_1}{\rho_1}\left\{1 - \left(\frac{p_2}{p_1}\right)^{1/\gamma}\right\}$.

Next, it is transformed for a control volume shown in Fig. 3.11, because the u-velocity is to be calculated at a mid-node location, as explained in Sections 3.4.1 and 3.4.2. The The transformed equation is:

$$u_i^2 = u_i^{*2} + \frac{2.\Delta x}{\rho.\Delta y.\text{Cos }\alpha}\cdot\left\{\left(\mu\frac{\partial u}{\partial y}\right)_{i+\frac{1}{2}} - \left(\mu\frac{\partial u}{\partial y}\right)_{i-\frac{1}{2}}\right\} \quad . \quad \text{(B.7)}$$

Here u_i^{*2} can be calculated as explained above for u_2^{*2}. Now in this equation by expressing $(\frac{\partial u}{\partial y})$'s in their finite-difference forms, we get:

$$u_i^2 = u_i^{*2} + \frac{2.\Delta x}{\rho.\Delta y.\text{Cos }\alpha}\cdot\left\{\mu_{i+\frac{1}{2}}\frac{u_{i+1} - u_i}{y_{i+1} - y_i} - \mu_{i-\frac{1}{2}}\cdot\frac{u_i - u_{i-1}}{y_i - y_{i-1}}\right\}$$

. (B.8)

On the other hand, a relation for u_i^2 is obtained by squaring both the sides of equation (B.5) and neglecting the u'^2 term; it is:

$$u_i^2 = u_i^{*2} + 2u_i^*u' \quad \text{(B.9)}$$

By comparing Equations (B.8) and (B.9) we get:

$$u_i^* u_i' = A(u_{i+1} - u_i) - B(u_i - u_{i-1}) \quad , \quad \text{(B.10)}$$

where $A \equiv \frac{\Delta x}{\rho . \Delta y . \text{Cos } \alpha} \cdot \frac{\mu_{i+\frac{1}{2}}}{y_{i+1} - y_i}$;

$$B \equiv \frac{\Delta x}{\rho . \Delta y . \text{Cos } \alpha} \cdot \frac{\mu_{1-\frac{1}{2}}}{y_i - y_{i-1}} \quad .$$

Finally, the substitution of $u_i' = u_i - u_i^*$ and re-arrangement of terms in Equation (B.10), yields:

$$(u_i^* + A_i + B_i).u_i = A_i u_{i+1} + B_i u_{i-1} + u_i^{*2} \quad . \quad \text{(B.11)}$$

Equation (B.11) is the desired form of u-momentum equation.

APPENDIX C

THE PRESSURE-CORRECTION EQUATION

The role of pressure correction equation has been explained in Section 3.4.6. In this appendix, its full derivation is presented.

As already mentioned in Section 3.3, the basis of pressure-correction equation is the requirement of kinematic compatibility of flow. For a control volume shown in Fig. 3.9, it can be expressed as:

$$\Delta y_e - \Delta y_w = \Delta x.(\tan\alpha_n - \tan\alpha_s) \quad . \quad (C.1)$$

This condition can be satisfied only if the pressure field is correct. The reason is that Δy's and α's are calculated from densities and velocities which themselves depend on the pressure field. Suppose that the pressure and velocities are expressed as:

$$p = p^* + p' \quad ; \quad (C.2)$$

$$u = u^* + u' \quad ; \quad (C.3)$$

$$v = v^* + v' \quad ; \quad (C.4)$$

where the primed quantities represent the corrections to the approximate (starred) values. Similarly, other flow variables, viz. ρ, α, Δy, etc. can be represented by two components.

Now for an approximate flow field, Equation (C.1) can be written as:

$$(\Delta y)_e^* - (\Delta y)_w^* = \Delta x. \left[(\tan \alpha_n)^* - (\tan \alpha_n)^* \right] + \varepsilon_p \quad , \quad (C.5)$$

where ε_p represents kinematic-compatibility error in the region surrounding grid node P; (ε_p is also defined in Section 3.4.6). By subtracting Equation (C.5) from Equation (C.1), we get:

$$(\Delta y)'_e - (\Delta y)'_w = \Delta x. \left[(\tan \alpha_n)' - (\tan \alpha_s)' \right] - \varepsilon_p \quad . \quad (C.6)$$

In this equation if the correction components are expressed, first, in terms of ρ', u', v' and then, in terms of pressure corrections; the final equation will be the desired pressure-correction equation. The remainder of this appendix describes the necessary algebra.

Expressions for $(\Delta y)'_e$ and $(\Delta y)'_w$

The continuity condition implies that:

$$(\Delta y)_e \equiv \left[\frac{\Delta \psi}{\rho u \cos \alpha} \right]_e \quad , \quad (C.7)$$

By taking, first, logarithm of both sides; and, then, total derivative of each term, we get:

$$\frac{d(\Delta y)_e}{(\Delta y)_e} = - \left[\frac{d(\rho_e)}{\rho_e} + \frac{d(u_e)}{u_e} + \frac{d(\cos \alpha_e)}{\cos \alpha_e} \right] \quad . \quad (C.8)$$

Or,
$$\frac{(\Delta y)'_e}{(\Delta y)_e} = - \left[\frac{\rho'_e}{\rho_e} + \frac{u'_e}{u_e} + \frac{(\cos \alpha_e)'}{\cos \alpha_e} \right] \quad . \quad (C.9)$$

In view of the convective-velocity practice (Equation 3.12), the above equation is rearranged as:

$$\frac{(\Delta y)'_e}{(\Delta y)_e} = - \left[\frac{(\rho u)'_e}{(\rho u)_e} + \frac{(\text{Cos } \alpha_e)'}{\text{Cos } \alpha_e} \right] \quad . \quad (C.10)$$

Let us now express (Cos α)' in terms of velocity corrections. First, Cos α_e is written as follows:

$$\text{Cos } \alpha_e \equiv \left[\frac{\sqrt{u^2 - v^2}}{u} \right]_e \quad . \quad (C.11)$$

It may be noted that Cos α is treated as a function of u and v. Therefore, total derivative of Cos α can be written as:

$$(\text{Cos } \alpha_e)' = \frac{\partial(\text{Cos } \alpha_e)}{\partial u_e} \cdot u'_e + \frac{\partial(\text{Cos } \alpha_e)}{\partial v_e} \cdot v'_e \quad . \quad (C.12)$$

Now v'_e is assumed to be zero, because v_e is not affected by the pressure corrections of grid nodes P and E which are ultimately responsible for $(\Delta y)'_e$. It may be reminded here that u and v are two separate variables and that u is affected by $\frac{\partial p}{\partial s}$ while v is affected by $\partial p / \partial y$. Thus, Equation (C.12) reduces to:

$$(\text{Cos } \alpha_e)' = \frac{\partial(\text{Cos } \alpha_e)}{\partial u_e} \cdot u'_e \quad . \quad (C.13)$$

By substituting Equation (C.11) into Equation (C.13) and carrying out the differentiation, we get:

$$(\text{Cos } \alpha_e)' = \left[\frac{v^2}{u^2} \cdot \frac{1}{\sqrt{u^2 - v^2}} \right]_e \cdot u'_e \quad (C.14)$$

$$\text{Or,} \quad (\text{Cos } \alpha_e)' = \left[\sin^2\alpha \frac{u}{\sqrt{u^2 - v^2}} \right]_e \cdot \frac{u'_e}{u_e} \qquad . \text{ (C.15)}$$

$$\text{Or,} \quad \frac{(\text{Cos } \alpha_e)'}{\text{Cos } \alpha_e} = \tan^2\alpha_e \cdot \frac{u'_e}{u_e} \qquad . \text{ (C.16)}$$

Substitution of Equation (C.16) into Equation (C.10) yields:

$$(\Delta y)'_e = - \Delta y_e \cdot \left[\frac{(\rho u)'_e}{(\rho u)_e} + \tan^2\alpha_e \cdot \frac{u'_e}{u_e} \right] \qquad . \text{ (C.17)}$$

Similarly, $(\Delta y)'_w$ can be written as:

$$(\Delta y)'_w = - \Delta y_w \cdot \left[\frac{(\rho u)'_w}{(\rho u)_w} + \tan^2\alpha_w \cdot \frac{u'_w}{u_w} \right] \qquad . \text{ (C.18)}$$

Expressions for $(\tan \alpha_n)'$ and $(\tan \alpha_s)'$

First, $\tan \alpha_n$ and $(\tan \alpha_n)'$ are written as follows:

$$\tan \alpha_n = \frac{v_n}{\sqrt{u_n^2 - v_n^2}} \qquad . \text{ (C.19)}$$

$$(\tan \alpha_n)' = \frac{\partial(\tan \alpha_n)}{\partial u_n} \cdot u'_n + \frac{\partial(\tan \alpha_n)}{\partial v_n} \cdot v'_n \qquad . \text{ (C.20)}$$

Next, u'_n is assumed to be zero for the same reason as explained in connection with $v'_e = 0$ in Equation (C.12). After completing the algebraic details of evaluating $\frac{\partial(\tan \alpha_n)}{\partial u_n}$, we get:

$$(\tan \alpha_n)' = \frac{1}{\sqrt{u_n^2 - v_n^2}} \cdot \frac{u_n^2}{(u_n^2 - v_n^2)} \cdot v'_n \qquad . \text{ (C.21)}$$

Similarly, $(\tan \alpha_s)'$ can be written as:

$$\boxed{(\tan \alpha_s)' = \frac{1}{\sqrt{u_s^2 - v_s^2}} \cdot \frac{u_s^2}{(u_s^2 - v_s^2)} \cdot v_s'} \quad . \text{(C.22)}$$

Expressions for ρ', u', v' in terms of p'

In this section ρ', u and v''s, appearing in Equations (C.17), (C.18), (C.21) and (C.22), are related to appropriate p''s. These relationships are obtained by differentiating the relevant equations, viz. equation of state and u- and v-momentum equations. For convenience, $v' \sim p'$ is considered first.

Equation (3.6) can be regarded as $v_n = f\{p_P, p_N\}$, and by differentiating it we get:

$$v_n' = \frac{\partial v_n}{\partial p_P} \cdot p_P' + \frac{\partial v_n}{\partial p_N} \cdot p_N' \quad . \text{(C.23)}$$

Or, $$\boxed{v_n' = \frac{\Delta x}{(\Delta \psi)_n} \cdot (p_P' - p_N')} \quad . \text{(C.24)}$$

Similarly, $$\boxed{v_s' = \frac{\Delta x}{(\Delta \psi)_s} \cdot (p_S' - p_P')} \quad . \text{(C.25)}$$

A similar procedure is used for obtaining $u' \sim p'$ relations. Instead of Equation (3.5), an equation similar to (A.1) can be used to simplify the differentiation details. The resultant expression for u_e' is:

$$u'_e = \frac{1}{(\rho u)_e} \cdot (p'_P - p'_E) \quad . \quad (C.26)$$

Similarly from an equation for u_w, we get:

$$u'_w = \frac{1}{(\rho u)_w} \cdot (p'_W - p'_P) \quad . \quad (C.27)$$

Now we assume that $p'_E = 0$ and $p'_W = 0$. This assumption is necessitated by the fact that in a line-by-line solution procedure, local pressure corrections can not be calculated on the constant-x lines containing E and W at the time in computation at which p, N and S are being attended to. Thus, Equations (C.26) and (C.27) can be written as:

$$\boxed{u'_e = \frac{1}{(\rho u)_e} \cdot p'_P} \quad ; \quad (C.27)$$

$$\boxed{u'_w = -\frac{1}{(\rho u)_w} \cdot p'_P} \quad . \quad (C.28)$$

Next, let us evaluate $(\rho u)'_e$ and $(\rho u)'_w$ which also appear in Equations (C.17) and (C.18). Consider $(\rho u)'_e$ first. According to the above-mentioned assumption ($p'_E = 0$), $(\rho u)'_e$ can be expressed as:

$$(\rho u)'_e = \frac{(\rho u)_e}{\partial p_P} \cdot p'_P \quad (C.29)$$

In Section 3.4.4, $(\rho u)_e$ has been expressed in two different ways depending on whether the flow, at point e, is subsonic or supersonic. Both the cases are considered, one by one.

Subsonic flow

$$(\rho u)_e = \rho_E u_e \quad . \quad (C.30)$$

Therefore $(\rho u)'_e = \rho_E u'_e \quad . \quad (C.31)$

By substituting Equation (C.27) into Equation (C.31), we get:

$$(\rho u)'_e = \frac{\rho_E}{(\rho u)_e} \cdot p'_P \quad (C.32)$$

Supersonic flow

$$(\rho u)_e = \rho_P u_w \quad (C.33)$$

For differentiating it w.γ.t. p_P, the following two assumptions are made:

(a) $\rho_P \alpha p_P^{1/\gamma}$, i.e. isentropic flow;

(b) u_w is treated as a constant, because it is a substitute for u_e.

Therefore, the expression for $(\rho u)'_e$ is:

$$(\rho u)'_e = u_w \cdot \frac{\rho_p}{\gamma p_P} \cdot p'_P \quad . \quad (C.34)$$

Equations (C.32) and (C.34) can be generalized as follows:

$$\boxed{\frac{(\rho u)'_e}{(\rho u)_e} = \left[\frac{1}{\rho_p u_e^2} \cdot (1-\delta) + \frac{1}{\gamma p_P} \cdot \delta\right] \cdot p'_P} \quad ; \quad (C.35)$$

where $\delta = 0$ for Mach number (at point e) < 1.0

$\delta = 1$ for Mach number ≥ 1.0

Similarly, by repeating the above steps for $(\rho u)'_w$, we get:

$$\boxed{\frac{(\rho u)'_w}{(\rho u)_w} = -\frac{1}{\gamma p_P} \cdot (1-\delta) \cdot p'_P} \quad . \quad (C.36)$$

It may be noted that the expressions for $(\rho u)'_e$ and $(\rho u)'_w$ are not quite similar.

Final expressions for $(\Delta y)'$ and $(\tan \alpha)'$

By combining the boxed equations, we get:

$$(\Delta y)'_e = -A_E \, p'_P \quad ; \quad (C.37)$$

$$(\Delta y)'_w = A_W \, p'_P \quad ; \quad (C.38)$$

$$(\tan \alpha_n)' = A_N \, (p'_P - p'_N) \quad ; \quad (C.39)$$

$$(\tan \alpha_s)' = -A_S \, (p'_P - p'_S) \quad . \quad (C.40)$$

where the A coefficients are given by the following equations:

$$A_E = (\Delta y)_e \cdot \left[\frac{1}{\rho_P u_e^2} \cdot (1-\delta) + \frac{1}{\gamma p_P} \cdot \delta + \frac{\tan^2 \alpha_e}{\rho_P u_e^2} \right] \quad ; \quad (C.41)$$

$$A_W = (\Delta y)_w \cdot \left[\frac{1}{\gamma p_P} \cdot (1-\delta) + \frac{\tan^2 \alpha_w}{\rho_w u_w^2} \right] \quad ; \quad (C.42)$$

$$A_N = \frac{\Delta x}{(\Delta \psi)_n} \cdot \frac{u_n^2}{(u_n^2 - v_n^2)^{3/2}} \quad ; \quad (C.43)$$

$$A_S = \frac{\Delta x}{(\Delta\psi)_s} \cdot \frac{u_s^2}{(u_s^2 - v_s^2)^{3/2}} \quad . \quad (C.44)$$

Finally, by substituting Equations (C.37) to (C.40) into Equation (C.6) and by re-arranging the terms we get:

$$(A_N + A_S + A_E + A_W)\, p'_P = A_N p'_N + A_S p'_S + \varepsilon_p \quad . \quad (C.45)$$

This is the desired pressure-correction equation.

APPENDIX D

FORMULA FOR BLOCK CORRECTION OF PRESSURE

This appendix is supplementary to Section 3.4.7 and its main purpose is to derive an appropriate formula for the block correction of pressure.

First consider one grid cell, shown shaded in Fig. 3.11. Let $(\Delta y)'_i$ be the error in the calculated width of cell at the right hand plane $(j+\frac{1}{2})$. If the flow is subsonic, in the cell under consideration $(\Delta y)'_i$ can be related to the pressure correction of either or both of the adjacent grid nodes (i,j) and (i,j+1); but, if the flow is supersonic, $(\Delta y)'_i$ must be related to $p'_{i,j}$ only. In the present practice, for the sake of generality, $(\Delta y)'_i$ is first related to $p'_{i,j}$ as follows:

$$(\Delta y)'_i = - \Delta y_i \cdot \left[\frac{1}{\rho u^2} (1-\delta) + \frac{1}{\gamma p} \cdot \delta + \frac{\tan^2 \alpha}{\rho u^2} \right]_i \cdot p'_{i,j} \quad . \quad \text{(D.1)}$$

This equation is same as Equation (C.35), except for the changes in the notation of suffixes. By considering i = 2, 3 .....n; Equation (D.1) represents a set of equations for the grid cells associated with section j. Now if we assume that the pressure corrections at all grid nodes are equal; then, the above-said equations can be summed up and we get:

$$\bar{p}' = \frac{\sum (\Delta y)'_i}{\sum_i \left[\Delta y_i \cdot \left\{ \frac{1}{\rho u^2} (1-\delta) + \frac{1}{\gamma p} \cdot \delta + \frac{\tan^2 \alpha}{\rho u^2} \right\}_i \right]} \quad , \quad (D.2)$$

where $\bar{p}' = p'_{i,j}$ for all i's; and

$\sum (\Delta y)'_i$ = Actual width - calculated width, (of section $(j+\frac{1}{2})$).

In the symbol for block pressure-correction ($\bar{p}'$), superscript (-) has been introduced so as to distinguish it from the local pressure-correction symbol (p').

The use of block pressure-correction ($\bar{p}'$) is explained in Section 3.4.7.

APPENDIX E

CONSERVATION EQUATION FOR THE STAGNATION ENTHALPY

In this appendix, a conservation equation for the stagnation enthalpy ($\tilde{h}$) is derived by considering the energy balance for a control volume shown in Fig. E.1.

In terms of the notations shown in the diagram, the energy balance can be written as:

$$\Delta\psi(\tilde{h}_2 - \tilde{h}_1) = -(J_4 - J_3).\Delta s + (\tau_4.u_4 - \tau_3.u_3).\Delta s \quad . \qquad (E.1)$$

Efflux of $\tilde{h}$ by convection	Influx of heat by diffusion	Work done by shear forces (on the control volume)

Like in Equations (B.1) and (B.2), here also diffusion fluxes through the vertical faces have been neglected. The heat flux (J) can be connected with the temperature gradient $(\partial T/\partial n)$, by way of the Fourier's law of heat conduction, as follows:

$$J = -\lambda . \frac{\partial T}{\partial n} \quad , \qquad (E.2)$$

where λ is the thermal conductivity of the fluid. For a turbulent flow, the Fourier's law can be generalised as follows:

$$J = -\frac{\mu_{eff}}{\sigma_{h,eff}} . Cp \left(\frac{\partial T}{\partial n}\right) \quad , \qquad (E.3)$$

where $\sigma_{h,eff}$ is the "effective Prandtl number", and Cp is

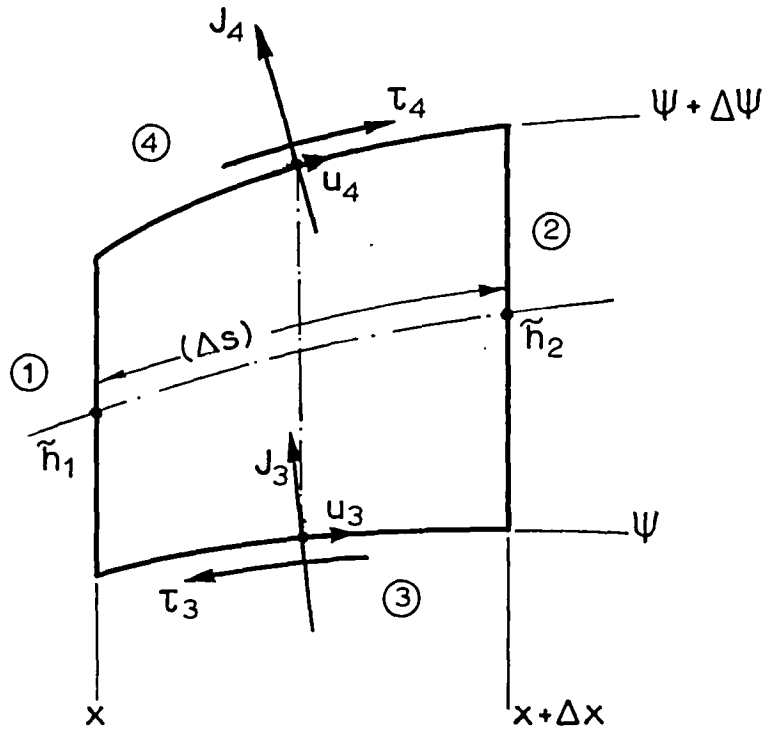


Fig. (E·1) Diagram illustrating the control volume and the notations for heat flux and shear stress, etc.

the constant-pressure specific heat of the fluid. $\mu_{eff}/\sigma_{h,eff}$ is also called the effective exchange coefficient of heat. Often, $\sigma_{h,eff}$ is a constant and is close to unity. Thus, the quantity $\mu_{eff}/\sigma_{h,eff}$ varies from point to point in the same manner as μ_{eff}.

Equation (E.3) can also be expressed in terms of $(\partial\tilde{h}/\partial n)$, by using the definition $\tilde{h} = CpT + u^2/2$ and by treating Cp as a constant, as follows:

$$J = -\frac{\mu_{eff}}{\sigma_{h,eff}} \cdot \left(\frac{\partial \tilde{h}}{\partial n} - \frac{\partial (u^2/2)}{\partial n}\right) \qquad . \quad (E.4)$$

Furthermore, substitution of Equations (3.13) and (E.4) into Equation (E.1) yields:

$$\Delta\psi(\tilde{h}_2 - \tilde{h}_1) = \left[\left\{\frac{\mu_{eff}}{\sigma_{h,eff}} \cdot \left(\frac{\partial \tilde{h}}{\partial n}\right)\right\}_4 - \left\{\frac{\mu_{eff}}{\sigma_{h,eff}} \cdot \frac{\partial \tilde{h}}{\partial n}\right\}_3\right] \cdot \Delta s$$

$$+ \left[\left\{\left(\mu_{eff} - \frac{\mu_{eff}}{\sigma_{h,eff}}\right) \cdot \frac{\partial (u^2/2)}{\partial n}\right\}_4 - \left\{\left(\mu_{eff} - \frac{\mu_{eff}}{\sigma_{h,eff}}\right) \cdot \frac{\partial (u^2/2)}{\partial n}\right\}_3\right] \cdot \Delta s$$

The quantity in the second [ ] parenthese on R.H.S. represents the "kinetic heating", i.e. the effect of viscous stresses on the enthalpy flux. It disappears when $\sigma_{h,eff} = 1$.

Equation (E.5) is further modified for: (a) the assumption of considering only y-direction diffusion fluxes, as explained in connection of Equation (B.3); (b) the

staggered-grid practice; and (c) the grid numbering notations on Fig. 3.11. The resultant equation can be written as follows:

$$(\Delta\psi_i + A_i + B_i).\tilde{h}_i = A_i\tilde{h}_{i+1} + B_i\tilde{h}_{i-1} + C_i \quad , \text{(E.6)}$$

wherein the coefficients are:

$$A_i = \left(\frac{\mu_{eff}}{\sigma_{h,eff}}\right)_{i+\frac{1}{2}} \cdot \frac{\Delta x}{y_{i+1} - y_i} \quad , \text{(E.7)}$$

$$B_i = \left(\frac{\mu_{eff}}{\sigma_{h,eff}}\right)_{i-\frac{1}{2}} \cdot \frac{\Delta x}{y_i - y_{i-1}} \quad , \text{(E.8)}$$

$$C_i = \Delta\psi_i.\tilde{h}_{i,U} \quad . \text{(E.9)}$$

In Equation (E.9), suffix U stands for the upstream value. It may be noted that the kinetic-heating term has been omitted; if desired, it can be included in the definition of C_i. Equation (E.6), supplemented with Equations (E.7) to (E.9), is the final equation for conservation of stagnation enthalpy.

APPENDIX F

THE CIRCUMFERENTIAL-DIRECTION MOMENTUM-CONSERVATION EQUATION FOR A VARIABLE STREAM ANNULUS

As mentioned in Section 4.5, this appendix presents a derivation of the circumferential-direction momentum-conservation equation. Because of the curvature of mean stream-surface, see line AB in Fig. 4.2, the control volume analysis is not very straightforward. Therefore, this equation is derived by carrying out the necessary transformations of the corresponding differential equation available in the cylindrical polar coordinate (z,r,θ) system; e.g. from Hawthorne (1964, p. 491). The relevant differential equation is:

$$\frac{W_\theta}{r} \cdot \frac{\partial W_\theta}{\partial \theta} + W_z \cdot \frac{\partial W_\theta}{\partial z} + \frac{W_r W_\theta}{r} = - \frac{1}{\rho} \frac{\partial p}{r \partial \theta} \quad , \quad (F.1)$$

where W_θ, W_z and W_r represent the velocity components in the coordinate directions. This equation can be transformed from (z,θ) coordinates to (x,θ) coordinate system by using the following chain-differentiation rule:

$$\frac{\partial}{\partial z} = \frac{\partial}{\partial x} \cdot \frac{\partial x}{\partial z} \quad ; \quad (F.2)$$

Or,
$$\frac{\partial}{\partial z} = \frac{1}{\text{Cos } \beta} \cdot \frac{\partial}{\partial x} \quad . \quad (F.3)$$

where is the angle between x and z directions, as shown in Fig. 4.2. Substitution of Equation (F.3) into Equation (F.1), yields:

$$\frac{W_\theta}{r} \cdot \frac{\partial W_\theta}{\partial \theta} + \frac{W_z}{\text{Cos } \beta} \frac{\partial W_\theta}{\partial x} + \frac{W_r W_\theta}{r} = - \frac{1}{\rho} \frac{\partial p}{r \partial \theta} \quad . \text{(F.4)}$$

Now the velocity components can be expressed in terms of u and v, as used in the present procedure, as follows:

$$W_\theta = v$$

$$W_z = u.\text{Cos } \alpha.\text{Cos } \beta$$

$$W_r = u.\text{Cos } \alpha.\text{sin } \beta$$

By substituting these equations into Equation (F.4) and also by using $\frac{1}{r\partial\theta} \equiv \frac{1}{\partial y}$, we get:

$$v \frac{\partial v}{\partial y} + u.\text{Cos } \alpha \frac{\partial v}{\partial x} + \frac{(u.\text{Cos } \alpha.\text{sin } \beta).v}{r} = - \frac{1}{\rho} \frac{\partial p}{\partial y} \quad . \text{(F.5)}$$

In this equation, third term on the L.H.S. is due to the curvature; it can be regarded as a volumetric source term. Except for this term, Equation (F.5) is like the v-momentum equation in the (x,y) cartesian coordinate system. To make it suitable for the present procedure, it should be further transformed into (x,ψ) coordinate system by using the following relations:

$$\frac{\partial v}{\partial x} = \frac{\partial v}{\partial x} \cdot \frac{\partial x}{\partial x} + \frac{\partial v}{\partial \psi} \frac{\partial \psi}{\partial x} \quad ; \text{(F.6)}$$

$$\frac{\partial v}{\partial y} = \frac{\partial v}{\partial x} \cdot \frac{\partial x}{\partial y} + \frac{\partial v}{\partial \psi} \cdot \frac{\partial \psi}{\partial y} \quad . \quad (F.8)$$

These are further simplified by $\frac{\partial x}{\partial x} \equiv 1$ and $\frac{\partial x}{\partial y} \equiv 0$. $\frac{\partial \psi}{\partial x}$ and $\frac{\partial \psi}{\partial y}$ can be expressed, from the definition of ψ, as follows:

$$\frac{\partial \psi}{\partial x} = - \rho v t \quad ; \quad (F.9)$$

$$\frac{\partial \psi}{\partial y} = \rho (u \text{ Cos } \alpha) t \quad ; \quad (F.10)$$

where t is the flow depth normal to x and y directions, and u Cos α is the x-direction component of velocity.

Substitution of Equations (F.6) to (F.10) into Equation (F.5) yields:

$$u \text{ Cos } \alpha \frac{\partial v}{\partial x} + \frac{(u \text{ Cos } \alpha \text{ sin } \beta).v}{r} = - u \text{ Cos } \alpha . t . \frac{\partial p}{\partial \psi} \quad . \quad (F.11)$$

Now by cancelling out u Cos α from all the terms of this equation and by integrating it over a control volume of Fig. 3.2, we get:

$$\Delta\psi(v_2 - v_1) + \left(\frac{v}{r} \sin \beta\right)_{avg} \Delta x . \Delta\psi = (p_3 - p_4) . \Delta x . t \quad (F.12)$$

where suffix 'avg' denotes the average value for the control volume. As already mentioned, the second term on L.H.S. is the source term due to curvature. Its magnitude will primarily depend on sin β which is a known quantity; often sin β is quite small. Further, v_{avg} is replaced by v_1; this makes Equation (F.12) a linear equation for calculating v_2.

APPENDIX G

CONVERGENCE-IMPROVEMENT DEVICES

This appendix presents three modifications to the calculation step no. 6, described in Section 3.6. The first modification improves the numerical stability while the other two help in procuring faster rates of convergence of solution.

(1) Under-relaxation of pressure correction, p'

The calculated local pressure corrections are under-relaxed by multiplying them with a factor which is less than unity. On the basis of computations reported in this thesis, the under-relaxation factor of 0.5 has been found to be optimum.

(2) Local iterations for calculation of p''s

In the first few integration sweeps, the calculation step 6, i.e. calculation of the local pressure corrections and other associated corrections, is repeated twice. It helps in the rapid development of a reasonable cross-stream distribution of pressure; and, therefore, improves the convergence rate. The larger numbers of such iterations have not been found to be beneficial.

(3) Upstream shifting of pressure corrections

In the partially-parabolic solution scheme, described in Section 3.6, the downstream influences travel upstream at a rate of one cross-stream plane per iteration. This rate of transmission of downstream events is slow; it can be improved by applying parts of the pressure corrections calculated at a constant-x section to the pressures at the upstream locations. This modification is similar to the one reported by Pratap (1975). The practice adopted in the present procedure is described below.

Suppose local pressure corrections have been just computed for the axial section j; then, the pressures at three upstream planes j-1, j-2 and j-3 are also corrected as follows:

$$p'_{i,j-k} = \beta^k p'_{i,j} \quad , \text{(G.1)}$$

where k takes the value of 1, 2 and 3 respectively; and β is a reduction factor which is calculated, from the 'A' coefficients of Equation (3.15), as follows:

$$\beta = \frac{A_E}{(A_N + A_S + A_E + A_W)} \quad ; \text{(G.2)}$$

Strictly speaking, this β value should be used only in the calculation of $p'_{i,j}$ from $p'_{i,j+1}$; however, its use for the neighbouring upstream planes also have been found to be adequate.

APPENDIX H

IMPERIAL COLLEGE OF SCIENCE & TECHNOLOGY

DEPARTMENT OF MECHANICAL ENGINEERING

EXHIBITION ROAD, LONDON, SW7 2AZ.

"Predictions of Two-Dimensional Boundary Layers with the Aid of the k - ε Model of Turbulence."

by

A.K. Singhal & D.B. Spalding

MAY 1975 HTS/75/15

IMPERIAL COLLEGE OF SCIENCE & TECHNOLOGY

DEPARTMENT OF MECHANICAL ENGINEERING

EXHIBITION ROAD, LONDON, SW7 2AZ.

"Predictions of Two-Dimensional Boundary Layers with the Aid of the k - ε Model of Turbulence."

by

A.K. Singhal & D.B. Spalding

MAY 1975 HTS/75/15

PREDICTIONS OF TWO-DIMENSIONAL BOUNDARY LAYERS WITH THE AID OF THE k - ε MODEL OF TURBULENCE

by

A.K. SINGHAL & D.B. SPALDING

Mechanical Engineering Department
Imperial College, London, S.W.7.

ABSTRACT

The paper presents numerical predictions of boundary layers exhibiting a large variety of streamwise pressure distributions, including those featuring in the 1968 Stanford Conference on Turbulent Boundary Layers (Ref. 1). The model of turbulence employed is one in which the local state of turbulence is characterised by two quantities, the turbulence kinecic energy k and its dissipation rate ε. Transport equations for both k and ε are solved simultaneously with that for the momentum of mean flow. The computed results are compared with the experimental data and the agreement is found to be in general good. The empirical constants in the model are the same as those used in earlier applications (Ref.2) of the model; thus the universality of the model is further demonstrated.

Results of two boundary layers, under infinite-swept-wing conditions, are also included.

CONTENTS

		PAGE
	ABSTRACT	
	NOMENCLATURE	
1.	INTRODUCTION	1
2.	THE k - ε MODEL	1
3.	SOLUTION PROCEDURE	2
4.	RESULTS OF PREDICTIONS	5
5.	DISCUSSION	6
6.	RESULTS OF INFINITE-SWEPT-WING PROBLEMS	7
7.	CONCLUDING REMARKS	8
8.	ACKNOWLEDGEMENTS	8
9.	REFERENCES	9
	APPENDIX:- INITIAL PROFILES FOR k AND ε	11
	TABLE I:- NAME OF INVESTIGATOR/S & NAUTRE OF THE EXPERIMENT FOR FLOWS OF FIG.2.	12
	FIGURES (1-12)	13

NOMENCLATURE

SYMBOLS	MEANING
C_1) C_2) C_μ)	Constants in the turbulence model.
E	Constant in the logarithmic law of wall.
H_{12}	Shape factor ($\equiv \delta_1/\delta_2$).
k	Turbulence kinetic energy.
K	Constant in the logarithmic law of the wall.
p	Time-mean pressure.
R_2	Momentum-thickness Reynolds number, $\equiv \frac{U\delta_2}{\nu}$.
s	Shear-stress coefficient, $\left(\equiv \frac{\tau}{\rho U^2}\right)$.
u	Time-mean velocity in the direction of main flow.
u'	Instantaneous fluctuating component of u.
U	Free-stream velocity.
u_τ	Shear velocity ($\equiv \sqrt{\tau/\rho}$).
v	Time-mean velocity in direction normal to the surface.
v'	Instantaneous fluctuating component of v.
x	Distance along the main flow direction.
y	Distance normal to x direction.

GREEK SYMBOLS

δ_1, δ_2	Respectively displacement thickness and momentum thickness.
ε	Rate of dissipation of turbulence energy.
μ	Molecular viscosity.
μ_τ	Turbulent viscosity.
ν	Kinematic viscosity.
ρ	Density.
σ_k	Turbulent Prandtl number for k.
σ_ε	Turbulent Prandtl number for ε.
τ	Shear stress.

SUBSCRIPTS

C	a point at the edge of the couette flow (Fig.1).
G	a point at the free stream.
S	a point at the wall.
o	starting station of the experiment.

1. INTRODUCTION

The Stanford Conference on Turbulent Boundary Layers (Ref. 1) provides an extensive set of experimental data which can be conveniently used to test the adequacy of a turbulence model. The turbulence model considered here is the k - ε model (Ref.2), which belongs to the category of two-equation models. The model has already been tested in several different situations (Refs. 2, 3 and 4), but not yet extensively for boundary layers near walls. The present study fills up this gap and also illustrates an application of the model to a somewhat more complex flow situation, i.e. the boundary layer on an infinite swept wing.

The salient features of the model are described in Section 2 of the paper. Section 3 contains information regarding the solution procedure. Predictions are presented in Section 4; and their comparison with the experimental data is discussed in Section 5. Section 6 presents some of the results of infinite swept-wing problems. The concluding remarks are given in Section 7.

2. THE k - ε MODEL OF TURBULENCE

Two quantities, turbulence kinetic energy k and its dissipation rate ε, are used to characterise the local state of turbulence. The magnitudes of both of these quantities are calculated from differential transport equations which are solved simultaneously with the continuity and streamwise-momentum equations of the mean flow. Full details of the model are given in Ref. 2; here, only the equations and empirical constants will be mentioned.

For a plane, uniform-density, turbulent boundary-layer flow, the set of governing equations can be written in the following form, the symbols having the meanings given in the nomenclature.

continued/...

Continuity equation:

$$\frac{\partial u}{\partial x} + \frac{\partial v}{\partial y} = 0 \qquad \ldots (2.1)$$

Streamwise-momentum equation:

$$\rho u \frac{\partial u}{\partial x} + \rho v \frac{\partial u}{\partial y} = \frac{\partial}{\partial y}\left(\mu \frac{\partial u}{\partial y} - \rho\overline{u'v'}\right) - \frac{dp}{dx} \qquad \ldots (2.2)$$

Turbulent-viscosity hypothesis:

$$-\rho\,\overline{u'v'} = \mu_T \frac{\partial u}{\partial y} \equiv \left(C_\mu \rho \frac{k^2}{\varepsilon}\right)\frac{\partial u}{\partial y} \qquad \ldots (2.3)$$

Turbulence-kinetic-energy equation:

$$\rho u \frac{\partial k}{\partial x} + \rho v \frac{\partial k}{\partial y} = \frac{\partial}{\partial y}\left(\frac{\mu_T}{\sigma_k}\frac{\partial k}{\partial y}\right) + \mu_T \left(\frac{\partial u}{\partial y}\right)^2 - \rho\varepsilon \qquad \ldots (2.4)$$

Turbulence-dissipation-rate equation:

$$\rho u \frac{\partial \varepsilon}{\partial x} + \rho v \frac{\partial \varepsilon}{\partial y} = \frac{\partial}{\partial y}\left(\frac{\mu_T}{\sigma_\varepsilon}\frac{\partial \varepsilon}{\partial y}\right) + C_1 \frac{\varepsilon}{k} \mu_T \left(\frac{\partial u}{\partial y}\right)^2 - C_2 \rho \frac{\varepsilon^2}{k} \qquad \ldots (2.5)$$

The last two equations of the above set are valid only for the regions of high turbulence Reynolds number (i.e. $\mu_T >> \mu$), which prevail everywhere except very close to the wall. A different treatment is employed for the wall-near region, as described in Section 3.

The quantities C_μ, C_1, C_2, σ_k and σ_ε are empirical constants; the values used are : $C_\mu = 0.09$, $C_1 = 1.44$, $C_2 = 1.92$, $\sigma_k = 1.0$ and $\sigma_\varepsilon = \frac{K^2}{\sqrt{C_\mu}(C_2 - C_1)}$, where K is von Karman's constant in the log law of the wall taken as equal to 0.4. The basis for choosing these values is given in References 2 and 3.

3. SOLUTION PROCEDURE

The set of simultaneous equations, given in the above

continued/...

section, is solved by the implicit, finite-difference method of Patankar and Spalding (Ref.5) with detailed modifications reported in Reference 6.

In order to solve wall-boundary-layer problems, the flow is divided into two regions, a and b, as shown in Fig. 1. Region a is close enough to the wall so that the influences of convection are negligible; the region can be treated as one-dimensional i.e. as a Couette flow, for which empirically (or theoretically) derived non-dimensional functions (wall functions) connect the shear stress, the velocity difference, etc.

In the larger region b, the laminar-viscosity influences are insignificant ($\mu << \mu_T$) and therefore the equations of Section 2 prevail. The wall functions provide boundary conditions at the inner boundary of region b.

In the present computations, boundary conditions and initial conditions for the dependent variables u, k and ε are specified in the following way, which can be regarded as conventional and well-established, apart from minor details.

WALL BOUNDARY CONDITIONS:

These are specified by way of wall functions, namely:

$$\frac{u_C}{u_\tau} = \frac{1}{K} \ln \left[E. \frac{y_C u_\tau}{\nu} \left(1 + \frac{1}{2} \frac{y_C}{\rho u_\tau^2} \frac{dp}{dx} \right)^{\frac{1}{2}} \right] \quad \ldots (3.1)$$

$$k_C = C_\mu^{-\frac{1}{2}} \left(\frac{\tau}{\rho}\right)_C \quad \ldots (3.2)$$

$$\varepsilon_C = k_C^{3/2} / (C_\mu^{\frac{1}{4}} . K y) \quad \ldots (3.3)$$

Here suffix C is used for specifying the flow properties at the point C (see Fig. 1). Eqn. 3.2 is a modified form of the logarithmic law of the wall, the basis of which is

continued/...

explained in Reference 6; the shear stress at the wall, τ_s, is obtained from it. K and E are the universal constants and are taken equal to 0.4 and 7.7 respectively. Eqn. 3.2 and 3.3 represent wall functions for k and ε and are the same as proposed in Reference 2.

FREE-STREAM BOUNDARY CONDITIONS:

At the free-stream edge of the boundary layer, the following boundary conditions are employed.

$$u = U \qquad \ldots (3.4)$$

$$U \frac{dk_G}{dx} = -\varepsilon_G \qquad \ldots (3.5)$$

$$U \frac{d\varepsilon_G}{dx} = -C_2 \frac{\varepsilon_G^2}{k_G} \qquad \ldots (3.6)$$

Suffix G specifies free stream conditions. Eqns. 3.5 and 3.6 are the reduced forms of the Eqns. 2.3 and 2.4 respectively.

In addition to the boundary conditions, we must specify the initial profiles, for each dependent variable, at the starting station of integration.

INITIAL CONDITIONS:

Initial velocity profiles are specified directly from the available data of mean-velocity measurements. It would have been equally simple to specify k and ε profiles if the measured data for turbulence kinetic energy and shear stress were also available. In the absence of any such data, the initial profiles for k and ε are assumed on the basis of available information such as wall shear stress, streamwise pressure gradient and free-stream turbulence intensity; the details of the practice adopted are explained in the Appendix.

continued/...

4. RESULTS OF PREDICTIONS

Computations have been made of the boundary layers which were specified for the 1968 Stanford Conference. These are cases of two-dimensional, turbulent flows, subjected to different streamwise pressure gradients. The experimental data for all the flows have been compiled by Coles and Hirst (Ref.1). The supplied information consists of: $U \sim x$ variations; mean velocity profiles; skin friction coefficients and the integral parameters, δ_1 and δ_2.

In Fig. 2, the present predictions are compared with the experimental data for all the flows excepting Riabouchinsky's moving-belt flow. Each flow in the diagram is identified by an IDENT number from Reference 1; the nature of the experiment and the names of investigator (s) can be obtained from Table I. For each flow, the predicted variations of shape factor H_{12}, wall-shear coefficient S_s and momentum-thickness Reynolds number R_2, are compared with the relevant experimental data; the lines represent predictions and the crosses represent the experimental data. The abscissa is distance x, measured along the surface in the direction of flow.

For five cases, i.e. IDENT = 1400, 2400, 2500, 2800 and 3300, the predictions of mean velocity, shear stress and turbulence kinetic-energy profiles are compared with the available data at the last station of the relevant experiment. These predictions and data are displayed in Figs. 3 to 7.

COMPUTATIONAL DETAILS:

For each flow, 25 cross-stream grid-points were used to cover the boundary layer. The nearest grid point to the wall was always located in the fully-turbulent region. Typical forward-step size in the x direction was one-fifth

continued/...

of the boundary-layer thickness, and the computing time on a CDC 6600 computer was 2 seconds per 100 forward-steps i.e. on average about 5 seconds for one flow. It was established, by variations of the grid fineness, that the physically significant results of the computations were substantially grid-independent.

5. DISCUSSION

From Fig. 2 it is obvious that, for the majority of cases, agreement between predictions and experimental data is quite good. For the few cases of poor agreement, comparison has been made with predictions reported by other authors contributing to the Stanford Conference; they also, by and large, experienced the same divergences of theory from experiment; it therefore appears that the predictions are in as good agreement with the data as the experimental accuracy warrants.

Some of the factors which affect accuracy of the experimental data and thus result in the apparent differences between predictions and data, are discussed below.

(a) Three-dimensionality effects

It is difficult to conduct experiments in which the flow is truly two-dimensional. Many of the experiments under investigation suffered from three-dimensionality effects. This fact was revealed by the lack of obedience of many of the measurements to the integral momentum equation of two-dimensional flow. To make a comparative assessment of the experiments, the discrepancies in momentum balance were computed by Coles and Hirst for each flow and these were presented by way of the quantities PI and PR; the definitions of these quantities are given in Fig. 8 which reproduces PL, PR ~ x graphs, from Reference 1, for the first three experiments i.e. IDENT = 1100, 1200 and 1300.

For a truly two-dimensional boundary-layer flow, PL and

continued/...

PR must be equal. Fig. 8 shows that the three experiments satisfy this requirement to different extents; and it can be seen from Fig. 2 that the agreement between predictions and data is also correspondingly good or poor. The predictions start to deviate from the experimental data at about the same position as PL deviates from PR. A similar correspondence is observed for the other flows too.

(b) Inadequate number of points to specify the mean velocity profile

The integral parameters can be wrongly ascribed when there are too few cross-stream points close to the wall for the velocity profile to be determined correctly. This is probably the cause of disagreement in H_{12} between experiments and predictions of flows 3100, 3600, 3700, and 4100 in Fig. 2.

COMPARISON OF PREDICTED u, τ AND k PROFILES WITH EXPERIMENTS

Figs. 3 to 7 display the predicted profiles of velocity, shear stress and turbulence kinetic energy at the last station of flows 1400, 2400, 2500, 2800 and 3300, and compare them with the experimental data, wherever available. The agreement seems to be generally satisfactory. It is important to note that none of the constants has been adjusted to secure better agreement for any particular case.

6. RESULTS OF INFINITE-SWEPT-WING PROBLEMS

Refs. 11 and 12 report two experimental studies on turbulent boundary layers under infinite-swept-wing conditions. These have also been predicted in a similar way to the other problems of Section 4, except for the obvious extensions required for the z-component of mean velocity (see Fig. 9 for the definitions of various co-

continued/...

ordinates and velocities).

Figs 10 and 11 show the comparison between measured and predicted variations of shear-stress coefficient and surface cross-flow angle, β_s. The agreement can be regarded as satisfactory everywhere except in the downstream part of Berg and Elsenaar's flow (Fig.11), where the divergence between predictions and experiments is due to non-uniformity of pressure in the spanwise direction. For Bradshaw and Terrell's flow (Ref. 11), measurements of turbulence quantities are also reported. Fig. 12 shows that the predicted profiles of turbulence kinetic energy and shear stress are in reasonable conformity with the experimental data.

7. CONCLUDING REMARKS

(i) The k - ε model of turbulence is capable of predicting two-dimensional turbulent boundary layers with non-uniform streamwise pressure gradients and also boundary layers under infinite-swept-wing conditions; all with one set of constants.

(ii) The same turbulence constants as have been used in several other applications are valid here also.

(iii) The predictions are as satisfactory as the accuracy of the experimental data warrants.

(iv) The computation time required is very modest.

8. ACKNOWLEDGEMENTS

One of the authors (A.K. Singhal) gratefully acknowledges the financial support of Combustion Heat and Mass Transfer Ltd.

9. REFERENCES

1. D.E. COLES & E.A. HIRST (1968)

"Proceedings of AFOSR-IFP-Stanford Conference on Turbulent Boundary Layers", Vol. 2: Compiled Data.

2. B.E. LAUNDER & D.B. SPALDING (1974)

"The numerical computation of turbulent flows".

Computer Methods in Applied Mechanics & Engineering, Vol. 3, pp 269-289.

3. B.E. LAUNDER & D.B. SPALDING (1972)

"Mathematical models of turbulence".

Academic Press.

4. B.E. LAUNDER, A. MORSE, W. RODI & D.B. SPALDING (1972)

"The prediction of free shear flows - a comparison of the performance of six turbulence models".

Proceedings of NASA Conference on Free Shear Flows, Langley. (Also Imperial College, Mechanical Engineering Dept. Report No. HTS/72/15.)

5. S.V. PATANKAR & D.B. SPALDING (1967)

"A finite-difference procedure for solving the equations of the two-dimensional boundary layer".

Int.J. Heat Mass Transfer, 10, pp 1389-1412.

6. D.B. SPALDING (1974)

"A general computer program for two-dimensional boundary-layer problems".

Imperial College, Mech.Engg. Dept. Report No. HTS/74/32.

7. H. HERRING & J. NORBURY (1967)

"Some experiments on equilibrium turbulent boundary layers in favourable pressure gradients".

J.Fluid Mech., 27, p 541.

8. P. BRADSHAW (1967)

"The turbulence structure of equilibrium boundary layers".

J.Fluid Mech., 29, p. 625.

9. P. BRADSHAW & D.H. FERISS

"The response of a retarded equilibrium turbulent boundary layer to sudden removal of pressure gradient".

NPL Aero Rep. 1145.

continued/...

10. K.H. NG & D.B. SPALDING (1970)

"Predictions of two-dimensional boundary layers on smooth walls with a two-equation model of turbulence".

Imperial College, MECH. Engg. Dept. Report No. HTS/70/1.

11. P. BRADSHAW & M.G. TERRELL (1969)

"The response of a turbulent boundary layer on an infinite swept wing to the sudden removal of pressure gradient".

NPL Aero Report 1305.
Also ARC 31 514 FM.4095.

12. B. VAN DEN BERG & A. ELSENAAR

"Measurements in a three-dimensional incompressible turbulent boundary layer in an adverse pressure gradient under infinite swept wing conditions".
NLR TR 72092 U.

APPENDIX

INITIAL PROFILES FOR k AND ε:

For the initial profile of k, we assume:

$$k = a + b\,\eta + c\eta^2 + d\eta^3$$

where $\eta = y/y_G$ and the quantities a, b, c and d are evaluated from the following conditions.

(i) At $\eta = \eta_C$: $k = c_\mu^{-\frac{1}{2}} (\tau/\rho)_C$

$$\text{and } \frac{dk}{d\eta} = g + |g|$$

$$\text{where } g = \frac{y_G}{2\,\rho\, C_\mu^{\frac{1}{2}}} \cdot \frac{dp}{dx}$$

The suffix C refers to point C of Fig. 1.

(ii) At $\eta = 1$:

$$k = .0005 \times U^2$$ (Free-stream turbulence intensity is assumed to be 0.05%. for all the cases)

$$\text{and } \frac{dk}{d\eta} = 0$$

For the initial profile of ε, we use the following relations:

$\varepsilon = C_\mu k^{3/2}/\ell$, where $\ell \equiv$ turbulence length scale

$\ell = C_\mu^{1/4} . \ell m$, where ℓm = mixing length

For the mixing-length distribution, we assume

$\ell m = \kappa y$ for $y \leq \frac{\lambda}{\kappa} y_G$

$\ell m = \lambda . y_G$ for $y > \frac{\lambda}{\kappa} . y_G$

where $\lambda = .09$, and $\kappa = .4$.

IDENT	Investigator/s	Nature of experiment	Year
1100	Ludwieg and Tillmann	Mild adverse pressure gradient	1949
1200	Ludwieg and Tillmann	Strong adverse pressure gradient	1949
1300	Ludwieg and Tillmann	Accelerating flow	1949
1400	Wieghardt and Tillmann	Flat plate flow	1944
1500	Tillmann	Ledge flow	1945
2100	Schubauer and Klebanoff		1950
2200	Clauser	Flow No. 1	1954
2300	Clauser	Flow No. 2	1954
2400	Bradshaw and Ferriss	Relaxing flow	1965
2500	Bradshaw	$\alpha = -.15$	1966
2600	Bradshaw and Ferriss	$\alpha = -.255$	1965
2700	Herring and Norbury	$\beta = -.35$	1967
2800	Herring and Norbury	$\beta = -.53$	1967
2900	Perry		1966
3000	Bell	Constant pressure	1966
3100	Bell	Series D	1966
3200	Bell	Series E	1966
3300	Bradshaw	$\alpha = 0 \rightarrow -.255$,C	1967
3500	Newman	Airfoil, Series 2	1951
3600	Moses	Case 1	1964
3700	Moses	Case 2	1964
3800	Moses	Case 3	1964
4000	Moses	Case 5	1964
4100	Moses	Case 6	1964

(Contd.)

Table I: Name of investigator/s and nature of the experiment for flows shown in Fig. 2.

IDENT	Investigator/s	Nature of experiment	Year
4400	Schubauer and Spangenberg	Flow A	1960
4500	Schubauer and Spangenberg	Flow B	1960
4800	Schubauer and Spangenberg	Flow E	1960
5000	Fraser	Flow A	1956
5100	Fraser	Flow B	1956
5200	Stratford	Experiment 5	1959
5300	Stratford	Experiment 6	1959
6300	Bauer	Spillway, 60^{o}	1951

Table I: (Contd.)

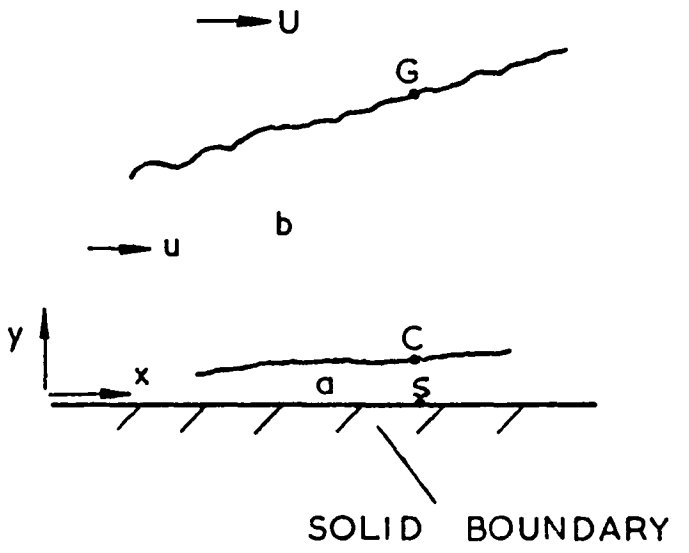


FIG. 1 : THE TWO REGIONS (a and b) WITHIN A WALL BOUNDARY LAYER .

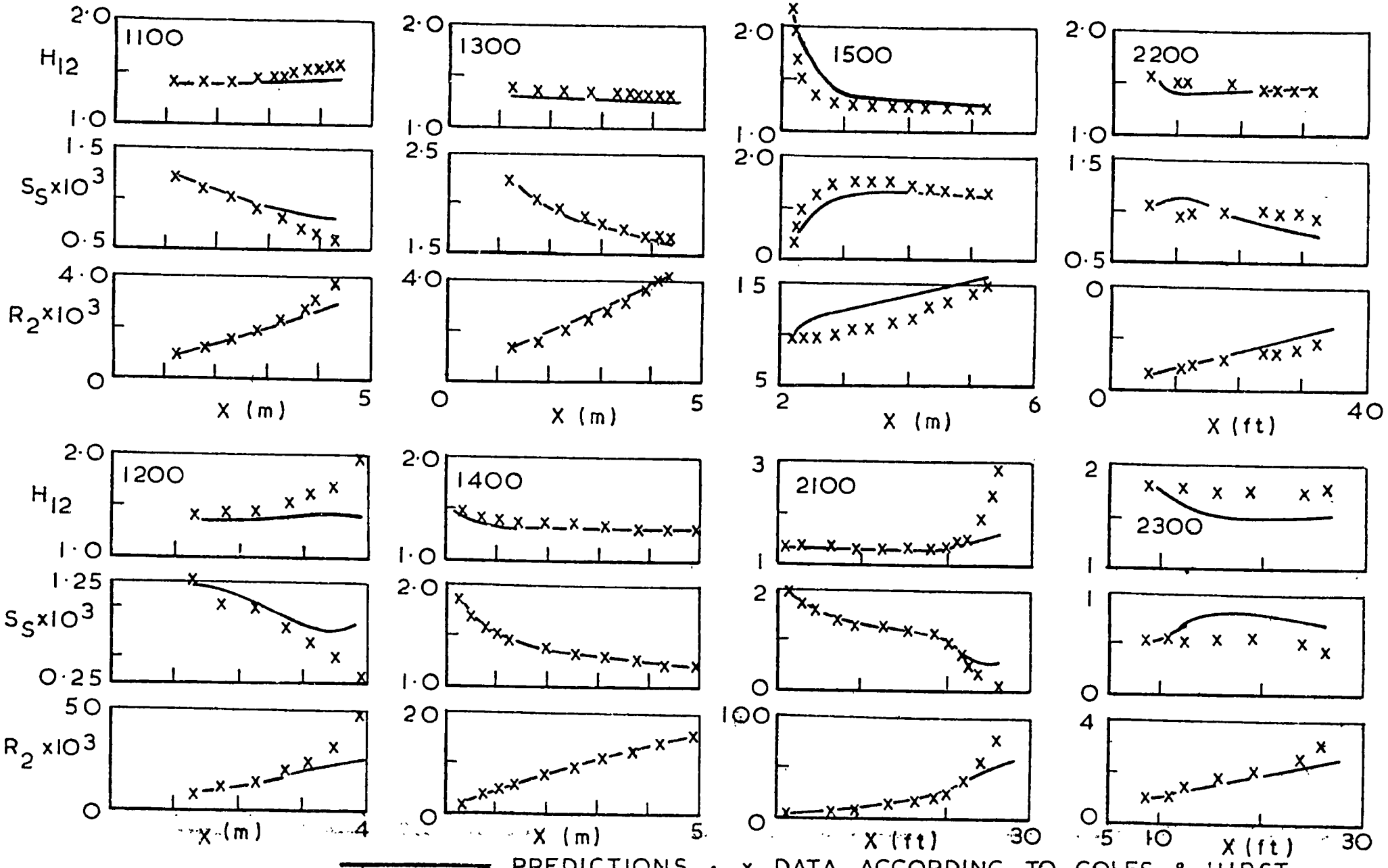
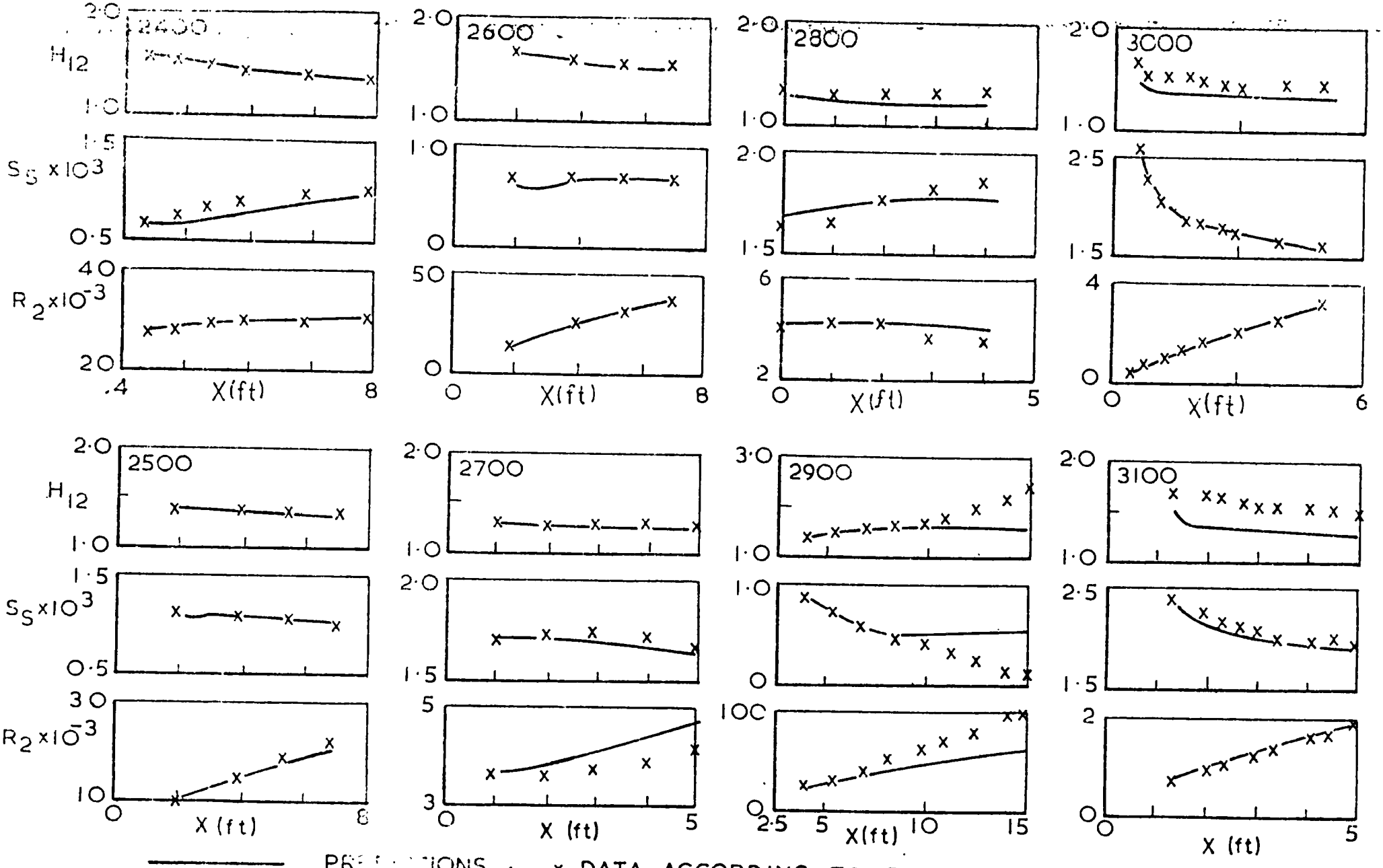
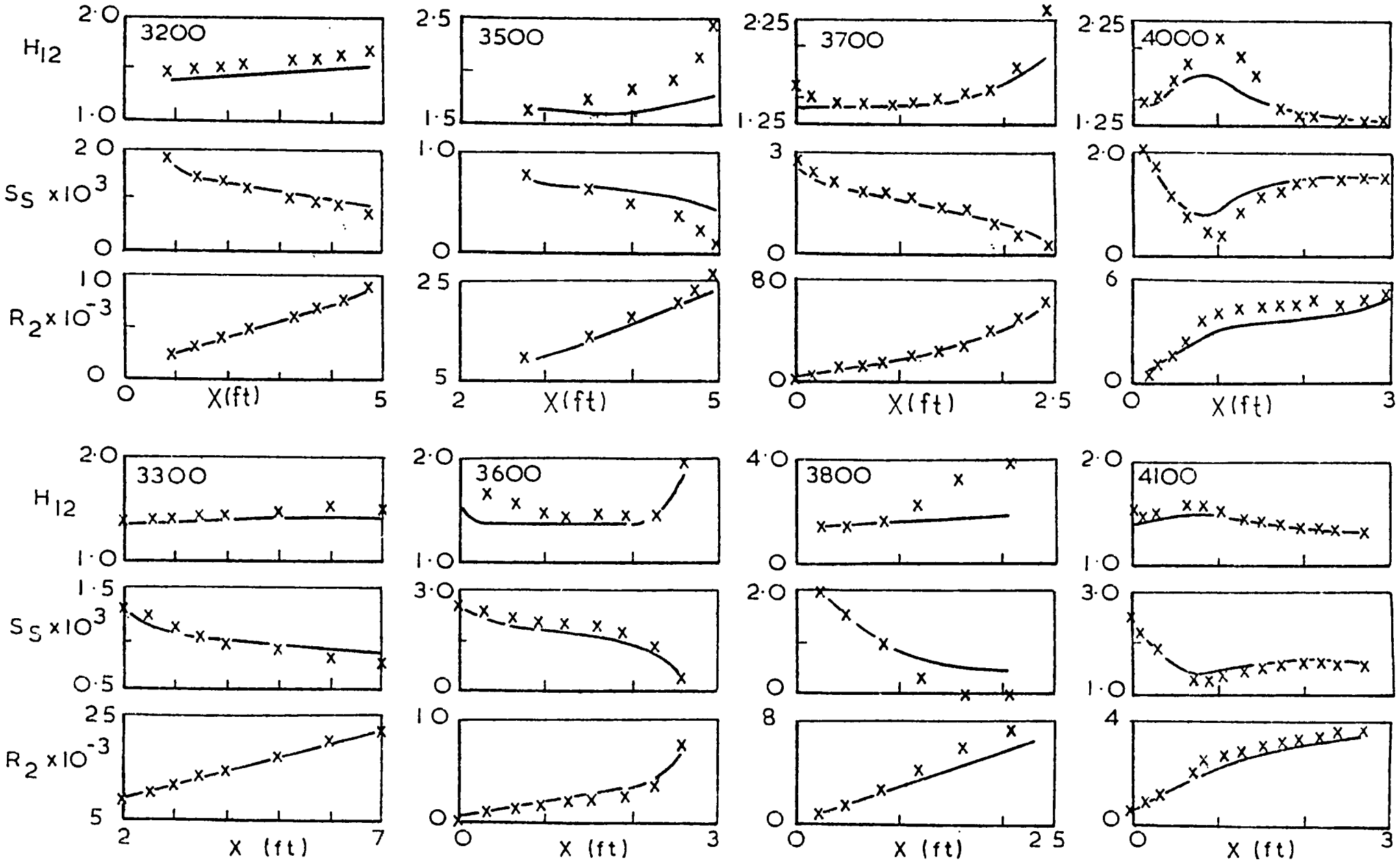


FIG. 2: COMPARISON OF H_{12}, S_S AND R_2 PREDICTIONS WITH EXPERIMENTS.



PREDICTIONS ; x DATA ACCORDING TO COLES & HIRST

FIG.2 (Cont'd). COMPARISON OF H_{12}, S_S AND R_2 PREDICTIONS WITH EXPERIMENTS.



——— PREDICTIONS ; x DATA ACCORDING TO COLES & HIRST

FIG. 2 (Cont'd) COMPARISON OF H_{12}, S_S AND R_2 PREDICTIONS WITH EXPERIMENTS.

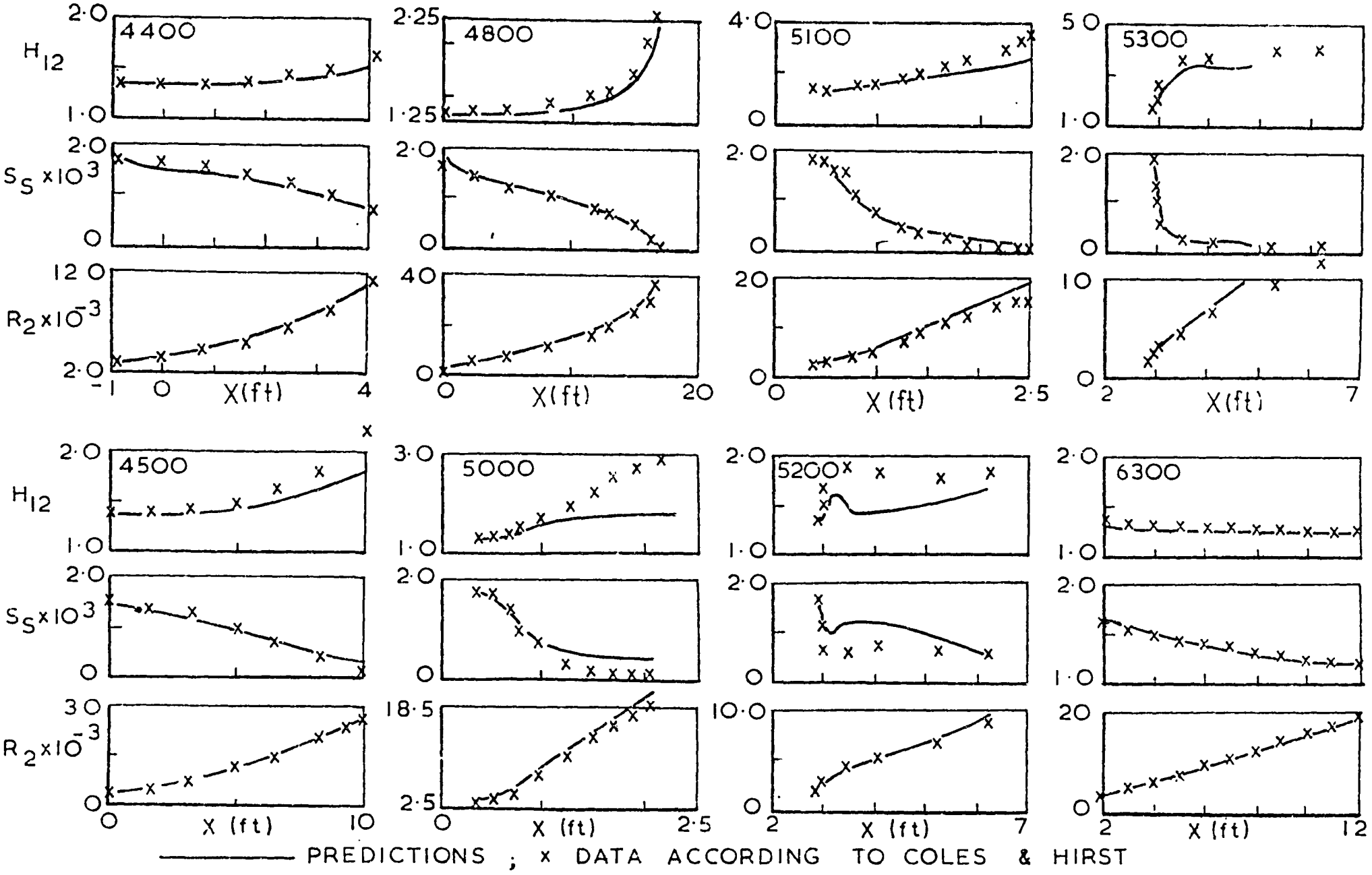
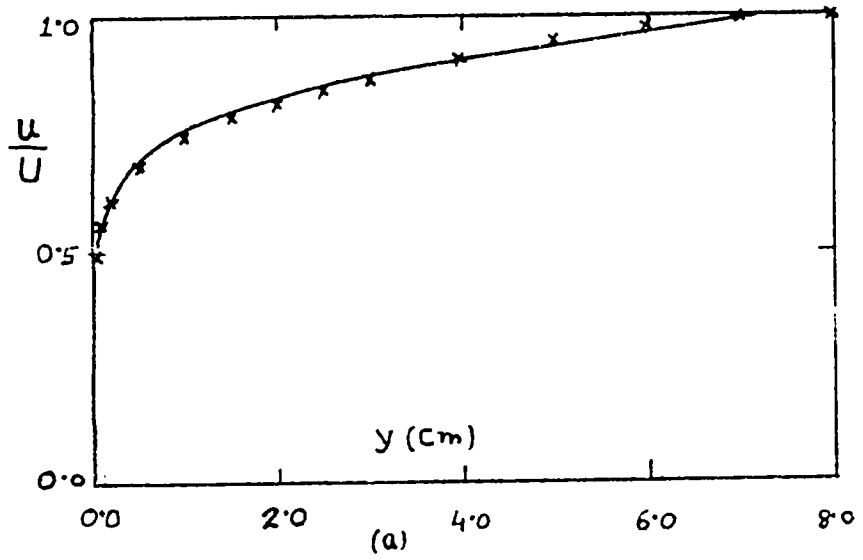
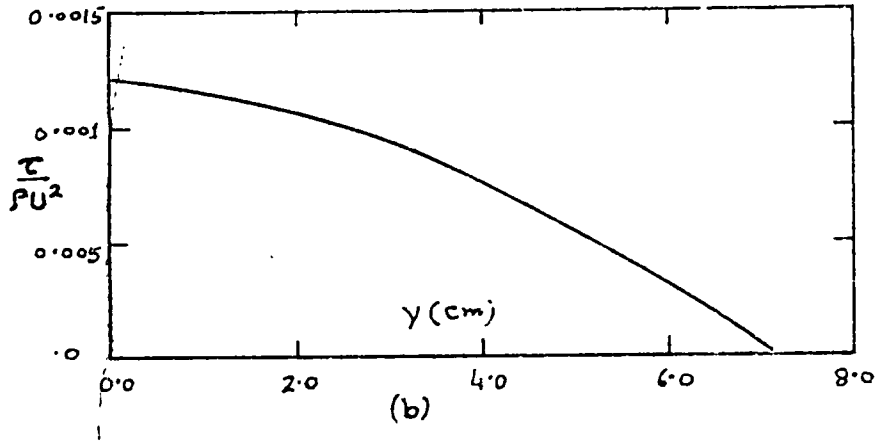


FIG. 2. (Cont'd) COMPARISON OF H_{12}, S_S AND R_2 PREDICTIONS WITH EXPERIMENTS





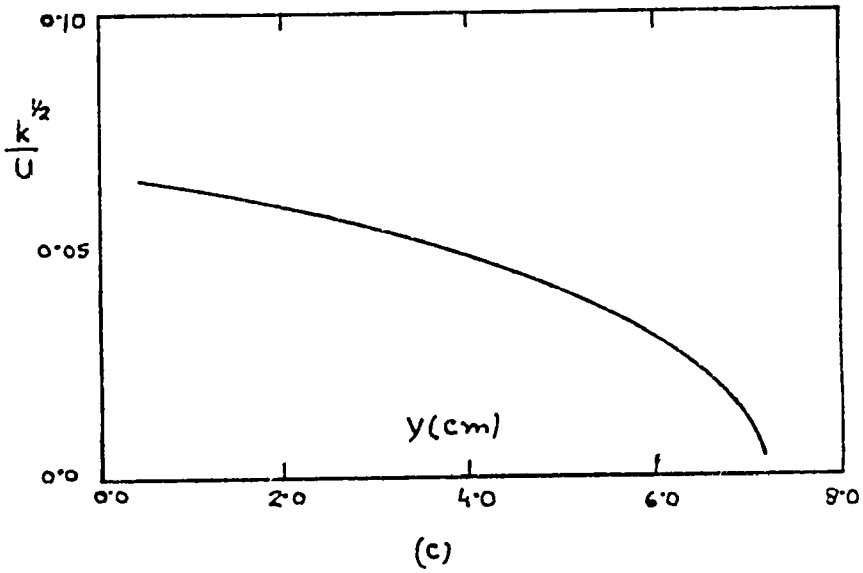
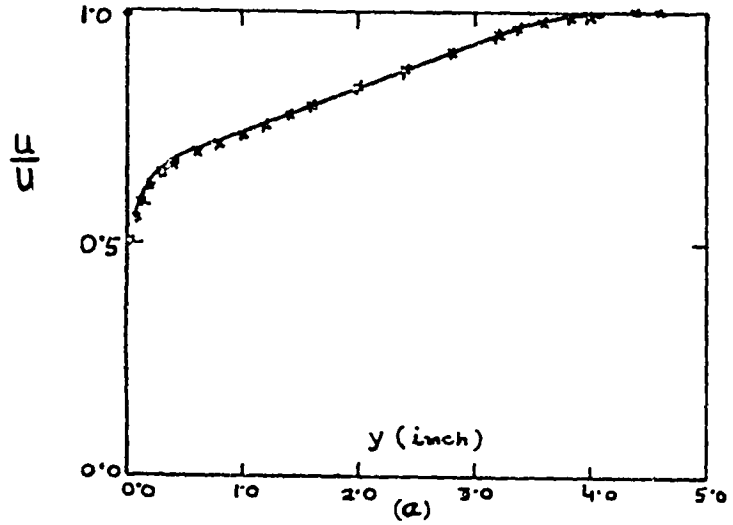


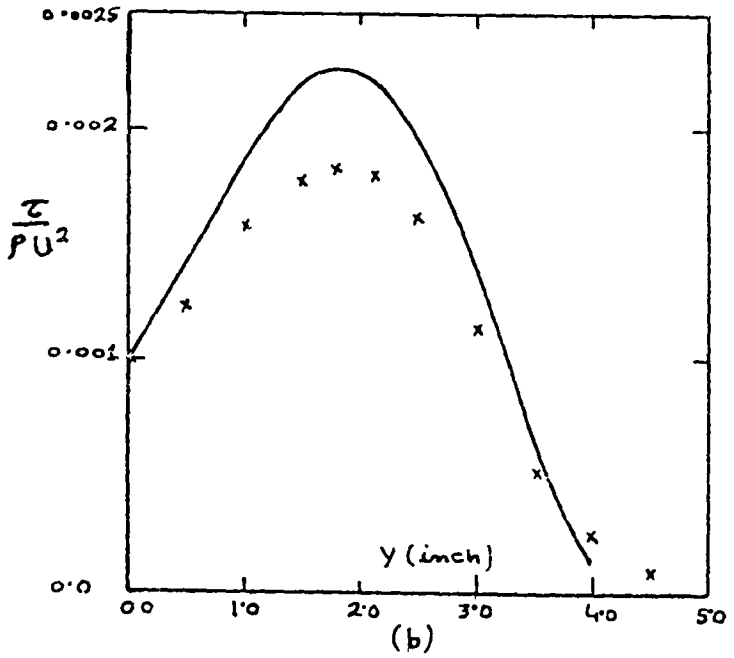
FIG.3. Comparison of predicted u, τ and k profiles with the experiment of Weighardt and Tillman (IDENT = 1400), at x = 4.987m.

(a) Comparison of the u/U profile.

(b) Predicted $\tau/(\rho U^2)$ profile; data not available.

(c) Predicted $k^{\frac{1}{2}}/U$ profile; data not available.





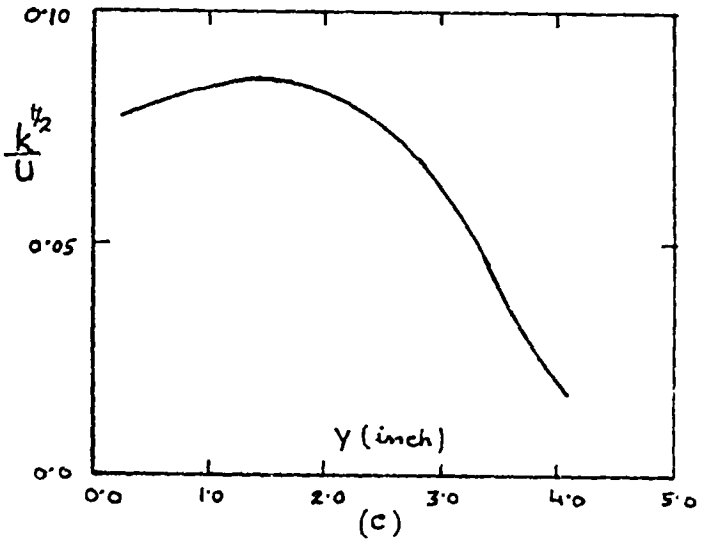
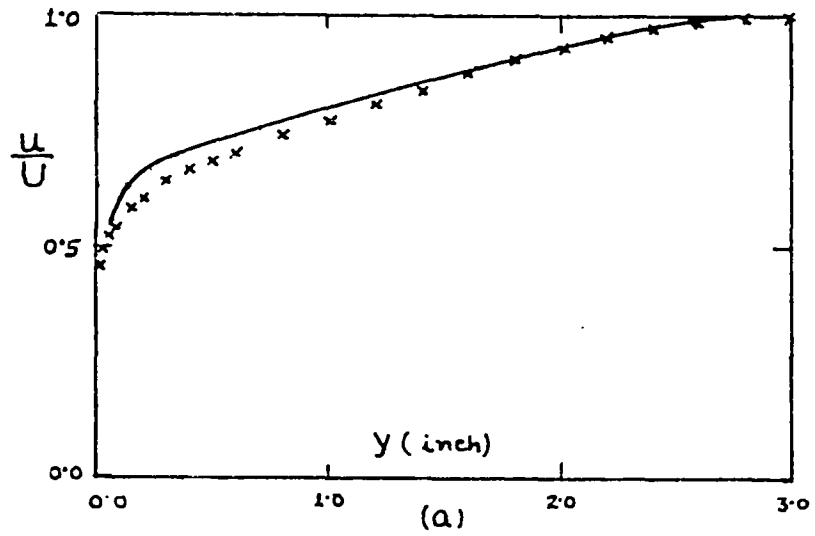


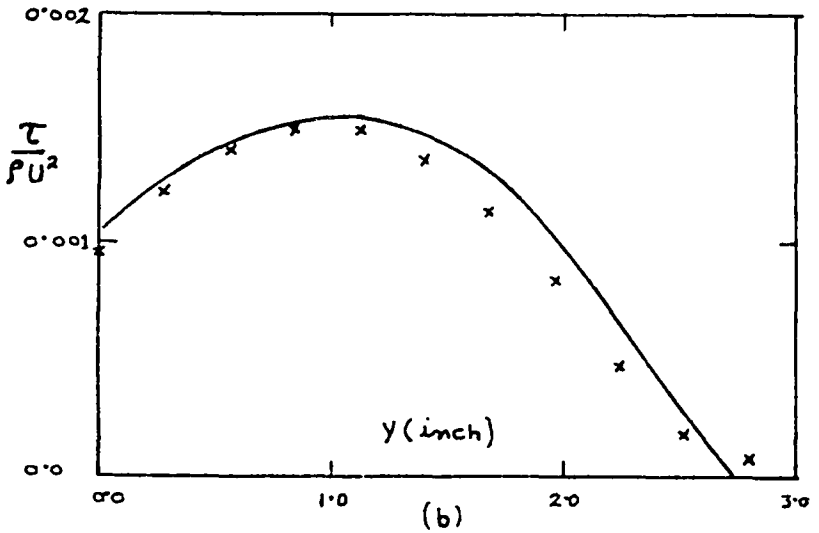
FIG. 4. Comparison of predicted u, τ and k profiles with the experiment of Bradshaw and Ferriss (IDENT = 2400) at x = 7.9 ft.

(a) Comparison of the u/U profile.

(b) Comparison of the $\tau/(\rho U^2)$ profile.

(c) Predicted $k^{\frac{1}{2}}/U$ profile; data not available.





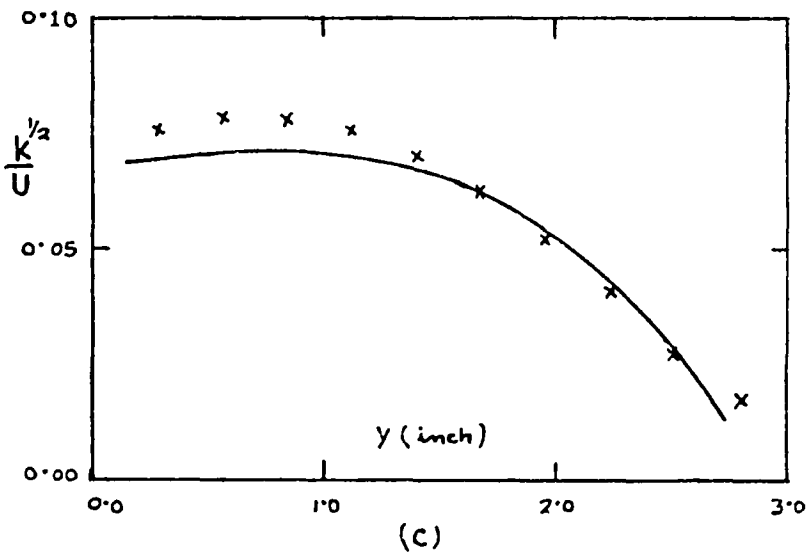
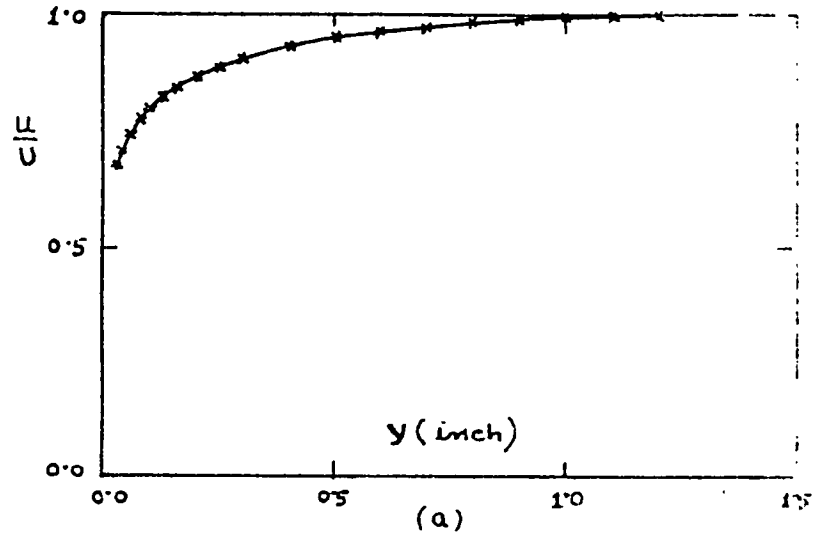
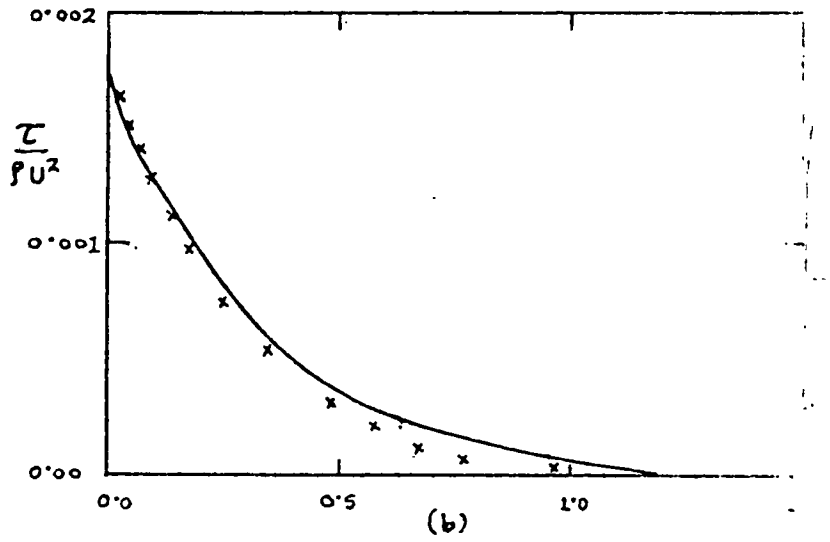


FIG.5. Comparison of predicted u , τ and k profiles with the experiment of Bradshaw, "α = -0.15" at x = 7 ft. (IDENT = 2500).

—— Predictions; X, Data





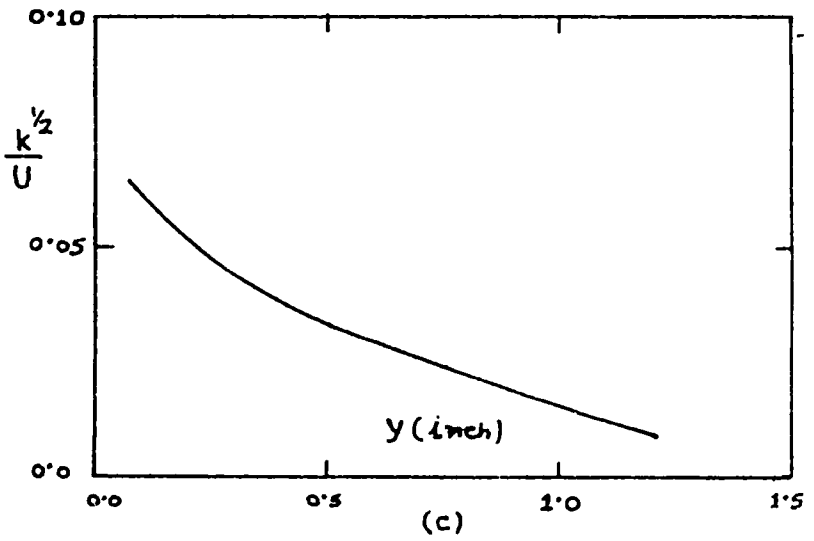
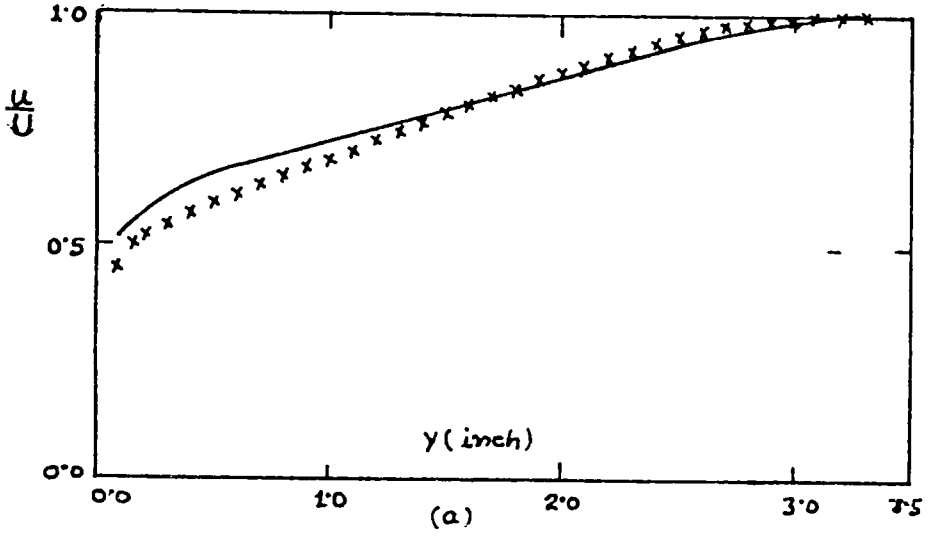


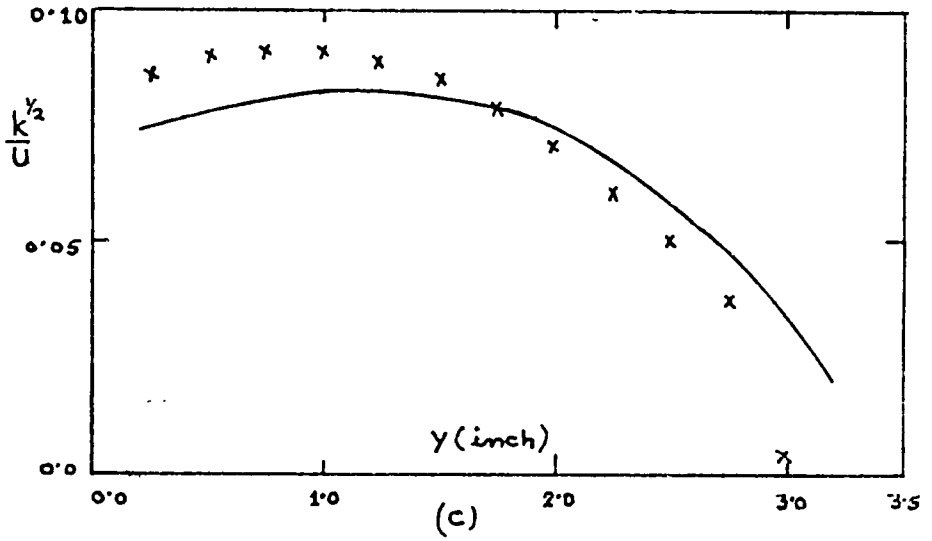
FIG.6. Comparison of predicted u, τ and k profiles with the experiment of Herring and Norbury "B = -0.53" at x = 4 ft. (IDENT = 2800).

(a) Comparison of the u/U profile.

(b) Comparison of the $\tau/\rho U^2$ profile.

(c) Predicted k/U profile, data not available.





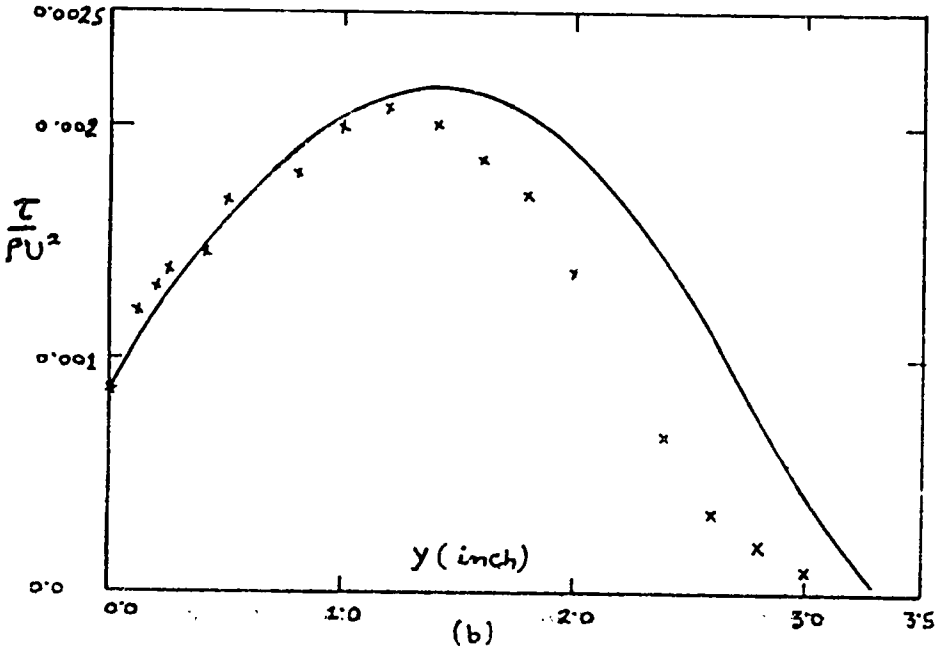
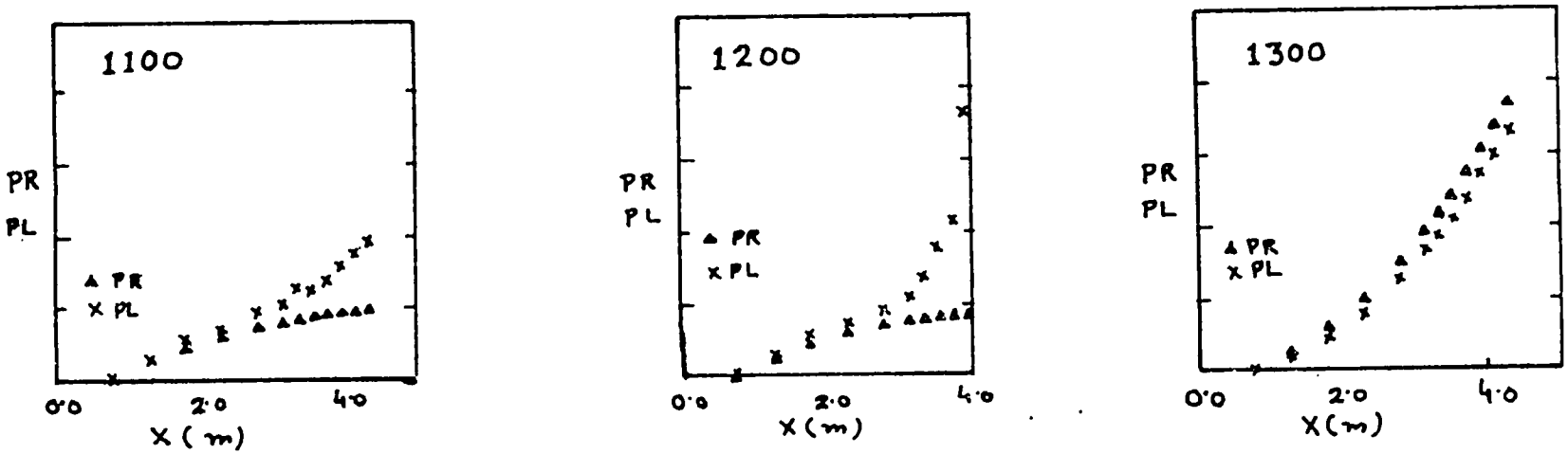


FIG.7. Comparison of predicted profiles of u, τ and k with the experiment of Bradshaw, "α = 0 → -0.255, Flow C" at x = 7 ft. (IDENT = 3300).

—— Predictions; X, Data



PL ≡ Left hand side of momentum integral equation balance.

$$PL = \frac{1}{(U^2 R_2)_o} (U^2 \times R_2) - 1 + \frac{1}{(U^2 R_2)_o} \int_{x_o}^{x} (\delta_2 \times U) \, dU \quad ;$$

PR ≡ Right hand side of momentum integral equation balance.

$$PR = \frac{1}{(U^2 R_2)_o} \int_{x_o}^{x} u_\tau^2 \, dx \quad ;$$ where suffix o stands for starting point of the experiment.

FIG.8. Discrepancies in momentum balance for first three experiments viz. IDENT = 1100, 1200 and 1300.

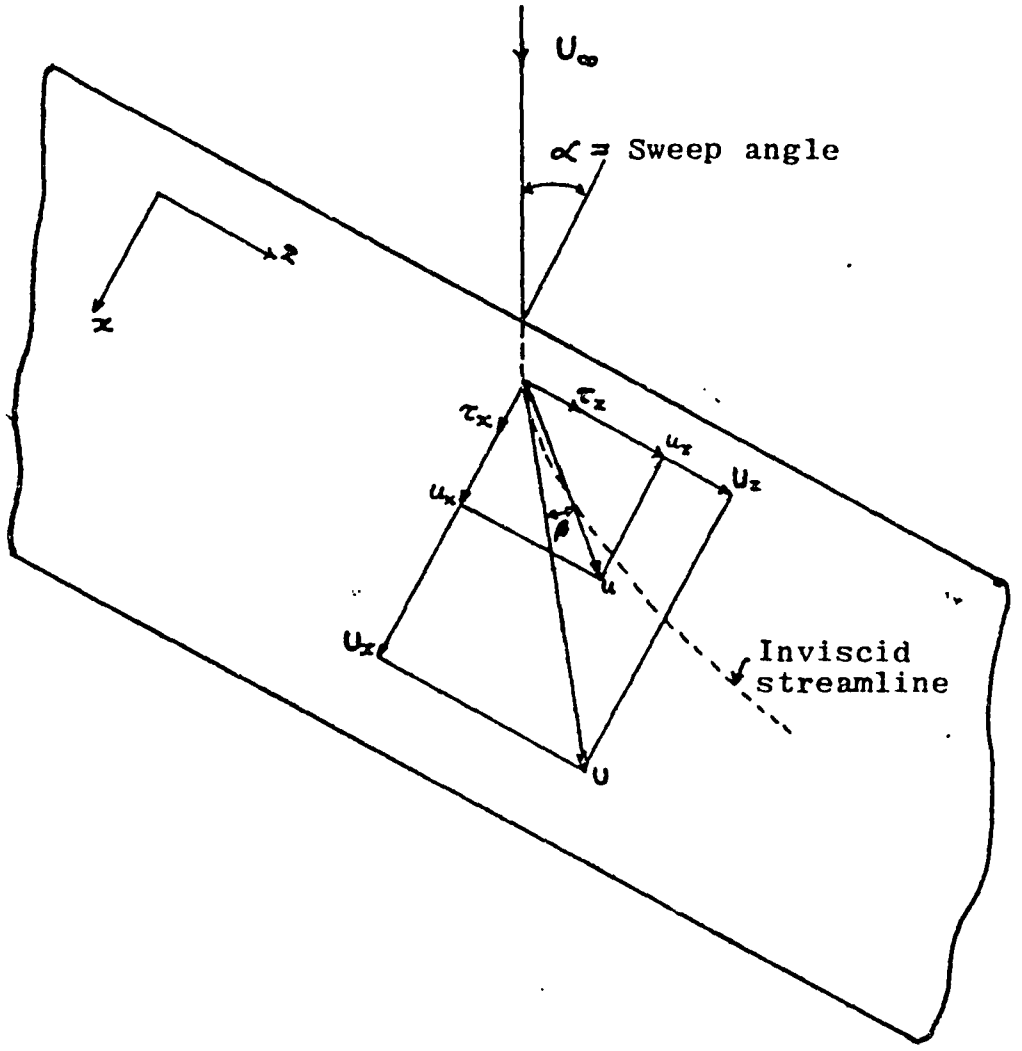


FIG.9. Sketch showing the definitions of various co-ordinates and velocities (for infinite swept wing problems).

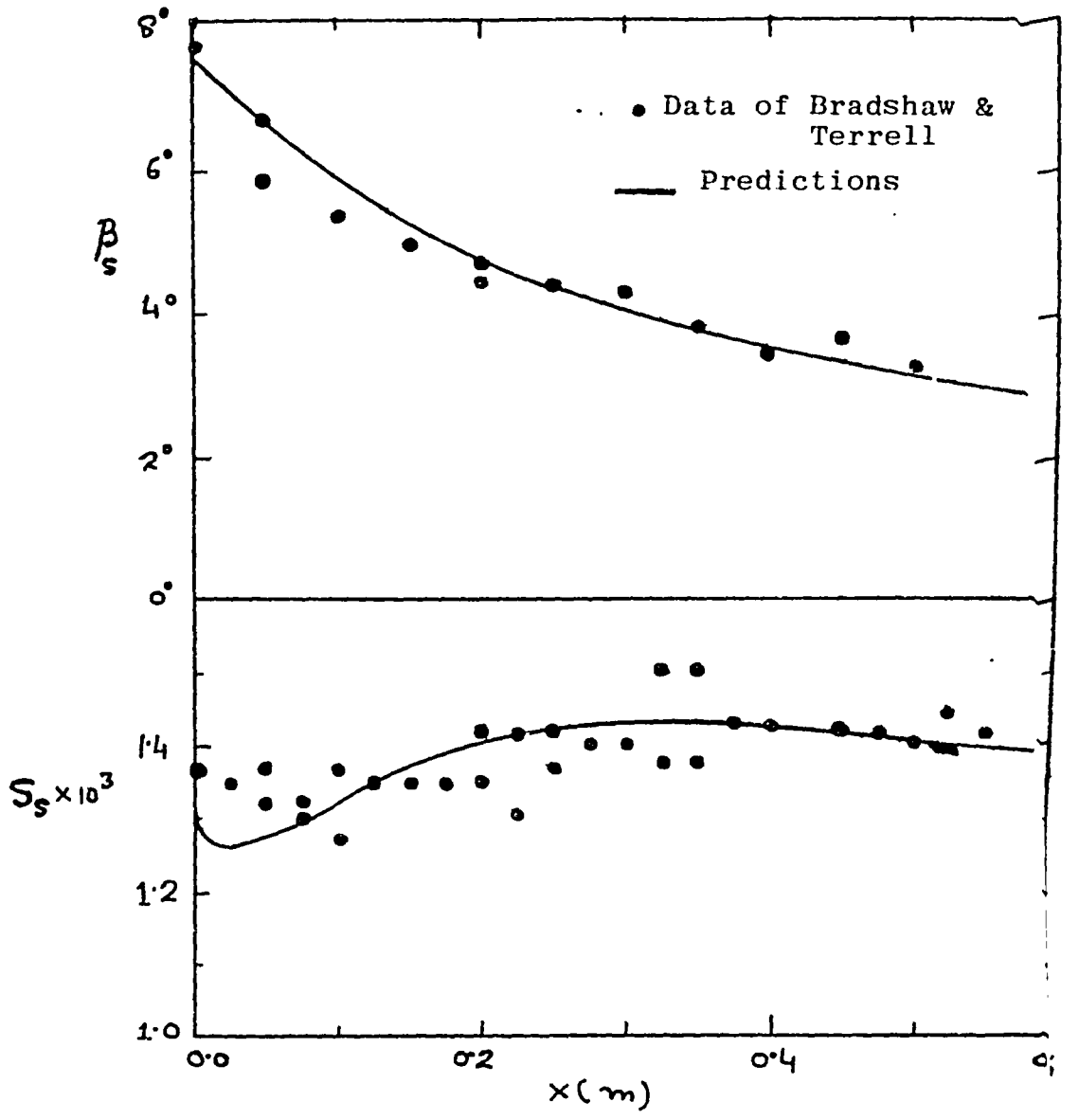


FIG.10. Predictions of surface cross-flow angle and shear stress coefficient compared with the experimental data of Bradshaw & Terrell (1969).

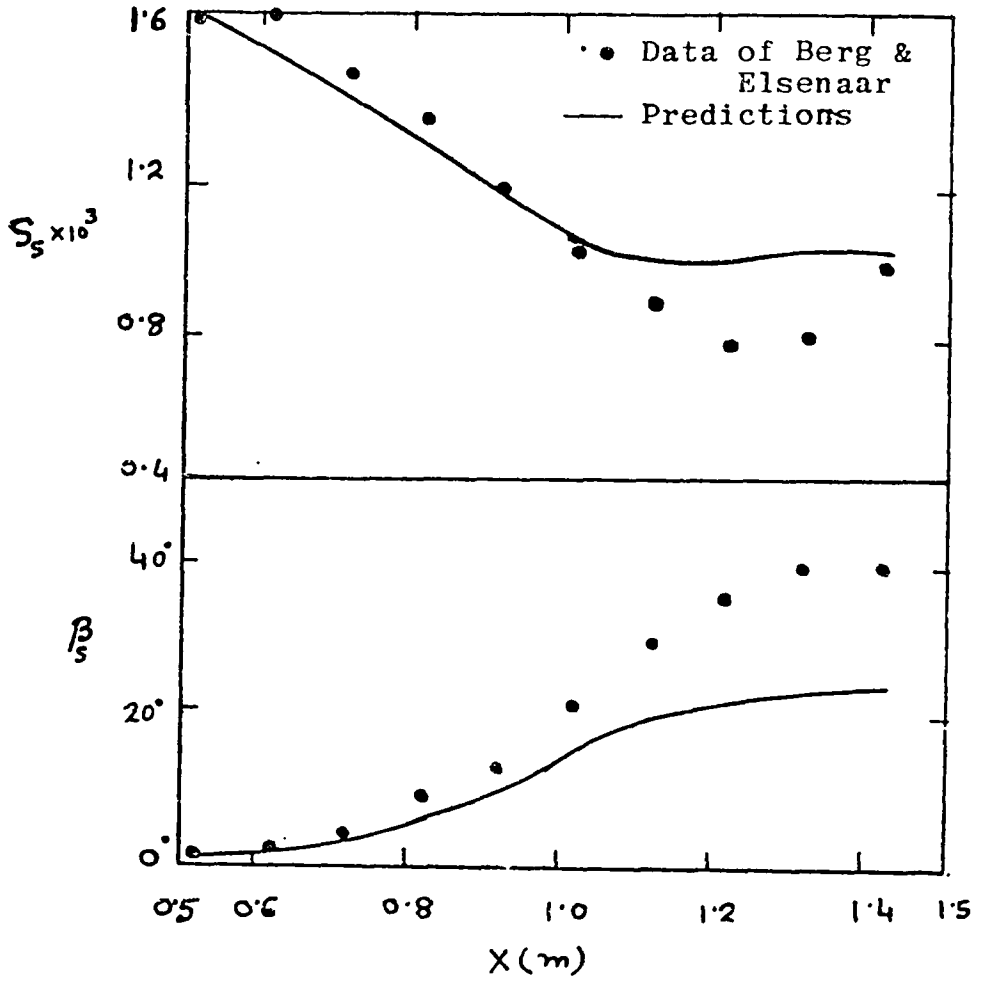


FIG.11. Predictions of shear stress coefficient and surface cross-flow angle compared with the experimental data of Berg and Elsenaar (1972).

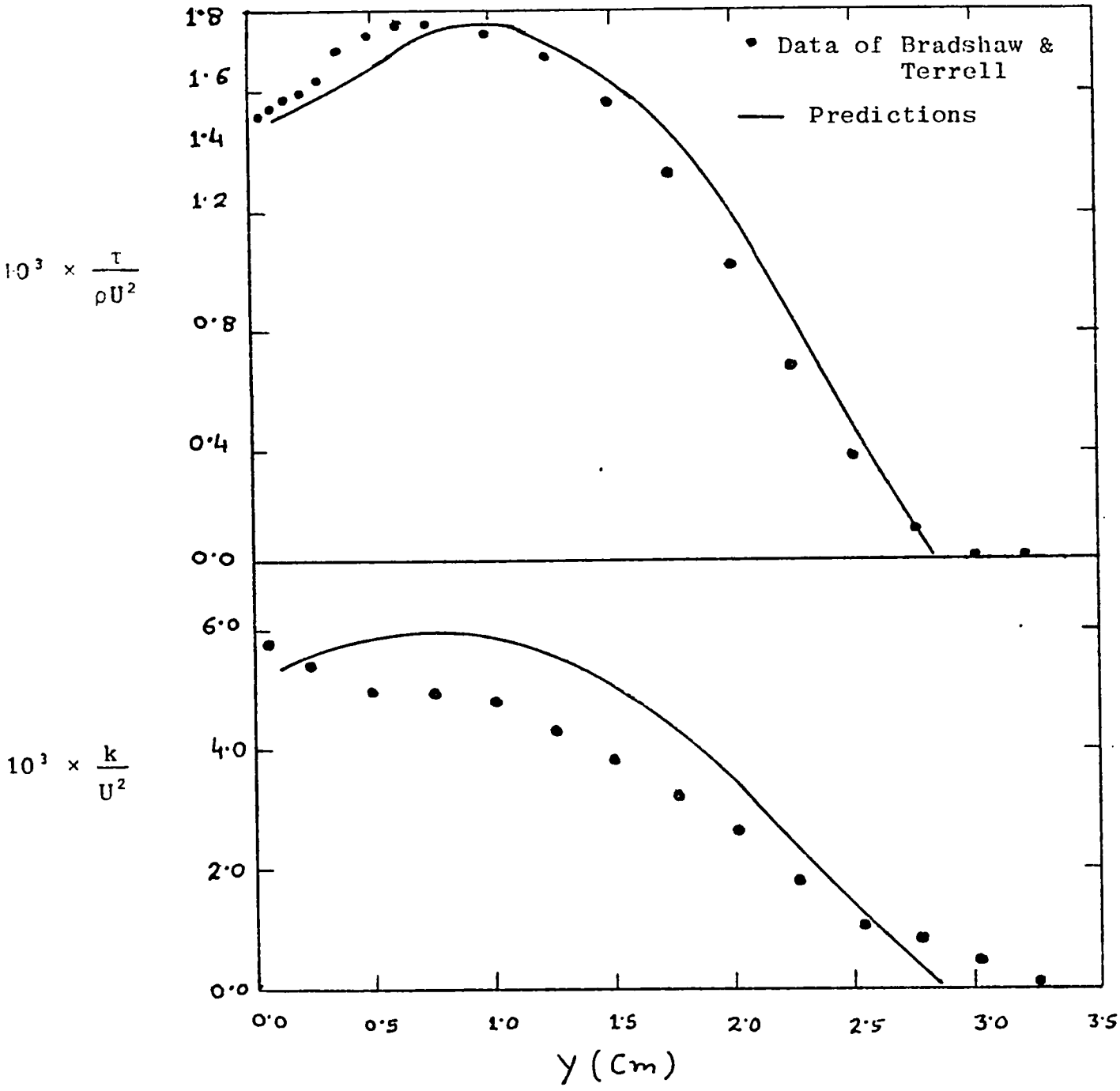


FIG.12. Predictions of shear stress and kinetic energy profiles compared with the experimental data. Bradshaw and Terrell, at x = 10 inches.